Section I

Reprints of Published Articles

July 1968-June 1969

1.E.4

Nuclear Physics A120 (1968) 489—492;

^{203m}Pb DECAY AND M4 TRANSITION PROBABILITIES IN NEUTRON-DEFICIENT LEAD ISOTOPES

R. E. DOEBLER and Wm. C. McHARRIS
Department of Chemistry †
and
Cyclotron Laboratory ††, *Department of Physics*

and

C. R. GRUHN
Cyclotron Laboratory ††, *Department of Physics*
Michigan State University
East Lansing, Michigan, USA

Received 9 September 1968

Abstract: The decay of 6.1 sec ^{203m}Pb has been examined with a high-resolution Ge(Li) spectrometer, and a 5.1 keV M2 transition was found to compete with the 825.2 keV M4 isomeric transition. The M4 transition probability, thus corrected, is now found to be consistent with those of the other M4 transitions in the lead region.

E RADIOACTIVITY ^{203m}Pb [from ^{206}Pb(p, 4n)^{203}Bi $\xrightarrow{\varepsilon}$ ^{203m}Pb];
measured E_γ, I_γ. ^{203}Pb deduced levels, J, π. Enriched target; Ge(Li) detector.

Among electromagnetic transitions, the reduced transition probabilities of M4 transitions appear to be remarkably regular and consistent with the predictions of single-particle estimates. This can perhaps be explained partly by the fact that collective nuclear deformations are not likely to contribute appreciably to a magnetic hexadecapole field. Also, most known M4 transitions are isomeric transitions just below major closed shells and involve the high-spin states depressed by spin-orbit coupling from the next higher, opposite parity oscillator shells. Consequently, it is difficult for these transitions to be enhanced by suitable admixtures in the single-particle states. When one encounters an M4 reduced transition probability that is abnormally large, one is thus tempted to look for an experimental explanation. Such was the situation with ^{203m}Pb.

The decay of the 6.1 sec isomer ^{203m}Pb has been the subject of a number of investigations [1–5]) using conversion electron and NaI(Tl) spectrometers. These studies found only a single transition of about 825 MeV, which was assigned an M4 multi-

† Supported in part by the U. S. Atomic Energy Commission.
†† Supported in part by the U. S. National Science Foundation.

polarity on the basis of conversion coefficient ratios and the mean life time of the γ-transition. The transition was assumed to go from a $\frac{13}{2}^+$ state to a $\frac{5}{2}^-$ ground state, similar to those in the other odd-mass isomers of Pb. Because the M4 reduced transition probability was abnormally large, Stockendal [1]) suggested the possibility of an additional 5 keV transition from the isomeric state to a state at 820 keV, which is populated in the electron capture decay of ^{203}Bi. Relatively little is known about the decay of ^{203}Bi, both because of its complexity and because of the difficulty of preparing ^{203}Bi free from ^{204}Bi, which has the same half-life. Nevertheless, some progress has been made, and various investigators report the spin and parity of the 820 keV state as $\frac{7}{2}^-$ [ref. [6])] or $\frac{9}{2}^-$ [ref. [1])]. If the level were $\frac{9}{2}^-$, the 5 keV transition would be an M2 and could possibly partially de-excite the 825 keV $\frac{13}{2}^+$ level along with the 825 keV M4 transition. This paper reports our observation of such a branching decay.

Because a 5 keV transition would be highly converted and very difficult to observe directly, the easiest approach is to look for the 820 keV transition that would follow the 5 keV transition. Thus, the presence or absence of an 820 keV transition in the decay of ^{203m}Pb would imply the presence or absence of the 5 keV transition.

Separated isotope ^{206}Pb in the form of $Pb(NO_3)_2$ was bombarded with 40 MeV protons from the Michigan State University Sector-Focused Cyclotron to produce ^{203}Bi ($t_{\frac{1}{2}}$ = 12 h) through the reaction ^{206}Pb(p, 4n)^{203}Bi. The ^{203}Bi activity was separated chemically from the Pb target, taken up in 6*M* HCl and loaded onto a heated 1.5 mm diameter × 5 cm long Dowex 1 × 8 200-mesh anion-exchange column. ^{203m}Pb was eluted with 0.3M HCl, at the rate of two drops every 6 sec for a 2 h period. Each drop was immediately transferred to a 7 cm^3 Ge(Li) γ-ray detector. The resolution of our system was 2.7 keV FWHM for the 825.2 keV γ-ray from ^{203m}Pb, and this could easily resolve the 820.1 and 825.2 keV γ-rays from ^{203}Bi decay and could hopefully allow us to detect any 820.1 keV γ-ray from ^{203m}Pb.

The spectrum in the region of interest of the ^{203}Bi activity (which unavoidably contained some ^{204}Bi with the same 12 h $t_{\frac{1}{2}}$) before being placed on the anion-exchange column is shown in fig. 1a. The spectrum of the ^{203m}Pb after separation, shown in fig. 1b, clearly shows a peak at 820.1 keV. The areas of the two peaks obtained after stripping and correcting for the detector efficiency yield relative γ-ray intensities of 10.6 ± 1.0 % and 89.4 ± 1.0 % for the 820.1 and 825.2 keV γ-rays, respectively. Using the theoretical conversion coefficients of Sliv and Band [7]) for the K and L shells and those of Rose [8]) for the M shell to correct for internal conversion, the $\frac{13}{2}^+$ state is found to decay 8 % by the 5.1 keV transition and 92 % by the 825.2 keV M4 transition. Our proposed decay scheme for ^{203m}Pb is shown in fig. 2. The previous uncertainty in the assignment for the 820.1 keV state can be removed; the 5.1 keV transition is an M2, making the state $\frac{9}{2}^-$.

To check the possibility that some of the ^{203}Bi might have been eluted from the anion-exchange column along with the ^{203m}Pb and thereby have caused the 820.1 keV peak, the drops of eluted activity were saved and counted after the ^{203m}Pb had died away. No ^{203}Bi activity was found in these drops.

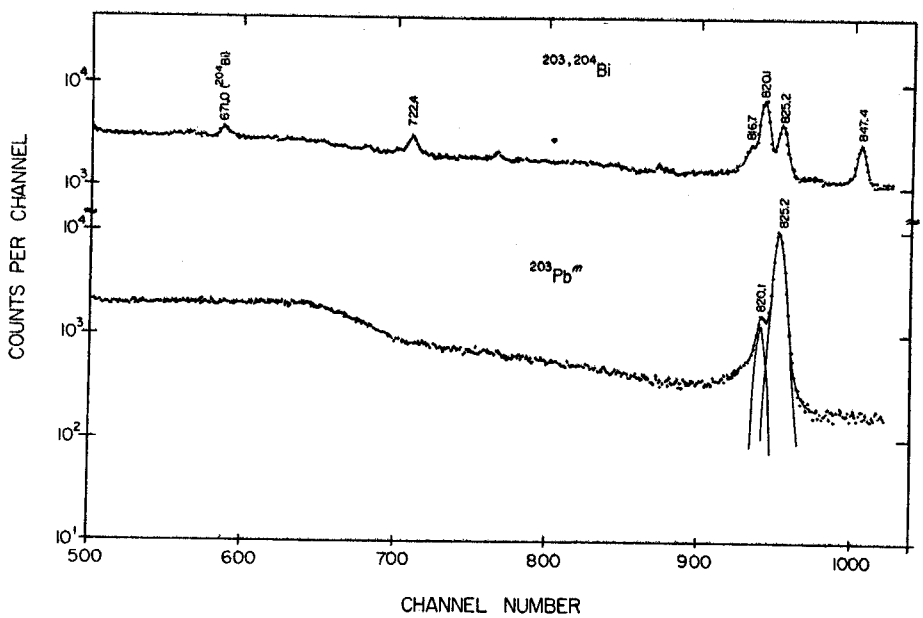

Fig. 1. a) The γ-ray spectrum of ^{203}Bi (unavoidably containing some ^{204}Bi, which has the same 12 h $t_{\frac{1}{2}}$) taken with a 7 cm^3 Ge(Li) detector. b) The γ-ray spectrum of ^{203m}Pb after chemical separation from its ^{203}Bi parent. The Compton edge at channel $\approx$ 670 is from the 899.1 and 912.0 keV γ-rays of ^{204m}Pb, which are off-scale in this figure.

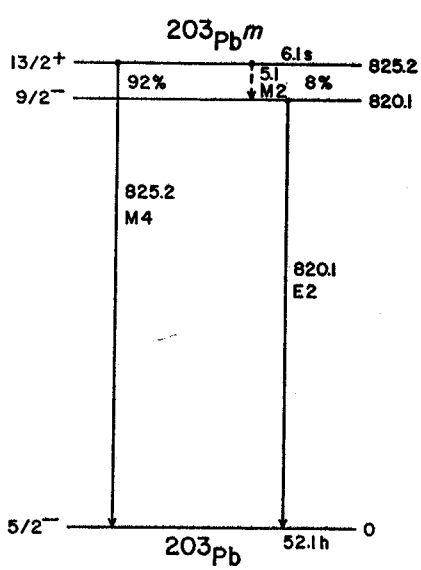

Fig. 2. The decay scheme of ^{203m}Pb.

Stockendal and his co-workers [1,2]) calculated the squares of the radial matrix elements for the $i_{\frac{13}{2}} \rightarrow f_{\frac{5}{2}}$ M4 γ-transitions in the odd-mass Pb isomers, using Moszkowski's approximations [9]). They found the $|M|^2$ value for the transition in ^{203m}Pb

TABLE 1

Radial matrix elements for M4 γ-transitions in odd-mass Pb isotopes

$\|M\|^2$ \ A	197	199	201	203	205	207
Stockendal [a])	3.8±0.5	3.8±0.2	3.5±0.2	4.3±0.1		3.7±0.1
present calc. [a])	3.6±0.4	3.7±0.2	3.5±0.2	3.8±0.2	(18±2) [b])	3.6±0.1

[a]) We have used our own experimental data for the ^{203m}Pb calculation and the most recent half-life values tabulated in ref. [10]) for the other calculations.

[b]) The value of $|M|^2$ for ^{205m}Pb is inexplicably large, perhaps because of the presence of two unresolved 1014 keV transitions, and is included only for the sake of completeness. See ref. [11]).

to be 15 % larger than the average of the others. Their later values [1]) are listed in table 1, along with those that we calculated in the same manner, using the most recent partial half-life values for all the M4 γ-transitions [10]). The $|M|^2$ value for the ^{203m}Pb transition now fits nicely in line with the others, indicating that this transition behaves regularly, as one would expect for M4 transitions.

References

1) R. Stockendal, Ark. Fys. **17** (1960) 579
2) R. Stockendal, J. A. McDonnell, M. Schmorak and I. Bergström, Ark. Fys. **11** (1955) 165
3) V. K. Fischer, Phys. Rev. **99** (1955) 764
4) A. R. Fritsch, Ph. D. thesis, Univ. of Calif. Lawrence Radiation Lab., Report UCRL 3452 (1956);
A. R. Fritsch and J. M. Hollander, J. Inorg. Nucl. Chem. **6** (1958) 165
5) L. Persson and R. Stockendal, Ark. Fys. **19** (1961) 303
6) T. Novakov, R. Stockendal, M. Schmorak and B. Johansson, Ark. Fys. **14** (1958) 85
7) L. A. Sliv and I. M. Band, in Alpha, beta and gamma-ray spectroscopy, ed. by K. Siegbahn (North-Holland, Amsterdam, 1965)
8) M. E. Rose, Internal conversion coefficients, (North-Holland, Amsterdam, 1958)
9) S. A. Moszkowski, Phys. Rev. **89** (1953) 474;
Siegbahn, *op. cit.*
10) E. K. Hyde, I. Perlman and G. T. Seaborg, The nuclear properties of the heavy elements, (Prentice-Hall, New Jersey, 1964) chap. 10;
C. M. Lederer, J. M. Hollander and I. Perlman, Table of isotopes (John Wiley, New York, 1967) 6th Ed.
11) R. Stockendal, Ark. Fys. **17** (1960) 553

SPECTRAL AVERAGES IN TRANSFER REACTIONS INVOLVING TARGETS WITH SINGLE ACTIVE SHELL *

R. K. BANSAL
Cyclotron Laboratory, Michigan State University, East Lansing, Michigan, USA
and Tata Institute of Fundamental Research, Bombay-5, India **

Received 10 May 1968

We have presented the equations relating the energies of the spectroscopic-weighted averages of the spectra obtained in equivalent nucleon transfer reactions involving single-active-shell targets containing only neutrons in their active shell. For the sake of completeness we have also given the results for the case of inequivalent transfer: in this latter case there is no restriction on the neutron-proton composition of the target state.

If we take a target nucleus with a isospin T_0 and perform a stripping or a pick up reaction on it, then the spectra of the residual nucleus, in general consists of two groups of levels, one with isobaric spin $T = T_0 - \frac{1}{2}$ and the other with $T = T_0 + \frac{1}{2}$. It is of physical interest to know the energies of the centroids (spectroscopic weighted averages) of these groups in terms of the average two-body interaction parameters, because this relationship between spectral averages and the interaction parameters, on the one hand is a valuable constraint on the nature of the effective two body interaction, for a given structure model governing the reaction; on the other hand, for a given nucleon-nucleon force, it is a test for the validity of the model.

We present in this paper the equations describing the above mentioned relationship for the case of equivalent transfer where the nucleon transferred to a single-active-neutron rich shell is characterized by the $(nlj \equiv \rho_1)$ of the active shell. For the shake of completeness we also give the results for inequivalent transfer where the transferred nucleon is characterised by the quantum numbers of any orbit other than the active one.

Following the procedures used earlier [1,2], for the case of single nucleon transfer reactions, we can relate the first energy moment of the spectroscopic factor $\mathcal{S}_\Gamma$, to the reduced matrix element of an operator containing the relevant part of the interaction Hamiltonian as:

$$\sum_\Gamma (-1)^{\Gamma_0+\rho_i-\Gamma}(2\Gamma+1)^{\frac{1}{2}}\, u(\Gamma_0\rho_i\Gamma_0\rho_i\,;\,\Gamma\Lambda)\,\mathcal{S}_\Gamma^{+}(E_\Gamma^{(+)}-E^{(+)}(RIZ)) = (-1)^{\Lambda}\,\langle n\Gamma_0 x_0 \| B^{\rho_i}\times H^{(a)}\times A^{\rho_i} \| n\Gamma_0 x_0\rangle \quad (1)$$

for stripping cases and

$$\sum_\Gamma (-1)^{\Gamma_0+\rho_i-\Gamma}(2\Gamma_0+1)(2\Gamma+1)^{-\frac{1}{2}}\, u(\Gamma_0\rho_i\Gamma_0\rho_i;\Gamma\Lambda)\,\mathcal{S}_\Gamma^{(-)}(E_\Gamma^{(-)}-E(RIZ)) = (-1)^{\Gamma}\,\langle n\Gamma_0 x_0 \| A^{\rho_i}\times H^{(a)}\times B^{\rho_i} \| n\Gamma_0 x_0\rangle \quad (2)$$

for pick up cases.

Here all the Greek letters refer to the product space (j-space as well as t-space); $\Gamma_0 \equiv J_0 T_0$ and $\Gamma = JT$ where J_0 and T_0 are the total angular momentum and total isospin of the target state and J and T refer to the same quantities in the residual nucleus; $(\rho_i \equiv j_i \frac{1}{2})$ characterises the orbit of the transferred nucleon and Λ $(\equiv k\tau)$ refers to the rank (in the product space) of the operator $(B^{\rho_i}\times H^{(a)}\times A^{\rho_i})$ or $(A^{\rho_i}\times H^{(a)}\times B^{\rho_i})$, as the case may be. $S_\Gamma \equiv \mathcal{S}_\Gamma(n\Gamma_0 x_0 \pm \rho_i \rightarrow n\pm 1, \Gamma x)$ is the spectroscopic factor connecting the target state $|n\Gamma_0 x_0\rangle$, and the final state $|n\pm 1, \Gamma x\rangle$ of the residual nucleus; the (+) and (-) signs symbolize the stripping and the pick-up cases respectively. H is the two-body interaction Hamil-

* This work was supported in part by the U. S. National Science Foundation.
** Present address.

tonian and is given by

$$H = H(\text{c.s}) + \epsilon_s n_{op}(\text{s}) + H^{(a)} \tag{3}$$

where $H(\text{c.s})$ and $\epsilon_s n_{op}(\text{s})$ refer to the contributions to the interaction Hamiltonian due to the closed shell and the one-body terms and $H^{(a)}$ is given by:

$$H^{(a)}(\rho_i - \rho_j) = -\sum_\gamma (2\gamma+1)^{\frac{1}{2}} \frac{1}{(1+\delta_{ij})} W^\gamma_{\rho_i\rho_j} [(A^{\rho i} \times A^{\rho j})^\gamma \times (B^{\rho i} \times B^{\rho j})^\gamma]^0 . \tag{4}$$

The quantity $(E(RIZ))$ is the energy of that state of the residual nucleus in which the residual interaction between the incoming nucleon and the active nucleons has been switched off.

In terms of G_Γ where

$$G^{(+)}_\Gamma = \left(C^{T_0 \frac{1}{2} T}_{T_{0z} m}\right)^2 \frac{(2J+1)}{(2J_0+1)} \delta^{(+)}_\Gamma \tag{5}$$

$$G^{(-)}_\Gamma = \left(C^{T \frac{1}{2} T_0}_{T_{0z} m}\right)^2 \delta^{(-)}_\Gamma \tag{6}$$

and m is the isospin projection of the transferred nucleon, the centroid energy for a particular T-group of levels is given by

$$\bar{E}_T = \sum_J G_{JT} (E_{JT} - E(RIZ)) \Big/ \sum_J G_{JT} + E(RIZ) . \tag{7}$$

Putting eqs. (1) to (6) together we find that for the case of *equivalent transfer* (remembering that the target has a neutron rich single active shell)

$$\overline{E^{(+)}_T} = \frac{a^{(+)}_T + b^{(+)}_T \overline{W^{T=1}} + c^{(+)}_T \overline{W^{T=0}}}{\sum_J \{(2J+1)/(2J_0+1)\} \delta_{JT}} + E^{(+)}(RIZ) \tag{8}$$

$$\overline{E^{(-)}_T} = \frac{-2}{n} E_t(\rho_1 - \rho_1) + E^{(-)}(RIZ) \tag{9}$$

where

$$a^{(+)}_T = -E_t(\rho_1 - \rho_1)(1 + f(T)/T_0) \tag{10}$$

$$b^{(+)}_T = (N-1)(\tfrac{3}{4}n + \tfrac{1}{2} f(T)) \tag{11}$$

$$c^{(+)}_T = (N+1)(\tfrac{1}{4}n - \tfrac{1}{2} f(T)) . \tag{12}$$

Here $(E_t(\rho_1 - \rho_1))$ is the two body energy of the active nucleons in the target state, the quality n is the total number of active nucleons (in this case neutrons) in the target state, $N = (2j_1 + 1) = \frac{1}{2}N$, and

$$f(T) = (T(T+1) - \tfrac{1}{2}(\tfrac{1}{2}+1) - T_0(T_0+1)) = \begin{pmatrix} T \\ -(T_0+1) \end{pmatrix} \quad \text{for} \quad \begin{matrix} T = T_> \\ T = T_< \end{matrix} . \tag{13}$$

Eq. (8) also leads to the pleasant result for the over-all centroid of the spectrum and this is

$$\overline{E^{(+)}} = \frac{-2E_t(\rho_1 - \rho_1)}{N-n} + \frac{n(N-1)}{(N-n)} \overline{W^{(2)}} + E(RIZ) \tag{14}$$

where

$$\overline{W^{(2)}} = \frac{\sum_{JT} (2J+1)(2T+1) W_J^T}{\sum_{JT} (2J+1)(2T+1)} . \tag{15}$$

For the case of *inequivalent transfer* of particle or hole to ρ_2-orbit

$$\overline{E_T^{(\pm)}} = \pm n \overline{E^{(2)}_{\rho_1-\rho_2}} + \langle \Delta E^{(2)}_{\rho_1-\rho_2} \rangle_{av} f(T) + E^{(\pm)}(RIZ) \tag{16}$$

where $\overline{E^{(2)}_{\rho_1-\rho_2}}$ is the J-weighted and T-weighted average of the two body energies between nucleons characterised by the ρ_1 and ρ_2 orbits and $\langle \Delta E^{(2)}_{\rho_1-\rho_2} \rangle_{av}$ is the splitting between the centroids with isospin $T = T_>$ and $T = T_<$ respectively.

Taking the values of $\overline{W^{T=1}} = -0.39$ MeV and $\overline{W^{T=0}} = -1.8$ MeV from the known spectrum of ^{42}Sc we have illustrated [4], in table 1, the case of equivalent transfer. The present set of parameters is rather crude but we hope to refine it as more data come along. For the sake of comparison we may mention that the "bare matrix elements" of Brown and Kuo [5] for $(f_{\frac{7}{2}})^2$ lead to $\overline{W^{T=1}} \approx 0.1$ MeV and $\overline{W^{T=0}} \approx -1.0$ MeV.

Table 1

$^{A}\mathrm{Ca} + \mathrm{p} \rightarrow {}^{A+1}\mathrm{Sc}$		^{43}Sc	^{44}Sc	^{45}Sc	^{46}Sc	^{47}Sc	^{48}Sc	^{49}Sc
E_T (MeV)	Calc.	0.5	1.5	0.85	0.95	0.35	0.05	< 0
	Expt.	0.34	-	0.45	-	0.20	-	0

With the understanding of the behaviour of both the *equivalent* and the *inequivalent* single nucleon transfer we now hope to develop closed expressions for the centroids and other spectral averages for the case of complex targets.

References

1. J.B. French, Phys. Letters 13 (1964) 249.
2. R.K. Bansal and J.B. French, Phys. Letters 19 (1965) 223.
3. R.K. Bansal and J.B. French, Phys. Letters 11 (1964) 145.
4. J.J. Schwartz and W.P. Alford, Phys. Rev. 149 (1966) 820.
5. Dr. T.T.S. Kuo, private communication.

* * * * *

THE SPIN-ISOSPIN DEPENDENT INTERACTION FROM INELASTIC PROTON SCATTERING ON ^{6}Li *

S. M. AUSTIN and G. M. CRAWLEY
Department of Physics, Michigan State University, East Lansing, Michigan, USA

Received 26 August 1968

The differential cross section for the inelastic scattering of protons leading to the ($J^\pi = 0^+$, $T = 1$) state of ^{6}Li at 3.56 MeV has been measured at $E_p = 24.4$ MeV. A real spin-isospin dependent interaction with a Yukawa shape, a strength of 12.7 MeV and a range of 1.0 fm fits the data well at small angles.

In a microscopic picture of an inelastic scattering reaction [1,2], the nuclear matrix element $\langle\Psi_f|V_{eff}|\Psi_i\rangle$ depends both on the wave functions of the nuclear states Ψ_f and Ψ_i and on the effective interaction V_{eff}. Thus one can obtain reliable spectroscopic information only if one has a prior knowledge of V_{eff}. Since very little is known about V_{eff} in the experimentally accessible energy region between 20 and 100 MeV it seems of most value to study reactions which involve relatively simple wave functions and in which V_{eff} is particularly simple so one may hope to obtain reliable information about the effective interaction.

This letter reports an experiment on the inelastic scattering of 24.4 MeV protons from ^{6}Li leaving this nucleus in its second excited state at 3.56 MeV ($J^\pi = 0^+$, $T = 1$). Since the ground state of ^{6}Li is 1^+, $T = 0$, only the spin-isospin dependent part of V_{eff} can contribute to the reaction in first order.

Protons from the Michigan State University Sector-Focussed Cyclotron bombarded a target of 99.3% ^{6}Li rolled to a thickness of about 4 mg/cm^2. Scattered protons were detected in a ΔE-E telescope consisting of a 1 mm thick surface barrier detector and a 3 mm Si(Li) detector. A particle identifier circuit was used to eliminate non-proton events. The best overall resolution obtained was about 110 keV. A typical spectrum is shown in fig. 1. The 3.56 MeV state was quite weakly excited and the main experimental difficulty was extracting the 3.56 MeV peak from the proton background produced by three-body breakup reactions.

In the calculation of the nuclear matrix element, L-S coupled harmonic oscillator wave functions were used to describe the ^{6}Li states and the oscillator parameter b was chosen to be

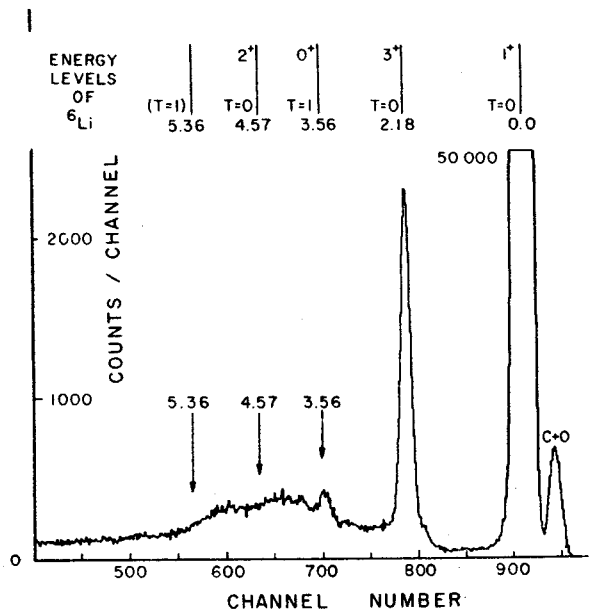

Fig. 1. The spectrum of protons from the ^{6}Li(p,p')^{6}Li reaction $E_p = 24.4$ MeV, $\theta_{LAB} = 30^o$. The relevant part of the energy level diagram for ^{6}Li taken from ref. 3 is also shown. The peak labeled C + O is due to carbon and oxygen impurities in the target.

1.9 fm, which yields an rms radius in agreement with the most recent electron scattering results [4].

The spin-isospin dependent part V_{11} of the effective interaction was taken to have a Yukawa form

* Research supported in part by the National Science Foundation.

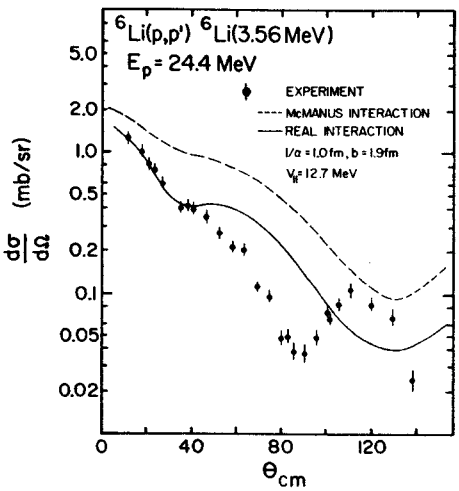

Fig. 2. The differential cross section of inelastically scattered protons leaving ^{6}Li in its 3.56 MeV state. The errors shown do not include an uncertainty in the normalization of 8%. The dashed curve is obtained using the McManus interaction, and the solid curve is obtained by fitting a real interaction to $\sigma(\theta)$ at small angles ($\theta < 50^o$).

$$V_{11}(r) = V \exp(-\alpha r)/\alpha r \qquad (1)$$

specified by two parameters, a strength V and a range $1/\alpha$. Two approaches were used. First, following Satchler [5], the interaction was chosen to be real with a range of 1.0 or 1.4 fm and V was adjusted to fit the data. Second, a comparison was made with the complex interaction obtained by McManus from a fit to the free nucleon-nucleon scattering amplitude [6]. Distorted wave calculations were made using a distorted wave approximation code [7] which allows spin-orbit terms in the optical model potential. The optical model parameters were determined by fitting the elastic scattering data. Exchange processes were neglected.

Results of the calculations are shown in fig. 2 together with the measured angular distribution for the 3.56 MeV state. The calculated cross sections have the same general slope as the data at the forward angles, but do not reproduce the minimum at 90° or the maximum at 110°. The calculation with the McManus interaction has no adjustable parameters and predicts a cross section which is too high by a factor of about two, even at forward angles. This is consistent with other recent measurements which show that the impulse approximation is a reasonable estimate of V_{11} only for $E_p \gtrsim 50$ MeV [8,9]. If one determines the strength V of a real potential with a range of 1.0 fm by fitting the data for $\theta < 50^o$ one obtains V = 12.7 MeV. If, on the other hand, one fits the total cross section, one obtains V = 11.1 MeV. This close agreement in spite of the poor fit at backward angles, reflects the fact that 65% of the total cross section lies forward of 50°. These results are in good agreement with other recent determinations of V_{11} in this energy region [8,9].

Table 1.
Results of fitting the differential cross section $\sigma(\theta)$ or the total cross section σ_T to the real potentials of eq. (1) by adjusting V.

Quantity fitted	$1/\alpha$ (fm)	b (fm)	V(MeV)
$\sigma(\theta)$. $\theta<50^o$	1.0	1.9	12.7
σ_T	1.0	1.9	11.1
σ_T	1.0	1.72	10.5
σ_T	1.4	1.9	4.5

Calculations with other values of α and b as listed in table 1 show that the predicted cross section is relatively insensitive to substantial changes in these parameters. Thus it seems unlikely that any reasonable modification of α and b can greatly improve the agreement with the back-angle data. The inclusion of exchange and second-order processes might remove the discrepancy but we have no reliable way of estimating the importance of these processes. It is also possible that the reaction is not a simple direct process at 24.4 MeV.
Calculations are being undertaken using wave functions which describe ^{6}Li better than the simple harmonic oscillator wave functions used in this letter.

The authors wish to thank P. Locard for performing the DWA calculations, and H. McManus and F. Petrovich for assistance with the theoretical interpretation of the data. We are especially grateful to R. Haybron and T. Tamura for making available their DWA code and to J. J. Kolata for adapting this code to the CDC 3600 computer.

References

1. A. K. Kerman, H. McManus and R. M. Thaler, Ann. of Phys. 8 (1959) 551.
2. V. A. Madsen, Nucl. Phys. 80 (1966) 177.
G. R. Satchler, Nucl. Phys. 77 (1966) 481.
N. K. Glendenning and M. Veneroni, Phys. Rev. 144 (1966) 839.

3. T. Lauritsen and F. Ajzenberg-Selove, Nucl. Phys. 78 (1966) 1.
4. L. R. Suelzle, M. R. Yearian and Hall Crannell, Phys. Rev. 162 (1967) 992.
5. G. R. Satchler, Nucl. Phys. A95 (1967) 1.
6. H. McManus, F. Petrovich and D. Slanina, Bull. Am. Phys. Soc. 12 (1967) 12.
F. Petrovich, D. Slanina and H. McManus, Michigan State University Report MSPT-103 (1967), unpublished.
7. R. Haybron and T. Tamura, private communication.
8. P. J. Locard, S. M. Austin and W. Benenson, Phys. Rev. Letters 19 (1967) 1141.
9. S. M. Austin, P. J. Locard, W. Benenson and G. M. Crawley, to be published.

* * * * *

ERRATA

A potential model for isobaric analogue states, J. P. Bondorg, H. Lütken and S. Jägare, Physics Letters 21 (1966) 185.*

Figs. 1 and 2 contain a numerical error which displaces the resonances from their correct positions. The figures should be replaced by the following two figures.

The new calculation has been made at the University of Washington, Seattle, and has been tested with an independent calculation by J. S. Blair and G. Bund.

* This work was supported in part by the U.S. Atomic Energy Commission.

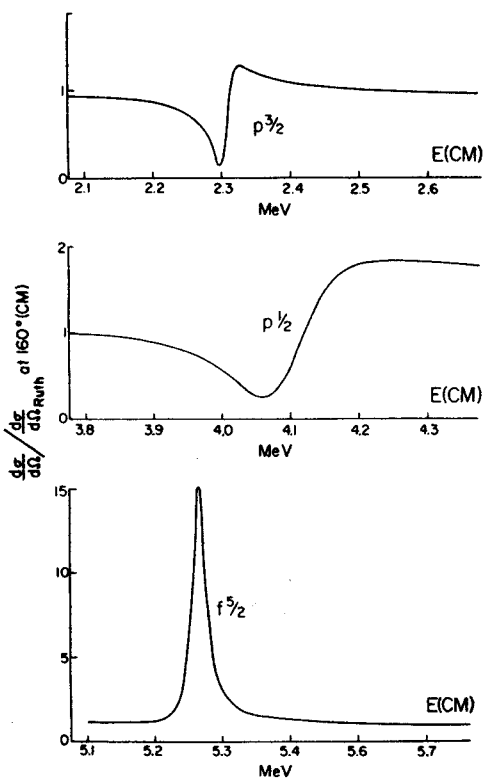

Fig. 1.

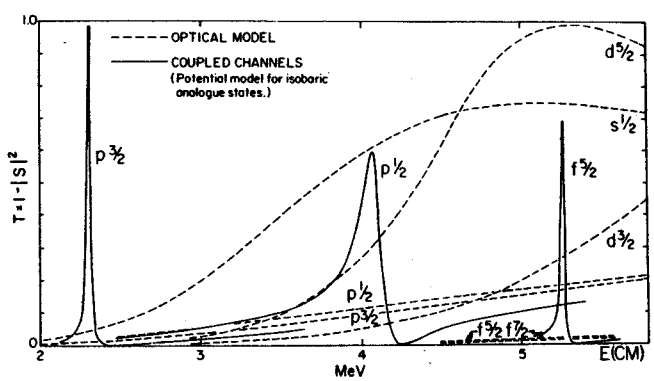

Fig. 2.

* * *

Reprinted from THE PHYSICAL REVIEW, Vol. 176, No. 4, 1227–1232, 20 December 1968
Printed in U. S. A.

^{6}Li$(p,p')^6$Li(3.56 MeV) Reaction from $E_p = 24.3$ to 46.4 MeV and the Effective Interaction*

S. M. AUSTIN, P. J. LOCARD,† W. BENENSON, AND G. M. CRAWLEY
Department of Physics, Michigan State University, East Lansing, Michigan
(Received 15 July 1968)

The total cross section for the ^{6}Li$(p,p')^6$Li(3.56 MeV) reaction was measured by observing the isotropic 3.56-MeV de-excitation γ rays in a 20-cm^3 Ge(Li) detector and was found to decrease slowly with energy. In a microscopic model of the reaction, this cross section depends only on the spin-isospin-dependent part V_{11} of the effective interaction. At energies above 34 MeV, the data are well described by a potential, $V_{11} = Ve^{-\alpha r}/\alpha r$, where the range $1/\alpha$ is taken to be 1.0 F, and $V = 12.1$ MeV. At 25 MeV, $V = 11.1$ MeV fits the data. The impulse approximation predicts a cross section larger than the data for the energy range of this experiment, the ratio decreasing from 2.9 at 25 MeV to 1.4 at 45 MeV. Available evidence on the spin-isospin-dependent interaction is summarized. For proton energies between 23 and 52 MeV, the strength of V_{11} lies in the range 12.5±2.5 MeV and does not appear to vary with energy.

I. INTRODUCTION

IN a microscopic model[1,2] the cross section for the inelastic scattering of protons depends on a nuclear matrix element which contains both the wave functions of the target and the effective interaction V_{eff} between the projectile and the target nucleons. Thus, if one wishes to use inelastic scattering as a spectroscopic tool, he must have foreknowledge of V_{eff}. However, except at energies well above 100 MeV, where V_{eff} is essentially the free nucleon-nucleon interaction,[1,3] there is no simple way to determine V_{eff} from external information. For this reason, several authors have studied inelastic scattering in cases where the wave functions are expected to be particularly simple or particularly well known.[3–6]

Two approaches have been taken. In one of these V_{eff} is obtained from the known two-body force (impulse approximation)[1] and the calculation contains no adjustable parameters. Such studies have been aimed primarily at determining the region of validity of the impulse approximation. Fairly good agreement with experiment is obtained for energies greater than 45 MeV.[3,5]

The other approach is empirical in nature. Here V_{eff} is assumed to have a simple form, often Yukawan, and its parameters are fixed by comparison with experiment.[4,6] If such an approach is to be useful for spectroscopy, the parameters of the empirical interaction must not depend strongly on the target nucleus and the multipolarity of the transition.

Most of the transitions studied to the present time are dominated by the spin-independent part of V_{eff}. However, certain transitions in the light nuclei are sensitive primarily to the spin-dependent part of the interaction. The energy dependence of the ^{7}Li(p,n)-^{7}Be(431 keV) reaction has been studied from 23 to 52 MeV[4] and is consistent with a constant value of the spin-isospin-dependent interaction V_{11}. Measurements of the ^{14}C$(p,n)^{14}$N and ^{18}O$(p,n)^{18}$F reactions[7,8] near 14 MeV have also yielded values of V_{11}.

In this paper, we describe a measurement of the variation with energy of the total cross section for the ^{6}Li$(p,p')^6$Li(3.56 MeV) reaction between 24.3 and 46.4 MeV. Because of the quantum numbers of the states involved only V_{11} can contribute to this reaction, so the cross section can be analyzed to yield this quantity directly. In Secs. II and III, the experimental procedure and results are described. In Sec. IV we present a brief resume of the theory. The available data on V_{11} are summarized in Sec. V and are discussed in Secs. VI and VII.

II. EXPERIMENTAL PROCEDURE

The energy levels of ^{6}Li are shown in Fig. 1. The 3.56-MeV state has a spin and parity of 0^+, so the angular distribution of γ rays leading to the ground state is isotropic in the rest frame of the recoiling nucleus and approximately isotropic in the lab. In addition, this state is the highest-lying particle-stable state,[9] so it is not fed with appreciable probability by γ-ray transitions from above. For these reasons, a measurement of the intensity of the 3.56-MeV γ-ray at a single angle is a measure of the total cross section for the ^{6}Li$(p,p')^6$Li-(3.56 MeV) reaction.

Protons from the Michigan State University isoch-

* Research supported in part by the National Science Foundation.

† On leave from the Laboratoire de Chimie Nucléaire et Radioactivité—Centre d'Etudes Nucléaires de Grenoble, Grenoble, France.

[1] A. K. Kerman, H. McManus, and R. M. Thaler, Ann. Phys. (N. Y.) 8, 551 (1959).

[2] V. A. Madsen, Nucl. Phys. 80, 177 (1966); G. R. Satchler, *ibid.* 77, 481 (1966); N. K. Glendenning and M. Veneroni, Phys. Rev. 144, 839 (1966).

[3] R. M. Haybron and H. McManus, Phys. Rev. 140, B638 (1965).

[4] P. J. Locard, S. M. Austin, and W. Benenson, Phys. Rev. Letters 19, 1141 (1967).

[5] H. McManus, F. Petrovich, and D. Slanina, Bull. Am. Phys. Soc. 12, 12 (1967); F. Petrovich, D. Slanina, and H. McManus, Michigan State University Report No. MSPT-103, 1967 (unpublished).

[6] G. R. Satchler, Nucl. Phys. A95, 1 (1967).

[7] C. Wong, J. D. Anderson, J. McClure, B. Pohl, V. A. Madsen, and F. Schmittroth, Phys. Rev. 160, 769 (1967).

[8] S. D. Bloom, J. D. Anderson, W. F. Hornyak, and C. Wong, Phys. Rev. Letters 15, 264 (1965).

[9] T. Lauritsen and F. Ajzenberg-Selove, Nucl. Phys. 78, 1 (1966).

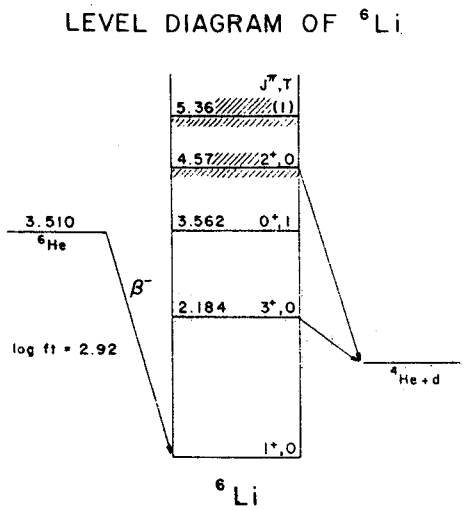

FIG. 1. Energy-level diagram of ^{6}Li adapted from Ref. 9.

ronous cyclotron bombarded a target rolled to a thickness of 1.0 mm from lithium metal enriched to 99.3% ^{6}Li.[10] The energy loss ΔE in this target ranged from 850 keV at 25 MeV to 500 keV at 46.4 MeV. The mean proton energies E_p were obtained by subtracting $\frac{1}{2}\Delta E$ from the proton energy determined from the beam transport system and are accurate to ± 0.1 MeV.

The de-excitation γ rays were detected in a 20-cm^3 Ge(Li) detector placed 12 cm from the target and at the largest convenient angle (155°) to the beam to minimize Doppler-shift effects and to reduce the background from the forward-peaked ^{6}Li(p,n) neutrons. The energy resolution of the detection system was 13 keV.

III. RESULTS

Figure 2 shows spectra taken at $E_p = 24.3$ and 46.4 MeV. Spectra at other angles were similar, with roughly the same ratio of signal to background. For the particular detector geometry used, the 3.56-MeV double-escape peak contained most of the events, and the analysis was performed on this peak. The peak is substantially broadened by Doppler shifts. To facilitate an accurate background subtraction, the line shape at 24.3 MeV was computed[11] using an angular distribution previously measured [12] at 24.4 MeV. The result is shown in Fig. 3, where the calculated line shape is compared with a line shape obtained from the γ-ray spectrum by subtracting a linear background fitted to the regions labelled "Bg" shown in Fig. 2. The calculated and experimental line shapes agree quite closely except in a region near channel 510, where background γ rays (see below) are known to contribute. The same channels

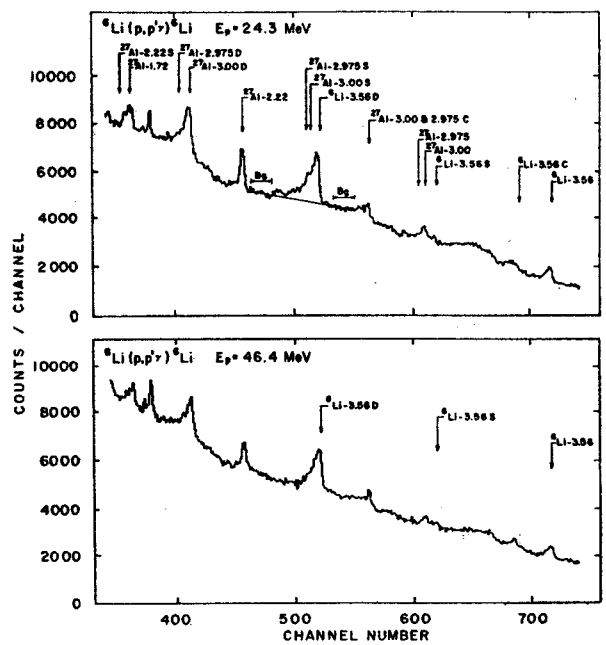

FIG. 2. γ-ray spectrum from ^{6}Li(p,p') at the highest and lowest energies of the experiment. In this figure C = Compton edge, S = single-escape peak, D = double-escape peak. Thus the peak labeled ^{6}Li-3.56D is the double-escape peak of the 3.56-MeV deexcitation γ ray from ^{6}Li. The labels are probable identifications of the source of the extraneous peaks in the spectrum. The regions marked Bg were least-squares-fitted with a linear background; the same channels were fitted at all energies.

fitted in the 24.3-MeV spectrum were fitted to determine backgrounds for all spectra in this experiment. As can be seen from the γ-ray spectrum taken at 46.4 MeV, the contribution from the tail of the line shape appears to be substantially less at the higher energies. This can be taken as evidence that the backward peak seen in the angular distribution at 24.4 MeV is less prominent at higher energies.

There are several sources of background which must be considered in the evaluation of these data. γ rays can be produced by interactions of scattered protons or neutrons in the aluminum beam pipe and neutron-induced reactions can take place in the Ge(Li) de-

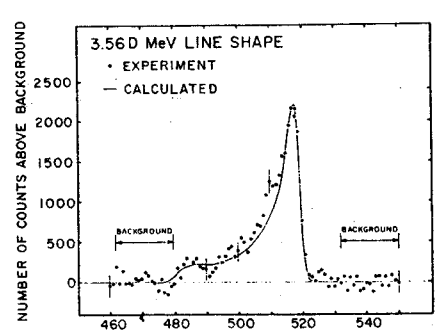

FIG. 3. γ line shape at 24.3 MeV. The method used to calculate the line shape and the deviation from the calculations near channel 510 are discussed in the text of Sec. III.

[10] Purchased from the Oak Ridge National Laboratory, Oak Ridge, Tenn.

[11] This computation was performed using a FORTRAN program written by J. J. Kolata and described by J. J. Kolata, R. Auble, and A. Galonsky, Phys. Rev. 162, 957 (1967).

[12] G. M. Crawley and S. M. Austin, in *Proceedings of the International Nuclear Physics Conference*, edited by R. L. Becker (Academic Press Inc., New York, 1967), p. 165.

tector. Several peaks due to the former effects are observed in the spectra of Fig. 2. A possible explanation for these peaks is found in neutron or proton inelastic scattering from aluminum. Similar peaks were observed in the target-out spectra but these peaks were somewhat smaller than those observed with the target in position. Thus we are forced to ascribe part of the background to neutrons from the ^{6}Li(p,n) reaction. For this reason, background spectra measured with the target removed were not adequate and were not used in the analysis of the data.

Based on the spectra in Fig. 2, one expects that the single-escape peaks of the 3.000 and 2.975 γ rays fall in the region of interest. However, estimates based on deviations from the calculated line shape of Fig. 3 and on the relative size of the single- and double-escape peaks indicate that they amount to only 7% of the counts ascribed to the 3.56-MeV γ ray. Since the ratio of the (3.000D+2.975D) peak to the 3.56D-MeV peak varies by at most 20%, this contamination introduces an error of at most 2% in the relative cross section.

Introduction of 5 cm of Pb reduced the 3.56-MeV peak by (94±6)% compared to the expected 91%. The transmission of neutrons with energies above 5 MeV is about 40%, so any contribution from neutron interactions in the detector must be small.

A correction should be applied to the data to account for the fact that an angular distribution of γ rays isotropic in the rest frame of the recoiling nucleus is anisotropic in the laboratory. An estimate of this effect has been made at 24.4 MeV, where a proton angular distribution is available and the total anisotropy is found to be about 4%. The anisotropy is expected to change only slowly with energy and not to substantially affect the relative cross section, so this correction was not made.

The data, normalized to a cross section obtained by integrating an existing angular distribution at 24.4 MeV,[12] are shown in Fig. 4. The errors shown include statistics and an allowance for difficulties in background subtraction. In addition, there is a possible error in the normalization of about 8%.

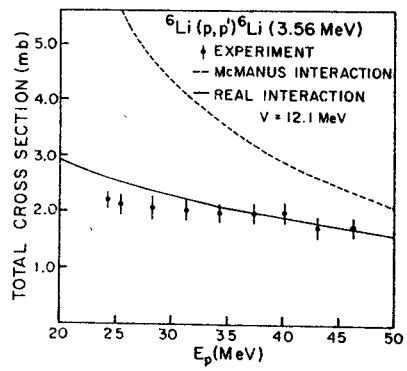

FIG. 4. Variation of the total cross section with energy. The solid curve was calculated using a real interaction with a constant strength of 12.1 MeV and a range $1/\alpha=1.0$ F. The dashed curve was obtained by using the impulse approximation interaction derived by McManus *et al.* (Ref. 5).

IV. THEORY

In the distorted-wave theory of inelastic scattering the transition amplitude has the form[1,2]

$$T_{fi}=\int \chi_f^{(-)*}(\mathbf{r})\langle\psi_f|V_{eff}|\Psi_i\rangle\chi_i^{(+)}(\mathbf{r})d\mathbf{r}.$$

The χ_f and χ_i are distorted waves generated from an optical model using parameters which fit the elastic scattering. In a microscopic picture of the reaction ψ_f and ψ_i are shell-model states and V_{eff} is the effective interaction causing transitions between these states. This expression neglects particle exchange.

It is usual[1-3,5,6] to write

$$V_{eff}=\sum_i t_{ip},$$

where t_{ip} is the scattering amplitude of the projectile from the ith target nucleon and the sum is over the active nucleons of the target nucleus. Further, t_{ip} is approximated[2,5,6] by the expression

$$t_{ip}=V_{00}+V_{10}\sigma_i\cdot\sigma_p+V_{01}\tau_i\cdot\tau_p+V_{11}(\sigma_i\cdot\sigma_p)(\tau_i\cdot\tau_p),$$

where σ_i and σ_p are the spin operators for the target nucleon and the projectile and τ_i and τ_p are the analogous isospin operators. This expression does not include the tensor and spin-orbit forces known to be present in the free nucleon-nucleon interaction. Thus one expects to find cases where V_{eff} is not sufficient to account for the phenomena. Tensor forces have been invoked to explain the results of studies of ^{14}C(p,n)-^{14}N(g.s.) and ^{14}N(p,p')^{14}N(2.311 MeV) reactions.[7,13]

The selection rules for this process are obtained from the following relationships:

$$\mathbf{J}_f-\mathbf{J}_i=\mathbf{J},\quad \mathbf{T}_f-\mathbf{T}_i=\mathbf{T},\quad \mathbf{S}_i-\mathbf{S}_f=\mathbf{S},\quad \mathbf{J}=\mathbf{L}+\mathbf{S},$$
$$(\pi_f)(\pi_i)=(-1)^L,$$

where the transition is $(J_i^\pi,T_i)\rightarrow(J_f^\pi,T_f)$. J, L, and S are the total, orbital, and spin angular momentum transferred in the reaction. T is the transferred isospin. Since the proton has spin and isospin equal to one-half, we have

$$S=0,1;\quad T=0,1.$$

The transition in ^{6}Li is $(1^+,0)\rightarrow(0^+,1)$, so that $J=1$; $L=0,2$; $S=1$; $T=1$. In the formulation of the theory outlined above, the subscripts on the V's are the transferred spin and isospin, so only $V_{ST}=V_{11}$ can contribute to the reaction.

The data have been compared to two forms of V_{11}. In the first of these V_{11} is taken to be real and to have

[13] V. A. Madsen (private communication).

TABLE I. Optical-model parameters[a] at 24.4 MeV.

V	r_0	a	W_d	r_0'	a'	V_s
44.8 MeV	1.13 F	0.62 F	5.87 MeV	1.12 F	0.68 F	7.40 MeV

[a] Notation that of G. R. Satchler, Nucl. Phys. **A92**, 273 (1967), with $r_s=r_0$, $a_s=a$.

the form

$$V_{11}=Ve^{-ar}/\alpha r.$$

Earlier analysis[6] has shown that $1/\alpha=1.0$ F is near the optimum range and this value is used throughout the analysis. The second form of V_{11} is obtained[5] from a fit of the nucleon-nucleon scattering amplitude to a Yukawa shape. This impulse approximation interaction is complex and both the ranges and strengths vary with energy.

The nuclear wave functions were taken to be LS-coupled harmonic-oscillator wave functions with an oscillator parameter, $b=1.90$ F, chosen to fit the most recent electron scattering results.[14] Form factors[2] for the reaction were calculated and were then inserted into a distorted-wave approximation code[15] which allows the use of spin-orbit potentials. Optical-model potentials obtained from a fit made to elastic scattering at 24.4 MeV[12] using the optical-model search code ABACUS[16] are shown in Table I. The real potential was scaled to other energies using the relationship

$$V(E)=V(24.4)-0.33(E-24.4).$$

The calculated total cross sections depend weakly on V and are changed by only 2.9% at 50.0 MeV if one completely neglects this energy dependence. Setting the spin-orbit part of the optical potential to zero and leaving the other parameters unchanged increased the total cross section by 4.5% at 50.0 MeV.

The results of these calculations are shown in Figs. 4 and 5. The solid curve in Fig. 4 is calculated from a real interaction of a Yukawa shape with $1/\alpha=1.0$ F and $V=12.1$ MeV. The data appear to be consistent with a constant value of V_{11} for energies above 34 MeV.

The dashed curve of Fig. 4 is the excitation function predicted by the impulse approximation.[5] There are no adjustable parameters in this calculation. The ratio of the cross section predicted by this theory to the experimental cross section decreases from 2.9 at 25 MeV to 1.4 at 45 MeV.

V. SUMMARY OF INFORMATION ON V_{11}

The results of this and other pertinent experiments are summarized in Fig. 5. The V_{11} were obtained by forcing the calculated cross section to match the experimental cross section. A range $1/\alpha=1.0$ F was used

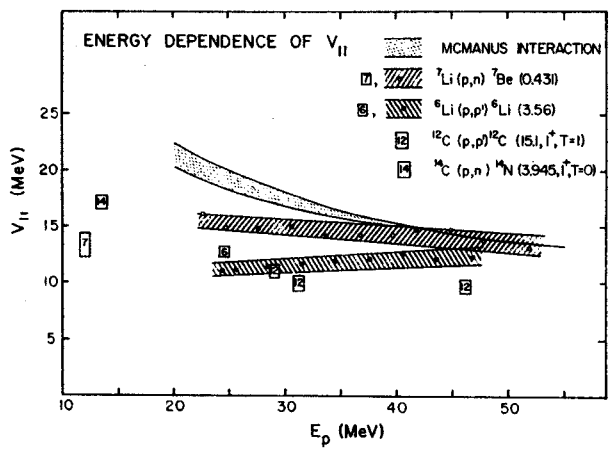

FIG. 5. Energy dependence of V_{11}. See the text of Secs. V and VI for a discussion of these results.

for all these calculations. An estimate of the equivalent strength for other values of the range may be obtained by using the approximate empirical relationship[17]

$$V(\alpha)/V(\alpha')=(\alpha/\alpha')^n, \quad n\simeq 2.7.$$

For example, for $1/\alpha=1.4$ F, V_{11} is obtained by dividing the values in Fig. 5 by 2.48. More accurate estimates can be obtained only by performing detailed calculations.

We now discuss the relevant experiments in turn.

A. Present Experiment: ^{6}Li$(p,p')^6$Li(3.56 MeV)

The solid circles correspond to the data points of Fig. 4, while the width of the cross-hatched area is an indication of the experimental errors. The single point at 24.4 MeV was taken from Ref. 18.

B. ^{7}Li$(p,n)^7$Be(0.431 MeV)

The data shown on the cross-hatched area between 23 and 52 MeV are from Ref. 4, and the single point at 12 MeV is taken from Ref. 19. These cross sections were measured by γ-ray techniques similar to those described in this paper. Four amplitudes can contribute to this $(\frac{3}{2}^-,\frac{1}{2})\rightarrow(\frac{1}{2}^-,\frac{1}{2})$ transition. However, a single one of these, $(LSJT)=(0111)$, contributes about 95% of the cross section, so the reaction is sensitive only to $V_{ST}=V_{11}$. V_{11} was corrected for the small contribution of V_{01} through the amplitude (2021). This correction decreased V_{11} by about 0.5 MeV for a value of $V_{01}=20$ MeV.[6,7]

LS wave functions with a harmonic-oscillator parameter, $b=1.72$ F, were used to describe the nucleus. The rms radius for this value of b agrees with recent electron scattering data.

[14] L. R. Suelzle, M. R. Yearian, and H. Crannell, Phys. Rev. 162, 992 (1967).
[15] This code was written by R. Haybron and T. Tamura and was modified for the Sigma 7 computer by J. J. Kolata.
[16] E. H. Auerbach, Brookhaven National Laboratory Report No. BNL-6562 (unpublished).
[17] F. Petrovich and H. McManus (private communication).
[18] S. M. Austin and G. M. Crawley, Phys. Letters **27B**, 570 (1968).
[19] P. Paul, S. M. Austin, and S. S. Hanna (to be published).

C. ^{12}C(p,p')^{12}C(15.1 MeV)

The transition in this case is $(0^+,0) \rightarrow (1^+,1)$ and is mediated by V_{11} alone. The points at 28.05, 31.1, and 46 MeV were obtained from our analysis of total cross sections extracted from the measurements of Locard *et al.*,[20] Dickens *et al.*,[21] and Petersen *et al.*[22] The wave functions of Gillet and Vinh Mau,[23] with a harmonic-oscillator parameter $b=1.64$ F, were used in the calculation of the form factor.

D. ^{14}C(p,n)^{14}N(3.945 MeV)

This transition is $(0^+,1) \rightarrow (1^+,0)$ and is again a pure V_{11} transition. The result quoted is the analysis of Wong *et al.*[7,13] The value obtained for the transition to the ground state of $N^{14}(J^\pi=1^+, T=0)$ has not been included since the analysis is complicated by a chance cancellation[7] of the (0111) amplitude.

E. Impulse Approximation

The area labeled "McManus Interaction" was obtained in the following manner. Total cross sections were calculated using the impulse approximation interaction.[5] These calculated cross sections were treated as experimental data and the strength of the real interaction was adjusted to give the same cross section. Since the equivalence depends somewhat on the nuclear wave functions, different transitions yield a different equivalent V_{11}. The lower limit of the band was calculated for ^{6}Li(p,p') ^{6}Li(3.56 MeV) and the width of the band encompasses results calculated by Petrovich and McManus[17] for transitions in ^{12}C and ^{40}Ca.

VI. DISCUSSION

A. Exchange Effects

It is difficult to estimate the uncertainties in analyses of this sort, and one is forced to appeal to consistency among transitions in different nuclei. The present results are encouraging from this point of view. The data for the four transitions cluster about $V_{11}=12.5$ MeV and there is no evidence that V_{11} depends on energy. It happens, however, that in all of these cases, the cross section is dominated by the monopole ($L=0$) amplitude, so these results give no information on a possible multipole dependence of V_{eff}.

Recent calculations[24] indicate that exchange processes contribute significantly to inelastic scattering and (p,n) cross sections. The exchange contribution generally interferes constructively with the direct scattering and becomes progressively more important for the higher multipoles. Since conventional calculations such as those reported in this paper neglect exchange effects, V_{eff} must increase with L to compensate for the neglected processes. For the same reason, the $L=0$ transitions considered in this paper should provide a more reliable estimate of the actual effective interactions than transitions for which $L>0$.

It is also possible that inclusion of exchange effects would reduce the small discrepancy between the ^{7}Li(p,n) and ^{6}Li(p,p') results since the negative correction to the (p,n) cross sections, which are $L=2$, would be larger at low energies where exchange effects are most important.

TABLE II. Comparison of the V_{ST} for energies between 20 and 60 MeV.

S,T	V_{ST} (MeV)[a]	Reference
0,0	50–100	b, c, d
0,1	20	e, f
1,0	20–50	g
1,1	10–15	Present

[a] For a 1.0-F range.
[b] Reference 26.
[c] W. G. Love, Phys. Letters 26B, 271 (1968).
[d] Reference 20.
[e] Reference 7.
[f] Reference 6.
[g] P. J. Locard and S. M. Austin (unpublished).

B. Wave Functions

The LS-coupled wave functions used in this analysis are known to describe ^{6}Li fairly well,[25] though they do not, for example, describe in detail the charge distributions derived from electron scattering.[14] We are undertaking calculations using more sophisticated intermediate-coupling wave functions. It seems likely, however, that using better wave functions would primarily affect transitions mediated by the spin-independent part V_{00} of the effective interaction since such transitions are enhanced when the wave functions have collective characteristics.[26] Collective spin-dependent phenomena are not important for these low-lying states, so for the present purpose the extreme single-particle wave functions are likely to be a good approximation.

C. Comparison with Other V_{ST}

Although V_{11} dominates the cross section for the reactions considered here, it is relatively small compared with other terms in V_{eff}. A comparison with typical values from the literature is given in Table II. No consistent studies of the energy dependence of V_{00}, V_{01}, and V_{10} are available and the values quoted are only meant to be illustrative of the range of energies above 20 MeV.

[20] P. J. Locard, S. M. Austin, and W. Benenson (unpublished).
[21] J. K. Dickens, D. A. Haner, and C. N. Waddell, Phys. Rev. 132, 2159 (1963).
[22] E. L. Petersen, I. Slaus, J. W. Verba, R. F. Carlson, and J. R. Richardson, Nucl. Phys. A102, 145 (1967).
[23] V. Gillet and N. Vinh Mau, Nucl. Phys. 54, 321 (1964).
[24] J. Atkinson and V. A. Madsen, Bull. Am. Phys. Soc. 13, 630 (1968); V. A. Madsen (private communication).
[25] See, for example, C. A. Levinson and M. K. Banerjee, Ann. Phys. (N. Y.) 2, 471 (1957).
[26] W. G. Love and G. R. Satchler, Nucl. Phys. A101, 424 (1967).

VII. CONCLUSIONS

The total cross section for the ^{6}Li$(p,p')^6$Li(3.56 MeV) reaction was measured in the proton energy range from 24.3 to 46.4 MeV. These data and relevant results from the literature were analyzed to yield values of the spin-isospin–dependent part of the effective interaction for proton energies between 12 and 52 MeV. The results are summarized in Fig. 5. The strengths of V_{11} obtained all lie in the range from 10 to 17 MeV for a Yukawa shape with a range of 1.0 F. There is no evidence that V_{11} depends on the proton energy. The impulse approximation predicts a cross section which is substantially too large at energies below 35 MeV, but which is in good agreement with the data near 50 MeV.

ACKNOWLEDGMENTS

The authors wish to thank Professor H. McManus and Professor V. Madsen and F. Petrovich for illuminating discussions regarding the theoretical interpretation of these data. We are grateful to R. Haybron and T. Tamura for making available their distorted-wave-approximation code and to J. J. Kolata for adapting this code to the CDC-3600 computer. The assistance of S. H. Fox, R. A. Paddock, and I. Proctor in taking the data is gratefully acknowledged. Professor C. R. Gruhn kindly provided the Ge(Li) detector used in these experiments.

NUCLEAR INSTRUMENTS AND METHODS 64 (1968) 40–44; © NORTH-HOLLAND PUBLISHING CO.

REMOTE CONTROLLED SLITS FOR THE MSU CYCLOTRON EXTERNAL BEAM SYSTEM*

W. BENENSON, R. DEFOREST, W. P. JOHNSON and E. KASHY

Cyclotron Laboratory, Michigan State University, East Lansing, Michigan, U.S.A.

Received 2 April 1968

Circuitry and mechanical design are described for the remotely-operated water-cooled slit jaws on the MSU cyclotron external beam line. The displacement of the slit jaw from the center of the beam line is automatically set on the reading of the fifteen-turn helipot on the console of the cyclotron. The setting accuracy and reproducibility is ± 0.05 mm.

1. Introduction

The external beam analysis system for the Michigan State University cyclotron has recently been completed. The central features of this system are described elsewhere[1]). One of the important requirements for the system is accurate definition of objects and images for the optical system. This function is performed by means of apertures with dimensions that can be varied to suit the desired beam quality. Apertures are used to control the spot size, energy spread, divergence and direction of the beam.

2. Mechanical

An aperture consists of 4 identical slit jaws mounted in a standard beam box. The standard boxes have dimensional tolerance of the order of 0.02 mm and are centered on an optical line in space (the beam line)

* Supported in part by the National Science Foundation.

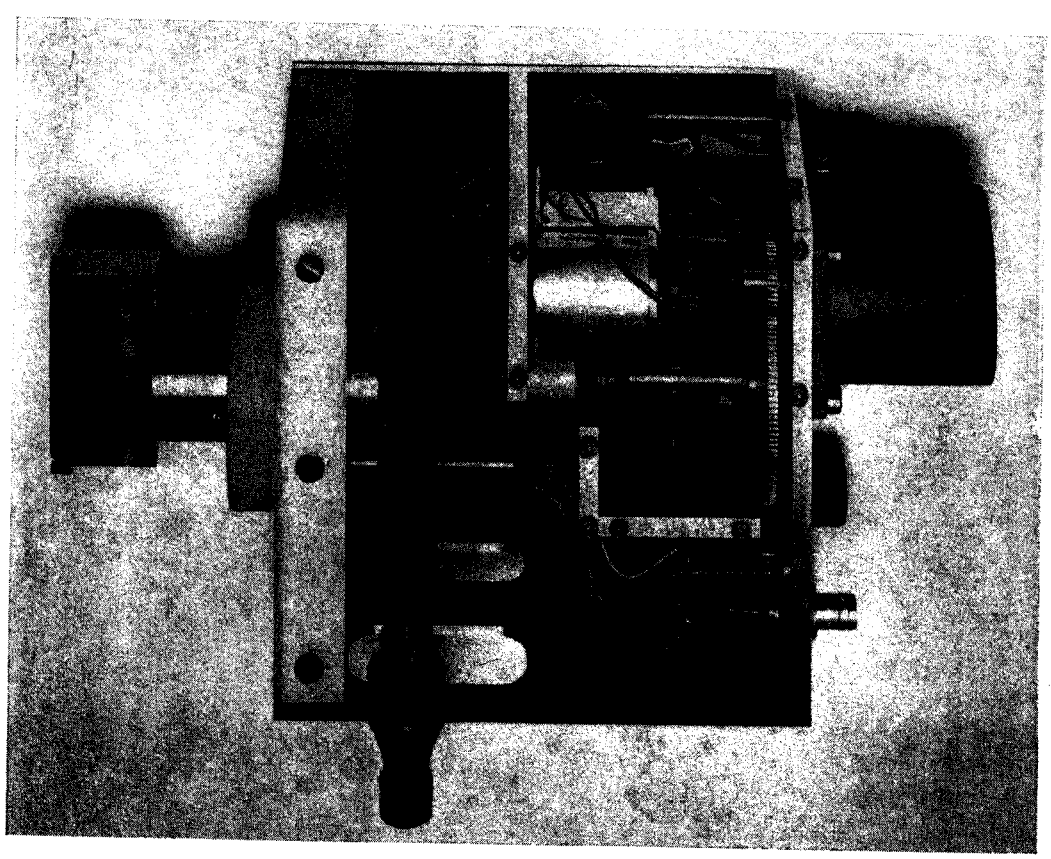

Fig. 1. Photograph of slit jaw and drive mechanism. Two covers have been removed to show the drive screw and gearing. The drive motor is mounted on the upper right hand corner. A tungsten strip is mounted on the water cooled aluminum block protruding through a vacuum seal on the left side of the box.

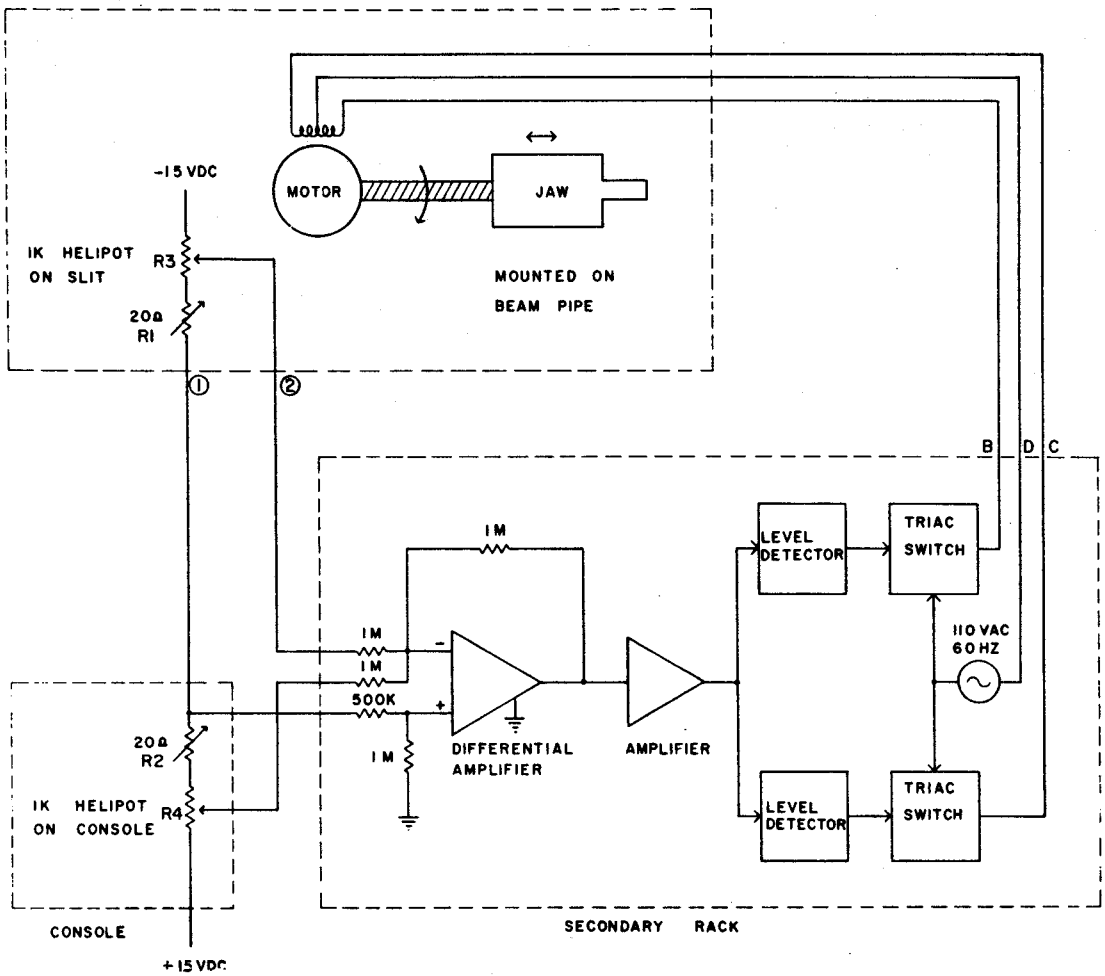

Fig. 2. Block diagram of the jaw controller.

with an accuracy of the same order of magnitude. Fig. 1 is a photograph of one of the four slit jaws. It consists of a water-cooled aluminum block which is driven by means of an axial screw and a stepping motor. The slit edge is a thin demountable tungsten strip which is attached to the block. The beam which does not pass through the aperture hits the tungsten strip or, with far greater probability, the aluminum block. It is desirable to have the beam that is not used, to hit aluminum as much as possible since the activity induced is much shorter lived than in higher Z materials such as tungsten.

3. Electronics

The jaw controller circuit (fig. 2) involves two 1 kΩ helipots, a differential amplifier, two level detectors and two switches which control the servo motor. One helipot is mounted so that its wiper moves in synchronism with the motion of the slit jaw. The other is mounted at the cyclotron control console. The two helipot settings are compared by the differential amplifier which controls the two switches through the level detectors.

The comparison circuit is so arranged that changes in the +15 or −15 V power supplies although affecting loop gain will not affect calibration. The variable, 20 Ω resistors, R_1 and R_2, in series with the helipots are for calibration. In order to make the slits interchangeable, R_1 was adjusted for each slit mechanism to present the same resistance across terminals 1 and 2 for a given position of the jaw. Calibration was made with the jaw in the vacuum system in order to include the effect of vacuum loading on the mechanical calibration of the slit drive mechanism. R_2 was adjusted to make the setting of the console helipot agree with the mechanical position of the jaw.

The error detector circuit (fig. 3) is solid state throughout using four Fairchild μA709 integrated

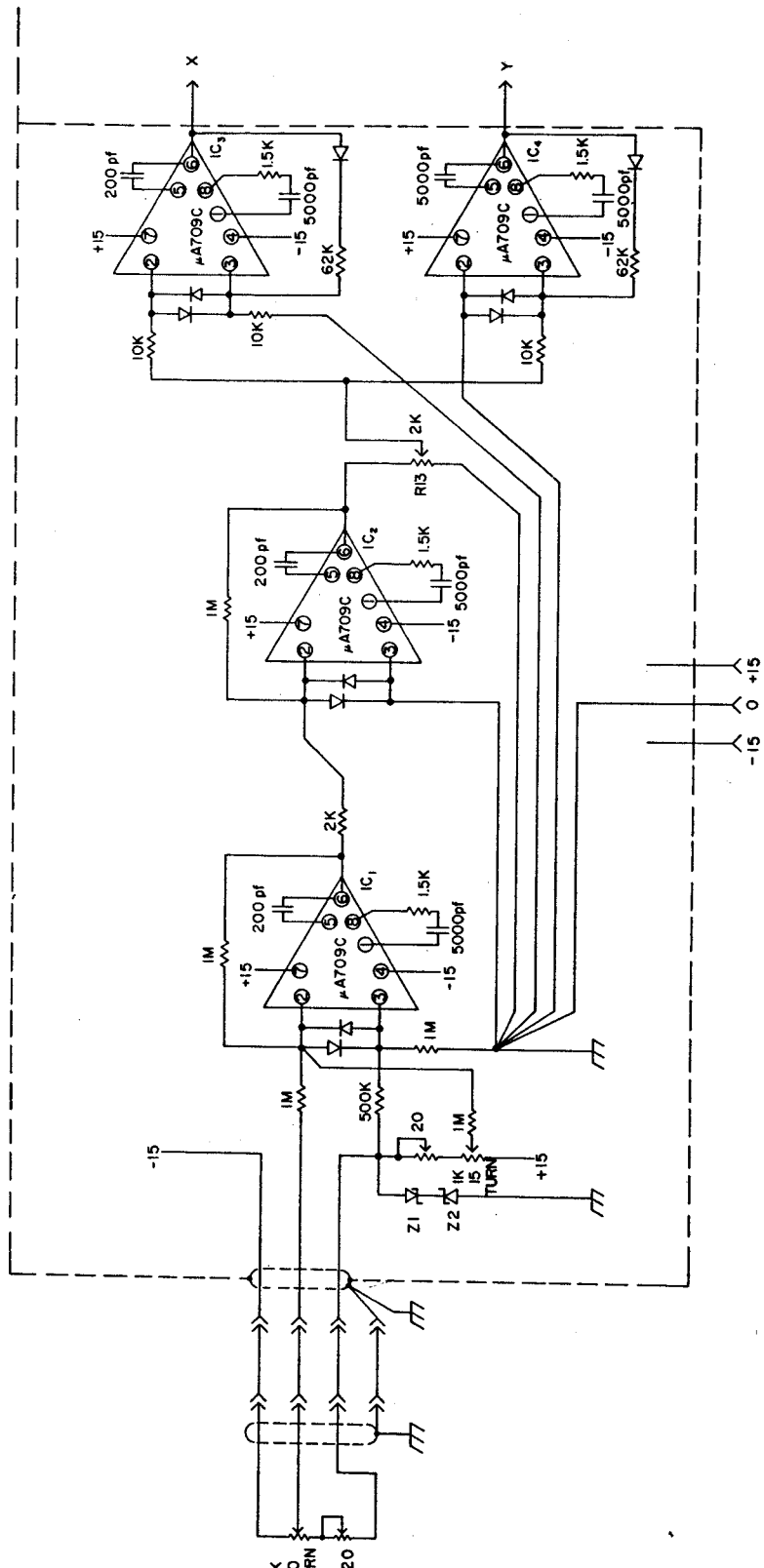

Fig. 3. Circuit diagram of the error detector. All resistances are in ohm. The diodes are general purpose silicon.

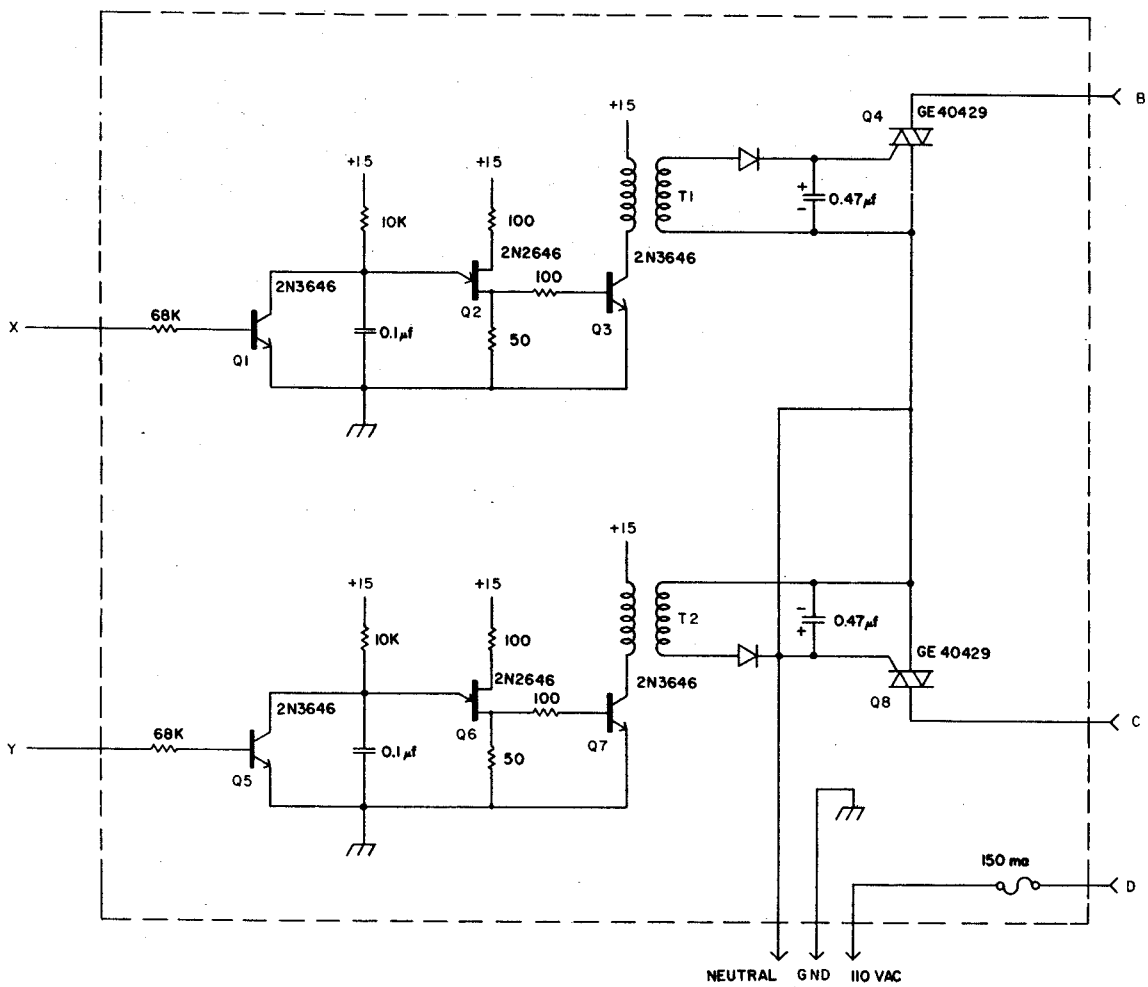

Fig. 4. Motor drive circuit diagram.

circuit amplifiers, which were compensated for 0 dB crossover around 500 kHz using component values specified by the manufacturer. Back-to-back diodes were provided at each amplifier input to protect against over-voltages. Diodes Z_1 and Z_2 protect IC_1 against possible failure of one of the power supplies.

Amplifiers IC_3 and IC_4 are the level detectors. A dead zone is provided in which neither detector is turned "on". The width of this dead zone in terms of mechanical error can be varied from 0.02 mm to any larger value by adjustment of R13 which controls the gain of the error amplifier.

In order to isolate the cyclotron control ground from the power network common, the switching triacs (fig. 4) Q_4 and Q_8 were driven by pulses through two isolating ferrite core pulse transformers T_1 and T_2. The unijunction transistors Q_2 and Q_6 are the central elements of two oscillators which drive the transformers. Transistors Q_1 and Q_5 gate the oscillators.

4. Calibration and accuracy

The console control helipot and the gears linking the jaw and the helipot R_3 (fig. 2) were chosen so that one division on the console helipot represents 0.001″ (0.0254 mm) of jaw motion. Using helipots with 0.1% linearity one can expect the absolute error attributable to the electronics not to exceed 0.05 mm. Positioning was found to be reproducible to within 0.05 mm provided one took care to circumvent the mechanical backlash.

5. Remote control and monitoring

Fig. 5 is a photo of the control panel. One sees two rows of five knobs each. Each knob drives two ganged helipots for simultaneous setting of the jaws as pairs. The upper row of knobs is used for slits which move in

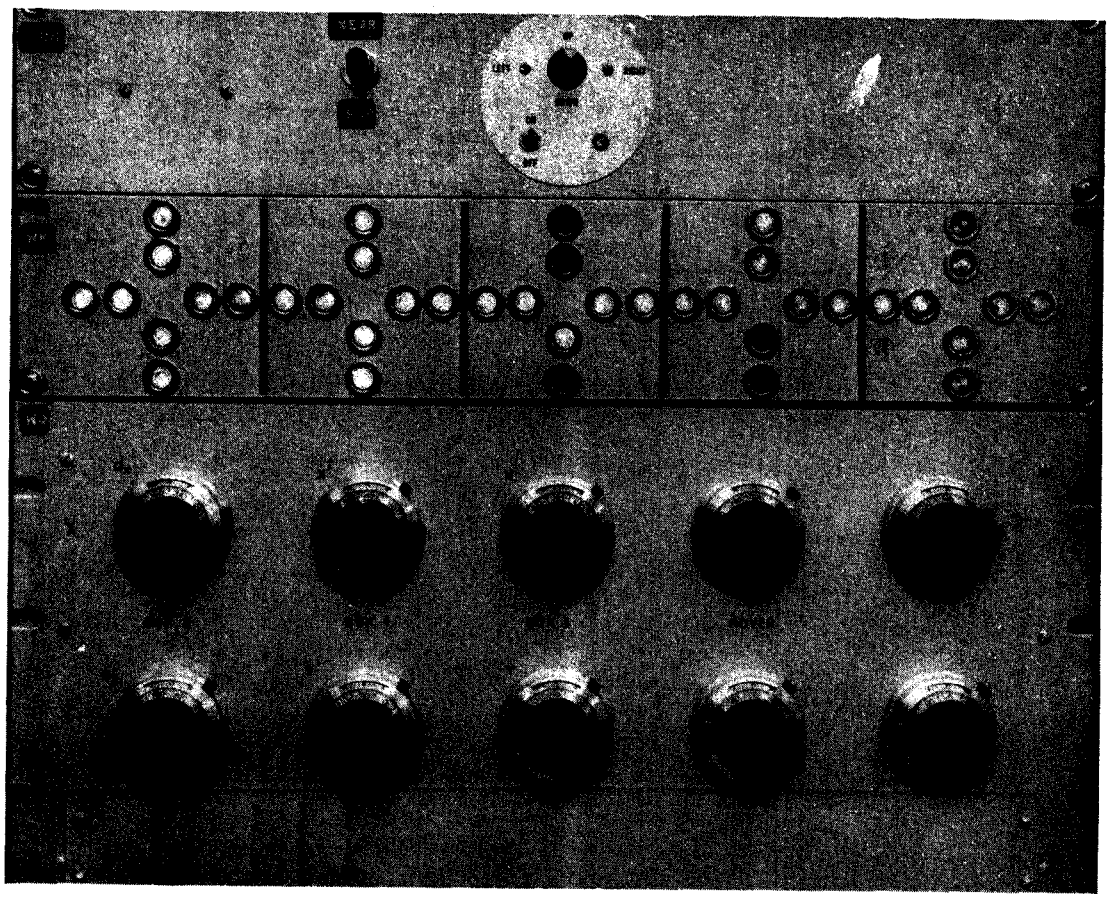

Fig. 5. Photograph of the console control panel (WQ) and the diagnostic indicator lights (WK).

the horizontal plane, the lower for vertical slits.

Above the knobs are five arrays of neon lights which are useful for diagnostic purposes. The lights are connected directly to the triac switches and are therefore lighted if their corresponding triacs are off and dark otherwise. A dark bulb therefore indicates that the slit has not reached the desired position.

Near the slit control panel on the console are four pairs of current meters which can read currents from 1 nA to 100 μA full scale. Each of these pairs of meters can be switched to read any pair of slit jaws. In this way, the centering of the beam and the amount of spillage can be monitored, and the beam progress can be monitored all along the beam line.

6. Present status

The system described in this paper has proved to be a convenient and reliable method for defining apertures along a beam line. Automatic positioning of slit jaws to a dial-setting on the console is a unique feature of the system.

At present one control circuit is used for each jaw. If the number of slit jaws used on the beam lines increases, it is planned to multiplex the controlling circuits by simply switching from one jaw to another. Future plans call for coupling of the cyclotron controls to the SIGMA 7 computer located nearby. In this case the helipots will be servo-coupled to the computer for automatic setting.

The authors appreciate the work done by Mr. G. Stork in the mechanical design. Jr. J. Snelgrove and Mr. D. Gilbert were of great help in installing and calibrating the equipment described in this paper.

Reference

[1] G. H. MacKenzie, E. Kashy, M. M. Gordon and H. G. Blosser, IEEE Trans. Nucl. Sci. NS-14 (1967) 450.

Reprinted from THE PHYSICAL REVIEW, Vol. 176, No. 4, 1268–1276, 20 December 1968
Printed in U. S. A.

Scattering of 24.5-MeV Protons from ^{89}Y

W. BENENSON, S. M. AUSTIN, AND R. A. PADDOCK
*Michigan State University, East Lansing, Michigan**

AND

W. G. LOVE†
Oak Ridge National Laboratory, Oak Ridge, Tennessee‡

(Received 12 July 1968)

Scattering of 24.5-MeV protons from ^{89}Y has been measured. Angular distributions were obtained for the ground state and the first four excited states as well as for several unresolved multiplets. The inelastic scattering data have been analyzed, using the collective model and a microscopic model with and without core-polarization effects.

I. INTRODUCTION

THE ground state and the first excited state of ^{89}Y are well understood in terms of the shell model. Analyses of data on transfer reactions[1,2] leading to ^{89}Y and of data on inelastic scattering of electrons,[3] protons,[2,4] and α particles[5] from ^{89}Y have given a clear picture of the nature of the second and third excited states. The situation for higher-lying states is not as promising. Some of the confusion concerning these states has been cleared up recently by high-resolution studies[6] of the level scheme of ^{89}Y. Several of the higher-lying states which had previously been thought to be single are now known to be closely spaced doublets or triplets.

In the present experiment the main aim was to study the microscopic model of inelastic proton scattering. Inelastic scattering from the first excited state of ^{89}Y is a good test for this theory, since the initial and final states are well represented by simple shell-model wave functions. Such an approach has been employed in interpreting data on the scattering of 61-MeV protons.[7] In this analysis, the inclusion of core-polarization effects was found to improve the theoretical situation by providing a better fit to the data with a more realistic effective interaction between target and projectile nucleons. A comparison of the results of the present experiment to those obtained at 61 MeV will give information on the energy dependence of the effective interaction. The effective interaction is expected to be energy-dependent, and the dependence of the spin- and isospin-independent part has been observed at proton bombarding energies between 23 and 52 MeV.[8] One can also obtain an upper limit on the spin-flip part of the effective interaction by setting the spin-independent part equal to zero. Inelastic scattering to the second excited state is a good case for this, since it has a strong monopole spin-flip amplitude. Scattering of protons from the first excited state of ^{89}Y is expected[9] to be a good test of an approximation made in the present microscopic scattering theory in which the space-exchange process is neglected.

A second aim of the experiment is the study of the higher-lying levels of ^{89}Y, using both collective and microscopic scattering theory. The picture of the second and third excited states that emerges is in good agreement with previous analyses of transfer reactions and inelastic scattering. The present experiment, however, sheds little light on states above the third excited state.

Figure 1 is a diagram of energy levels in ^{89}Y below 3 MeV. The ground state has been described as a pure single-particle state with a $2p_{1/2}$ proton outside a closed ^{88}Sr core. The first excited state at 0.908 MeV is obtained by promoting this proton to the $1g_{9/2}$ shell. The electromagnetic transition rate for the first-excited-state to ground-state transition is in good agreement with single-particle estimates with small configuration mixing.[10] Attempts have been made to describe the $\frac{3}{2}^-$, $\frac{5}{2}^-$ doublets at 1.507 and 1.745 MeV as a $2p_{1/2}$ proton coupled to the ^{88}Sr 2^+ first excited state.[11] The (α,α') and (e,e') data of Alster *et al.*[5] and of Peterson and Alster[3] have shown this to be a rather poor description. The shell-model description of these states would be obtained by promoting a $2p_{3/2}$ and a $1f_{5/2}$ particle into the $2p_{1/2}$ shell. The ^{90}Zr$(d,$He$^3)^{89}$Y results of Preedom *et al.*[1] are in agreement with this model, since they show

* Work supported in part by the National Science Foundation.
† Research Fellow from the University of Tennessee under appointment from Oak Ridge Associated Universities.
‡ Research sponsored by the U. S. Atomic Energy Commission under contract with the Union Carbide Corporation.

[1] B. M. Preedom, E. Newman, and J. C. Hiebert, Phys. Rev. 166, 1156 (1968).
[2] M. M. Stautberg, J. J. Kraushaar, and B. W. Ridley, Phys. Rev. 157, 977 (1967).
[3] G. A. Peterson and J. Alster, Phys. Rev. 166, 1136 (1968).
[4] Y. Awaya, J. Phys. Soc. Japan 23, 673 (1967).
[5] J. Alster, D. C. Shreve, and R. J. Peterson, Phys. Rev. 144, 999 (1966).
[6] P. F. Hinrichsen, S. M. Shafroth, and D. M. Van Patter, Phys. Rev. 172, 1134 (1968); P. F. Hinrichsen, Bull. Am. Phys. Soc. 13, 583 (1968).
[7] A. Scott, M. L. Whiten, and J. B. Ball, Phys. Letters 25B, 463 (1967).
[8] P. J. Locard, S. M. Austin, and W. Benenson, Phys. Rev. Letters 19, 1141 (1967).
[9] K. A. Amos, V. A. Madsen, and I. E. McCarthy, Nucl. Phys. A94, 103 (1967).
[10] H. Horie and T. Oda, Progr. Theoret. Phys. (Kyoto) 32, 65 (1964).
[11] S. M. Shafroth, P. N. Trehan, and D. M. Van Patter, Phys. Rev. 129, 704 (1963).

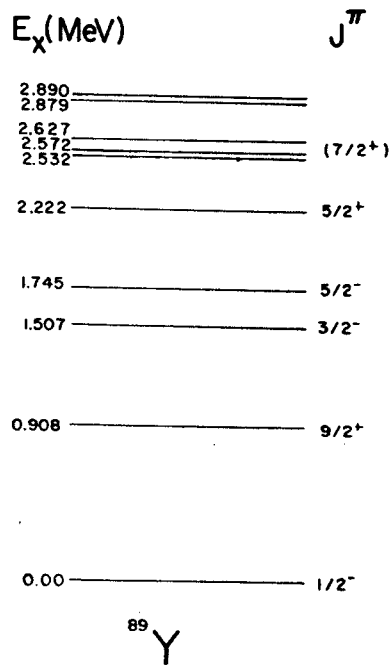

FIG. 1. Energy levels of ^{89}Y below 3 MeV. The excitation energies are taken from Ref. 6.

strong transitions to these two states from the ^{90}Zr ground state. It is difficult to make any qualitative statement concerning the states above 1.745 MeV. There are too many states to be described by the coupling of a $2p_{1/2}$ particle to the ^{88}Sr 3^- state at 1.84 MeV or $2p_{1/2}$ proton hole to the ^{90}Zr 3^- state at 2.75 MeV. The sorting out of these states awaits higher-resolution data than are presently available.

II. EXPERIMENTAL METHOD

This experiment was performed using the Michigan State University sector-focused cyclotron. An H^- beam was stripped inside the cyclotron and then focused by quadrupoles and bent 15° into a 36-in.-diam scattering chamber. The energy of the beam was determined to be 24.5±0.2 MeV by a kinematic method using scattering from hydrogen and the first excited state of ^{12}C.[12] A ΔE-E silicon-detector telescope was used. The ΔE counter was a 1-mm surface-barrier detector, whereas the E counter was an Li-drifted 3-mm detector. The E counter was cooled to dry-ice temperature but was still a substantial contributor to the over-all energy resolution of 100 keV.

The target was a 1.75-mg/cm^2 self-supporting foil on loan from Oak Ridge National Laboratory. Elastic scattering from small carbon and oxygen contaminants was strong enough to obscure some of the data at many forward angles.

Particular attention was given to establishing an accurate normalization of the data, which were taken relative to a monitor counter at 90°. First, a normalization was obtained by weighing the target and assuming it to be uniform. The integrated charge and the various geometric factors were then used to calculate the cross section. As a check in this result a method of normalization using a thick target was devised. This method, which will be described in more detail,[13] eliminates the effect of target nonuniformity. The spectrum from a 0.001-in.-thick Y foil was obtained at a back angle (101°). The shape of the elastic-scattered peak was used to determine the target thickness and uniformity over the actual beam spot. The thick-target spectrum obtained is shown in Fig. 2. Also shown is a calculated fit to the shape assuming that the target had several regions of different thickness within the beam spot. The calculated fit gives both the total number of counts and the average target thickness. The two methods of obtaining the normalization agreed to within 2%. The over-all error due to normalization is less than 6% and is essentially due to uncertainties in geometric factors such as beam position and collimator dimensions. The errors shown on the angular-distribution figures are the sum of statistical errors and those due to uncertainties in background subtraction. The difficulty in obtaining accurate backgrounds is illustrated by a typical spectrum shown in Fig. 3. The first excited state at 0.908 MeV is very weak and rides on the tail of the elastic peak. Another problem in background subtraction is illustrated by the broadening of the 1.745-MeV state. This broadening is due to a peak near 1.78 MeV which has been shown to be inelastic scattering of the elastically scattered protons within the detector volume.[14] We were able to subtract these events because they are proportional to the number of elastic events detected. Nonetheless, the errors in the cross section to the 1.745-MeV state become large at forward angles.

III. ANALYSIS

A. Elastic Scattering

The elastic scattering was analyzed in terms of an optical-model potential of the usual form,

$$U(r) = -VF(x) + 4W_D i \frac{d}{dx'} F(x') + \left(\frac{\hbar}{m_\pi c}\right)^2 V_s \frac{1}{r}\frac{d}{dr} F(x_s)\boldsymbol{\sigma}\cdot\mathbf{l} + U_c(r),$$

where $F(y) = (e^y+1)^{-1}$,

$$x = (r - r_0 A^{1/3})/a,$$
$$x' = (r - r_0' A^{1/3})/a',$$
$$x_s = (r - r_s A^{1/3})/a_s,$$

[12] B. M. Bardin and M. E. Rickey, Rev. Sci. Instr. 35, 902 (1964).

[13] R. A. Paddock, W. Benenson, and S. M. Austin (to be published).

[14] K. M. Thompson, C. R. Gruhn, and J. Frink, Phys. Letters 24B, 503 (1967).

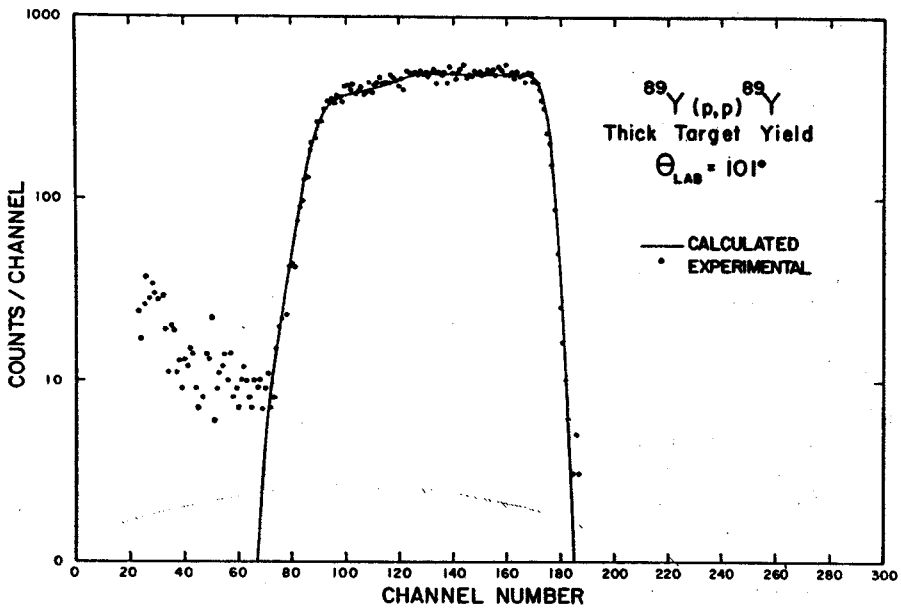

FIG. 2. Elastically scattering protons from a thick ^{89}Y target at 101° in the laboratory. The calculated curve was obtained by assuming the beam spot included several regions of different target thickness.

and $U_c(r)$ is the Coulomb potential for a uniformly charged sphere of radius $1.31A^{1/3}$ F. The spin-orbit strength V_s was constrained to be real. The parameter values were obtained by minimizing the quantity χ^2 by an automatic search routine:

$$\chi^2 = N^{-1} \sum_{i=1} \{[\sigma_{\text{theor}}(\theta_i) - \sigma_{\text{expt}}(\theta_i)]/\Delta\sigma_{\text{expt}}(\theta_i)\}^2,$$

where $\sigma_{\text{theor}}(\theta_i)$ and $\sigma_{\text{expt}}(\theta_i)$ are the theoretical and measured differential cross sections at angle θ_i, and $\Delta\sigma_{\text{expt}}(\theta_i)$ is the error assigned to σ_{expt} at the angle θ_i.

The fit to the experimental differential cross section divided by the Rutherford differential cross section is shown in Fig. 4. The parameters of the optical model given on the figure were used for the distorted-wave analysis of the inelastic scattering.

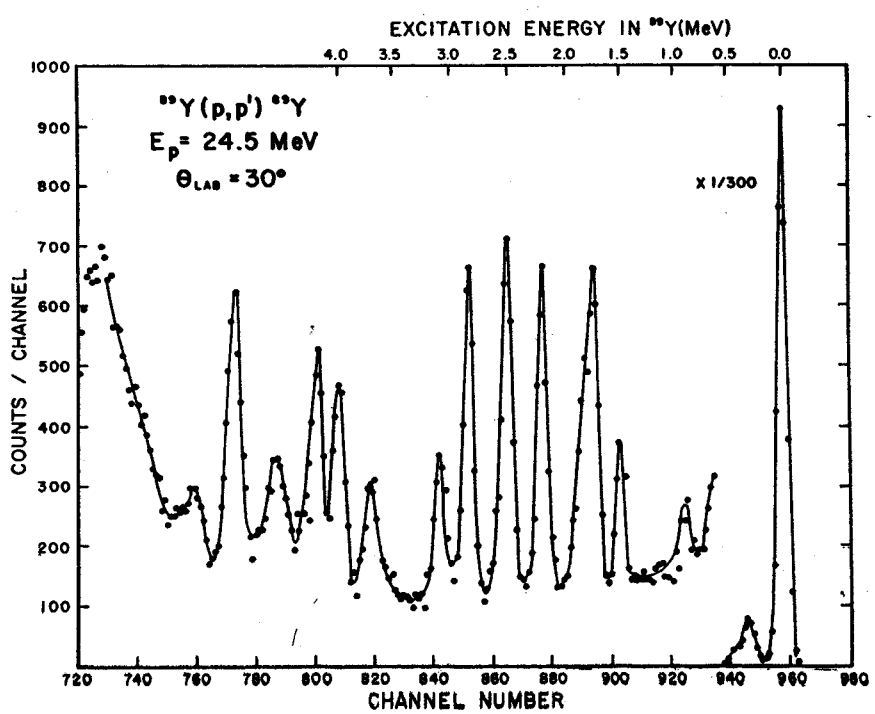

FIG. 3. Spectrum of protons scattered from ^{89}Y at 30° in the laboratory. The broad peak near channel 945 is due to contaminants in the target.

B. Inelastic Scattering

The theoretical predictions for the inelastic scattering were computed in the distorted-wave approximation.[15] All exchange effects between the projectile and target are ignored except insofar as they are included in the effective interactions or form factors. The data are analyzed using both the macroscopic collective model and the microscopic shell model. In the microscopic description, however, some core-polarization effects are included by means of a macroscopic model.[16]

1. Collective-Model Analysis

In this model the ground state of ^{89}Y is a single proton occupying a $2p_{1/2}$ state outside a closed ^{88}Sr core. The excited states are then the $2p_{1/2}$ proton coupled to the various collective excitations of the ^{88}Sr core. The cross section is proportional to β_L^2, where β_L is the deformation parameter and is the only unknown parameter in the theory.[17] The β_L may also be determined from the electromagnetic transition strength.

Another interesting consequence of the simple collective model is the sum rule relating transition probabilities. In particular, if the extra core particle has $j=I_i$, then one expects for every core excitation with $J_c>I_i$ of ^{88}Sr, $2I_i+1$ excited states of the core plus one-particle system. (In our case $2I_i+1=2$ and we expect a sequence of doublets if this model is correct.)

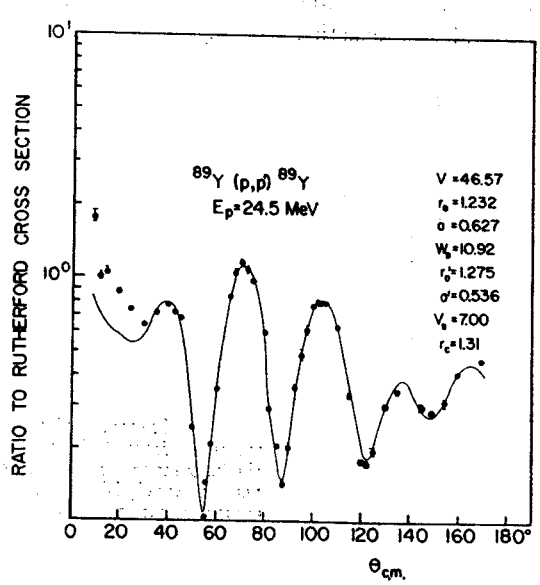

FIG. 4. Ratio of elastically scattered protons from ^{89}Y to the Rutherford cross section. The solid curve is an optical-model fit to the data points. The errors shown are statistical and do not include angular errors, which are important in the forward angles where the Rutherford cross section depends very strongly on angle.

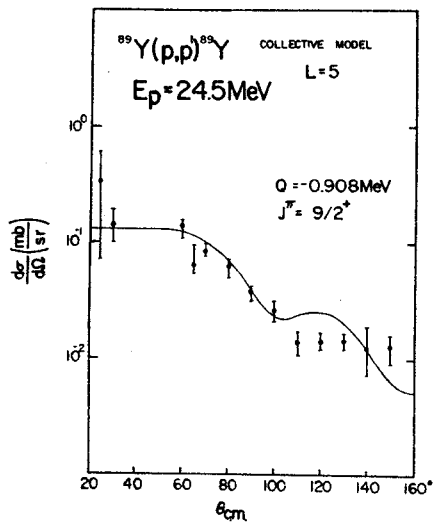

FIG. 5. Collective-model fit to the scattering of 24.5-MeV protons from the first excited state of ^{89}Y.

In this case the sum rule reads

$$\sum_{I_f} \sigma_{I_i \to I_f}(\theta) = \sigma_{0 \to \lambda}(\theta)_{\text{core}}.$$

It is convenient to introduce a partial deformation parameter,

$$\beta_L(I_f)[(2I_f+1)/(2I_i+1)(2L+1)]^{1/2}\beta_L.$$

The sum rule then reads

$$\sum_{I_f} \beta_L^2(I_f) = \beta_L^2.$$

The 0.908-MeV state. Although the 0.908-MeV $\frac{9}{2}^+$ level in ^{89}Y is not believed to be a collective level, it is convenient to analyze it as such for comparison with other collective analyses as well as for comparison with a microscopic analysis. Figure 5 shows the experimental cross section along with the collective-model prediction. A β_5 of 0.06 is found in good agreement with Awaya's value of 0.07.[4] This value of β_5 is also in rough agreement with that obtained by Gray *et al.*[18] for the excitation of the 5^- state in ^{90}Zr. Such a value is more suggestive of a single-particle transition.

The 1.51- and 1.74-MeV states. The 1.51-MeV level has been assigned a $J^\pi=\frac{3}{2}^-$ and the 1.74-MeV level a $J^\pi=\frac{5}{2}^-$.[3-5] Such a doublet suggests the collective model, since these are just the values of J^π expected to arise from the coupling of a $p_{1/2}$ particle to the 2^+ excitation of the core. However, the $B(E2)$ values[3] to these levels are about one single-particle unit, which suggests a less collective description of these states. The results of the collective model, including Coulomb excitation, are shown in Fig. 6. The angular distributions are in reasonable agreement with experiment and, as can be seen

[15] G. R. Satchler, Nucl. Phys. 55, 1 (1964).
[16] W. G. Love and G. R. Satchler, Nucl. Phys. A101, 424 (1967).
[17] G. R. Satchler, Nucl. Phys. A95, 1 (1967).
[18] W. S. Gray, R. A. Kenefick, J. J. Kraushaar, and G. R. Satchler, Phys. Rev. 142, 735 (1966).

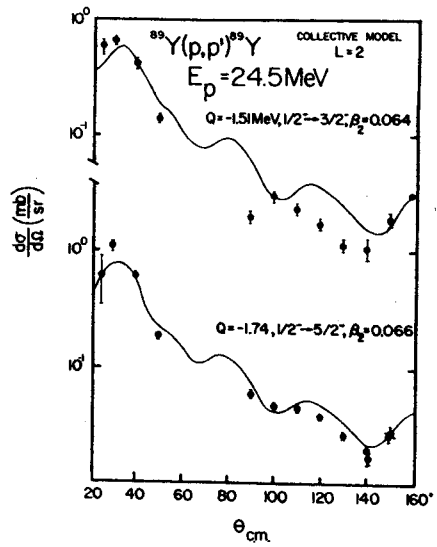

FIG. 6. Collective-model fits to inelastic scattering from the second and third excited states of ^{89}Y.

from Table I, the cross sections are approximately proportional to $2I_f+1$ as predicted by the simple collective model. The values obtained are consistent with those extracted from the corresponding electromagnetic measurements. The inelastic scattering to the $\frac{5}{2}^-$ level does seem to be slightly enhanced compared to the corresponding electromagnetic transition. As in the case of the electromagnetic transitions,[3] we find here that the transition strengths to this doublet exhausts only about 30% of the sum rule if we take $\beta_2=0.114$ in ^{88}Sr.[3] The value of β_2 found for these two states indicates that they might be more reasonably described by the shell model.

Higher-lying states. Angular distributions were obtained for the $\frac{5}{2}^+$ 2.21-MeV state as well as for multiplets at 2.52 and 2.86 MeV. One can analyze the data under the assumption that only one level was excited at each energy. This could easily be the case if there is just one level of strong collective character near 2.52 and 2.86 MeV. Previous to the high-resolution work[6] which resolved these levels into multiplets, the 2.52-MeV state was thought to be $\frac{7}{2}^+$ and the 2.86-MeV state either $\frac{7}{2}^+$ or $\frac{5}{2}^+$.

As can be seen from Fig. 7, scattering from these three states has angular distributions that are well described by an angular-momentum transfer of $L=3$ when the cross sections are calculated using the collective model including Coulomb excitation. In this simple model one would expect only a doublet, however, with J^π of $\frac{5}{2}^+$ and $\frac{7}{2}^+$. Furthermore, all three are very strongly excited, yielding electromagnetic transitions about 10 times the single-particle value.[3] In this experiment, as can be seen in Table I, the sum rule is exhausted only if all three of the octupole excitations are included. Although the 2.21- and 2.52-MeV levels fail to exhaust the sum rule, their excitation strengths are in the ratio predicted by the simple collective model.

TABLE I. Deformation parameters. The electromagnetic β_L's are taken from the work of Peterson and Alster (Ref. 3). The β_L's from (p,p') on ^{88}Sr are from the work of Stautberg *et al.* (Ref. 2).

E_x (MeV)	J^π	Nucleus	L	Electromagnetic $\beta_L(I_f)$	From (p,p') $\beta_L(I_f)$	$\beta_L^2(I_f)$	β_L
0.908	$\frac{3}{2}^+$	^{89}Y	5		0.0408	0.00166	0.0604
1.507	$\frac{3}{2}^-$	^{89}Y	2	0.0378±0.0183	0.0404	0.00163	0.0639
1.745	$\frac{5}{2}^-$	^{89}Y	2	0.0413±0.0060	0.0512	0.00261	0.0660
1.84	2^+	^{88}Sr	2	0.111 ±0.003	0.13	0.017	0.13
2.222	$\frac{5}{2}^+$	^{89}Y	3	0.116 ±0.005	0.103	0.0106	0.157
2.532	$\frac{7}{2}^+$	^{89}Y	3	0.123 ±0.005	0.115	0.0132	0.152
2.86	$(\frac{7}{2}^+)$	^{89}Y	3	0.114 ±0.005	0.975	0.0095	0.129
2.74	3^-	^{88}Sr	3	0.180 ±0.003	0.200	0.040	0.200

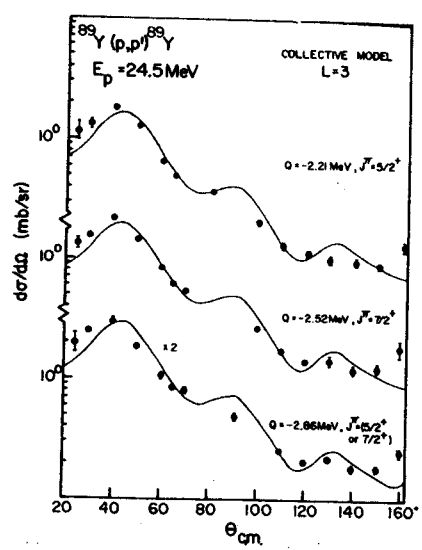

FIG. 7. Collective-model fits to inelastic scattering from states in ^{89}Y near 2.21, 2.52, and 2.86 MeV.

2. *Shell-Model Analysis*

In this description the zero-order ground state of ^{89}Y is taken to be a single proton occupying a $2p_{1/2}$ state outside a closed core. The excited states are then described either by exciting this particle to a higher-lying shell-model orbit or by promoting one of the core particles to one of the unoccupied levels lying above the closed shell. By zero-order is meant the simple individual particle state without the inclusion of core polarization. The single-particle states are taken as eigenstates of a Woods-Saxon potential. The relevant parameters are given in Table II. In this case the form factor is given by the nuclear matrix element of some effective operator V. Following Johnson *et al.*,[19] we write $V=\sum_i v_{ip}$, where v_{ip} is an effective two-body

[19] M. B. Johnson, L. W. Owen, and G. R. Satchler, Phys. Rev. 142, 748 (1966).

interaction between the projectile p and the ith target nucleon. Also,

$$v_{ip} = -(V_0 + V_1 \sigma_i \cdot \sigma_p) g(r_{ip}),$$

where

$$V_S = V_{S\alpha} + V_{S\beta}(\tau_i \cdot \tau_p), \quad S = 0 \text{ or } 1.$$

This yields a form factor $F_{LSJ}(r)$ as follows:

$$F_{LSJ}(r_p) = [M_L \delta(S,0) + N_{LJ} \delta(S,1)] I_L(r_p),$$

where these quantities are defined by Johnson *et al.*[19] The first term corresponds to a spin transfer of 0; the second term to a spin transfer of 1. **L** is the orbital angular-momentum transfer and **J**=**L**+**S** is the total angular-momentum transfer. It has recently been shown that if one includes core polarization, one should use,

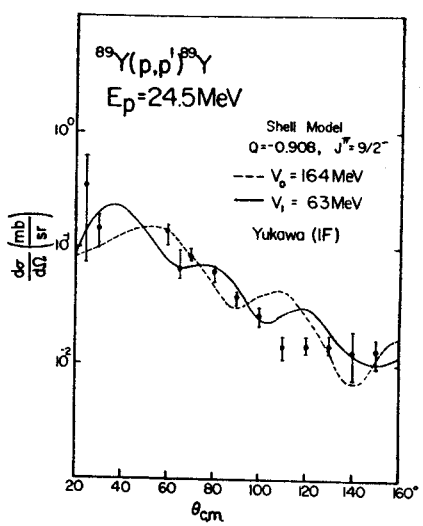

FIG. 8. Microscopic-shell-model fit to inelastic scattering from the first excited state of ^{89}Y neglecting core polarization. The dashed curve was obtained by setting $V_1=0$ and the solid curve by setting $V_0=0$.

instead of $F_{LSJ}(r_p)$, $\tilde{F}_{LSJ}(r_p)$, where

$$\tilde{F}_{LSJ}(r_p) = [M_L \delta(S,0) \tilde{I}_L(r_p) + N_{LJ} \delta(S,1) I_L(r_p)]$$

and

$$\tilde{I}_L(r_p) = I_L(r_p) + (4\pi V_0)^{-1} Y_L(Q) \langle n_2 L_2 f_2 | k_v | n_1 L_1 f_1 \rangle k_p(r_p),$$

and $k_p(r_p)$ is the usual collective form factor. The other quantities are defined elsewhere.[16] There is, of course, an isospin dependence of $F_{LSJ}(r)$, but since we shall only be concerned with the excitation of protons by protons, we only use the combination $V_S = V_{S\alpha} + V_{S\beta}$.[18] Throughout the analysis the form of $g(r)$ will be taken to be that of Yukawa potential with a range of 1.0 F.

With each form factor $F_{LSJ}(r)$ there will be associated one amplitude and a labeling triad (LSJ). Since the amplitudes belonging to different values of J are rigorously incoherent and those corresponding to different values of S are approximately so,[4] we may write

$$\frac{d\sigma}{d\theta} = \text{const} \times \frac{2J_f+1}{2J_i+1} \sum_{LSJ} \sigma_{LSJ}(\theta),$$

where $\sigma_{LSJ}(\theta)$ is the partial cross section corresponding to the form factor $\tilde{F}_{LSJ}(r)$.

TABLE II. Shell-model parameters.

Potential parameters for bound protons				
Orbit	$2p_{1/2}$	$2p_{3/2}$	$1f_{5/2}$	$1g_{9/2}$
Binding energy (MeV)	7.88	9.65	9.46	5.68
Well depth (MeV)	61.0	61.0	61.0	61.9
Nuclear radius $=r_0A^{1/3}$,				$r_0=1.2$ F
Coulomb radius $=r_CA^{1/3}$,				$r_C=1.25$ F
Diffuseness $=a$,				$a=0.7$ F
Spin-orbit parameter $=\lambda$,				$\lambda=25$

Three of the states to which the collective model was applied in Sec. III B 1 exhibit deformation parameters more suggestive of shell-model transitions than of collective ones. These are the $\frac{9}{2}^+$ state at 0.908 MeV, the $\frac{3}{2}^-$ state at 1.51 MeV, and the $\frac{5}{2}^-$ state at 1.74 MeV.

The 0.908-MeV state. The zero-order shell-model description of this state is taken to be that of a single proton outside a closed ^{88}Sr core occupying the $1g_{9/2}$ single-particle state. The participating triads (LSJ) for this transition are (505), (515), (514), and (314). The (514) component is negligible because of its small nuclear matrix element (N_{LJ}). Table III gives the values of the nuclear matrix elements used in the shell-model description. Because small angular-momentum transfers are favored, the $S=1$ term is dominated by the (314) triad. One can get an upper limit to both V_0 and V_1 by setting V_1 and V_0, respectively, to zero and ignoring any core polarization. The resulting angular distributions are shown in Fig. 8. The upper limits obtained are 164 MeV for V_0 and 63 MeV for V_1. If one still ignores core polarization but takes $V_0=100$ MeV, which was recently[16] found to be a reasonable value, then an upper limit to V_1 is about 50 MeV. Figure 8 shows that the angular distribution is rather poorly reproduced by either the $S=0$ or $S=1$ term alone. Although the angular distribution can be improved by adjusting the ratio $|V_1/V_0|$, this has not been done here, since the effects of core polarization are not known for this transition. To get a rough estimate of the core

TABLE III. The nuclear matrix elements M_L and N_{LJ} relevant to the shell-model analysis in the text.

Transition					
$\frac{1}{2}^- \to \frac{9}{2}^+$	$p_{1/2} \to g_{9/2}$	M_5	N_{34}	N_{54}	N_{55}
		−0.28209	−0.37613	−0.04205	0.30902
$\frac{1}{2}^- \to \frac{3}{2}^-$	$p_{1/2}^{-1} \to p_{3/2}^{-1}$	M_2	N_{01}	N_{21}	N_{22}
		−0.28209	−0.32573	−0.11516	0.34549
$\frac{1}{2}^- \to \frac{5}{2}^-$	$p_{1/2}^{-1} \to f_{5/2}^{-1}$	M_2	N_{22}	N_{23}	N_{43}
		−0.28209	−0.23033	−0.06156	0.42649

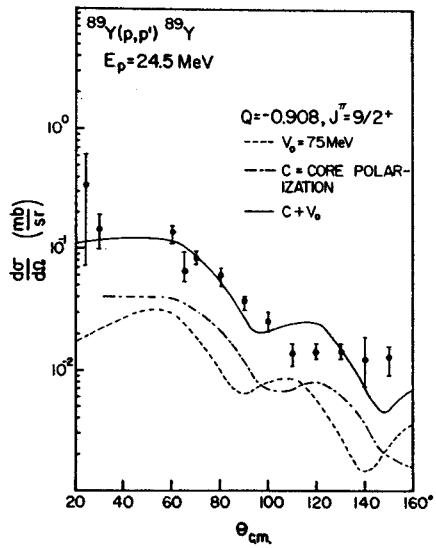

FIG. 9. Microscopic-shell-model fit to inelastic scattering from the first excited state of ^{89}Y including core polarization. Also shown are the individual contributions from the core and the single-particle transitions.

participation, however, the coupling parameter $Y_L(Q)$ [16] was taken to be the same as that found in the electromagnetic excitation of the 2.31-MeV 5$^-$ level in ^{90}Zr. With this estimate of the strength of the core participation, a V_0 of about 75 MeV is required with $V_1=0$. The fit to the experimental cross section including core polarization is shown in Fig. 9. It is similar to that found when the collective model alone is used. This value of V_0 is intermediate between the value ($\sim$100 MeV) found at 19 MeV [16] for the excitation of the 5$^-$ level in ^{90}Zr and the value (50 MeV) found at 62 MeV [7] for the excitation of this same level in ^{89}Y using the ^{90}Zr core parameters. This energy dependence is very similar to that found from analysis of ^{7}Li(p,p')^{7}Li.[8]

The 1.51- and 1.74-MeV states. Excitation of these states is considered to be via the excitation of a proton in the $2p_{3/2}$ or $1f_{5/2}$ state to the $2p_{1/2}$ state. For example,

$$|\tfrac{3}{2}^-\rangle = |2p_{3/2}^{-1};2p_{1/2}^{2}\rangle|^{88}\mathrm{Sr}\rangle,$$
$$|\tfrac{5}{2}^-\rangle = |1f_{5/2}^{-1};2p_{1/2}^{2}\rangle|^{88}\mathrm{Sr}\rangle,$$
$$|\tfrac{1}{2}^-,GS\rangle = |2p_{1/2}\rangle|^{88}\mathrm{Sr}\rangle.$$

This description is consistent with the small deformation parameters found for these states as well as the spectroscopic factors from a recent (d,^{3}He) experiment by Preedom *et al.*[1] Actually the spectroscopic factor found for the pickup of a $1f_{5/2}$ proton indicates that there should perhaps be a $(f_{5/2}^{-1}g_{9/2}^{2})$ component present in the $\frac{5}{2}^-$ state which is neglected in the present work. Coulomb excitation is included with the macroscopic form factors.

These two states are particularly interesting since excitation of the $\frac{3}{2}^-$ state introduces the (LSJ) triads (011), (211), (202), and (212), whereas excitation of the $\frac{5}{2}^-$ states involves the triads (212), (202), (213), and (413). Again the interference between different triads is neglected. Contributions from the (211) and (213) triads are negligible compared with the others because of small nuclear matrix elements. In the case of the excitation of the $\frac{3}{2}^-$ state, the nuclear matrix elements N_{01} and N_{22} are approximately equal but the calculation favors the lower L component. In the case of the $\frac{5}{2}^-$ state, however, the nuclear matrix element N_{43} is about equal to $2N_{22}$, so that, although small L transfers are favored, the triads (212) and (413) contribute about equally. The net result is that in the excitation of the $\frac{3}{2}^-$ state the $S=1$ part of the force gives a cross section that for $V_0=V_1$ is about 10 times as large as the $S=0$ cross section.[4] For the excitation of the $\frac{5}{2}^-$ state, however, the $S=1$ part of the force introduces an additional cross section that is approximately equal of that of the $S=0$ component with $V_0=V_1$. The relatively strong monopole $S=1$ term participating in the excitation of the $\frac{3}{2}^-$ state places an upper limit on V_1 of $\sim$36 MeV. An upper limit to V_0 obtained from this excitation is $\sim$120 MeV. For a V_0 of 100 MeV, a V_1 of 20 MeV is required. When core polarization is included, V_1 is reduced still further. When one compares the experimental angular distributions to these two states (Fig. 6), one realizes that the similarities rather than the differences in angular distributions are most apparent. As is shown in Fig. 10, any large component of $S=1$ in the case of the $\frac{3}{2}^-$ excitation will be hard to reconcile, since the (202) part of the cross section has a peak near 30°, whereas the monopole part does not. Having seen that the evidence points towards a rather weak $S=1$ term, we ignore it in studying the effects of core polarization.

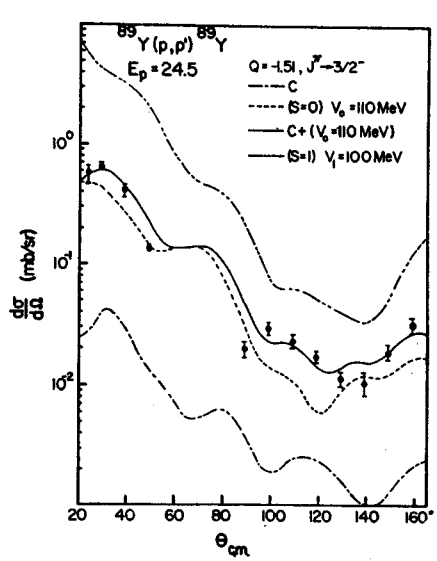

FIG. 10. Microscopic-model fits to scattering from the second excited state of ^{89}Y. The curve labeled C is the core-polarization contribution. The dashed curve labeled $S=0$ includes no core polarization or spin flip, whereas the solid curve includes core polarization. The curve labeled $S=1$ includes only spin flip.

The core-polarization parameters[16] are calculated from the measured electromagnetic transitions to these states as obtained from a recent electron scattering experiment.[8] These calculations yield

$$\tfrac{1}{2}^- \rightarrow \tfrac{3}{2}^-: \quad 1.08 \leq e_{\text{eff}}/e \leq 1.68, \quad 1260 \leq C_2 \leq 10\,700 \text{ MeV},$$
$$\tfrac{1}{2}^- \rightarrow \tfrac{5}{2}^-: \quad 1.39 \leq e_{\text{eff}}/e \leq 1.65, \quad 1150 \leq C_2 \leq 2550 \text{ MeV},$$

where C_2 is a measure of the core deformability.[16] Using the hydrodynamical value of $\hbar\omega_2$ ($\sim$15 MeV), the energy of the virtual core excitations, we find that the intensity of the admixed core state in the ground and excited states is on the order of 1%. The values obtained for the core parameter $Y_2(Q)$ associated with these excitations are given below in MeV^{-1}:

$$0.094\times10^{-3} < Y_2(1.51 \text{ MeV}) < 0.80 \times10^{-3},$$
$$0.39 \times10^{-3} < Y_2(1.74 \text{ MeV}) < 0.872\times10^{-3},$$

whereas in the excitation of the first 2^+ state in ^{90}Zr the $Y_2(2.18 \text{ MeV})$ was found to be 1.61×10^{-3} MeV^{-1}. The approximate factor of 3 difference between these values and that found for ^{90}Zr seems significant. If the core excitation strength actually measured the participation of the ^{88}Sr core, then, ignoring the blocking effects due to the Pauli principle, one would expect the values of Y_2 for the three states to be approximately equal. Inclusion of the blocking effects due to the Pauli principle would tend to lower the value of Y_2 in ^{90}Zr relative to that in ^{89}Y. Since Y_2 is much larger in ^{90}Zr, we interpret the core-excitation process in a more general way as representing that part of Hilbert space that is omitted in the simple shell-model description. Figure 10 shows the inclusion of core excitation as described above applied to the excitation of the $\frac{3}{2}^-$ state. The calculation uses the mean value of the $B(E2)$'s and requires a V_0 of 110 MeV. However, because of the uncertainty in the value of the $B(E2)$, it can really only be said that $90 \lesssim V_0 \lesssim 120$ MeV. This is in agreement with other calculations[16] that include core polarization. The fit seems to be qualitatively better than either the direct or core-polarization terms alone. The range of values is an upper limit to V_0 because the $S=1$ part of the interaction has been neglected.

A similar analysis of the $\frac{5}{2}^-$ excitation was performed including core polarization. A discrepancy arises in this case, however, in that it is found that $165 \leq V_0 \leq 195$ MeV even when core polarization is included. This condition prevails because the $(2p_{1/2},1f_{5/2})$ form factor is smaller than the $(2p_{1/2},2p_{3/2})$ form factor by about a factor of $\sqrt{2}$. If the two form factors were approximately equal in strength, then a consistent value of V_0 could be found. In terms of the core participation, the coupling strength needs to be enhanced by about a factor of 2.4 in order to yield the correct magnitude for the cross section for a V_0 of 100 MeV. It is unlikely that the $S=1$ mechanism can account for the large experimental cross section of the $\frac{5}{2}^-$ state, since its inclusion would have a much larger effect on the $\frac{3}{2}^-$ cross section and lead to a much smaller value of V_0 for the $\frac{3}{2}^-$ excitation. Our phenomenological representation of the effective interaction may not represent the correct multipole behavior of the various parts of the force, although the inconsistency is, perhaps, more likely to be suggestive of a poor description of the $\frac{5}{2}^-$ state. An admixture of a $g_{9/2}^2$ configuration will improve the agreement of the state description with the available spectroscopic factor. Such an admixture would imply stronger core participation, since the $g_{9/2}^2$ component would not contribute to the excitation of this level. This might make the core parameters more compatible with those associated with ^{90}Zr. A similar admixture of a $g_{9/2}^2$ component in the $\frac{3}{2}^-$ state would also imply a stronger participation of the core in that transition and would also allow the upper limit on the magnitude of the $S=1$ term to be raised. Since a small admixture of the core might boost the cross section to agree with experiment, a description of the $\frac{5}{2}^-$ state was attempted which is just a generalization of the weak-coupling model, namely,

$$|\tfrac{5}{2}^-\rangle = a|1f_{5/2}^{-1}\rangle + b|(2p_{1/2}\times\hbar\omega_2)\tfrac{5}{2}^-\rangle.$$

The quantities a and b were taken to be real and were selected to yield the correct value of $B(E2)$ and approximately the correct cross section, V_0 being taken equal to 100 MeV. Such an analysis yields $a \simeq 0.87$ and $b \simeq -0.035\langle\hbar\omega_2\|\alpha_2^*\|0\rangle$. The fit to the data is then shown in Fig. 11. Also shown is the contribution due to the core and that due to the direct terms ($V_0=100$ MeV). Consistency between the cross section and $B(E2)$ is obtained for this state only by allowing the core and direct terms to interfere destructively. Now,

$$\langle\hbar\omega_\lambda\|\alpha_\lambda^*\|0\rangle = -(2\lambda+1)^{-1/2}\beta_\lambda,$$

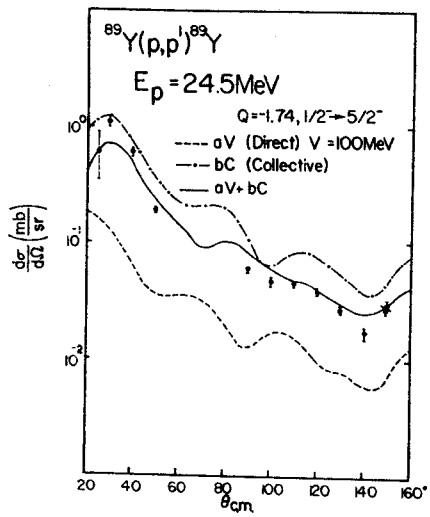

FIG. 11. Fit to the scattering of protons from the third excited state of ^{89}Y. A weak-coupling model is used with interference between direct and collective contributions.

where β_λ is the deformation parameter of the ^{88}Sr core in the presence of the extra core proton. Taking $\beta_2=0.114$ [1] (R_c is taken to be $1.25A^{1/2}$),

$$b\approx 0.64.$$

a^2+b^2 need not equal 1, since the two states are not necessarily orthogonal. This must certainly be regarded as a tentative and incomplete description of this state.

IV. CONCLUSION

The $\frac{9}{2}^+$ state at 0.908 MeV is characterized by a small ($\beta_5=0.06$) deformation parameter and seems to be reasonably well described in terms of a single-particle state when the coupling to the core is included. The quality of the fit is only fair, but neither the range of the force nor the mixture of $S=1$ was optimized.

Although the $\frac{3}{2}^-$ and $\frac{5}{2}^-$ states at 1.51 and 1.74 MeV are reasonably well described in terms of the collective model, a microscopic analysis in which the $\frac{3}{2}^-$ state was taken to be a hole in the $2p_{3/2}$ shell plus two $p_{1/2}$ particles outside the core was also found to be consistent with the data. The analysis of both of these states in terms of single-hole states is suggested by the small transition probabilities and by the large spectroscopic factors. The analysis of the $\frac{5}{2}^-$ state was not so straightforward, however, because the inelastic cross section seems to be enhanced relative to the electromagnetic transition. In this case, therefore, a V_0 much larger than that needed for the other states is required. Alternatively, the participation of the core is incompletely accounted for in terms of the corresponding electromagnetic transition. Other important uncertainties arise because we ignore knock-out terms and multiple excitation. In addition, the multipole dependence of the spin-dependent part of the force is unknown. Information obtained on the effective forces V_0 and V_1 are summarized in Tables IV and V. For a Yukawa force of range 1 F an upper limit to $|V_1|=|V_{1\alpha}+V_{1\beta}|$ of 36 MeV has been established. Since $V_{1\beta}$ has been shown to be approximately 11 MeV[20] at this energy, this puts an upper limit on $V_{1\alpha}$ of 47 MeV. Ignoring the difficulty with the $\frac{5}{2}^-$ state, it seems that a real Yukawa of range 1 F and a strength of about 75 to 100 MeV does represent at least the strength of the effective proton-proton interaction at 24.5 MeV when core polarization is included.

TABLE IV. Measured values of V_0 and V_1 assuming a Yukawa shape with range of 1 F.

State (MeV)	Core polarization	V_0 (MeV)	V_1 (MeV)
0.908	No	164	0
0.908	No	0	63
0.908	No	100	50
0.908	Yes	75	0
1.51	No	120	0
1.51	No	0	36
1.51	No	100	20
1.51	Yes	110	0

TABLE V. Information on V_0, the central part of the effective interaction, from ^{89}Y$(p,p')^{89}$Y* (0.908 MeV). The spin-flip part of the interaction V_1 is set equal to zero. A Yukawa shape with a range of 1 F is assumed.

E_p (MeV)	Core polarization	V_0 (MeV)	Reference
14.7	No	205	4, 17
18.9	No	205	2, 17
24.5	No	164	Present work
24.5	Yes	75	Present work
61.2	No	91	7
61.2	Yes	50	7

ACKNOWLEDGMENTS

We are indebted to G. R. Satchler for many helpful discussions and to R. M. Drisko for the use of the optical-model code HUNTER and the distorted-wave code JULIE. We are also indebted to Professor H. McManus and F. Petrovich for their continued interest and help in this project. The loan of the ^{89}Y target by Dr. J. B. Ball of Oak Ridge National Laboratory is greatly appreciated.

[20] P. J. Locard, S. M. Austin, W. Benenson, and G. M. Crawley, Bull. Am. Phys. Soc. 12, 1178 (1967).

PRODUCTION OF ^{11}B AND ^{10}B BY PROTON SPALLATION OF ^{12}C†

Cary N. Davids, Helmut Laumer, and Sam M. Austin
Physics Department, Michigan State University, East Lansing, Michigan 48823
(Received 20 December 1968; revised manuscript received 9 May 1969)

Measurements of the ^{10}B and ^{11}B spallation production in ^{12}C are presented. These cross sections are related to theories on the origin of the elements lithium, beryllium, and boron.

The nucleosynthesis of the light elements lithium, beryllium, and boron (LiBeB) is a problem of great astrophysical interest.[1-3] Since these elements have very short lifetimes for destruction by stellar thermal protons, they will not survive if produced in the inner regions of stars. It is generally believed that they are produced in a cool stellar environment by the proton-induced spallation of abundant heavier nuclei. The fast protons, with energies of several MeV and high-

er, are supplied by the acceleration processes associated with flares on the stellar surface. In order to compare the observed abundances of these elements with theoretical predictions, the experimental formation cross sections of LiBeB in the abundant stellar targets ^{12}C, ^{14}N, ^{16}O, ^{20}Ne, and ^{28}Si are required. The proton energies of interest lie in the region just above the LiBeB production thresholds, where the cross sections rise to their peak values and the flux of incident protons is high. In ^{12}C these thresholds range from 15 to 30 MeV. Unfortunately, the only data available in this low-energy region are on the production of the unstable isotopes, and there is a total absence of data for the boron isotopes.

We have measured proton spallation cross sections in ^{12}C for isobars with $6 \leq A \leq 11$, at proton energies between 24.5 and 44 MeV. These cross sections, together with estimated and measured cross sections for other important targets, seem consistent with a recent model[3] locating the spallation site in the stellar atmosphere.

At these proton energies the mass-6 particles are ^{6}He and ^{6}Li. The mass-7 particles are ^{7}Li and ^{7}Be, while masses 8 and 9 are, respectively, ^{8}B and ^{9}Be. Mass 10 consists of ^{10}Be, ^{10}B, and ^{10}C, with ^{11}B and ^{11}C comprising the mass 11 yield. For each mass there is only one stable isobar (except for mass 8, which has none), and the radioactive isobars decay rapidly to it on an astrophysical time scale.[4] Thus for our purposes a mass measurement is sufficient, and mass-$6 \equiv {}^{6}Li$, mass-$7 \equiv {}^{7}Li$, mass-$9 \equiv {}^{9}Be$, mass-$10 \equiv {}^{10}B$, and mass-$11 \equiv {}^{11}B$.

In our experiment, identification was performed by measuring the energy (E) and time of flight (T) of the ions following their production in a thin target. A thin semiconductor detector and the pulsed beam of the Michigan State University sector-focused cyclotron were used. On-line calculation of the quantity ET^2 in a digital computer produced displays such as that shown in Fig. 1, from which total mass yields could be extracted. Integration of the energy and angular distributions permitted the determination of total cross sections for each mass.

A theory describing the origin of LiBeB must explain any deviations from the formation values of the observed isotopic ratios $^{11}B/^{10}B$ and $^{7}Li/^{6}Li$. These ratios are observed to be 4.1 and 12.5, respectively, both terrestrially and in meteorites.[5] The original theory of Fowler, Greenstein, and Hoyle[1] (later modified by Burnett, Fowler, and Hoyle[2]) assumed these ratios were

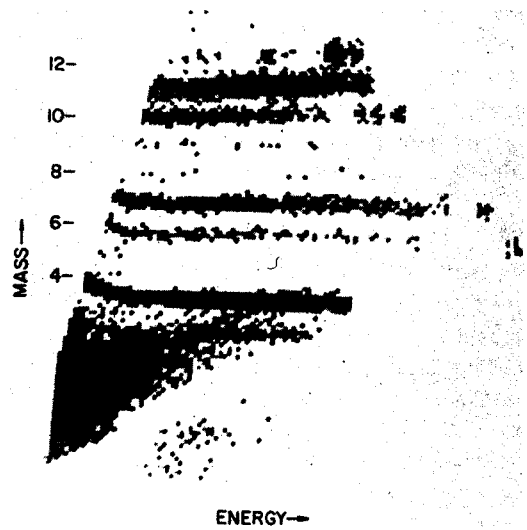

FIG. 1. Computer-oscilloscope display of ET^2 (mass) vs E, showing mass separation.

approximately unity. In order to explain the solar-system ratios, a slow-neutron flux was proposed, which would deplete ^{6}Li and ^{10}B.

A recent theory due to Bernas et al.[3] takes a slightly different viewpoint. These authors suggest that the observed $^{11}B/^{10}B$ ratio is the unaltered formation ratio. Their estimate of 2.5 for the $^{7}Li/^{6}Li$ formation ratio is consistent with our results for ^{12}C. In addition, the large observed $^{7}Li/^{6}Li$ ratio is attributed to depletion of ^{6}Li, but in this case via reactions with low-energy stellar protons. The energy of these protons is assumed to be low enough so that the $^{11}B/^{10}B$ ratio is unaffected. The stellar atmosphere is proposed as the site of the spallation reactions, and hence in the sun the principal targets are the abundant nuclei ^{12}C, ^{14}N, ^{16}O, and possibly ^{20}Ne. No neutrons are required, and in fact their presence would only serve to further increase the $^{11}B/^{10}B$ ratio.

From the above, it is clear that the experimental formation cross sections for ^{10}B and ^{11}B play a key role in determining the origin of LiBeB.

The results of the present experiment on mass-10 and mass-11 production cross sections are shown in Fig. 2. Using these results to calculate the yields of ^{10}B and ^{11}B from ^{12}C requires knowledge of the range of proton energies involved. Recent studies of solar flares[6] show proton energy spectra having an energy dependence of the form $E^{-\gamma}$, where γ varies between 3 and 4. Such a steep energy dependence means that, for the case of ^{12}C, the product of proton flux and pro-

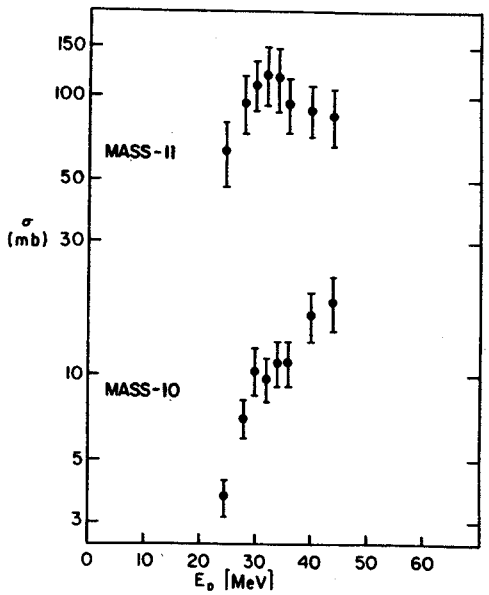

FIG. 2. Cross sections for production of mass-10 and mass-11 isobars by proton-induced reactions in ^{12}C.

duction cross section is significant only for proton energies between 15 and 50 MeV. The cross sections of Fig. 2 show that the production of ^{11}B from ^{12}C considerably exceeds that of ^{10}B under such conditions. The target ^{14}N will also serve as a prolific source of ^{11}B via the low-threshold reaction $^{14}N(p, \alpha)^{11}C$. The low-energy $^{11}B/^{10}B$ ratio for ^{16}O is as yet unknown, but has a value of 2.3 at 135 MeV,[7] in agreement with calculations.[3] These results are consistent with the view of Bernas et al.[3] that the observed $^{11}B/^{10}B$ ratio is the formation ratio, and that the spallation occurs in the stellar atmosphere. Measurements of the ^{10}B and ^{11}B production from ^{14}N and ^{16}O in the threshold region are currently under way in this laboratory.

†Work supported in part by the National Science Foundation.

[1]W. A. Fowler, J. L. Greenstein, and F. Hoyle, Geophys. J. Roy. Astron. Soc. 6, 148 (1962).

[2]D. S. Burnett, W. A. Fowler, and F. Hoyle, Geochim. Cosmochim. Acta 29, 1209 (1965).

[3]R. Bernas, E. Gradsztajn, H. Reeves, and E. Shatzman, Ann. Phys. (N.Y.) 44, 426 (1967).

[4]Although ^{10}Be could be considered stable with its half-life of 2.7×10^6 yr, its production rate is expected to be negligible compared with the total mass-10 yield [Ref. 3; J. Audouze, M. Epherre, and H. Reeves, in High-Energy Nuclear Reactions in Astrophysics, edited by B. S. P. Shen (W. A. Benjamin, Inc., New York, 1967), p. 255; E. Gradsztajn, ibid., p. 247].

[5]M. Shima, J. Geophys. Res. 67, 4251 (1962); D. Krankowsky and O. Muller, Geochim. Cosmochim. Acta 28, 1625 (1964).

[6]J. A. Simpson, private communication.

[7]F. Yiou, M. Basil, J. Dufaure deCitres, P. Fontes, E. Gradsztajn, and R. Bernas, Phys. Rev. 166, 968 (1968).

Reprinted from THE PHYSICAL REVIEW, Vol. 172, No. 4, 1078–1094, 20 August 1968
Printed in U. S. A.

(p,d) Reaction on $N=Z$ Nuclei in the $2s$-$1d$ Shell*

R. L. KOZUB†
Cyclotron Laboratory, Michigan State University, East Lansing, Michigan
(Received 26 January 1968)

An investigation of the (p,d) reaction on $N=Z$ nuclei in the $2s$-$1d$ shell has been made to obtain spectroscopic information and to study the $l_n=2$ J-dependence for the (p,d) reaction. The experiments were performed with ^{24}Mg, ^{28}Si, ^{32}S, ^{36}Ar, and ^{40}Ca as target nuclei, and virtually all of the $2s$-$1d$ shell hole strength was observed. Deuteron angular distributions for strongly excited levels in ^{23}Mg, ^{27}Si, ^{31}S, ^{35}Ar, and ^{39}Ca were measured for laboratory angles from 10° to 155°, and spectroscopic factors were obtained using distorted-wave Born-approximation (DWBA) calculations. The J dependence for the pickup of an $l_n=2$ neutron appears mostly in the forward angles of the angular distributions and seems to follow systematic trends through the $2s$-$1d$ shell, thus suggesting spin assignments for levels in ^{31}S, ^{35}Ar, and ^{39}Ca. Appreciable configuration mixing is found to exist in the ground-state wave functions of all the nuclei investigated. Of particular interest are the $l_n=1$ levels excited in the ^{24}Mg$(p,d)^{23}$Mg and ^{28}Si$(p,d)^{27}$Si reactions, which could arise from the removal of either $1p$- or $2p$-shell neutrons. The ground states of ^{36}Ar and ^{40}Ca are observed to contain appreciable mixing with the $f_{7/2}$ shell, and evidence exists for a small $[2p]^8$ admixture in the ^{40}Ca ground state. The level orders of the residual nuclei and the DWBA spectroscopic factors are discussed in terms of the strong-coupling rotational model and Nilsson-model wave functions. Evidence for strong rotational band mixing is apparent in many cases.

I. INTRODUCTION

SINCE its original observation by Standing in 1954,[1] the (p,d) reaction has been found to be a valuable tool for the experimental investigation of nuclear properties. This has proven to be particularly true at higher bombarding energies, where the direct-reaction theory is most successful. The widely used theory of direct-reaction processes is the distorted-wave Born approximation (DWBA)[2] and, to the extent that one can trust the DWBA calculations, the (p,d) reaction provides a direct measure of the overlap of the target wave function with the wave functions of the excited states of the residual nucleus. Configuration admixtures in the target nucleus are thus easily detectable by this reaction.

In 1964 it was observed by Lee and Schiffer[3] that the angular distributions for $l_n=1$ levels excited in the (d,p) reaction on spin-zero targets showed a dependence on the total angular momentum of the final nuclear state. Similar effects have also been observed in the (p,d) reaction,[4–7] where most of the previous investigations have been with nuclei in the $1p$ and $1f_{7/2}$ shells. However, relatively few (p,d) experiments have been performed on the $N=Z$ targets in the $2s$-$1d$ shell. This probably reflects the very negative reaction Q values (−13 to −15 MeV) and the close level spacings involved, which require both a high bombarding energy and good resolution in order to observe the level structure over a reasonable region of excitation in the residual nucleus.

The subject of this paper is an investigation of the (p,d) reaction on ^{24}Mg, ^{28}Si, ^{32}S, ^{36}Ar, and ^{40}Ca. The primary objectives were to study the configuration mixing in the ground-state wave functions of the target nuclei and the $l_n=2$ J-dependence in the deuteron angular distributions. In addition, information concerning the level structures of the residual nuclei (^{23}Mg, ^{27}Si, ^{31}S, ^{35}Ar, and ^{39}Ca) was obtained. The bombarding energy of 33.6 MeV was low enough to be compatible with the use of commercially available, high-resolution semiconductor detectors; at the same time it was high enough to expose 10–12 MeV of excitation in the residual nuclei.

II. EXPERIMENTAL METHODS

The 33.6-MeV protons were obtained by accelerating negative hydrogen ions with the 64-in. Michigan State University sector-focusing cyclotron[8] and extracting a single turn with a 0.0001-in. aluminum stripper foil. Two quadrupole magnets and a 20° bending magnet were used to focus the beam into the 36-in. scattering chamber. The beam was collected in a Faraday cup at the rear of the scattering chamber, and the charge was summed by a current integrator with an error of less than 1%. Beam currents ranged from 1 to 100 nA, depending on the scattering angle. The energy of the proton beam from the cyclotron was measured by the kinematic crossover method[9] and checked by an independent range-energy calibration. The two methods were in agreement to within ~200 keV.

* Research supported by the National Science Foundation.
† Present address: Cyclotron Institute, Texas A & M University, College Station, Tex.
[1] K. G. Standing, Phys. Rev. 94, 731 (1954).
[2] G. R. Satchler, Nucl. Phys. 55, 1 (1964).
[3] L. L. Lee, Jr., and J. P. Schiffer, Phys. Rev. Letters 12, 108 (1964).
[4] R. Sherr, E. Rost, and M. E. Rickey, Phys. Rev. Letters 12, 420 (1964).
[5] C. Glashausser and M. E. Rickey, Phys. Rev. 154, 1033 (1967).
[6] C. A. Whitten, Jr., E. Kashy, and J. P. Schiffer, Nucl. Phys. 86, 307 (1966).
[7] R. L. Kozub and E. Kashy, Bull. Am. Phys. Soc. 12, 644 (1967).
[8] H. G. Blosser and A. I. Galonsky (unpublished).
[9] B. M. Bardin and M. E. Rickey, Rev. Sci. Instr. 35, 902 (1964).

The reaction products were observed with a dE/dx–E counter telescope consisting of a 279-μ silicon surface-barrier detector (ΔE) and a 3-mm lithium-drifted silicon counter (E). This thickness for the ΔE counter would stop only those deuterons having energy $\lesssim 8$ MeV, which permitted the observation of 10–12 MeV of excitation in the nuclei studied. The telescope was mounted on a movable arm in the scattering chamber which could be positioned by remote control to an angular accuracy of $\pm 0.5°$. The solid angle was defined by a tantalum collimator subtending an angle of $\sim 1°$. For the gas targets used in the $^{32}S(p,d)^{31}S$ and $^{36}Ar(p,d)^{35}Ar$ experiments, an additional collimator was necessary to define the solid angle.

The deuteron pulses were electronically selected and sorted by a particle-identification circuit.[10] An over-all electronic noise width of 50 keV was obtained and the over-all deuteron energy resolution varied from 95 to 130 keV. The error in the absolute cross sections is estimated to be $\pm 7\%$, excluding the statistical error.

A detector consisting of CsI(Tl) crystal mounted on a photomultiplier tube was used as a monitor throughout the work. This same detector was used to obtain the $^{26}Mg(p,p)^{26}Mg$ and $^{36}Ar(p,p)^{36}Ar$ elastic scattering data with an over-all resolution of approximately 650 keV.

The ground-state (p,d) reaction Q values for the nuclei studied ranged from -14.95 MeV for the $^{28}Si(p,d)^{27}Si$ reaction to -12.86 MeV for the $^{32}S(p,d)^{31}S$ reaction. Since the Q values for the $^{16}O(p,d)^{15}O$ and $^{12}C(p,d)^{11}C$ reactions are in the same region (-13.44 and -16.50 MeV, respectively) and the ^{15}O and ^{11}C energy levels are well known,[11] deuteron spectra from ^{16}O and ^{12}C provided an excellent energy calibration.

The target used for the $^{24}Mg(p,d)^{23}Mg$ experiment was a rolled foil of 1.07 mg/cm^2 thickness which was enriched to $>99\%$ ^{24}Mg. A 0.88 ± 0.04-mg/cm^2 SiO target was fabricated by evaporating chemically pure SiO of natural isotopic abundance (92.2% ^{28}Si) to a 0.0001-in. nickel backing, and etching away a 2-cm^2 area of the nickel with HNO_3.

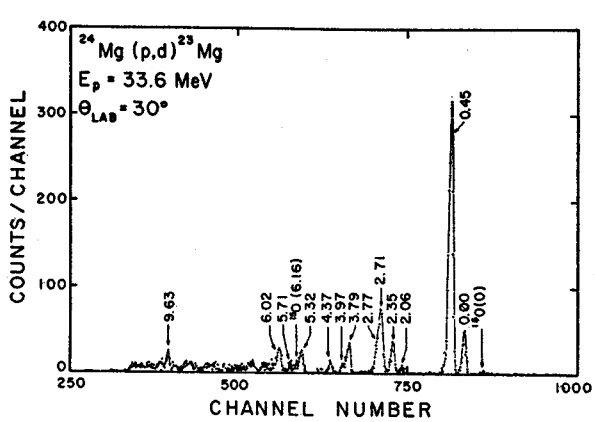

FIG. 1. Deuteron spectrum from $^{24}Mg(p,d)^{23}Mg$ reaction at $\theta_{lab}=30°$, showing levels of ^{23}Mg. A small oxygen contaminant is observed.

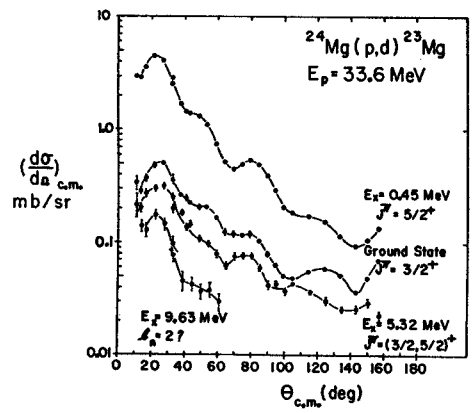

FIG. 2. Deuteron angular distributions corresponding to $l_n=2$ pickup in the $^{24}Mg(p,d)^{23}Mg$ reaction. The error bars refer only to statistics and, where not shown, are smaller than the data points. The curves are drawn only to guide the eyes. The J dependence in the distributions for the ground and 0.45-MeV levels is generally opposite to that observed for most of the other s-d shell nuclei studied.

A gas target containing H_2S was used to study the $^{32}S(p,d)^{31}S$ reaction. The gas cell consisted of a 5-in.-diam by 1-in.-high copper cylinder with 0.001-in. Kapton walls. The cell was filled to a pressure of 45 cm of Hg with natural H_2S (95.0% ^{32}S). A leakproof cell with Havar walls of 10 mg/cm^2 thickness was constructed for the purpose of making a permanent, isotopically enriched ($>99\%$) ^{36}Ar gas target. A compound pressure gauge was mounted on the cell, which was filled with ^{36}Ar to a pressure of 45.1 ± 1.0 cm of Hg at 25°C.

Natural calcium foils (97.0% ^{40}Ca) were used in the study of the $^{40}Ca(p,d)^{39}Ca$ reaction. These targets were made by evaporating calcium metal, and experimental data was obtained with foils of 1.10, 1.67, and 2.27 mg/cm^2 thickness.

III. EXPERIMENTAL RESULTS

A. $^{24}Mg(p,d)^{23}Mg$

A typical deuteron spectrum from the (p,d) reaction on the ^{24}Mg target (Fig. 1) shows that several levels of ^{23}Mg are strongly excited. The excitation of ^{15}O levels at 0.00 and 6.16 MeV indicates a slight oxidation of the target. An over-all deuteron energy resolution of 115–120 keV was obtained. This was insufficient to resolve the 2.71- and 2.77-MeV levels of ^{23}Mg; a similar situation exists for the 3.79- and 3.86-MeV levels. Consequently, the 2.71- and 3.79-MeV levels were analyzed by assuming that their peak shapes were the same as the well-resolved 0.45-MeV level.

Deuteron angular distributions for 10 of the excited levels were measured for laboratory angles from 10° to

[10] F. S. Goulding, D. A. Landis, J. Cerny, and R. J. Pehl, Nucl. Instr. Methods 31, 1 (1964).

[11] T. Lauritsen and F. Ajzenberg-Selove, *Energy Levels of Light Nuclei* (National Academy of Sciences–National Research Council, Washington, D. C., 1961).

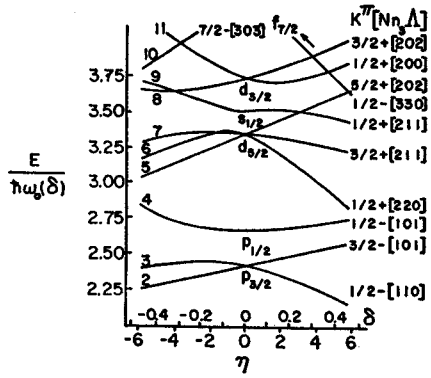

FIG. 3. Nilsson diagram of single-particle levels in a deformed well (Ref. 14). Each level can hold at most two protons and two neutrons; the first $K=\frac{1}{2}$ ($2s_{1/2}$) level is not shown. (From Ref. 15.)

155°. The distributions for levels of ^{23}Mg at 0.00, 0.45, and 5.32 MeV shown in Fig. 2 indicate a neutron pickup from the $1d$ shell ($l_n=2$) and are consistent with spin and parity assignments $J^\pi=\frac{3}{2}^+$, $\frac{5}{2}^+$, and $(\frac{3}{2},\frac{5}{2})^+$, respectively. The angular distribution for a level at 9.63 MeV is also shown, and corresponds to an l_n of either 1 or 2. The position of the forward maximum seems to favor slightly the $l_n=2$ assignment, although the statistical errors are quite large. The assignments for the 0.00- and 0.45-MeV levels correspond to well-known mirror levels in ^{23}Na, and have been confirmed recently by ^{24}Mg-(^{3}He,α)^{23}Mg experiments.[12,13] They are interpreted[13] as corresponding to members of a rotational band based on a $K=\frac{3}{2}$ hole in Nilsson orbit 7 [14] (See Fig. 3). This seems reasonable since the nuclear deformations in this mass region are assumed to be prolate ($\delta>0$).[15] The third member of this band should be the $\frac{7}{2}^+$ level at 2.06 MeV. The angular distribution for this level (Fig. 4) is relatively isotropic, indicating that a compound-nucleus reaction mechanism is involved rather than a direct

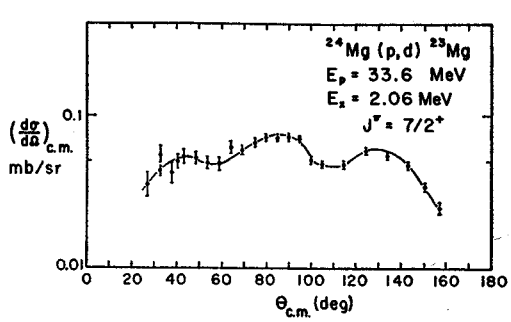

FIG. 4. Deuteron angular distribution for the 2.06-MeV level of ^{23}Mg from the ^{24}Mg(p,d)^{23}Mg reaction.

[12] J. M. Joyce, R. W. Zurmühle, and C. M. Fou, Bull. Am. Phys. Soc. 11, 908 (1966).
[13] J. Dubois and L. G. Earwaker, Bull. Am. Phys. Soc. 11, 908 (1966).
[14] S. G. Nilsson, Kgl. Danske Videnskab. Selskab, Mat. Fys. Medd. 29, No. 16 (1955).
[15] M. A. Preston, *Physics of the Nucleus* (Addison-Wesley Publishing Co., Inc., Reading, Mass., 1962).

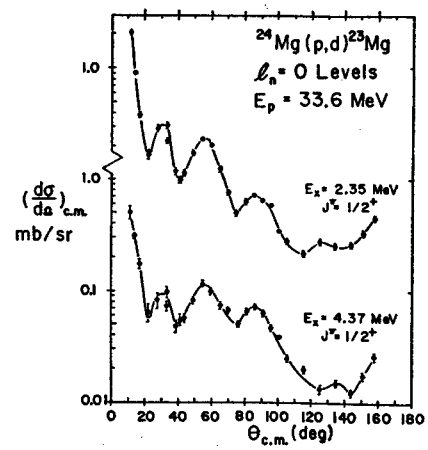

FIG. 5. Deuteron angular distributions corresponding to $l_n=0$ pickup in the ^{24}Mg(p,d)^{23}Mg reaction.

process, which would have indicated some admixture with the $g_{7/2}$ shell in the target state.

The levels at 2.35 and 4.37 MeV are excited by an $l_n=0$ pickup (Fig. 5) and therefore have $J^\pi=\frac{1}{2}^+$. Levels in ^{23}Na with the same J have been observed at similar excitation energies.[16] The 2.35-MeV level is assumed to be excited mainly by a pickup from Nilsson orbit 6.[13] On the basis of the Nilsson model (Fig. 3), there should be just one $\frac{1}{2}^+$ level excited in ^{23}Mg by a direct pickup. The excitation of both the 2.35- and 4.37-MeV levels is therefore evidence for configuration mixing between Nilsson orbits.

The angular distributions obtained for the 2.71-, 3.79-, and 6.02-MeV levels of ^{23}Mg have shapes corresponding to $l_n=1$ pickup, which indicates that these levels have negative parity with $J=\frac{1}{2}$ or $\frac{3}{2}$ (Fig. 6). The spin and parity of the 2.64-MeV level of ^{23}Na, which could be the mirror to the 2.71-MeV level of ^{23}Mg, has

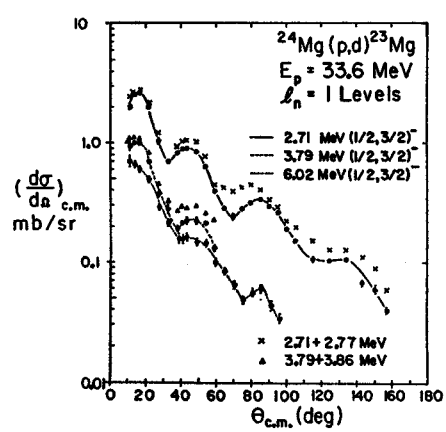

FIG. 6. Deuteron angular distributions corresponding to $l_n=1$ pickup in the ^{24}Mg(p,d)^{23}Mg reaction. The distributions for the composite peaks at 2.7 and 3.8 MeV are also shown.

[16] O. Hansen, E. Koltay, N. Lund, and B. S. Madsen, Nucl. Phys. 51, 307 (1964).

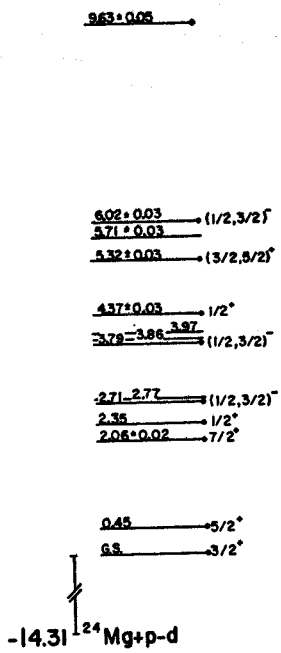

FIG. 7. ^{23}Mg levels observed in the ^{24}Mg(p,d)^{23}Mg reaction. The heavy dots indicate levels for which angular distributions were measured.

been previously reported as $\frac{1}{2}^+$.[17] DuBois and Earwaker,[18] who have recently studied the ^{24}Mg(^{3}He,α)^{23}Mg reaction, have confirmed the assignments given here for the 3.79- and 6.02-MeV levels. However, they conclude that the excitation of the 2.77-MeV level is due to an $l_n=1$ pickup, while the level at 2.71 MeV is possibly excited by an $l_n=3$ transfer. The energies measured for these two levels in the present work are estimated to be in error by about ± 20 keV, and it appears from the deuteron spectrum (Fig. 1) that the most strongly excited level in the doublet corresponds to the lowest excitation energy. It was this portion of the composite peak that was analyzed by the method discussed earlier to obtain the angular distribution shown in Fig. 6.

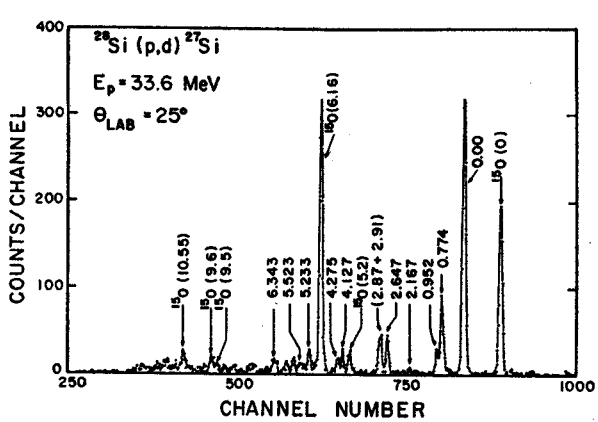

FIG. 8. Deuteron spectrum from the ^{28}Si(p,d)^{27}Si reaction at $\theta_{lab}=25°$. A SiO target was used, and levels of ^{15}O and ^{27}Si are indicated.

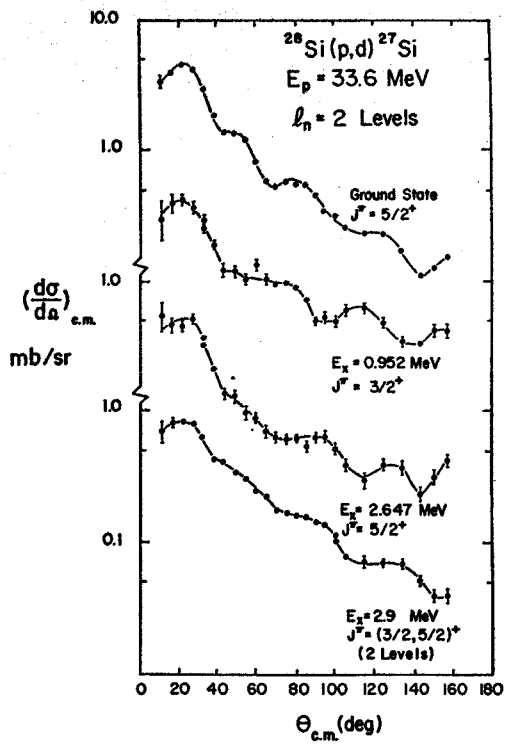

FIG. 9. Deuteron angular distributions corresponding to $l_n=2$ pickup in the ^{28}Si(p,d)^{27}Si reaction. Very little J dependence is observed in the distributions for the ground and 0.952-MeV levels.

A summary of the results obtained from the ^{24}Mg(p,d)^{23}Mg reaction is given in the level diagram of Fig. 7. In addition to the levels shown here, several others have been observed recently in ^{24}Mg(^{3}He,α)^{23}Mg experiments.[12,13,19] The energies for four of the levels are

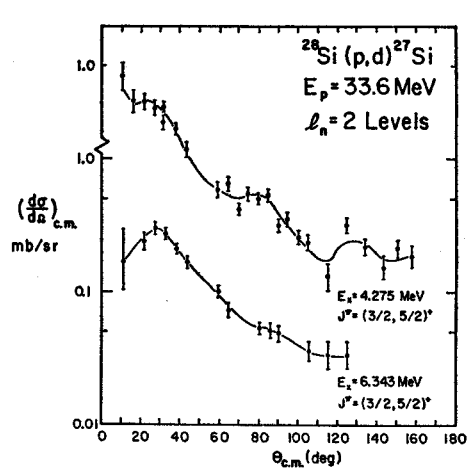

FIG. 10. Deuteron angular distributions corresponding to $l_n=2$ pickup in the ^{28}Si(p,d)^{27}Si reaction.

[17] D. W. Braben, L. L. Green, and J. C. Willmott, Nucl. Phys. 32, 584 (1962).

[18] J. Dubois and L. G. Earwaker, Phys. Rev. 160, 925 (1967).

[19] H. J. Hay and D. C. Keen, Nucl. Phys. A98, 330 (1967).

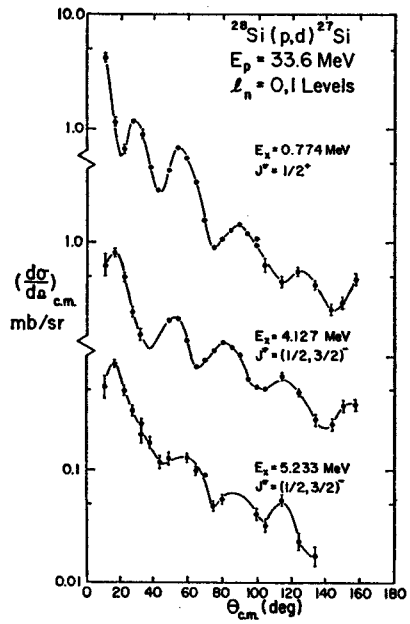

FIG. 11. Deuteron angular distributions corresponding to $l_n=0$ and 1 pickup in the ^{28}Si$(p,d)^{27}$Si reaction.

in agreement with those found by Ref. 19 at 4.362, 5.286, 5.7 (doublet), and 5.986 MeV.

J dependence for the ^{24}Mg$(p,d)^{23}$Mg reaction is observed in the angular distributions for the ground ($\frac{3}{2}^+$) and 0.45-MeV ($\frac{5}{2}^+$) levels of ^{23}Mg (Fig. 2). The $\frac{5}{2}^+$ distribution has a steeper over-all slope versus angle than the $\frac{3}{2}^+$ distribution, while the forward maximum for $J=\frac{5}{2}$ seems to occur at a slightly smaller angle than for $J=\frac{3}{2}$. Although the J dependence here seems relatively weak, the effects are generally opposite to those observed for most of the other nuclei investigated in this study.

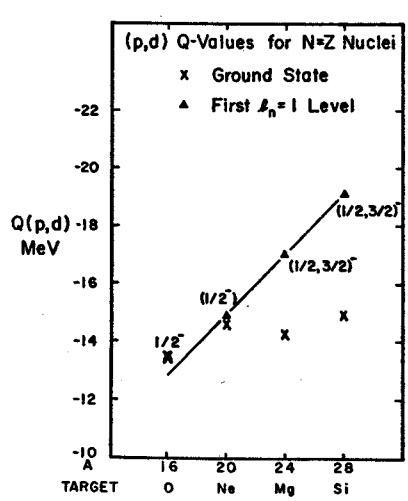

FIG. 12. Plot of (p,d) reaction Q values to the first $l_n=1$ level in $N=Z$ nuclei versus target mass number. A straight line is drawn for comparison.

B. ^{28}Si$(p,d)^{27}$Si

A typical deuteron spectrum from the (p,d) reaction on the SiO target is shown in Fig. 8. Several excited levels of ^{27}Si and ^{15}O were observed with an over-all energy resolution of 95–100 keV. The differential cross sections for the ^{27}Si levels were obtained at angles where, because of kinematic effects, they were unresolved from ^{15}O levels, by interpolating both the oxygen and silicon angular distributions.

1. Positive Parity Levels

Six deuteron groups from the ^{28}Si$(p,d)^{27}$Si reaction are observed to arise mainly from an $l_n=2$ neutron pickup (Figs. 9 and 10). Spin and parity assignments of $\frac{5}{2}^+$, $\frac{3}{2}^+$, and $\frac{5}{2}^+$ for excitation energies 0.00, 0.952, and 2.647 MeV, respectively, are obtained from corresponding levels of known spin and parity in the ^{27}Al mirror nucleus.[20] The 2.90-MeV peak is known to consist of two levels which are separated by about 40 keV, one of which has been assigned $J=\frac{3}{2}^+$.[20] Since the full width at half-maximum (FWHM) of this group in the spectrum (Fig. 8) is about 40 keV larger than that for the other levels, it appears that both levels may be strongly excited. Therefore, since the sum of their angular distributions retains the $l_n=2$ shape, the assignment $J^\pi=(\frac{3}{2},\frac{5}{2})^+$ may be reasonable for both levels, unless one of them is not excited by a direct process. A recent ^{28}Si$(d,^3$He$)^{27}$Al experiment, where the mirror of this doublet was resolved, has indicated that the angular distribution for one of the levels is relatively isotropic.[21]

The angular distribution for the 4.275-MeV level (Fig. 10) indicates some admixtures from other unresolved levels having $l_n\neq 2$, but the main contribution appears to be from the $1d$ shell, resulting in a $(\frac{3}{2},\frac{5}{2})^+$ assignment for this level and the level at 6.343-MeV

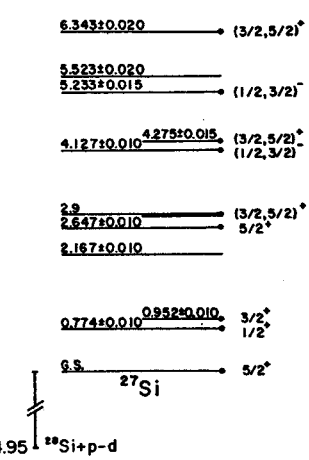

FIG. 13. ^{27}Si levels observed in the ^{28}Si$(p,d)^{27}$Si reaction.

[20] P. M. Endt and C. Van der Leun, Nucl. Phys. 34, 1 (1962).
[21] H. E. Gove *et al.*, Bull. Am. Phys. Soc. 12, 665 (1967); H. E. Gove (private communication).

excitation. This assignment has also been obtained for a level in ^{27}Al at 4.403 MeV from the ^{28}Si(d,^{3}He)^{27}Al reaction.[22]

The excitation of the 0.77-MeV level is evidence for a $2s_{1/2}$ admixture in the ^{28}Si ground state. The $l_n=0$ angular distribution for this level is shown in Fig. 11, and the $\frac{1}{2}^+$ assignment is consistent with that for the first excited state of ^{27}Al.[20]

The fact that the ^{27}Si ground state has $J^\pi=\frac{5}{2}^+$ would suggest a spherical or prolate shape ($\delta\geq 0$) on the basis of the Nilsson model (Fig. 3), but the existence of the $\frac{1}{2}^+$ level at low excitation energy (0.774 MeV) suggests a pickup from Nilsson orbit 6 with an oblate deformation ($\delta<0$). Also, the 0.952-MeV $\frac{3}{2}^+$ level could be excited by removing a neutron from orbit 7 with either a positive or a negative δ. It is thus difficult to interpret the ground state of ^{28}Si in terms of a simple Nilsson model.

Little J dependence is observed in the ^{28}Si(p,d)^{27}Si reaction. The angular distributions for the ground ($\frac{5}{2}^+$) and 0.952-MeV levels ($\frac{3}{2}^+$) (Fig. 9) are similar in shape, although there seems to be a flattening of the cross section for the $\frac{3}{2}^+$ level for $\theta_{c.m.}\gtrsim 60°$. The angle at which the forward maximum appears in the $\frac{3}{2}^+$ distribution is about the same, or slightly smaller, than for $J=\frac{5}{2}$.

2. *Negative Parity Levels*

The angular distributions for two $l_n=1$ levels of ^{27}Si at 4.127- and 5.233-MeV excitation are also shown in Fig. 11. The corresponding levels in the mirror nucleus have been observed by Wildenthal and Newman in the ^{28}Si(d,^{3}He)^{27}Al proton pickup reaction.[22] The predictions of Hartree-Fock calculations[23] and the conclusions of proton knockout experiments[24,25] indicate a separation energy difference between the $1p$ and $2s$-$1d$ shells of 10 to 20 MeV in this mass region. Because of their low excitation energy these levels might be thought of as being excited mainly by a pickup from the $2p$ shell. In Fig. 12 the (p,d) reaction Q values to the $l_n=1$ levels of lowest excitation are plotted for the $N=Z$, even-even nuclei for $A=16$–28 (Ref. 11 and this paper). Since the transition to the ^{15}O ground state is due to a pickup from the $1p_{1/2}$ shell, it seems reasonable, from the ob-

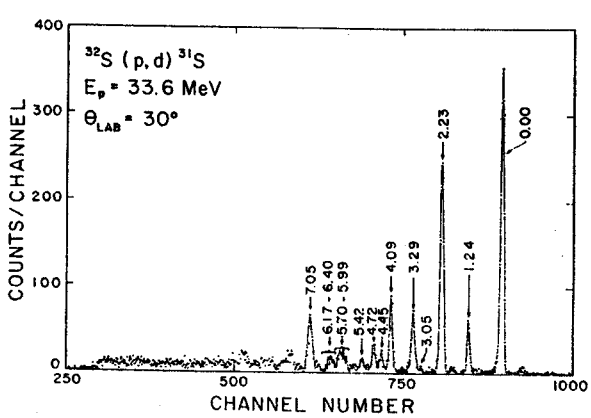

FIG. 14. Deuteron spectrum from the ^{32}S(p,d)^{31}S reaction at $\theta_{lab}=30°$, showing levels of ^{31}S. No strongly excited levels are observed at excitation energies greater than 7.05 MeV in ^{31}S.

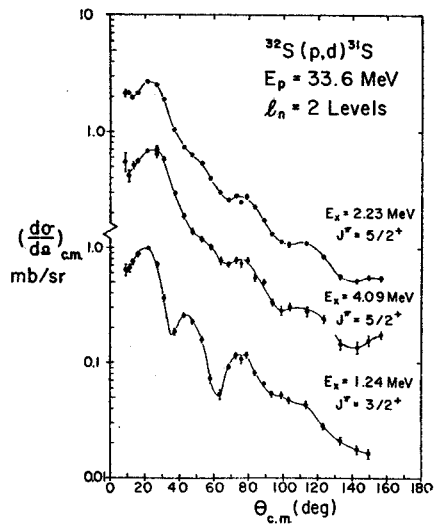

FIG. 15. Deuteron angular distributions corresponding to $l_n=2$ pickup in the ^{32}S(p,d)^{31}S reaction. The pronounced J dependence is similar to that observed by Ref. 5.

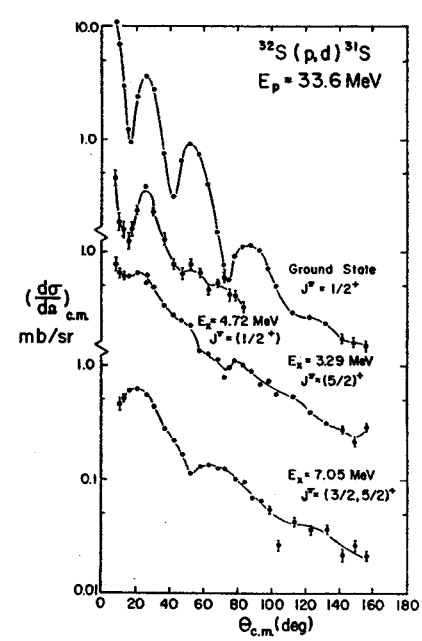

FIG. 16. Deuteron angular distributions corresponding to $l_n=0$ and 2 pickup in the ^{32}S(p,d)^{31}S reaction.

[22] B. H. Wildenthal and E. Newman, Phys. Rev. 167, 1027 (1968).

[23] K. T. R. Davies, S. J. Kreiger, and M. Baranger, Nucl. Phys. 84, 545 (1966).

[24] M. Riou, Rev. Mod. Phys. 37, 375 (1965).

[25] Gerhard Jacob and Th. A. J. Maris, Rev. Mod. Phys. 38, 121 (1966).

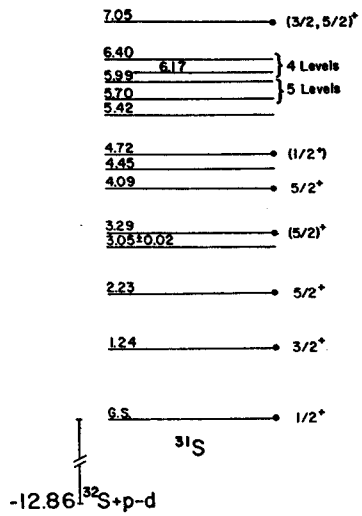

FIG. 17. ^{31}S levels observed in the ^{32}S$(p,d)^{31}$S reaction. The level energies for all but the 3.05-MeV level are in agreement with those measured by Ref. 26.

served trend in the neutron separation energy, that the $l_n=1$ levels in the other nuclei are also excited by a $1p$ pickup. The strengths of these excitations are of little help in resolving this ambiguity, since a DWBA calculation predicts a much lower spectroscopic factor for a $2p$ pickup than for a $1p$ pickup. Considering the plot in Fig. 12, however, one can conclude that the evidence for $1p$ hole-state assignments for these levels is at least as strong as for an origin due to a $2p$ admixture.

The excitation energies, spins and parities of the levels excited in the ^{28}Si$(p,d)^{27}$Si reaction are shown in Fig. 13. The energy measurements for the first six excited levels are in agreement with Ref. 20 to within the experimental error. Due to the constant presence of well-known ^{15}O levels in the spectrum, energy measurements with ± 10 keV error were possible in many cases.

C. ^{32}S$(p,d)^{31}$S

Figure 14 shows a deuteron spectrum from the (p,d) reaction on the H_2S gas target at a laboratory angle of 30°. The over-all resolution is about 120 keV. Many of the 39 levels observed in a ^{32}S$(^3$He$,\alpha)^{31}$S experiment[26] are confirmed, in addition to a very weak level at $E_x=3.05\pm0.02$ MeV which had been observed earlier.[27,28] No strongly excited ^{31}S levels are observed for $E_x>7.05$ MeV.

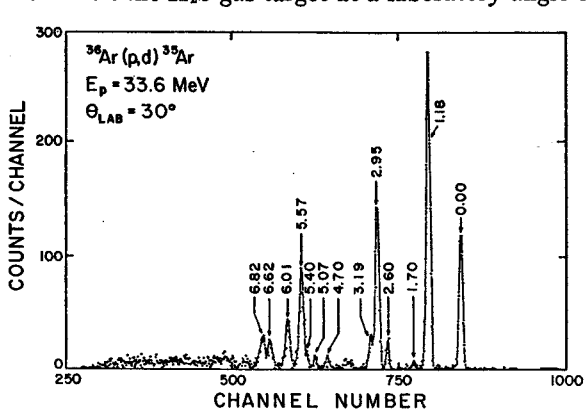

FIG. 18. Deuteron spectrum from the ^{36}Ar$(p,d)^{35}$Ar reaction at $\theta_{lab}=30°$, showing levels of ^{35}Ar. It is apparent that most of the $2s$-$1d$ shell hole strength is observed.

The deuteron angular distributions from levels of ^{31}S at 1.24-, 2.23-, and 4.09-MeV excitation energies are shown in Fig. 15. All of these distributions correspond to an $l_n=2$ neutron pickup, and the respective assignments $\frac{3}{2}^+$, $\frac{5}{2}^+$, and $\frac{5}{2}^+$ are consistent with those for corresponding levels in the mirror nucleus ^{31}P. Angular distributions were also measured for the 0.00-, 3.29-, 4.72-, and 7.05-MeV levels and are shown in Fig. 16. The ground state corresponds to an $l_n=0$ pickup and has the expected spin and parity of $\frac{1}{2}^+$. The distribution for the 4.72-MeV level probably also corresponds to an $l_n=0$ pickup. The 3.29-MeV level appears to be excited mainly by an $l_n=2$ pickup, although the angular distribution indicates the presence of other admixtures. Ajzenberg-Selove and Wiza[26] have reported a level at 3.359 ± 0.015 MeV, which would be unresolved here. A $(\frac{5}{2})^+$ assignment would be consistent with the assignment for a mirror level in ^{31}P at the same energy. The distribution for the 7.05-MeV level also corresponds to an $l_n=2$ pickup, indicating that $J^\pi=(\frac{3}{2},\frac{5}{2})^+$ for this level.

The first three levels of ^{31}S are the $0.00(\frac{1}{2}^+)$, $1.24(\frac{3}{2}^+)$, and 2.23 MeV $(\frac{5}{2}^+)$ levels, whose spins and parities are

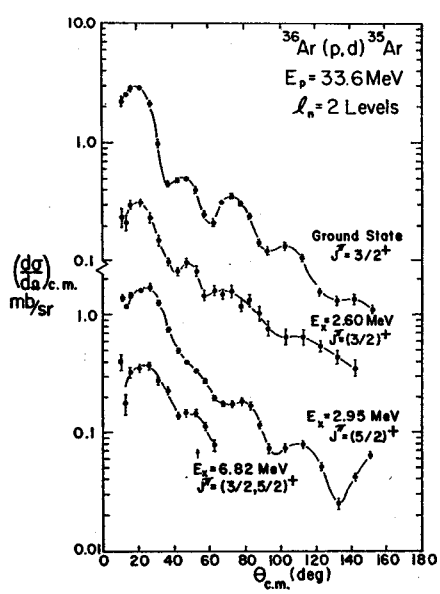

FIG. 19. Deuteron angular distributions corresponding to $l_n=2$ pickup in the ^{36}Ar$(p,d)^{35}$Ar reaction. The J dependence in the distributions for the ground and 2.95-MeV levels is similar to that observed in the ^{32}S$(p,d)^{31}$S reaction.

[26] F. Ajzenberg-Selove and J. L. Wiza, Phys. Rev. 143, 853 (1966).
[27] J. J. Wesolowski, J. D. Anderson, L. F. Hansen, C. Wong, and J. W. McClure, Nucl. Phys. 71, 586 (1965).
[28] J. W. Nelson, E. B. Carter, G. E. Mitchell, and R. H. Davis, Phys. Rev. 129, 1723 (1963).

consistent with a rotational band based on a neutron hole in Nilsson orbit 9 (Fig. 3), if the deformation is such that the decoupling parameter for $K=\frac{1}{2}$ does not affect the level order. However, the only sizable admixture with higher shells is with the $d_{3/2}$ shell, which results in the strong excitation of the 1.24-MeV level.

Figure 17 shows the ^{31}S levels excited in this reaction. The energy measurements are in agreement with the results of Ref. 26, with an experimental error of about ± 20 keV for each level.

The $J^\pi=\frac{3}{2}^+$ and $\frac{5}{2}^+$ angular distributions shown in Fig. 15 exhibit a striking example of J dependence in the $1d$ shell, similar to that observed in the (p,d) reaction with 28-MeV protons.[5] The forward maximum of the 1.24-MeV level ($\frac{3}{2}^+$) in ^{31}S occurs at a smaller angle than the distributions for either the 2.23- or 4.09-MeV levels (both $\frac{5}{2}^+$), and drops off much more rapidly to the first minimum. The oscillatory structure is much more pronounced for $J=\frac{3}{2}^+$; in fact, the second maximum ($\theta_{c.m.}\approx 45°$) is barely noticeable in the angular distributions for the $\frac{5}{2}^+$ levels. It is evident that for the 4.09-MeV level a spin and parity of $J^\pi=\frac{5}{2}^+$ could have been assigned on the basis of J dependence alone.

D. ^{36}Ar$(p,d)^{35}$Ar

Thirteen deuteron groups, corresponding to levels in ^{35}Ar, were observed in the ^{36}Ar$(p,d)^{35}$Ar reaction. A typical spectrum is shown in Fig. 18, where the over-all resolution is about 130 keV.

Angular distributions were measured for 10 levels of ^{35}Ar and are shown in Figs. 19–21. The $l_n=2$ distributions for levels at 0.00-, 2.60-, 2.95-, and 6.82-MeV excitation (Fig. 19) show that they are excited by neutron pickup from the $d_{3/2}$ and $d_{5/2}$ shells. The spin assignments for the 2.60($\frac{3}{2}^+$) and 2.95-MeV ($\frac{5}{2}^+$) levels are made on the basis of the observed J dependence discussed below. The ground-state assignment of $\frac{3}{2}^+$ corresponds to the spin and parity of the ^{35}Cl mirror nucleus.[20] The spin of the 6.82-MeV level is uncertain but must be either $\frac{3}{2}^+$ or $\frac{5}{2}^+$. The distributions for the 5.57- and 6.01-MeV levels also correspond to an $l_n=2$ pickup (Fig. 20) and are therefore assigned $J^\pi=(\frac{3}{2},\frac{5}{2})^+$.

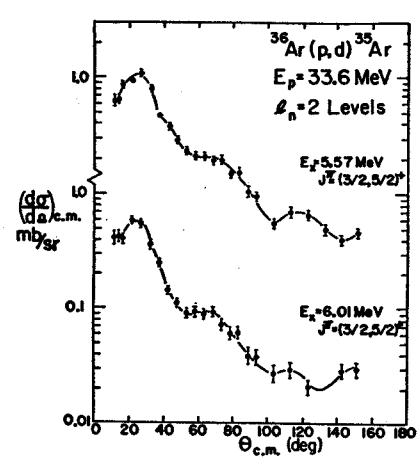

FIG. 20. Deuteron angular distributions corresponding to $l_n=2$ pickup in the ^{36}Ar$(p,d)^{35}$Ar reaction.

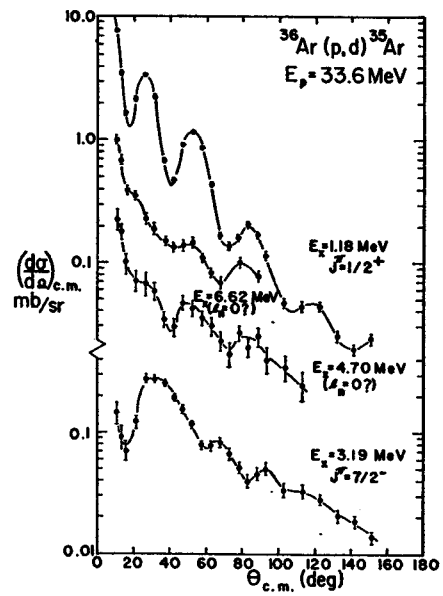

FIG. 21. Deuteron angular distributions from the ^{36}Ar$(p,d)^{35}$Ar reaction. The excitation of the $l_n=3$ level at 3.19 MeV is evidence for appreciable configuration mixing with the $f_{7/2}$ shell in the ^{36}Ar ground state.

The angular distributions for the 1.18-, 3.19-, 4.70-, and 6.62-MeV levels of ^{35}Ar are shown in Fig. 21. The first of these corresponds to an $l_n=0$ pickup and has $J=\frac{1}{2}^+$. The distribution for the 3.19-MeV level peaks at $\theta_{c.m.}\approx 30°$, which indicates that this level is excited by the pickup of an $l_n=3$ neutron and corresponds to configuration mixing with the $1f$ shell in the ^{36}Ar ground state. The level is assigned $J^\pi=\frac{7}{2}^-$ since it is most prob-

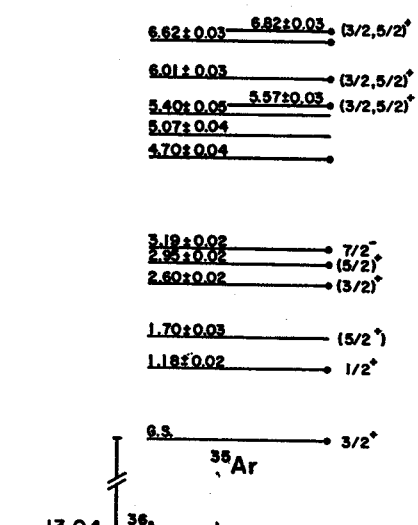

FIG. 22. ^{35}Ar levels observed in the ^{36}Ar$(p,d)^{35}$Ar reaction.

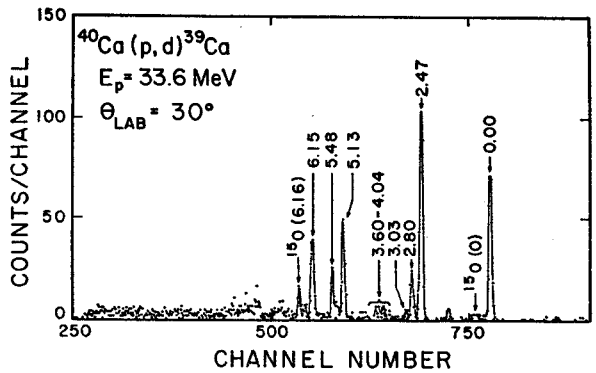

FIG. 23. Deuteron spectrum from the ^{40}Ca$(p,d)^{39}$Ca reaction at $\theta_{lab}=30°$, showing levels of ^{39}Ca. It is apparent that most of the $2s$-$1d$ shell hole strength is observed. A small oxygen contaminant is also indicated.

able from a shell-model standpoint, and the mirror level in ^{35}Cl is believed to have the same assignment.[20]

The assignments of the ^{35}Ar levels at 0.00, 1.18, 1.70, 2.60, and 2.95 MeV as $\frac{3}{2}^+$, $\frac{1}{2}^+$, $(\frac{5}{2}^+)$, $\frac{3}{2}^+$, and $(\frac{5}{2})^+$, respectively, gives a level order consistent with that of rotational bands based on Nilsson orbits 8 (first and third levels) and 9 (second, fourth, and fifth levels) if the deformation is oblate and no inversions occur in the $K=\frac{1}{2}[211]$ band. The assignment for the 1.70-MeV level as $(\frac{5}{2}^+)$ is assumed from the mirror level in ^{35}Cl.[20]

The diagram in Fig. 22 summarizes the information obtained about the level structure of ^{35}Ar from the (p,d) reaction. The energies of the low-lying levels correspond closely to levels in the ^{35}Cl mirror nucleus.[20]

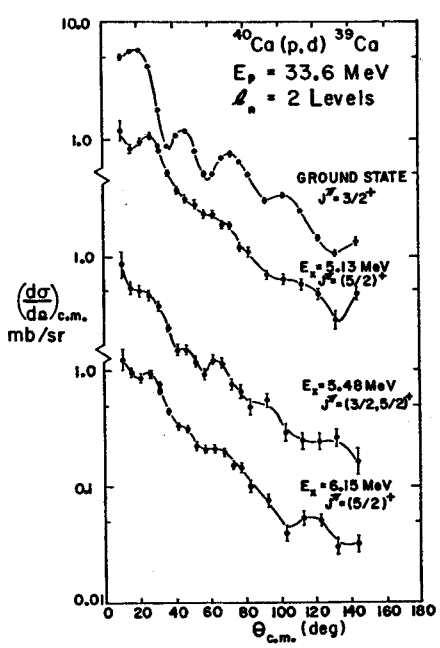

FIG. 24. Deuteron angular distributions corresponding to $l_n=2$ pickup in the ^{40}Ca$(p,d)^{39}$Ca reaction. The J dependence in the distributions for the ground and 5.13-MeV levels is similar to that observed in the (p,d) reaction on ^{36}Ar and ^{32}S.

The J dependence observed in the ^{36}Ar$(p,d)^{35}$Ar reaction for $\frac{3}{2}^+$ and $\frac{5}{2}^+$ levels (Fig. 19) is very similar to that for the ^{32}S$(p,d)^{31}$S reaction. The angular distributions for the 2.23- and 4.09-MeV levels of ^{31}S (Fig. 15) and the 2.95-MeV level of ^{35}Ar are practically identical in shape for $\theta_{c.m.}\lesssim 90°$. Since both of the ^{31}S levels have $J=\frac{5}{2}^+$, the 2.95-MeV level of ^{35}Ar is assigned $J^\pi=(\frac{5}{2})^+$. The distributions for the ground and 2.60-MeV levels in ^{35}Ar are similar to the distribution for the ^{31}S 1.24-MeV level $(\frac{3}{2}^+)$, although the oscillatory structure is not quite so pronounced. The existence of the 45° maximum and the relatively small angle for the forward maximum in the distribution for the 2.60-MeV level favors the assignment of $J^\pi=(\frac{3}{2})^+$.

E. ^{40}Ca$(p,d)^{39}$Ca

The deuteron spectrum shown in Fig. 23 is similar to those obtained from the ^{40}Ca$(p,d)^{39}$Ca reaction by Glashausser *et al.*[29] with 27.3-MeV protons. A natural calcium foil of 1.10 mg/cm^2 was used and a resolution of 100 keV was obtained; the normalization was checked with 1.67- and 2.27-mg/cm^2 foils. A small oxygen contaminant on the target is indicated by the presence of the ^{15}O ground and 6.16-MeV levels in the spectrum. About 12 MeV of excitation in ^{39}Ca is observed, and no appreciable strength appears beyond the 6.15-MeV level.

The angular distributions for the 0.00-, 5.13-, 5.48-, and 6.15-MeV levels shown in Fig. 24 all correspond to

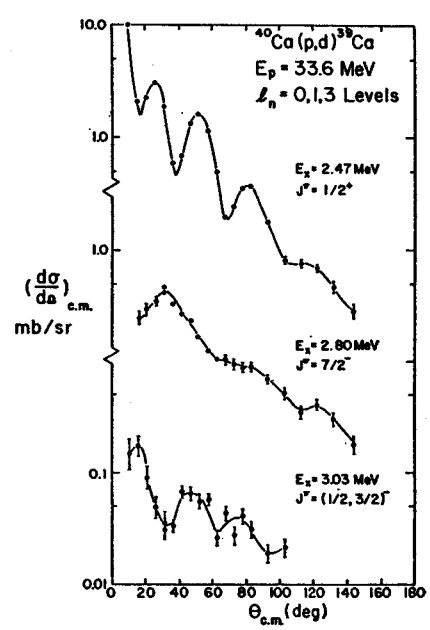

FIG. 25. Deuteron angular distributions from the ^{40}Ca$(p,d)^{39}$Ca reaction. The excitation of the 2.80- $(l_n=3)$ and 3.03-MeV $(l_n=1)$ levels corresponds to configuration mixing in the ^{40}Ca ground state with the $1f_{7/2}$ and $2p_{1/2}$ shells, respectively.

[29] C. Glashausser, M. Kondo, M. E. Rickey, and E. Rost, Phys. Letters 14, 113 (1965).

an $l_n=2$ pickup. The ground state has $J^\pi=\frac{3}{2}^+$, which corresponds to the spin and parity of the mirror nucleus ^{39}K. The peak differential cross section obtained at 33.6-MeV bombarding energy was 5.6±0.4 mb/sr. Glashausser *et al.*[29] obtained a value of ~3 mb/sr at 27.3-MeV bombarding energy, while Cavanagh *et al.*[30] measured ~4.5 mb/sr for the peak cross section with 30-MeV protons. This indicates that differential cross section is quite sensitive to the bombarding energy.

The 5.13-MeV level is assigned $J^\pi=(\frac{5}{2})^+$ on the basis of the J dependence observed in the angular distributions (see below). Although the angular distribution for the 5.48-MeV level has the basic $l_n=2$ shape, it also appears to contain contributions from unresolved levels corresponding to different l_n values. The angular distribution for the 6.15-MeV level is very similar to that for the 5.13-MeV level and is given the tentative assignment $J^\pi=(\frac{5}{2})^+$.

Figure 25 shows the angular distributions from ^{39}Ca levels at 2.47, 2.80, and 3.03 MeV. The 2.47-MeV level corresponds to $l_n=0$ and thus has $J^\pi=\frac{1}{2}^+$. The shape of the distribution for the 2.80-MeV level is very similar to that for the transition to the 3.19-MeV level in ^{35}Ar, which corresponds to an $l_n=3$ pickup. Therefore, configuration mixing with the $f_{7/2}$ shell is apparent in the ^{40}Ca ground state, in qualitative agreement with the results of Ref. 29.

The 3.03-MeV level has been variously quoted as corresponding to an $l_n=1$ and 2 neutron pickup in ^{40}Ca(^{3}He,α)^{39}Ca reactions,[31,32] while the mirror level appears to be excited by an $l_p=1$ proton pickup in the ^{40}Ca(d,^{3}He)^{39}K reaction.[33] The present result favors an $l_n=1$ pickup with $J^\pi=(\frac{1}{2},\frac{3}{2})^-$, in agreement with Refs.

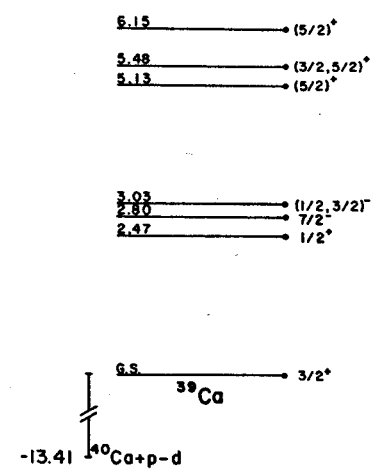

FIG. 26. ^{39}Ca levels observed in the ^{40}Ca(p,d)^{39}Ca reaction.

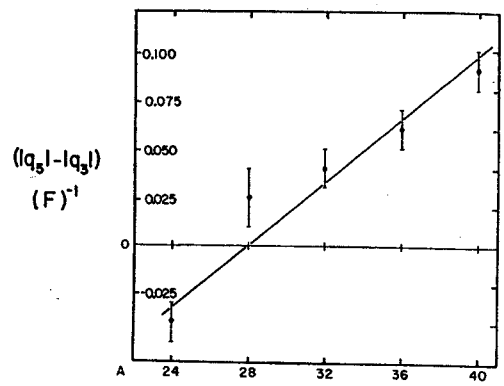

FIG. 27. Summary of experimental results for forward-angle J dependence. $|q_5|$ ($|q_3|$) is the momentum transferred to the residual nucleus for the forward maximum of the strongly excited $\frac{5}{2}^+$ ($\frac{3}{2}^+$) distribution of lowest energy. $|q_5|-|q_3|$ is plotted versus mass number and a straight line is drawn for comparison. Estimates of the errors in determining the positions of the forward maxima are also shown.

31 and 33. Even though the statistics are poor, the angular distribution seems to be peaked at $\theta_{c.m.}\approx 15°$, while the forward maxima of the $l_n=2$ distributions are peaked at 20° to 25° at this bombarding energy. These results indicate that there is some configuration mixing with the $2p$ shell as well as the $f_{7/2}$ shell in the ^{40}Ca ground state. The strengths of these admixtures are given in Sec. IV of this paper.

A summary of the excitation energies, spins, and parities of the ^{39}Ca levels observed in the ^{40}Ca(p,d)^{39}Ca reaction is shown in Fig. 26. The energy measurements are in agreement with those of Refs. 29 and 20, with an experimental error of about ±20 keV. The J dependence in the angular distributions for the 0.00($\frac{3}{2}^+$), 5.13($\frac{5}{2}^+$), and 6.15-MeV ($\frac{5}{2}^+$) levels in ^{39}Ca (Fig. 24) is very

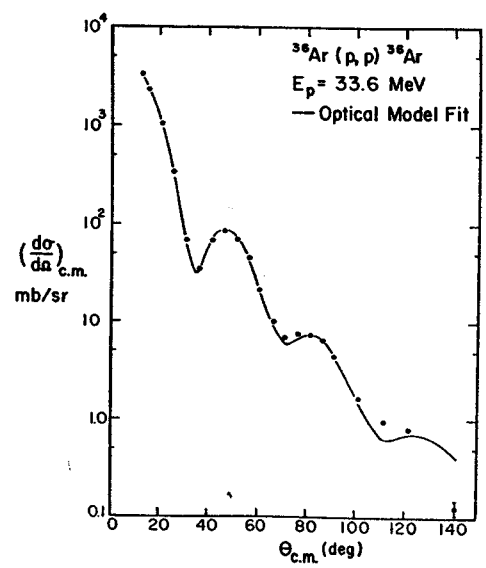

FIG. 28. Optical-model fit to the ^{36}Ar(p,p)^{36}Ar elastic scattering data. The parameters are listed in Table I.

[30] P. E. Cavanagh, C. F. Coleman, G. A. Gard, B. W. Ridley, and J. F. Turner, Nucl. Phys. 50, 49 (1964).
[31] D. Cline, W. Parker Alford, and L. M. Blau, Nucl. Phys. 73, 33 (1965).
[32] R. Bock, H. H. Duhm, and R. Stock, Phys. Letters 18, 61 (1965).
[33] J. C. Hiebert, E. Newman, and R. H. Bassel, Phys. Rev. 154, 898 (1967).

TABLE I. Optical-model parameters for DWBA analysis.

	V_0(MeV)	W(MeV)	r_0(F)	r_I(F)	r_c(F)	a_0(F)	a_I(F)	Target A	Source
Protons	49.8	6.50	1.16	1.16	1.16	0.64	0.64	24, 28	^{26}Mg(p,p)
	47.1	6.87	1.18	1.18	1.18	0.66	0.66	32, 36, 40	^{38}Ar(p,p)
Deuterons	90.0	25.0[a]	1.25	1.30	1.30	0.62	0.58	24–40	b

[a] For the ^{24}Mg(p,d)^{23}Mg reaction, an imaginary deuteron well depth of 35 MeV was used.
[b] Reference 38.

similar to that observed in the ^{36}Ar(p,d)^{35}Ar and ^{32}S(p,d)^{31}S reactions.

F. Summary of J-Dependence Results

The J dependence observed in the forward angles of the $l_n=2$ angular distributions seems to follow a systematic trend through the $2s$-$1d$ shell. The forward maxima of the $\frac{3}{2}^+$ angular distributions occur at smaller angles than the forward maxima of the $\frac{5}{2}^+$ distributions for (p,d) reactions on ^{40}Ca, ^{36}Ar, and ^{32}S. The opposite effect is observed in the ^{24}Mg(p,d)^{23}Mg reaction, while almost no effect is seen in the ^{28}Si(p,d)^{27}Si reaction. Since there is evidence that the quadrupole deformation changes sign in the mass region $A=28$–30,[34] it appears there may be some correlation between J dependence and the nature of the nuclear deformation. The effects for $A>28$ are similar to those observed in the (p,d) reaction in the $1f$ shell.[4–6] The J dependence at large angles appears to follow no definite pattern. For $\theta_{c.m.}\lesssim 90°$, all of the $\frac{5}{2}^+$ distributions are very similar in shape, while the $\frac{3}{2}^+$ distributions sometimes undergo very distinct changes from nucleus to nucleus. The usefulness of J dependence as a spectroscopic tool has been demonstrated by the assignment of spins to levels in ^{31}S, ^{35}Ar, and ^{39}Ca.

The experimental results for J dependence have been summarized by plotting the difference in positions of the forward maxima of $\frac{3}{2}$ and $\frac{5}{2}$ distributions versus mass number (Fig. 27). The vertical axis is in terms of the momentum transferred to the residual nucleus, which reduces the phase differences that may arise from the two levels of a given pair having different reaction Q values. The $\frac{3}{2}^+$ and $\frac{5}{2}^+$ distributions represented correspond to the strongly excited level of each respective spin having the lowest excitation energy. A DWBA analysis of J dependence and the extraction of spectroscopic factors to provide quantitative information on configuration mixing is presented in the next section.

IV. ANALYSIS WITH THE DWBA AND COMPARISON TO THEORY

The experimental (p,d) angular distributions discussed in Sec. III were analyzed in the DWBA with respect to J dependence and the calculation of spectroscopic factors. The calculations were performed with the Macefield computer code in the zero-range approximation.

A. Optical-Model Parameters

The optical-model parameters used to generate the incident-channel wave functions for the DWBA calcu-

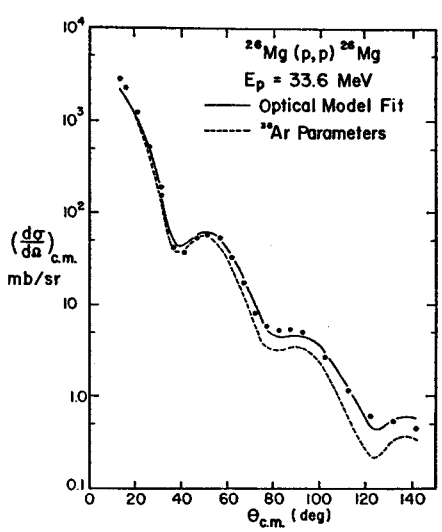

FIG. 29. Optical-model fits to the ^{26}Mg(p,p)^{26}Mg elastic scattering data with ^{36}Ar and ^{26}Mg parameters. The parameters are listed in Table I.

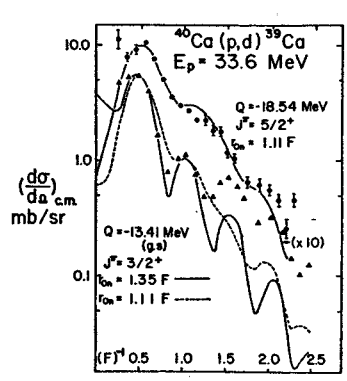

FIG. 30. DWBA fits to the $l_n=2$ J-dependence for the 5.13-($\frac{5}{2}^+$) and 0.00-MeV ($\frac{3}{2}^+$) levels of ^{39}Ca excited in the ^{40}Ca(p,d)^{39}Ca reaction. The fit to the $\frac{3}{2}^+$ distribution with the parameters for the $\frac{5}{2}^+$ calculation is shown by the dashed curve. The forward maxima occur at $\theta_{c.m.}=20°$–25°, while a momentum transfer of 1.5 F^{-1} corresponds to a center-of-mass angle of approximately 70°.

[34] G. M. Crawley and G. T. Garvey, Phys. Rev. **160**, 981 (1967), and references therein.

lations were obtained from ^{26}Mg$(p,p)^{26}$Mg and ^{36}Ar$(p,p)^{36}$Ar elastic scattering experiments at 33.6-MeV bombarding energy. A best fit to the angular distributions was obtained by varying the parameters in an optical potential of Woods-Saxon form with surface absorption. The optical-model search program ABACUS[35] was used to obtain the fits to the data shown in Figs. 28 and 29. No spin-orbit interaction was included, since the DWBA code was not equipped to perform a spin-orbit calculation. The fit to the ^{26}Mg data with the ^{36}Ar parameters and the fit obtained in the search on ^{26}Mg are shown in Fig. 29. As can be seen from Table I, the parameters are very similar for the two nuclei. It was therefore assumed that the basic optical parameters are reasonably constant with mass number in the 2s-1d shell, and the ^{26}Mg parameters were used in the DWBA calculations for the (p,d) reaction on ^{24}Mg and ^{28}Si while the ^{36}Ar parameters were used for ^{32}S, ^{36}Ar, and ^{40}Ca.

Deuteron optical parameters have been obtained by Perey and Perey[36,37] for Ca and Mg nuclei at various bombarding energies, and by Cowley *et al.*[38] for ^{27}Al and ^{32}S targets at 15.8-MeV bombarding energy. An attempt to fit a (p,d) angular distribution was made with each set of parameters, but only those obtained in Ref. 38 for ^{32}S resulted in reasonable DWBA fits to the data. These parameters are also listed in Table I and were used for all the targets in this work. An imaginary surface well depth (W) of 25 MeV resulted in slightly better fits than the depth of 20 MeV obtained from the elastic scattering. It was necessary to further increase this depth to 35 MeV in order to obtain reasonable fits to the data from the ^{24}Mg$(p,d)^{23}$Mg reaction.

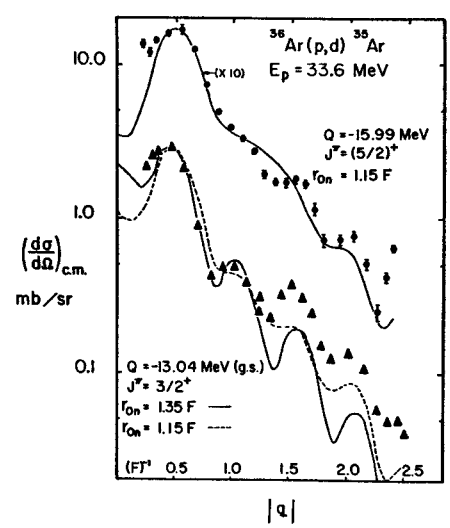

FIG. 31. DWBA fits to the $l_n=2$ J-dependence for the 2.95-($\frac{5}{2}^+$) and 0.00-MeV ($\frac{3}{2}^+$) levels of ^{35}Ar excited in the ^{36}Ar$(p,d)^{35}$Ar reaction.

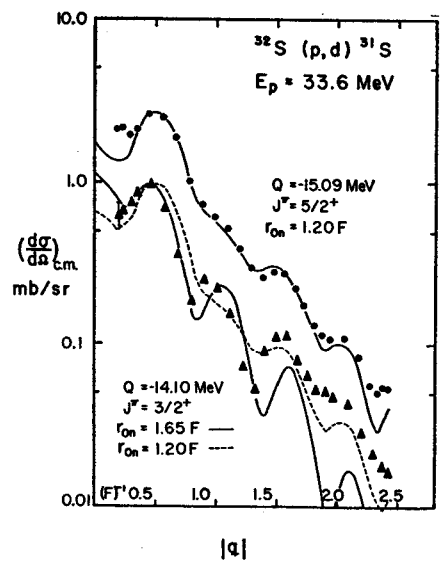

FIG. 32. DWBA fits to the $l_n=2$ J-dependence for the 2.23-($\frac{5}{2}^+$) and 1.24-MeV ($\frac{3}{2}^+$) levels of ^{31}S excited in the ^{32}S$(p,d)^{31}$S reaction.

B. DWBA Analysis of J Dependence

There have been two main approaches to the DWBA analysis of J dependence in the (p,d) reaction with regard to the bound-state form factor of the picked-up neutron. One is to assume different binding energies for neutrons that have different spins, even though their actual separation energies may be nearly the same. Both Sherr *et al.*[4] and Glashausser[5] have obtained satisfactory DWBA fits to the $l_n=3$ J-dependence using

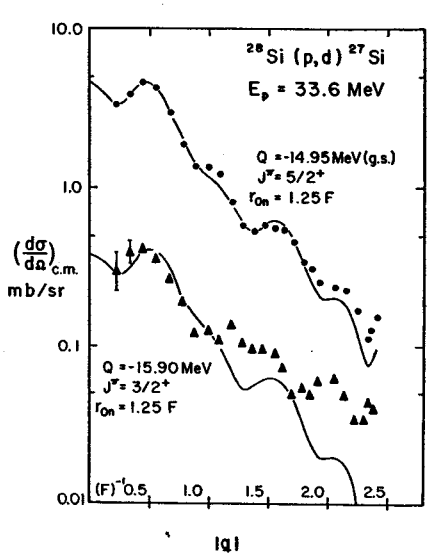

FIG. 33. DWBA fits to the 0.00- ($\frac{5}{2}^+$) and 0.95-MeV ($\frac{3}{2}^+$) levels of ^{27}Si excited in the ^{28}Si$(p,d)^{27}$Si reaction. Since little J dependence is observed in the forward angles, the same parameters are used in both calculations.

[35] E. H. Auerbach, Brookhaven National Laboratory Report No. 6562, 1962 (unpublished).
[36] C. M. Perey and F. G. Perey, Phys. Rev. 132, 755 (1963).
[37] C. M. Perey and F. G. Perey, Oak Ridge National Laboratory Report No. ORNL-TM-1529, 1966 (unpublished).
[38] A. A. Cowley, G. Heymann, and R. L. Keizer, Nucl. Phys. 86, 363 (1966).

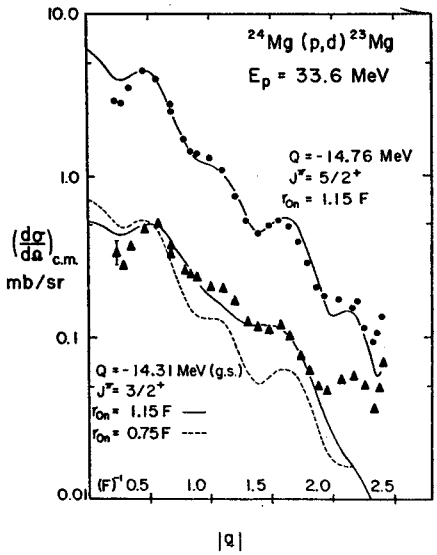

FIG. 34. DWBA fits to the $l_n=2$ J-dependence for the 0.45-($\frac{5}{2}^+$) and 0.00-MeV ($\frac{3}{2}^+$) levels of ^{23}Mg excited in the ^{24}Mg(p,d)-^{23}Mg reaction.

this method. However, this approach gives an incorrect asymptotic form for the neutron wave function. It has therefore been suggested[39] that other changes in the neutron well (e.g., radius or diffuseness) be employed, while maintaining the correct separation energy. An attempt to fit the $l_n=3$ J-dependence in the ^{56}Fe(p,d)-^{55}Fe reaction by changing the neutron well radius has been made by Glashausser[5] and was partially successful at his highest bombarding energy (27.5 MeV). The same method has been used to fit the $l_n=2$ J-dependence at the forward angles in the present work.

The Woods-Saxon potential

$$V(r)=-V_0\{1+\exp[(r-r_{0n}A^{1/3})/a_n]\}$$

was used for the bound neutron, where the depth V_0 is determined by the neutron binding energy. The radius corresponding to the pickup of a $d_{5/2}$ neutron was kept constant at 3.79 F$=1.25(28)^{1/3}$ F for all targets having $A\geq 28$. This effectively assumes a ^{28}Si core that does not change in physical size. The radius parameter r_{0n} was then varied in an attempt to obtain a fit to the positions and shape of the forward maximum in a $J^\pi=\frac{3}{2}^+$ angular distribution for each nucleus. The diffuseness a_n was kept constant at 0.65 F for all cases shown here, except for the fit to the $\frac{3}{2}^+$ distribution in ^{31}S (see below).

A pair of levels from each nucleus, one having $J^\pi=\frac{3}{2}^+$ and one $\frac{5}{2}^+$, was selected for this analysis. The strongly excited level corresponding to the lowest excitation energy was chosen for each spin, and the differential cross sections of these levels are plotted in Figs. 30–34 versus $|\mathbf{q}|$, the momentum transferred to the residual nucleus. The $\frac{5}{2}^+$ distributions always appear at the top of the figure, and are renormalized as indicated. A momentum transfer of 1.5 F^{-1} corresponds to a center-of-mass angle of approximately 70°.

[39] W. T. Pinkston and G. R. Satchler, Nucl. Phys. 72, 641 (1965).

TABLE II. Summary of neutron parameters for DWBA analysis of J dependence.

Target	a_{0n}(F)	$R_{3/2}$(F)	$R_{5/2}$(F)	$R_{3/2}/R_{5/2}$	$\sigma(R_{3/2})/\sigma(R_{5/2})$[a]
^{24}Mg	0.65	2.16	3.32	0.65	0.5
^{28}Si	0.65	3.79	3.79	1.00	1.0
^{32}S	0.65	5.55	3.79	1.46	5.0
	0.75	5.23	(3.79)	(1.37)	
^{36}Ar	0.65	4.46	3.79	1.17	1.7
^{40}Ca	0.65	4.62	3.79	1.22	1.9

[a] Ratio of DWBA cross sections at forward maxima.

1. $^{40}Ca(p,d)^{39}Ca$

Figure 30 shows DWBA fits to the distributions for the ground ($\frac{3}{2}^+$) and 5.13-MeV ($\frac{5}{2}^+$) levels of ^{39}Ca. The neutron well radius parameter of 1.11 F for the $J^\pi=\frac{5}{2}^+$ calculations arises from the assumption of a constant $d_{5/2}$ radius ($R_{5/2}=3.79$ F), and seems to give a reasonable fit to the data. As is shown by the dashed curve, this same radius does not result in a good fit to the forward maximum of the ground-state ($\frac{3}{2}^+$) distribution. A larger radius ($r_{0n}=1.35$ F) predicts the oscillatory structure of the $J^\pi=\frac{3}{2}^+$ distribution more accurately for $|\mathbf{q}|\lesssim 1.2$ F^{-1}, but it predicts too small a cross section for higher momentum transfers.

2. $^{36}Ar(p,d)^{35}Ar$

The J dependence observed in the distributions for the ground ($\frac{3}{2}^+$) and 2.95-MeV ($\frac{5}{2}^+$) levels of ^{35}Ar (Fig. 31) is very similar to that from the ^{40}Ca$(p,d)^{39}$Ca reaction, and similar neutron parameters were used in the DWBA calculation with about the same degree of success. The assumed $d_{5/2}$ radius of 3.79 F corresponds to an r_{0n} of 1.15 F, while the r_{0n} for $J^\pi=\frac{3}{2}^+$ (1.35 F) is the same as that used to fit the ^{39}Ca ground-state distribution.

3. $^{32}S(p,d)^{31}S$

As was described earlier (Sec. III), the J dependence for the 2.23-MeV ($\frac{5}{2}^+$) and 1.24-MeV ($\frac{3}{2}^+$) levels of ^{31}S is very pronounced. The DWBA fits to the data for these levels are shown in Fig. 32, where it is seen that the fit to the $J^\pi=\frac{5}{2}^+$ distribution is quite good. The $\frac{3}{2}^+$ distribution drops much more rapidly from the forward maximum than the $\frac{5}{2}^+$ data, and this is not reproduced by using the assumed $d_{5/2}$ neutron well radius ($r_{0n}=1.20$ F) in the DWBA calculation. The radius parameter was increased to 1.65 F and the diffuseness to 0.75 F in order to fit the data for $|\mathbf{q}|\gtrsim 0.8$ F^{-1}; however, this resulted in a wrong prediction for the position of the second maximum at $|\mathbf{q}|\sim 0.9$ F^{-1}. A calculation where $r_{0n}=1.75$ F and $a_n=0.65$ F (not shown) fits the forward angles equally well but results in an even worse prediction for the second maximum.

TABLE III. Spectroscopic factors for the $^{24}Mg(p,d)^{23}Mg$ reaction.

E_x(MeV)	σ_{max}(mb/sr)	J^π	$S_{expt}(r_{0n}=1.15$ F)	Theory[a] J^π	Theory[a] S_T
0.00	0.52	$\frac{3}{2}^+$	0.72		
0.45	4.5	$\frac{5}{2}^+$	5.66	$\frac{5}{2}^+$	3.22
2.35	0.31(30°)	$\frac{1}{2}^+$	0.20	$\frac{1}{2}^+$	0.37
2.71	2.65	$(\frac{1}{2},\frac{3}{2})^-$	3.40[b]		
			0.80[c]		
3.79	1.0	$(\frac{1}{2},\frac{3}{2})^-$	1.69[b]		
			0.38[c]		
4.37	0.09(30°)	$\frac{1}{2}^+$	0.10	$\frac{1}{2}^+$	0.007
5.32	0.31	$(\frac{3}{2},\frac{5}{2})^+$	0.54		
6.02	0.62	$(\frac{1}{2},\frac{3}{2})^-$	2.04[b]		
			0.44[c]		
9.63	0.17	$(\frac{3}{2}^+,\frac{5}{2}^+)$	1.05		

[a] Predictions of Ref. 42.
[b] Assuming pickup from $1p$ shell.
[c] Assuming pickup from $2p$ shell.

4. $^{28}Si(p,d)^{27}Si$

The distributions for the ground ($\frac{5}{2}^+$) and 0.95-MeV ($\frac{3}{2}^+$) levels of ^{27}Si are shown in Fig. 33, where little J dependence is observed. The position of the forward maximum of the $\frac{3}{2}^+$ distribution appears to occur at a slightly smaller $|\mathbf{q}|$ than the $\frac{5}{2}^+$ maximum. However, the slope following the maximum is, if anything, *less* steep for $J=\frac{3}{2}$ than for $J=\frac{5}{2}$. These two effects compete when the neutron radius or diffuseness is varied in the distorted-wave calculation, so no variations were made in this case. The DWBA prediction is shown normalized to the data for both levels and is in good agreement with the shape of the ground-state ($\frac{5}{2}^+$) distribution.

5. $^{24}Mg(p,d)^{23}Mg$

The experimentally observed J-dependence effects in the distributions for the ground ($\frac{3}{2}^+$) and 0.45-MeV ($\frac{5}{2}^+$) levels of ^{23}Mg are generally opposite to those observed in the (p,d) reaction on the other nuclei studied. The DWBA calculations for these distributions were made with an imaginary deuteron well depth of 35 MeV and are shown in Fig. 34. A depth of 25 MeV, which was used for all of the other nuclei, resulted in a curve having much less structure and no relative minimum for small $|\mathbf{q}|$. Also, the $d_{5/2}$ radius used here is $1.15(24)^{1/3}$ F $=3.32$ F instead of the 3.79 F used for all the other nuclei. It is seen that the value for r_{0n} of 1.15 F is too large to yield an acceptable DWBA fit to the $\frac{3}{2}^+$ distribution. This was decreased to 0.75 F to obtain a reasonable approximation to the forward maximum and overall slope of the data.

6. *Summary of J-Dependence Analysis*

The use of different radii in the neutron form factor for $d_{3/2}$ and $d_{5/2}$ pickups was at least partially successful in predicting the $l_n=2$ J-dependence at the forward angles. It must be emphasized, however, that this analysis serves only to illustrate the extent to which the radius must be changed. The results are summarized in Table II, where $R_{3/2}$ and $R_{5/2}$ correspond to $r_{0n}A^{1/3}$ for $d_{3/2}$ and $d_{5/2}$ pickups, respectively. The radial change is quite large for most of the targets studied and, as can be seen from the ratio $\sigma(R_{3/2})/\sigma(R_{5/2})$ in Table II, a large change in radius results in a large change in the magnitude of the calculated DWBA cross section. This gives rise to problems in extracting absolute spectroscopic factors, as will be seen in Sec. IV C. It is interesting to note, however, that the ratio of the $d_{3/2}$ radius to the $d_{5/2}$ radius ($R_{3/2}/R_{5/2}$) is, in general, closer to unity than the ratio of the semiaxes of the nuclear ellipsoid if one assumes reasonable values for the deformation parameter.[40,41] The only exception to this is the case of ^{40}Ca.

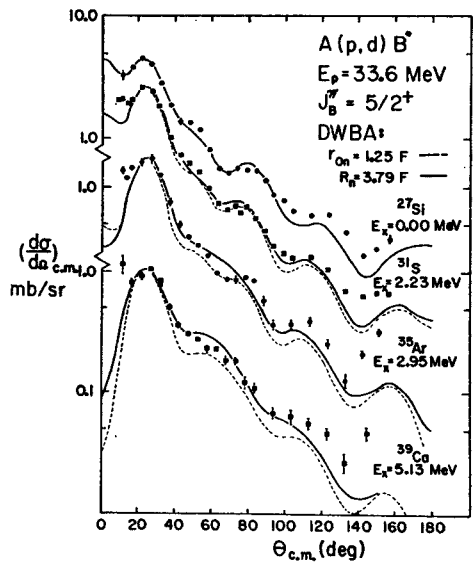

FIG. 35. DWBA fits to the $\frac{5}{2}^+$ angular distributions for levels excited in the (p,d) reaction on ^{28}Si, ^{32}S, ^{36}Ar, and ^{40}Ca. The DWBA predictions for a constant total neutron-well radius (3.79 F) and a constant well-radius parameter (1.25 F) are represented by solid and dashed curves, respectively.

The effect of using a constant radius for a $d_{5/2}$ neutron is summarized in Fig. 35, which shows a comparison of the DWBA fits to the $\frac{5}{2}^+$ angular distributions for $R_{5/2}=3.79$ F and 1.25 $A^{1/3}$ F. The fits to the distributions for all the levels are reasonable at forward angles with the smaller radius (3.79 F), while the predictions for a radius of 1.25 $A^{1/3}$ F are in less agreement with the data as A increases. The effect is not large, however, and the quality of the DWBA fits for $R_{5/2}=3.79$ F is not the same for the distributions of all the nuclei at large angles.

C. DWBA Spectroscopic Factors

The (p,d) spectroscopic factors were calculated using the optical-model parameters mentioned earlier, and are presented for each nucleus in Tables III–VII. The

[40] P. H. Stelson and Lee Grodzins, Nucl. Data **A1**, 21 (1965).
[41] J. L. Snelgrove and E. Kashy, Bull. Am. Phys. Soc. **12**, 681 (1967).

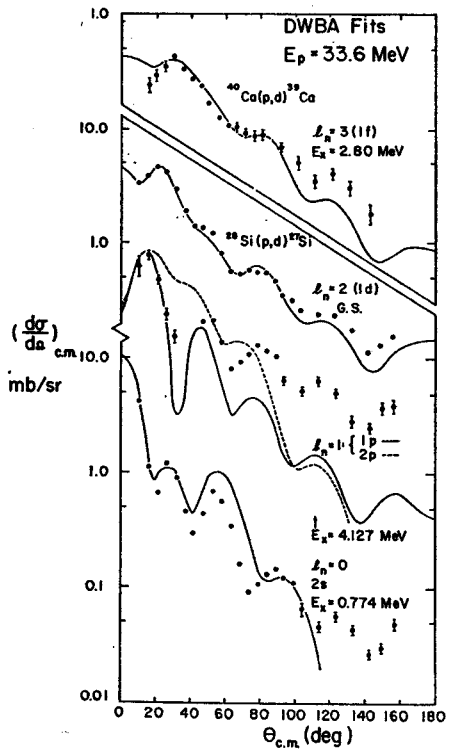

FIG. 36. DWBA calculations for different values of l_n. Fits for the 2.80-MeV level of ^{39}Ca ($l_n=3$) and for the 0.00- ($l_n=2$), 4.127- ($l_n=1$), and 0.774-MeV ($l_n=0$) levels of ^{27}Si are shown.

neutron parameters were chosen from those used for the J-dependence analysis (Table II), and DWBA results for both neutron well radii are present for some of the levels in ^{31}S, ^{35}Ar, and ^{39}Ca. Although the DWBA calculations resulted in quite satisfactory fits to the $l_n=2$ data (especially the $\frac{5}{2}^+$ distributions), the predictions for the other l_n values were not as good. Figure 36 shows DWBA fits to the data corresponding to $1d$, $2s$, $1p$, and $2p$ neutron transfers in the ^{28}Si$(p,d)^{27}$Si reaction and the fit to the $l_n=3$ distribution in the ^{40}Ca$(p,d)^{39}$Ca reaction.

TABLE IV. Spectroscopic factors for the ^{28}Si$(p,d)^{27}$Si reaction.

E_x(MeV)	σ_{max}(mb/sr)	J^π	$S_{expt}(r_{0n}=1.25$ F)
0.00	4.6	$\frac{5}{2}^+$	3.45
0.774	1.2(28°)	$\frac{1}{2}^+$	0.64
0.952	0.41	$\frac{3}{2}^+$	0.34
2.647	0.5	$\frac{5}{2}^+$	0.47
2.90[a]	0.84	$(\frac{3}{2},\frac{5}{2})^+$	(0.81)
4.127	0.80	$(\frac{1}{2},\frac{3}{2})^-$	1.20[b]
			0.21[c]
4.275	0.3	$(\frac{3}{2},\frac{5}{2})^+$	0.34
5.233	0.84	$(\frac{1}{2},\frac{3}{2})^-$	1.67[b]
			0.28[c]
6.343	0.30	$(\frac{3}{2},\frac{5}{2})^+$	0.45

[a] Unresolved doublet.
[b] Assuming pickup from $1p$ shell.
[c] Assuming pickup from $2p$ shell.

TABLE V. Spectroscopic factors for the ^{32}S$(p,d)^{31}$S reaction.

E_x(MeV)	σ_{max}(mb/sr)	J^π	$S_{expt}(r_{0n}=1.20$ F)
0.00	3.6(27°)	$\frac{1}{2}^+$	1.04
1.24	1.0	$\frac{3}{2}^+$	0.94
			0.18[a]
2.23	2.7	$\frac{5}{2}^+$	2.77
3.29	0.6	$(\frac{5}{2})^+$	0.73
4.09	0.7	$\frac{5}{2}^+$	0.86
4.72	0.4(27°)	$(\frac{1}{2}^+)$	0.07
7.05	0.6	$(\frac{3}{2},\frac{5}{2})^+$	1.00

[a] $r_{0n}=1.65$ F, $a_n=0.75$ F.

The experimental spectroscopic factors for levels excited in the ^{24}Mg$(p,d)^{23}$Mg reaction are listed in Table III along with the results of shell-model calculations by Wildenthal.[42] An unusually deep imaginary well (35 MeV) was required in the deuteron channel in order to obtain reasonable DWBA fits to the data. This caused a decrease in magnitude of the calculated $l_n=2$ cross sections, which resulted in values for the spectroscopic factors that are unreasonably large if one assumes ^{24}Mg has a closed ^{16}O core. The values in Table III are therefore to be trusted only on a relative basis. Nevertheless, the ratio of the experimental spectroscopic factors (S_{expt}) for the $\frac{1}{2}^+$ levels at 2.35 and 4.37 MeV is in poor agreement with the ratio obtained from Wildenthal's calculations for levels at 1.80 and 4.81 MeV.

The experimental spectroscopic factors were compared to those predicted by the Nilsson-model wave functions of Chi.[43] However, since each Nilsson orbit can hold only two neutrons, the spectroscopic factors for the low-lying levels in ^{27}Si, ^{31}S, and ^{35}Ar (Tables IV–VI) are too large to correspond to pure rotational bands. As can be seen from the spectroscopic factors listed in Table IV, approximately half of the $2s$-$1d$ shell strength is contained in the ground-state ($d_{5/2}$) transition for the ^{28}Si$(p,d)^{27}$Si reaction. The value of 3.45 for S_{expt} agrees reasonably well with values of 3.9 and 3.97 obtained from ^{28}Si$(d,^3$He$)^{27}$Al proton pickup reactions.[21,22]

TABLE VI. Spectroscopic factors for the ^{36}Ar$(p,d)^{35}$Ar reaction.

E_x(MeV)	σ_{max}(mb/sr)	J^π	S_{expt} $r_{0n}=1.15$ F	S_{expt} $r_{0n}=1.35$ F
0.00	2.9	$\frac{3}{2}^+$	3.03	1.76[a]
1.18	3.4(26°)	$\frac{3}{2}^+$	1.29	1.05
1.70	...	$(\frac{5}{2}^+)$	0.1	
2.60	0.3	$(\frac{3}{2})^+$	0.42	0.28[a]
2.95	1.7	$(\frac{5}{2})^+$	2.31[a]	1.53
3.19	0.3	$\frac{7}{2}^-$	0.64	0.37[a]
4.70	0.07(26°)	$(\frac{1}{2}^+)$	0.05	0.04
5.57	1.0	$(\frac{3}{2},\frac{5}{2})^+$	1.77[a]	1.25
6.01	0.6	$(\frac{3}{2},\frac{5}{2})^+$	1.18	0.83[a]
6.62	0.3(24°)	$(\frac{1}{2}^+)$	0.24	0.19
6.82	0.4	$(\frac{3}{2},\frac{5}{2})^+$	0.72[a]	0.51

[a] Value for radius giving best DWBA fit.

[42] B. H. Wildenthal (private communication).
[43] B. E. Chi, Nucl. Phys. 83, 97 (1966).

TABLE VII. Spectroscopic factors for the ^{40}Ca$(p,d)^{39}$ reaction.

E_x(MeV)	σ_{max}(mb/sr)	J^π	S_{expt} $r_{0n}=1.11$ F	$r_{0n}=1.35$ F
0.00	5.6	$\frac{3}{2}^+$	7.11	3.70[a]
2.47	3.0(26°)	$\frac{1}{2}^+$	2.31	1.82
2.80	0.4	$\frac{7}{2}^-$	1.04	0.58[a]
3.03	0.2	$(\frac{1}{2},\frac{3}{2})^-$		0.02
5.13	1.1	$(\frac{5}{2})^+$	2.08[a]	1.43
5.48	0.5	$(\frac{3}{2},\frac{5}{2})^+$	0.97	0.67
6.15	1.0	$(\frac{5}{2})^+$	2.15[a]	1.48

[a] Values for radius giving best DWBA fit.

It has been suggested[20] that the ^{27}Al mirror nucleus has a prolate deformation where the first few excited levels correspond to a rotational band based on the $K=\frac{1}{2}$ [211] Nilsson orbit (Fig. 3). The excitation of the corresponding levels in ^{27}Si by a direct-pickup process [such as the (p,d) reaction] would then indicate configuration mixing with Nilsson orbit 9 in the ^{28}Si ground state. However, there seems to be no prolate value for $\delta(>0)$ for which the $K=\frac{1}{2}$ [211] wave function of Chi[43] is in reasonable relative agreement with the experimental values for the levels at 0.774($\frac{1}{2}^+$), 0.952-($\frac{3}{2}^+$), and 2.647($\frac{5}{2}^+$) MeV (Table IV). Since the $\frac{5}{2}^+$ assignment for the ^{27}Si ground state is inconsistent energywise with an oblate deformation (Fig. 3), it appears that no simple form of the strong-coupling model can explain the results. The large spectroscopic factor for the ground-state transition is some indication that the average deformation is probably small and that the mixing of rotational bands is extensive. It has been suggested that the ^{28}Si nucleus undergoes shape oscillations, since the energy minima for the prolate and oblate solutions are nearly equal in a Hartree-Fock calculation.[44]

Spectroscopic factors for the $l_n=1$ levels excited in the (p,d) reaction on ^{24}Mg and ^{28}Si were calculated for both a $1p$ and a $2p$ origin for the transferred neutron. As can be seen from Tables III and IV, the values assuming a $2p$ pickup are considerably smaller than those for a $1p$ pickup.

DWBA spectroscopic factors were calculated for both neutron well radii used in the analysis for J dependence for the 1.24-MeV level in ^{31}S (Table V) and for several levels in ^{35}Ar and ^{39}Ca (Tables VI and VII). These results illustrate the ambiguity involved in extracting spectroscopic factors when the J dependence is strong. The results from the ^{32}S$(p,d)^{31}$S reaction (Table V) are in good agreement with the relative spectroscopic factors obtained from the ^{32}S$(^3$He,$\alpha)^{31}$S reaction,[45] except that in the (^{3}He,α) reaction the level at 4.45 MeV is also strongly excited. The S_{expt} value corresponding to the best DWBA fit for the $l_n=2$ and $l_n=3$ levels of ^{35}Ar and ^{39}Ca are denoted by a superscript a in Tables VI and VII and appear to be in good agreement with the total expected $l_n=2$ strength ($\sim$8 and 10, respectively).

[44] R. Muthukrishnan, Nucl. Phys. A93, 417 (1967).
[45] C. M. Fou and R. W. Zurmühle, Phys. Rev. 151, 927 (1966).

The spectroscopic factor of 0.58 for the $l_n=3$ level at 2.80 MeV in ^{39}Ca (Table VII) is in good agreement with the value of 0.53 obtained by Bock *et al.*[32] from the ^{40}Ca$(^3$He,$\alpha)^{39}$Ca reaction and with the result of 0.5 obtained for the excitation of the mirror level in the ^{40}Ca$(d,^3$He$)^{39}$K reaction.[33] Glashausser *et al.*[29] extracted values of 0.14 and 0.28 by assuming different neutron separation energies in the ^{40}Ca$(p,d)^{39}$Ca reaction at 27.3-MeV bombarding energy. The excitation of the $l_n=1$ level at 3.03 MeV is assumed to be due to a $2p$ shell admixture with an estimated spectroscopic factor of $\sim$0.02, as compared to a value of 0.04–0.05 obtained by Hiebert *et al.*[33] for the mirror level in the $(d,^3$He) reaction mentioned above. Both of these results are considerably smaller than the value 0.11 obtained by Cline *et al.*[31] from the ^{40}Ca$(^3$He,$\alpha)^{39}$Ca reaction. The spectroscopic factors for the $l_n=2$ levels at 5.13, 5.48, and 6.15 MeV in ^{39}Ca, together with the lack of any strong excitation above 6.15 MeV, indicate that these levels represent most of the $d_{5/2}$ strength.

V. SUMMARY AND CONCLUSIONS

The investigation of the (p,d) reaction on $N=Z$ nuclei in the $2s$-$1d$ shell has provided new information about the level structures of the ^{23}Mg, ^{27}Si, ^{31}S, and ^{35}Ar residual nuclei, while previous results for ^{39}Ca have been confirmed.[29,31] The 33.6-MeV bombarding energy and particle-detection techniques have permitted the observation of 10–12 MeV of excitation in the residual nuclei, with the interesting result that virtually all of the observed $2s$-$1d$ shell hole strength exists at excitation energies $\lesssim$8 MeV. (A possible exception to this is the 9.63-MeV level in ^{23}Mg.) It is therefore apparent that most of the $2s$-$1d$ shell hole states have been excited; the DWBA spectroscopic factors obtained here are in support of this fact.

The forward-angle J dependence observed in the $l_n=2$ angular distributions appears to vary in a systematic way with mass number (for $N=Z$ targets) (Fig. 27), and seems to be correlated with the nature of the nuclear deformation. The attempts to reproduce J-dependence effects by varying the neutron well radius in distorted-wave calculations were partially successful. Large changes were necessary in most cases, however, which produced correspondingly large changes in the magnitude of the calculated DWBA cross section and led to uncertainties in extracting spectroscopic factors. However, there is some evidence that the radius parameter corresponding to the best DWBA fit to the data might also result in the most trustworthy value for the spectroscopic factor. It is apparent from the results of this and other investigations[3–6] that additional experimental information and more theoretical work is necessary to obtain an understanding of J dependence. Distorted-wave calculations which explicitly account for nuclear deformations may give further insight to this problem.

Of particular interest is the excitation of low-lying (E_x= 2.7–6.0 MeV) l_n= 1 levels in ^{32}Mg and ^{27}Si, which could be due to configuration mixing with the $2p$ shell. However, a plot of (p,d) reaction Q values for the excitation of the first l_n= 1 level versus mass number (Fig. 12) seems to be strong evidence that these levels are $1p$ shell hole states.

The ordering of the first few levels in ^{23}Mg, ^{31}S, and ^{35}Ar seems to be qualitatively consistent with rotational bands based on neutron holes in Nilsson orbits (Ref. 14 and Fig. 3). However, the extraction of DWBA spectroscopic factors has shown that the states are considerably more complex. The large spectroscopic factors measured for the excitation of low-lying levels in ^{31}S, ^{35}Ar, and especially ^{27}Si are indications of considerable rotational band mixing.

ACKNOWLEDGMENTS

The author is greatly indebted to Professor E. Kashy for his advice and many helpful discussions concerning this work. He also wishes to thank Dr. L. A. Kull and P. J. Plauger for their help in taking the data, and Professor W. P. Johnson for his advice in the operation of the cyclotron.

Reprinted from THE PHYSICAL REVIEW, Vol. 172, No. 4, 1124–1126, 20 August 1968
Printed in U. S. A.

Precise Energies of ^{40}Ca Levels*

E. KASHY AND J. L. SNELGROVE†
Cyclotron Laboratory, Michigan State University, East Lansing, Michigan 48823
(Received 25 March 1968)

Energies of excited levels of ^{40}Ca have been measured with high precision using a Ge(Li) detector to observe γ-ray transitions. The present work, which resolves some discrepancies in the literature, yields $E_x=3737.1\pm0.3$ keV for the lowest 3^- level and $E_x=7658.9\pm0.5$ keV for the ^{40}Ca $T=1$ analog of the ^{40}Sc ground state. Energies of a number of other levels of ^{40}Ca are also given.

INTRODUCTION

THE systematics of Coulomb analog levels have been the subject of many of the recent investigations in nuclear physics. As the general trends have been understood, attention has been directed toward the small deviations of the Coulomb energies and their implications both in terms of nuclear structure effects and average properties of nuclei.[1,2] However, since the deviations are in general quite small, it is essential that the energies of analog levels be known to high accuracy. The development of Ge(Li) detectors has made γ-ray measurements an ideal method for determining the energies of certain analog levels. A number of authors[3–6] have used such techniques to obtain the energy of the lowest $T=1$ level of ^{40}Ca, and a ^{41}K(^{3}He,d)^{40}Ca charged-particle spectrograph result of comparable accuracy has also been reported.[7] Since Armini, Sunier, and Richardson,[6] whose result for that level is $E_x=7669.1\pm3.3$, have questioned the precision of the Berg and Kashy[5] value of $E_x=7660.8\pm1.2$, and in view of the significant difference between the two results, the present work was undertaken. It is also worth noting that accuracies of the order of 1 in 10^4 are not unusual and are in fact much more the norm of present-day γ-ray energy measurements rather than the exception. Finally, precise γ-ray measurements such as those reported here can be extremely useful by providing calibration data for other experiments.

TABLE I. Standard γ rays used for calibration.[a]

Source	E_γ (keV)
m_0c^2	511.003±0.002
ThC″	583.139±0.023
^{137}Cs	661.632±0.069
^{22}Na	1274.552±0.055
^{24}Na	1368.526±0.044
ThC″	2614.47 ±0.10
^{24}Na	2753.92 ±0.12

[a] These and other γ rays are found conveniently tabulated by D. C. Camp, University of California Radiation Laboratory Report No. UCRL-50156, 40, 1967 (unpublished) and also by J. B. Marion, University of Maryland, Technical Report No. 656 (revised), 1967 (unpublished).

EXPERIMENTAL PROCEDURE

The Michigan State University sector-focused cyclotron provided a 24-MeV proton beam which was allowed to strike a thick natural calcium target. A 20-cm^3 Ge(Li) detector of coaxial configuration which was fabricated in our laboratory was placed at a distance of 16 cm from the target and at 90° to the beam direction. The γ-ray pulses were amplified, then sorted in a 40-MHz 12-bit analog-to-digital converter (ADC) connected on line to the laboratory's Sigma 7 digital computer. Two types of measurements were carried out. The first consisted of continuously counting the sample while a very small beam current was incident on target. At the same time, the adjacent calibration γ rays were being detected at a rate approximating that of the ^{40}Ca de-excitation γ ray from the lowest 3^- level. A list of the standards used in this work is given in Table I. Figure 1 shows a small section of a "beam-on" spectrum, where the broad γ-ray peak seen reflects the de-excitation of a short-lived ^{40}Ca level.

The second type of measurement consisted of pulsing the beam on for 600 msec, allowing 70 msec for the

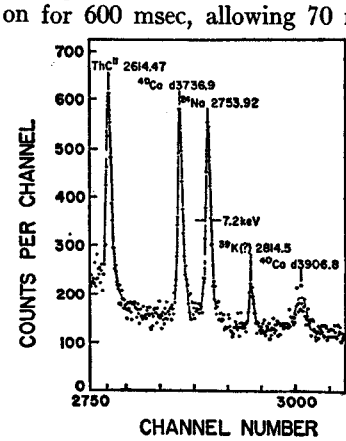

FIG. 1. Section of a prompt γ-ray spectrum showing the 3^- double-escape peak bracketed by two calibration γ rays. The source of 2814.5-keV peak is not definitely established, and the ^{39}K assignment is tentative.

* Supported in part by the National Science Foundation.
† National Science Foundation Graduate Fellow.
[1] R. Sherr, Phys. Letters 24B, 321 (1967), and references therein.
[2] J. A. Nolen, Jr., J. P. Schiffer, and N. Williams, Bull. Am. Phys. Soc. 13, 65 (1968).
[3] M. E. Rickey, E. Kashy, and D. Knudsen, Bull. Am. Phys. Soc. 10, 550 (1965).
[4] W. C. Anderson, L. T. Dillman, and J. J. Kraushaar, Nucl. Phys. 77, 401 (1966).
[5] R. E. Berg and E. Kashy, Bull. Am. Phys. Soc. 11, 477 (1966). A preliminary value for the $T=1$ level of $E_x=7661.1\pm1.4$ keV is given therein and a final value of $E_x=7660.8\pm1.2$ keV was reported at that conference.
[6] A. J. Armini, J. W. Sunier, and J. R. Richardson, Phys. Rev. 165, 1194 (1968).
[7] J. R. Erskine, Phys. Rev. 149, 854 (1966).

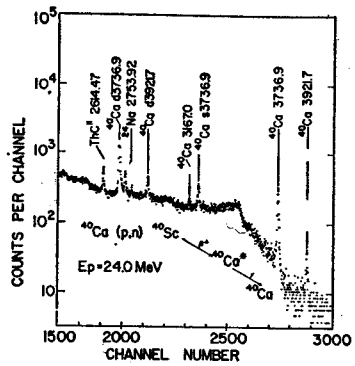

FIG. 2. Section of a spectrum showing some prominent delayed γ rays following the decay of ^{40}Sc.

electronics to recover from the resulting strong γ-ray burst, then counting the sample for 700 msec. Most of the delayed γ rays one then observes come from ^{40}Sc, which β^+-decays principally by a superallowed transition to the 4^- $T=1$ analog in ^{40}Ca and to the lowest 3^- level of ^{40}Ca. Again the calibration γ rays were counted simultaneously, thus minimizing the chances of error due to electronic drifts. Figure 2 shows the high-energy part of such a spectrum.

TABLE II. Energies measured for the ^{40}Ca 3^- γ ray.

Run No.	$E_\gamma - 2m_0c^2$ (keV)	Beam condition
1	2715.1	on
2	2715.0	on
3	2714.7	on
4	2714.7	on
5	2714.7	on
10	2714.7	pulsed
11	2715.2	pulsed
12	2715.1	pulsed
13	2715.1	pulsed
	Average 2714.9 keV	

RESULTS

A special effort was made to obtain to high accuracy the energy of the lowest ^{40}Ca 3^- level. Table II lists the energy of the double-escape peak from each of 9 runs, five beam-on and four with pulsed beams. For delayed γ rays, the data represent the values obtained by taking centroids of the peaks including only the upper two-thirds of each peak. This was done in order to reduce pileup effects on the ^{40}Ca lines, whose yield decreased strongly during each counting period as opposed to the constant yield of the ThC'' and ^{24}Na standards. In the beam-on data, full centroids and $\frac{2}{3}$ height centroids gave very nearly the same value (the variation was 0.2 keV in the worst case) and the average value is given. This 0.2-keV variation served as an estimate of the systematic error introduced by variation of counting rates between the sample and the standards due to beam current fluctuations, and represents the largest single contribution to the error in the final value of $E_\gamma = 3736.9 \pm 0.3$ keV for that γ ray. For most of the other γ rays, both the full-energy peak and double-escape peaks were used and found in all instances to be in excellent agreement, reflecting the overall goodness of the calibration curves. The results for the γ-ray energies observed in this work are listed in Table III, where the relatively large errors appearing on some γ-ray transitions reflect Doppler broadening arising from the short lifetimes of the states.[8] Table IV shows the ^{40}Ca excitation energies compiled by Endt and van der Leun,[9] the recently reported results of Armini *et al.*[6] and MacDonald *et al.*,[8] and the present results for which recoil corrections have been made. A graphical comparison of the most precise recent

TABLE III. γ-ray energies in ^{40}Ca.

E_γ (keV)	Transition[a]
754.6±0.4	(4-2)
1121.7±0.7	(8-4)
1877.0±0.5	(8-2)
2044.9±0.5	(31-8)
3167.0±0.4	(31-4)
3736.9±0.3	(2-0)
3906.8±2.0	(3-0)
3921.7±0.5	(31-2)
5255.0±4.0	(6-0)

[a] See Table IV.

TABLE IV. Energy levels of ^{40}Ca.

Level No.	E_x [a] (keV)	J^π [a]	E_x [b] (keV)	E_x [c] (keV)	E_x [d] (keV)
0	0	0^+	0	0	0
1	3352±2	0^+			
2	3734±3	3^-	3741.7±2.1	3735.5±2.0	3737.1±0.3
3	3903±3	2^+		3906.1±2.0	3907.0±2.0
4	4487±3	5^-	4496.2±3.3		4491.8±0.5
5	5201±6	0^+ [e]		5215.5±3.0	
6	5242±5	2^+ [e]		5255.5±5.0	5255.4±4.0
7	5275±4	4^+		5281.4±3.0	
8	5609±4	4^-	5621.4±2.7		5613.9±0.6
...					
31	7661.1±1.4[e]	4^-, $T=1$	7669.1±3.3		7658.9±0.5

[a] Reference 9.
[b] Reference 6.
[c] Reference 8.
[d] Present results.
[e] See Ref. 5.

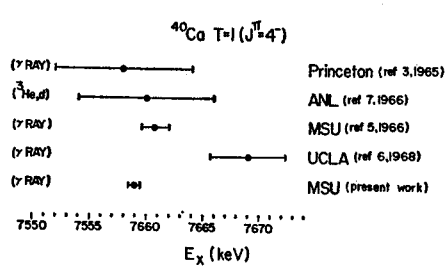

FIG. 3. Comparison of recent results for the ^{40}Ca 4^-, $T=1$ level.

[8] J. R. MacDonald, D. F. H. Start, R. Anderson, A. G. Robertson, and M. A. Grace, Nucl. Phys. A108, 6 (1968).
[9] P. M. Endt and C. van der Leun, Nucl. Phys. A105, 1 (1967).

results for the energy of the $T=1$ analog to the ^{40}Sc ground state is shown in Fig. 3. The present result for the energy of this analog level differs from that of Berg and Kashy[5] by 1.9±1.3 keV, of which about 0.5 keV may be due to the differential pileup effect mentioned above. However, the difference of 10.2±3.4 keV from the result of Armini *et al.*[6] appears to be too large to be accounted for by such an effect.

ACKNOWLEDGMENTS

We would like to express our appreciation to Professor C. R. Gruhn for providing us with the large-volume Ge(Li) detector. We also wish to thank R. Au for his data-taking and analysis code, and R. deForest, who kindly put together certain instruments well ahead of schedule for this experiment.

Reprinted from THE PHYSICAL REVIEW, Vol. 171, No. 4, 1283–1289, 20 July 1968
Printed in U. S. A.

High-Resolution Gamma-Ray Spectroscopic Studies of the Decays of 2.6-h Nd^{141g} and 60-sec Nd^{141m}

D. B. BEERY AND W. H. KELLY*
Department of Physics,† Michigan State University, East Lansing, Michigan 48823

AND

WM. C. MCHARRIS
Department of Chemistry and Department of Physics,†
Michigan State University, East Lansing, Michigan 48823

(Received 26 February 1968)

γ rays emitted in the decays of 2.6-h Nd^{141g} and 60-sec Nd^{141m} have been investigated with Ge(Li) and NaI(Tl) detectors. Following the decay of Nd^{141g}, γ rays with the following energies (and relative intensities) have been observed: 145.4 (30.0), 981.3 (3.0), 1126.8 (≡100), 1147.1 (38.2), 1292.8 (61.2), 1298.7 (16.3), 1434.6 (3.0), 1579.9 (0.74), 1607.9 (2.3), and 1657.2 keV (0.12). On the basis of coincidence and anticoincidence experiments, energy sums, and relative intensities, states were placed in Pr^{141} at 0, 145.4, 1126.8, 1292.5, 1298.4, 1580.0, 1607.9, and 1657.2 keV. An upper limit of 0.1% of the intensity of the Nd^{141m} 756.5-keV isomeric-transition γ ray was placed on the intensity of any other γ ray between 130 and 2600 keV following direct transitions from the $\frac{11}{2}-$ Nd^{141m} to high-spin states of Pr^{141}. Limits are placed on the spins of Pr^{141} states on the basis of logft values and relative photon intensities, and the structures of the states are discussed in terms of current nuclear models.

I. INTRODUCTION

SINCE the first production of Nd^{141} in 1937 by Pool and Quill,[1] who used fast neutrons to induce the $Nd^{142}(n,2n)Nd^{141}$ reaction, this nuclide has been produced by a number of reactions involving the use of protons, deuterons, α particles, and photons as projectiles.[2] Similarly, there have been various more or less successful studies of its decay scheme.[2] Among the more complete γ-ray spectroscopic studies that utilized only NaI(Tl) detectors,[3–6] however, there exist some serious discrepancies. Also, in none of these studies are more than three Pr^{141} excited states reported, whereas, as a result of the study of inelastically scattered deuterons on Pr^{141}, Cohen and Price[7] have reported levels at 140, 1140, 1300, 1500, and 1630 keV, with additional levels at 1800 keV and higher energies. Some studies on inelastically scattered neutrons[8] and N^{14}-induced Coulomb excitation,[9] although with poorer resolution, have also indicated the existence of a number of levels starting in the vicinity of 1 MeV. In the only previous published work of Nd^{141} decay utilizing Ge(Li) detectors, Koehler and Grissom,[10] using a very small detector, report only four γ rays, depopulating the first three of the excited states reported by Cohen and Price.

Since the energy for Nd^{141} electron-capture decay is 1800 keV,[5,11] one might expect some of the other higher-lying Pr^{141} levels also to be populated from its decay. For this reason and because of the discrepancies among the earlier studies, we felt that a reinvestigation of Nd^{141} decay was in order. We have produced Nd^{141} by the relatively clean $Pr^{141}(p,n)Nd^{141}$ reaction and have used Ge(Li) and NaI(Tl) detectors in singles, coincidence, and anticoincidence configurations to study its γ rays. Additionally, as no specific rare-earth chemical separations had been performed on the targets in any of the previous work, we separated Nd chemically from the other rare earths in order to insure that the activities we were observing came from a Nd isotope. As a result of our studies we have found six new γ rays, and these can be fitted into a decay scheme that includes the population of three additional excited states in Pr^{141}. We also investigated the decay of the short-lived isomer Nd^{141m},[12,13] to see if it might decay directly to high-spin states in Pr^{141}; our results allow us to place an upper limit of 0.1% on any direct population of such levels.

II. SOURCE PREPARATION

The Nd^{141} sources were prepared by bombarding 99.97% pure Pr_2O_3 with protons from the Michigan State University sector-focused cyclotron; these protons were degraded from higher energies to 9 MeV by the use of Al absorbers. Typically, ≈100-mg targets

* At present on leave at the Lawrence Radiation Laboratory, Berkeley, Calif.

† Supported in part by the National Science Foundation.

[1] M. L. Pool and L. L. Quill, Phys. Rev. 53, 437 (1938).

[2] *Nuclear Data Sheets*, compiled by K. Way *et al.* (U. S. Government Printing Office, National Academcy of Sciences—National Research Council, Washington, D. C.); C. M. Lederer, J. M. Hollander, and I. Perlman, *Table of Isotopes* (John Wiley & Sons, Inc., New York, 1966), 6th ed.

[3] H. L. Polak, W. Schoo, B. L. Schram, R. K. Girgis, and R. van Lieshout, Nucl. Phys. 5, 271 (1958).

[4] E. W. Cybulska and L. Marquez, Nucl. Phys. 14, 117 (1959).

[5] E. I. Biryukov and N. S. Shimanskaya, Izv. Akad. Nauk SSSR, Ser. Fiz. 27, 1402 (1963).

[6] W. L. Alford, D. R. Koehler, and R. G. Polk, Nucl. Phys. 44, 439 (1963).

[7] B. L. Cohen and R. E. Price, Phys. Rev. 123, 283 (1961).

[8] V. A. Bukarev and V. I. Popov, Yadern. Fiz. 1, 443 (1965) [English transl.: Soviet J. Nucl. Phys. 1, 316 (1965)].

[9] D. G. Alkhazov, K. I. Erokhina, and I. Kh. Lemberg, Izv. Akad. Nauk SSSR, Ser. Fiz. 29, 139 (1965).

[10] D. R. Koehler and J. T. Grissom, Nucl. Phys. 84, 235 (1966).

[11] G. Wilkinson and H. G. Hicks, Phys. Rev. 75, 1687 (1949).

[12] R. A. James and C. D. Bingham, Phys. Rev. 117, 810 (1960).

[13] K. Kotajima and H. Morinaga, Nucl. Phys. 16, 231 (1960).

were bombarded with a ≈1-μA beam for 1 h. Sources were normally allowed to decay for at least 1 h to let any short-lived contaminants decay away, and then they were counted for two to four half-lives, more source being added with the passage of time in order to retain a relatively constant counting rate. It was found that no competing γ rays with different half-lives were observed for approximately four half-lives of the Nd^{141}. Most of the coincidence experiments, which required several days' counting time, were performed with multiple bombardments.

To insure that we were observing radiations only from Nd, we confirmed the singles γ-ray spectrum with a chemically separated source. In this source the Nd was separated from the Pr target and any other contaminating rare earths by eluting it from a Dowex-50 cation-exchange column with α-hydroxy-isobutyrate.[14]

The Nd^{141m} sources were produced by bombarding similar Pr_2O_3 targets for ≈10 sec. No chemical separations were performed on these sources.

III. Nd^{141g} γ-RAY SPECTRA

A. Singles Spectra

A 7-cm^3 five-sided coaxial Ge(Li) detector was used to determine the energies and intensities of the Nd^{141} γ rays. It was mounted in a dip-stick cryostat. The wall thickness of the evacuated Al can covering the detector was 0.16 cm. Typical resolution obtained with this detector was ≈4.3 keV full width at half-maximum (FWHM) for the 661.6-keV γ ray of Cs^{137}, using a room-temperature FET preamplifier, a low-noise *RC* linear amplifier with pole-zero compensation, and a 1024-channel analyzer. A 3-cm^3 planar Ge(Li) detector mounted in a similar fashion was used to confirm the energy values and intensity ratios of the γ rays observed. Both of these detectors were manufactured in this laboratory.

TABLE I. γ rays used as energy standards.

Nuclide	γ-ray energy (keV)	Reference
Co^{57}	121.97 ±0.05	a
Co^{57}	136.33 ±0.04	a
Ce^{139}	165.84 ±0.03	b
Cs^{134}	644.744±0.027	c
Cs^{137}	661.595±0.076	d
Cs^{134}	795.806±0.050	c
Mn^{54}	834.84 ±0.07	e
Y^{88}	898.01 ±0.07	e
Sc^{46}	1120.50 ±0.07	e
Co^{60}	1173.226±0.040	f
Co^{60}	1332.483±0.046	f
Na^{24}	1368.526±0.044	f
Tl^{208} (D.E.)	1592.46 ±0.10	f
Na^{24} (D.E.)	1731.91 ±0.012	f
Y^{88}	1836.08 ±0.07	e

[a] J. B. Marion, University of Maryland Technical Report No. 653, 1957 (unpublished).
[b] Reference 20.
[c] D. E. Raeside, J. J. Reidy, and M. L. Wiedenbeck, Nucl. Phys. A98, 54 (1967).
[d] J. S. Geiger, R. L. Graham, and F. Brown, Can. J. Phys. 40, 1258 (1962).
[e] W. W. Black and R. L. Heath, Nucl. Phys. A90, 650 (1967).
[f] G. Murray, R. L. Graham, and J. S. Geiger, Nucl. Phys. 63, 353 (1965).

[14] G. R. Choppin, B. G. Harvey, and S. G. Thompson, J. Inorg. Nucl. Chem. 2, 66 (1956).

The energies of the γ rays were measured by counting the Nd^{141} sources simultaneously with a number of well-known calibration sources, which are listed in Table I. In order that activities decaying with different half-lives could be identified, spectra were recorded periodically as the sources aged. A background correction was made for each peak by fitting a cubic equation to several channels above and below the peak and then subtracting. The centroid of each calibration peak was then determined and a least-squares fit made to a quadratic calibration curve. The centroids of unknown peaks were similarly determined and the corresponding energies calculated from the calibration curve. The energies of weak Nd^{141} γ rays, which would be obscured by the calibration standards, were determined by using the now-well-determined stronger γ rays as internal standards. A γ-ray spectrum taken with the 7-cm^3 detector is shown in Fig. 1.

A list of γ-ray energies and relative intensities is given in Table II. The energies assigned are mean values taken from a number of different measurements recorded at different times, different system gains, and with each of the two Ge(Li) detectors. The corresponding uncertainties in energies are based on the reproducibilities both of the standard energies and the Nd^{141} energies from the calibration curves, the sizes of the Nd^{141} photopeaks above the background, and the quoted errors of the standard energies listed in Table I.

The relative peak areas obtained are also averages from a number of runs, and the associated statistical uncertainties include estimated uncertainties in the backgrounds. Relative photopeak efficiency curves for the Ge(Li) detectors were obtained in two ways: First, a set of standard γ-ray sources whose relative intensities had been measured with NaI(Tl) detectors was used. Second, a set of points was obtained from sources emitting several γ rays whose relative intensities were known from well-established decay schemes. The efficiency curves resulting from the separate methods were in very good agreement.

The *K* x-ray intensity was obtained by comparing the low-energy portion of the spectrum directly with the γ-ray spectrum of Ce^{141}; the comparison was made using the 3-cm^3 detector. Ce^{141} also decays to Pr^{141}, with 70% of its decay populating the 145.4-keV state. Its ratio of *K* x rays to 145.4-keV γ's has been measured to be[15] 0.341±0.010, and, using this value, we found the corresponding ratio for Nd^{141} decay to be 264±71.

B. Coincidence Spectra

From the Nd^{141} disintegration energy[5,11] of 1800 keV and the measured γ-ray energies listed in Table II,

[15] L. Nemet, Izv. Akad. Nauk SSSR, Ser. Fiz. 25, 681 (1961).

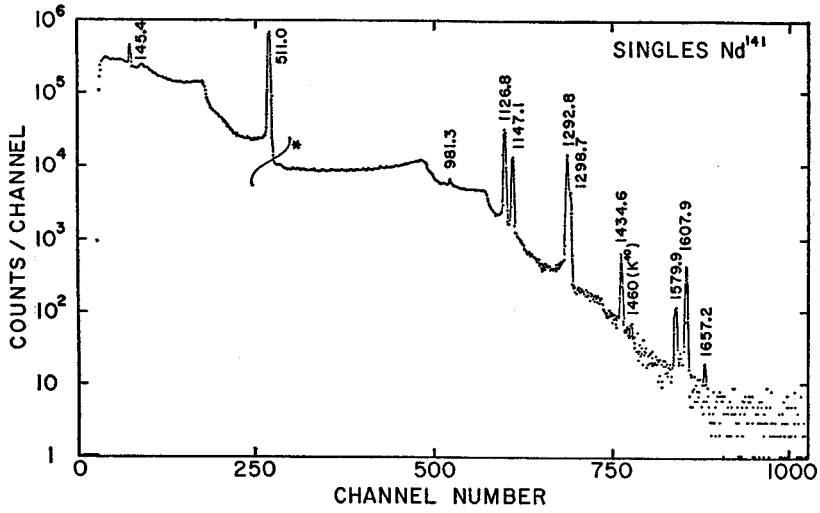

FIG. 1. Singles γ-ray spectrum from the decay of Nd^{141} taken with a 7-cm³ Ge(Li) detector. Because of analyzer spillover, the portion of the spectrum to the left of the asterisk was recorded for a shorter period of time and then normalized to the remainder of the spectrum.

it is evident that only coincidences involving the 145.4-keV γ ray are energetically allowed. Thus, we gated a 3×3-in. NaI(Tl) detector on the 145.4-keV photopeak and displayed the resultant coincidence spectrum seen by the 7-cm³ Ge(Li) detector; the resolving time of the system was ≈50 nsec. Figure 2 shows this coincidence spectrum. The relative intensities from this experiment are also included in Table II; these have been corrected for chance coincidences. Comparison of the relative intensities of the 145.4-keV γ-γ coincidence spectrum with those of the singles spectra clearly indicate that the 981.3-, 1147.1-, and 1434.6-keV γ's are in coincidence with the 145.4-keV γ, whereas the 1126.8-, 1292.8-, and 1298.7-keV γ's are not.

In order to search for additional weak γ rays that might have passed unobserved in the other measurements, an experiment was also performed in which the NaI(Tl) gate was set to accept all transitions greater than 130 keV in energy. This "integral" γ-γ coincidence spectrum is shown in Fig. 3, and the relative intensities from it are listed in Table II. They verify the results of the 145.4-keV γ-γ coincidence experiment, but no new, weak γ rays are indicated.

To complement these experiments and confirm which γ rays appeared in cascades and which came from directly-fed ground-state transitions, we then employed an 8×8-in. NaI(Tl) split annulus detector[16] in an anticoincidence experiment with the 7-cm³ Ge(Li) detector. The single-channel analyzer on the annulus gate was set so that the gate would be active for all γ rays above 80 keV. The Nd^{141} sources were placed inside the annulus tunnel and on top of the Ge(Li) detector. An additional 3×3-in. NaI(Tl) anticoincidence detector was placed in the tunnel above the sources and the

TABLE II. Energies and relative intensities of γ rays from the decay of Nd^{141}.

Measured γ-ray energy (keV)	Relative intensity: Singles spectra[a]	145.4-keV γ-γ coincidence spectrum[b]	Integral γ-γ coincidence spectrum[b]	Anticoincidence spectrum
K x rays	(8.0 ± 2.0)×10³	...	...	...
145.4±0.3	30.3 ± 3.0	46± 5(16±6)	81± 10(51±11)	11.1 ±1.1
511.006 (annih.)	832 ±83[c]	955±300	1340±150	60 ±6
981.3±0.6	3.0 ± 0.3	147± 30(144±30)	90± 25(87±25)	1.1 ±0.3
1126.8±0.4	≡100	≡100(0)	≡100(0)	≡100
1147.1±0.4	38.2 ± 3.8	1810±200(1770±200)	720± 70(680±70)	14.3 ±1.4
1292.8±0.6	61.2 ± 6.1	67± 12(0)	87± 12(0)	58.7 ±5.9
1298.7±0.7	16.3 ± 2.0			15.5 ±2.0
1434.6±0.5	3.0 ± 0.3	107± 40(104±40)	27± 9(24±9)	1.6 ±0.2
1579.9±1.0	0.74± 0.12	...	...	0.83±0.15[d]
1607.9±0.6	2.3 ± 0.2	...	...	2.2 ±0.2
1657.2±1.0	0.12± 0.04	...	...	0.15±0.05

[a] J. S. Geiger *et al.* (Ref. 20) report $\alpha = 0.46$ for the 145.4-keV transition; this indicates a total transition intensity of 44.2±4.4 on the above scale. Although all the intensities in the table are photon intensities, the conversion coefficients for the higher-energy transitions should be small enough such that the photon and transition intensities should be nearly the same.

[b] The intensities given in parentheses are those corrected for chance coincidences.

[c] Two 0.32-cm Cu absorbers forming a sandwich around the Nd^{141} source were used for the determination of the intensity of 511-keV photons in total annihilation.

[d] After subtraction of the 1575-keV Pr^{143} contaminant peak produced by a $Pr^{141}(n,\gamma)Pr^{143}$ reaction, where the neutrons were produced predominantly in the degrading foils.

[16] R. L. Auble, D. B. Beery, G. Berzins, L. M. Beyer, R. C. Etherton, W. H. Kelly, and Wm. C. McHarris, Nucl. Instr. Methods 51, 61 (1967).

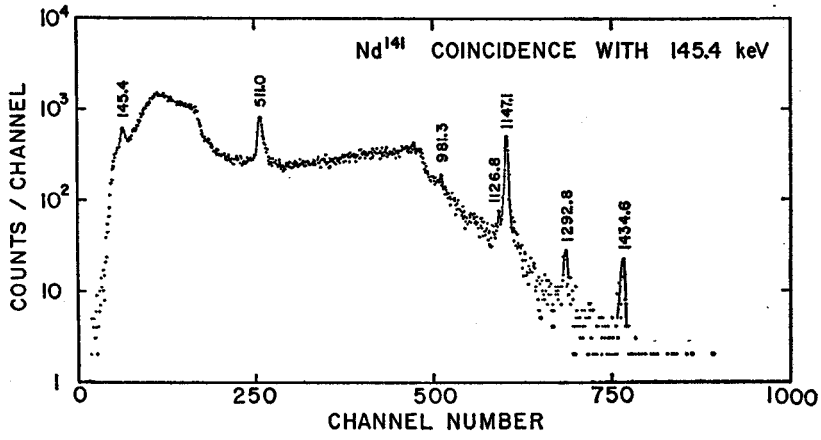

FIG. 2. Spectrum of γ rays in coincidence with the 145.4-keV γ. The gate detector was a 3×3-in. NaI(Tl) scintillator, while the signal detector was the 7-cm³ Ge(Li) crystal.

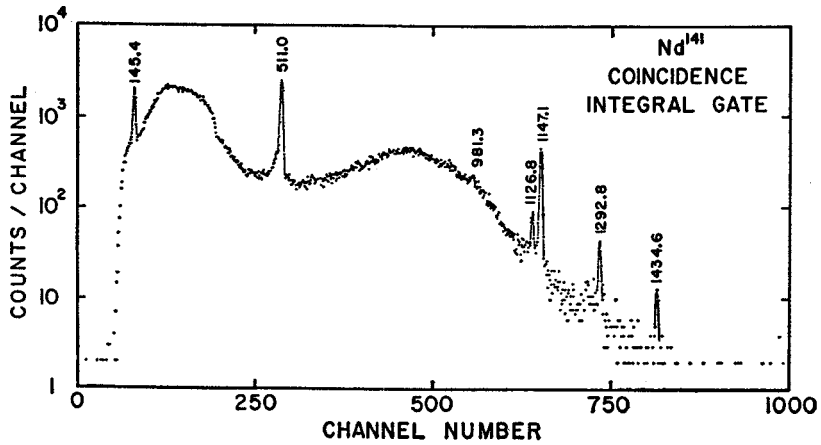

FIG. 3. Integral γ-ray coincidence spectrum. This spectrum was recorded by the 7-cm³ Ge(Li) detector in coincidence with a 3×3-in. NaI(Tl) scintillator that was set to accept all γ rays above 120 keV.

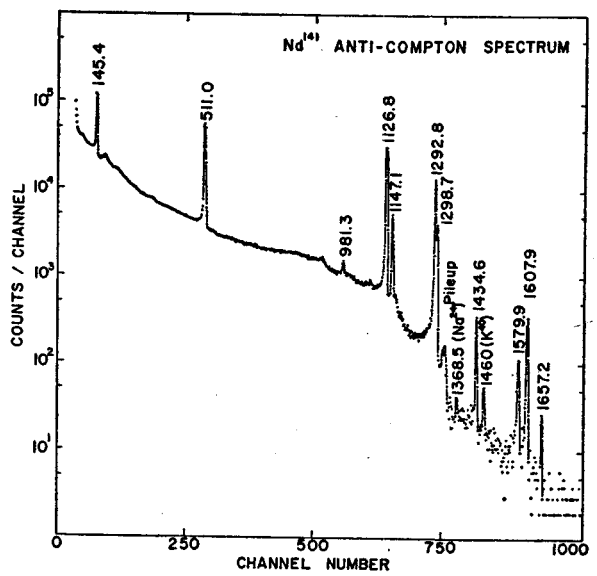

FIG. 4. Anticoincidence spectrum recorded by the 7-cm³ Ge(Li) detector when placed inside the tunnel of an 8×8-in. NaI(Tl) split annulus with a 3×3-in. NaI(Tl) detector at the other end of the tunnel. For details, see the text or Ref. 16.

Ge(Li) detector to reduce further the sharp Compton edges formed by backscattering in the Ge(Li) detector. The resulting anticoincidence spectrum is shown in Fig. 4. The intensities of all ten of the Nd^{141} γ rays, which were seen in this spectrum, are included in Table II. Only four of these γ rays, the same four indicated by the other coincidence experiments, appear to be in coincidence with another γ ray because of the large reductions in their intensities as compared with the intensities from the singles spectra.

IV. Nd^{141m} γ-RAY SPECTRA

We measured the energy of the 60-sec Nd^{141m} isomeric transition to the ground state to be 756.5±0.3, in excellent agreement with the recent work of Geiger and Graham,[17] who obtained 756.8±1.3 keV. We have also conducted a search for γ rays resulting from direct electron-capture transitions from Nd^{141m} to states of Pr^{141} and/or from alternate transitions depopulating Nd^{141m} to Nd^{141g}. Approximately 1 min after a 10-sec bombardment of Pr_2O_3 with the 9-MeV protons, a

[17] J. S. Geiger and R. L. Graham, Can. J. Phys. 45, 2281 (1967).

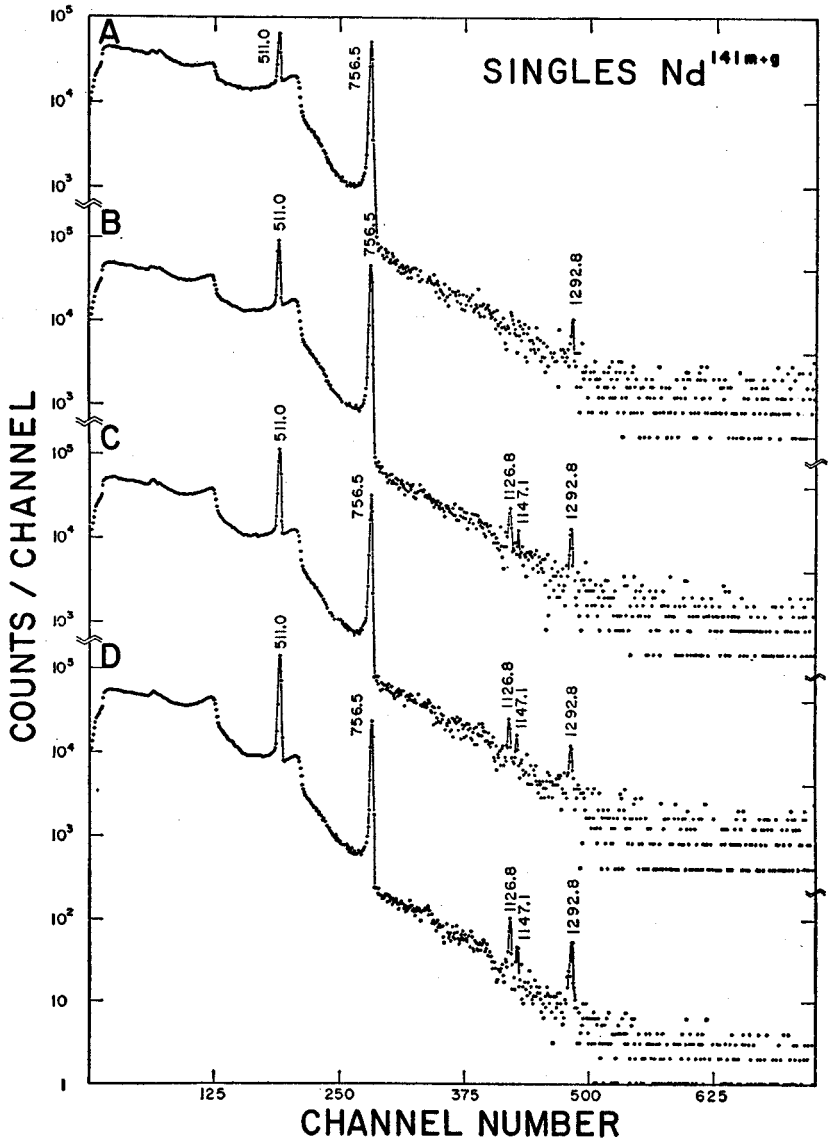

FIG. 5. Singles γ-ray spectra of Nd^{141m}+Nd^{141g}. A: The spectrum from the sum of 60 runs, each started $\approx$1 min after a 10-sec activation and lasting 59 sec. B: Same, except started 60 sec later. C: 120 sec later. D: 180 sec later.

59-sec count of the Nd^{141m}(+Nd^{141g}) spectrum was stored in the first quadrant of an analyzer having 4096 channels of memory. The Nd^{141m}(+Nd^{141g}) source was gradually moved toward the Ge(Li) detector during this time in order to maintain the analyzer dead time at approximately a constant 12%; this procedure allowed us to collect data more rapidly than with a fixed source position. Following intervals of $\approx$1 sec for switching analyzer quadrants, 59-sec counts were stored successively in the three remaining quadrants. The entire process was performed 60 times to reduce statistical errors and to search carefully for weak γ rays.

The resulting four spectra, each representing 59 min of counting time, are shown in Fig. 5. The 756.5-keV γ is clearly the only observable γ ray that decays with a 60-sec half-life. The other γ rays in Fig. 5 are the three most intense Nd^{141g} decay transitions. These spectra allow us to place an upper limit of 0.1% of the 756.5-keV γ intensity on any γ ray with an energy between 130 and 2600 keV following direct electron-capture transitions from $\frac{11}{2}$—Nd^{141m} to high-spin states in Pr^{141}; the same limit applies to alternate transitions to lower-lying states in Nd^{141}.

V. DECAY SCHEME AND DISCUSSION

The decay scheme that we were able to deduce from the foregoing measurements is shown in Fig. 6. Transition energies and excited-state energies are given in keV, the β^+ energy coming from the work of Biryukov and Shimanskaya.[5] The β^+/ϵ ratio for decay to the Pr^{141} ground state (also the limits placed for decay to the 145.4-keV state) is a calculated value, using the method of Zweifel.[18] The other transition intensities, both for

[18] P. F. Zweifel, Phys. Rev. 107, 329 (1957).

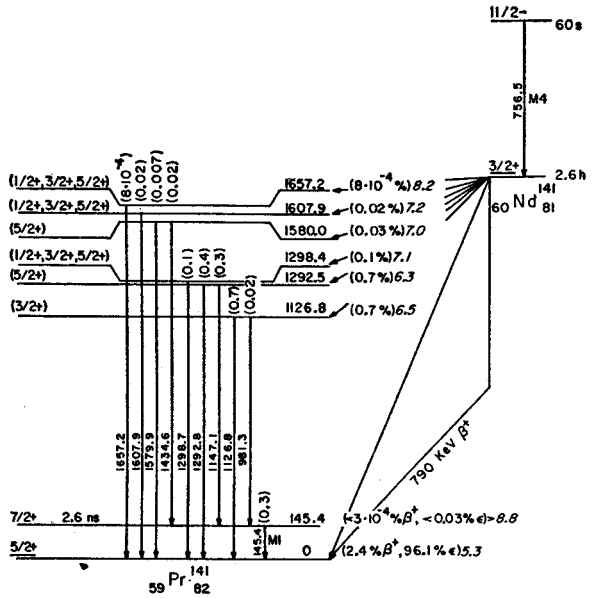

FIG. 6. Decay scheme of Nd^{141g+m}. Excited-state and γ-ray energies are given in keV. The intensities of all transitions are total transition intensities and are given in percent of the total Nd^{141g} disintegrations. Log ft values are based on a 2.6-h half-life. The spin and parity assignments to the upper six states in Pr^{141} are tentative; see text.

electron capture and for the (total) electromagnetic transitions, are adjusted to this value and read in percent of the total Nd^{141} disintegrations. Using our own measured value of 9.6 for the ratio of K x rays to 511-keV γ's, which is in good agreement with that measured by Biryukov and Shimanskaya,[5] and making reasonable assumptions about the K fluorescence yield and the ratio of K capture to capture from higher shells (see, e.g., Ref. 19), we arrived at values of 4.3%β^+ and 94.3%ϵ. However, since this is quite clearly an allowed transition, we feel there is at least as much uncertainty in our number as in the theoretical value; we have chosen the theoretical value since any needed future adjustments could be made more easily with respect to it. The log ft values were calculated on the basis of a 2.6-h half-life[5] for Nd^{141}.

The 981.3-, 1298.7-, 1434.6-, 1579.9-, 1607.9-, and 1657.2-keV γ's have not been previously reported in decay schemes. The energy of the 145.4-keV state in Pr^{141} has been well calibrated from Ce^{141} decay,[20] the photon energy being given as 145.43 keV. Our evidence for the 1126.8- and 1292.5-keV states, as well as the new state at 1580.0 keV, is based both on the coincidence results with the 145.4-keV γ and the enhancement of the 1126.8-, 1292.8-, and 1579.9-keV γ's in the anticoincidence experiment, indicating that they are ground-state transitions. The energies of these states were chosen on the basis of the best-defined γ rays depopulating them, although it can be seen that the cascade energy sum gives excellent agreement with the crossover energy in each case. The placement of states at 1298.4, 1607.9, and 1657.2 keV is based on the enhancement of the respective γ rays in the anticoincidence experiment and the fact that these γ rays were suppressed in both coincidence experiments. We saw no evidence for the state at 880 keV reported by Cybulska and Marquez.[4]

The ground-state spins of both Nd^{141} and Pr^{141} have been measured by atomic-beam methods, that of the former[21] being $\frac{3}{2}$ and the latter[22] $\frac{5}{2}$. In shell-model terms, Nd^{141} is predicted to be a $(d_{3/2})^{-1}$ neutron state, while the ground state of Pr^{141} should be a $d_{5/2}$ proton state outside a closed $g_{7/2}$ proton subshell. Thus, 98.5% of the Nd^{141} disintegrations consist of its $\frac{3}{2}+$ ground state populating the Pr^{141} $\frac{5}{2}+$ ground state directly, and the log ft value of 5.3 is about what one would expect for an allowed transition between such similar states.

Now, the 145.4-keV transition in Pr^{141} has been well characterized[20] from Ce^{141} decay as an l-forbidden $M1$ with an $E2$ admixture of 0.4 ± 0.3%, having a mean life of 2.63 ± 0.10 nsec. The state itself is presumed to have a $(g_{7/2})^{-1}(d_{5/2})^2$ configuration. This configuration forms the ground state of Pr^{143}, the $\frac{5}{2}+$ state in this nucleus[23,24] being at 57 keV, so the $\frac{5}{2}+$ and $\frac{7}{2}+$ states cross over between Pr^{143} and Pr^{141}. One would not expect the $\frac{7}{2}+$ 145.4-keV state in Pr^{141} to receive observable direct population from Nd^{141}, again in accord with our measurements.

Considering that Pr^{141} is a single-closed-shell nucleus, one encounters unexpected difficulties in characterizing its higher-lying states. Basically, the problem is as follows: Pr^{141} can be considered to be a single proton outside a Ce^{140} even-even core, so one is tempted to use the core-coupling model in describing the Pr^{141} higher-lying states. Ce^{140}, with a closed neutron shell and a closed $g_{7/2}$ proton subshell, is expected to be rather rigid and not subject to low-lying vibrations. This appears to be true, for its first excited state is a 2+ state at 1.596 MeV that decays via a nonenhanced $E2$ transition.[25] Currie,[26] in trying to account for the retardation of the $E2$ transition from a 4+ level at 2.083 MeV to this level, invoked a quasiparticle representation for both states, but his best numerical results implied a $[(g_{7/2})(d_{5/2})]_2$ configuration instead of the anticipated (and probably more likely) $[(g_{7/2})^2]_2$ or perhaps $[(d_{5/2})^2]_2$. This means that, although the Ce^{140} 2+ state

[19] A. H. Wapstra, G. J. Nijgh, and R. van Lieshout, *Nuclear Spectroscopy Tables* (North-Holland Publishing Co., Amsterdam, 1959).

[20] J. S. Geiger, R. L. Graham, I. Bergström, and F. Brown, Nucl. Phys. 68, 352 (1965).

[21] S. S. Alpert, B. Budick, E. Lipworth, and R. Marrus, Bull Am. Phys. Soc. 7, 239 (1962).

[22] P. Brix, Phys. Rev. 89, 1245 (1953); R. W. Kedzie, M. Abraham, and C. D. Jeffries, *ibid.* 108, 54 (1957).

[23] K. P. Gopinathan, M. C. Joshi, and E. A. S. Sarma, Phys. Rev. 136, B1247 (1964).

[24] D. W. Martin, M. K. Brice, J. M. Cook, and S. B. Burson, Phys. Rev. 101, 182 (1955).

[25] S. Ofer and A. Schwarzschild, Phys. Rev. 116, 725 (1959).

[26] W. M. Currie, Nucl. Phys. 48, 561 (1963).

definitely appears to be a two-quasiparticle state, its exact structure is not clear.

On the other hand, the first excited state of Ce^{142}, having only two additional neutrons, lies at 0.65 MeV and appears to be a 2+ quadrupole vibrational state.[27] The first few Pr^{143} excited states, which lie much lower than those in Pr^{141}, can probably be explained by a coupling of the $\frac{7}{2}+$ ground state and the $\frac{5}{2}+$ 57-keV state to this Ce^{142} 2+ collective state.[23,28]

The known Pr^{141} states lie at an intermediate energy, so one cannot *a priori* decide whether they are three-quasiparticle states, one-quasiparticle states coupled to a vibrational core, or perhaps a mixture of the two. Granted that the two neutrons of Ce^{142} are probably more effective in softening the Ce^{140} core than is the single proton (outside only a subshell) of Pr^{141}, one still has to be quite cautious, especially with $E2$ transition probabilities which may or may not be enhanced over the single-particle estimates. In the following, keeping in mind the different kinds of states possible, we make tentative predictions for the spins and parities of the six upper states on the basis of β- and γ-decay systematics. It must be borne in mind, however, that these are only tentative, and for quite definite assignments one needs more information about the levels. High-resolution scattering reactions of various kinds that populate these states would be particularly valuable.

The logft values are all more or less in the range expected for allowed transitions. One cannot exclude first-forbidden decay, especially to the highest-lying states, on the basis of the logft values, but then the only negative-parity states would be those resulting from the $h_{11/2}$ shell-model state or from octupole vibrations. The $d_{3/2}$ ground state of Nd^{141} should not populate the former, although the $h_{11/2}Nd^{141m}$ might. The latter have not been reported near this excitation in any of the neighboring even-even nuclei. Thus, one can reasonably say that all six states are probably $\frac{1}{2}+$, $\frac{3}{2}+$, or $\frac{5}{2}+$. This set is consistent with either interpretation of the states—by coupling the $\frac{5}{2}+$ or $\frac{7}{2}+$ single-quasiparticle states to a 2+ vibrational core, one can get $\frac{1}{2}+$ through $\frac{11}{2}+$, with two sets of $\frac{3}{2}+$ through $\frac{9}{2}+$ states, and on the basis of three quasiparticles, the range is even broader.

Assignments for the three states that exhibit γ-ray branching can be narrowed down from the above limits. The intensity ratio of the 1126.8-keV γ to the 981.3-keV γ from the 1126.8-keV state is 35. The mere existence of the 981.3-keV γ rules out a $\frac{1}{2}+$ assignment, for such would force the 981.3-keV transition to be $M3$. For a $\frac{5}{2}+$ assignment, the single-particle estimate[19] yields a ratio (both $M1$'s) of less than 2, while for a $\frac{3}{2}+$ it predicts a ratio ($M1/E2$) of about 200. Even a slight $E2$ enhancement or $M1$ retardation would thus favor a $\frac{3}{2}+$ assignment.

For the 1292.5- and 1580.0-keV states, which have ground-state–to–cascade ratios of 1.33 and 0.35, respectively, we can similarly eliminate the $\frac{1}{2}+$ assignment. And, unless there is some quite gross $M1$ retardation or $E2$ enhancement, we can also eliminate the $\frac{3}{2}+$, so we favor a $\frac{5}{2}+$ assignment.

The 756.5-keV excited state of Nd^{141} has been shown to have a half-life of 60.3 ± 1.0 sec.[17] It is one of the series of $h_{11/2}$ isomers found just below the $N=82$ shell. Since the $\frac{11}{2}-$ (presumably single-quasiparticle $h_{11/2}$) state lies[29] at 822 keV in Pr^{139}, it is quite conceivable that the same state lies in the 1-MeV vicinity in Pr^{141} and there could be some direct population of it from Nd^{141m}. From the data displayed in Fig. 5, however, it can be deduced that such population must be less than 0.1% of the intensity of the 756.5-keV isomeric γ ray. Depending on the exact location of the $h_{11/2}$ state in Pr^{141}, this upper limit means merely that the logft for electron capture has to be greater than approximately 6.0. We can place the same upper limit on any branching γ decay to lower states in Nd^{141} itself, provided that at least one γ ray having an energy greater than 130 keV is involved.

ACKNOWLEDGMENTS

We are indebted to K. Kosanke, R. Eppley, and R. Doebler for assistance with the data acquisition, to R. Goles for assistance with the ion-exchange apparatus and experiments, to Dr. G. Berzins for help with computer programs and for fabrication of the 7-cm³ Ge(Li) detector, to Dr. W. P. Johnson for help with operation of the Michigan State University cyclotron, and to Dr. C. R. Gruhn for direction of the Ge(Li) detector development program at Michigan State University.

[27] W. V. Prestwich and T. J. Kennett, Phys. Rev. **134**, B485 (1964).

[28] K. P. Gopinathan, Phys. Rev. **139**, B1467 (1965).

[29] K. Ya. Gromov, A. S. Danagulyan, L. N. Nitityuk, V. V. Murav'eva, A. A. Sorokin, M. Z. Shtal', and V. A. Shpinel', Zh. Eksperim. i Teor. Fiz. **47**, 1644 (1964) [English transl.: Soviet Phys.—JETP **20**, 1104 (1965)].

3.A

Nuclear Physics **A123** (1969) 649—663;

THE STATES OF ^{117}Sn

D. B. BEERY

Cyclotron Laboratory †, *Department of Physics, Michigan State University, East Lansing, Michigan, USA, 48823*

and

G. BERZINS ††

Cyclotron Laboratory †, *Department of Physics, Michigan State University, East Lansing, Michigan, USA, 48823*

and

Los Alamos Scientific Laboratory †††, *University of California, Los Alamos, New Mexico, USA*

and

W. B. CHAFFEE and W. H. KELLY

Cyclotron Laboratory †, *Department of Physics, Michigan State University, East Lansing, Michigan, USA, 48823*

and

Wm. C. McHARRIS

Department of Chemistry ‡

and

Cyclotron Laboratory †, *Department of Physics, Michigan State University, East Lansing, Michigan, USA, 48823*

Received 16 September 1968

Abstract: Gamma rays emitted in the decay of 2.8 h ^{117}Sb have been investigated with 2.5 to 45 cm^3 Ge(Li) detectors. Gamma rays of energies (and relative intensities) 158.5 (99.6), 553.2 (0.07), 846.2 (0.04), 861.7 (0.29), 1004.5 (0.22), 1020.6 (0.09), 1021.0 (0.10), 1287.6 (0.026), 1339.5 (0.009), 1420.1 (0.016), 1446.4 (0.051) and 1578.0 (0.018) keV have been observed. On the basis of energy sums, relative intensities and two-dimensional Ge(Li)-Ge(Li) coincidence experiments, states are placed in ^{117}Sn at 0 ($\frac{1}{2}^+$), 158.5 ($\frac{3}{2}^+$), 711.7 ($\frac{7}{2}^+$), 1004.5 ($\frac{3}{2}^+$), 1020.2 ($\frac{5}{2}^+$), 1179 ($\frac{5}{2}^+$), 1446.4 ($\frac{3}{2}^+$, $\frac{5}{2}^+$), 1498.0 ($\frac{5}{2}^+$, $\frac{3}{2}^+$) and 1578.3 keV ($\frac{5}{2}^+$, $\frac{3}{2}^+$). The spin assignments and limits have been made on the basis of log *ft* values and relative photon intensities from ^{117}Sb decay, which were aided in some cases by ^{117}In decay, and also by information gleaned from nuclear reaction data. The structures of the states are discussed in terms of current nuclear models, and the behavior of these states is followed as a function of neutron number.

E

RADIOACTIVITY ^{117}Sb [from ^{117}Sn(p, n) and ^{116}In(α, 2n)] and ^{117}In [from ^{116}Cd(n, γ)]; measured E_γ, I_γ, γγ-coin. ^{117}Sn deduced levels, J, π. Enriched ^{117}Sn target; Ge(Li) detectors.

† Work supported in part by the U.S.National Science Foundation.

†† Present address: Los Alamos Scientific Laboratory, Los Alamos, New Mexico, USA.

††† Operated under the auspices of the U.S. Atomic Energy Commission.

‡ Work supported in part by the U.S. Atomic Energy Commission.

1. Introduction

As a result of a recent study of (d, p) reactions on ^{116}Sn, levels in ^{117}Sn have been reported [1]) at 0.16, 0.32, 0.72, 1.03, 1.19, 1.31, 1.51, 1.59 and 1.67 MeV, with additional levels at 2.06 MeV and higher energies. These levels and possibly some additional ones have also been populated by (p, p′) reactions [2]). The lowest two of these excited states have been the subject of several γ-ray and conversion-electron studies [3-9]) of the decay of 14.0 d ^{117m}Sn. The third state has been observed following 1.93 h ^{117m}In decay [10-15]). Coulomb excitation has populated [16-17]) levels at 1004 and 1019 keV. Various combinations of these states have also been observed following (d, t), (p, d) and (t, d) reactions (refs. [1,2,18]), respectively).

In previous ^{117}Sb decay scheme studies, only the 158.5 keV state has been reported [10,19,20]) to be populated. Since the disintegration energy for ^{117}Sb decay is [10]) 1790±30 keV one might expect some of the other higher-lying ^{117}Sn levels also to be populated from its electron-capture decay. For this reason and as a part of a study of the odd-mass isotopes of Sn, we initiated this investigation. As a result, 12 γ-rays have been placed in a decay scheme that includes the population of eight excited states in ^{117}Sn. We also briefly investigated the decay of $^{117g+m}$In to confirm the assignment of one of the new γ-rays following ^{117}Sb decay.

Somewhat more complete information is available about the states in this region than in many regions of the nucleidic chart. Consequently, we are able not only to follow the progression of states from one Sn nucleus to another but also to have some insight in describing the composition of many of the states in ^{117}Sn.

2. Source preparation

The ^{117}Sb sources were prepared initially by the ^{117}Sn(p, n)^{117}Sb reaction;, SnO_2 powder (enriched to 78.8 % ^{117}Sn) was bombarded with protons from the Michigan State University sector-focused cyclotron. These protons were degraded from higher energies to energies between 5 and 13 MeV by the use of Al absorbers. Typically, ≈ 100 mg targets were bombarded with a 1 μA beam for 1 h. The enriched SnO_2 (obtained from Isotope Division, Oak Ridge National Laboratory) was specified to contain 8.03±0.05 % ^{118}Sn, 7.19±0.05 % ^{119}Sn, 2.84±0.05 % ^{120}Sn, 2.57±0.05 % ^{116}Sn, 0.24±0.02 % ^{122}Sn and <0.25 % of any other contaminant isotope. Chemical separations were not performed because the competing γ-rays were clearly identified to be primarily from other Sb isotopes in expected quantities and with half-lives clearly distinguishable from the 2.8 h ^{117}Sb.

Sources of ^{117}Sb were also prepared by bombarding natural In_2O_3 with ≈ 22 MeV α particles from the Michigan State University cyclotron. These sources appeared to contain fewer contaminant isotopes and confirmed all the ^{117}Sb γ-rays.

The ^{117}In sources were prepared by the β^- decay of ^{117}Cd, which had been made by bombarding natural Cd targets with neutrons produced by 25 MeV protons

stopped in Al. The ^{117}In activity was identified by its characteristic growth and decay [21]).

Some sources for multi-parameter coincidence experiments were prepared by bombarding the same samples of SnO_2 (enriched to 78.8 % ^{117}Sn) with $\approx$ 5.5 MeV protons in the Los Alamos cyclotron. Because the (p, n) reaction thresholds [22]) of neighboring ^{116}Sn and ^{118}Sn are approximately 2.5 MeV higher than the 2.5 MeV threshold in ^{117}Sn, the relative amounts of ^{116}Sb and ^{118}Sb activities produced at this proton energy were found to be very small.

3. Gamma-ray spectra

3.1. SINGLES SPECTRA

Six Ge(Li) detectors were used in this investigation to determine the energies and intensities of the γ-rays that depopulate the excited states of ^{117}Sn. The active volumes of these detectors ranged from 2.5 to 45 cm^3. Our best system resolution was 1.8 keV FWHM for the 661.6 keV γ-ray of ^{137}Cs. The apparatus used for counting included room-temperature FET preamplifiers, low-noise RC linear amplifiers with pole-zero compensation and 1024- or 1600-channel pulse-height analysers.

In order that activities decaying with different half-lives could be identified, spectra were recorded periodically as the sources aged. The energies of the γ-rays were measured by counting the ^{117}Sb sources simultaneously with a number of well-known calibration sources, which are listed in table 1. Following subtraction of an

TABLE 1

Gamma rays used as energy standards

Nucleide	γ-ray energy (keV)	Ref.
^{57}Co	121.97 $\pm$0.05	[23])
^{57}Co	136.33 $\pm$0.04	[23])
^{139}Ce	165.84 $\pm$0.03	[23])
^{203}Tl	238.61 $\pm$0.01	[23])
^{203}Tl	583.139$\pm$0.023	[24])
^{137}Cs	661.595$\pm$0.076	[25])
^{60}Co	1173.226$\pm$0.040	[24])
^{60}Co	1332.483$\pm$0.046	[24])
^{24}Na	1368.526$\pm$0.044	[24])
^{208}Tl (D.E.)	1592.46 $\pm$0.10	[24])
^{24}Na (D.E.)	1731.91 $\pm$0.012	[24])
^{208}Tl (S.E.)	2103.46 $\pm$0.10	[24])
^{208}Tl	2614.47 $\pm$0.10	[24])

interpolated background from under each peak, a least-squares fit was performed which related the centroids of the energy-calibration peaks to a quadratic calibration curve. Energies corresponding to the centroids of unknown peaks were calculated from the calibration curve. The energies of weak ^{117}Sb γ-rays, which were obscured by the calibration standards, were determined by using the well-determined energies

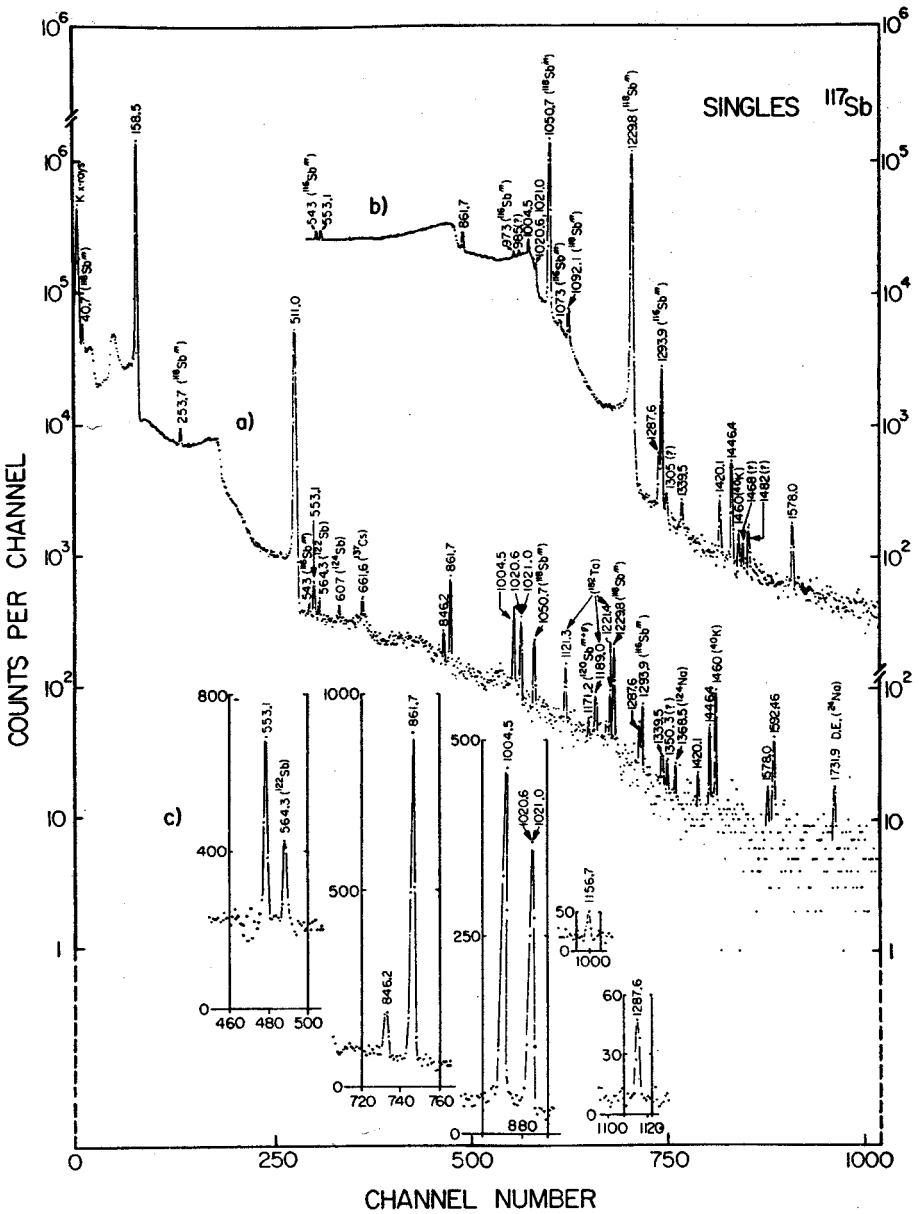

Fig. 1. Singles γ-ray spectra of ^{117}Sb decay to levels in ^{117}Sn. (a) Recorded with a 7 cm^3 Ge(Li) detector at MSU following a ^{117}Sn(p, n)^{117}Sb reaction. Peaks resulting from Sb isotopes other than ^{117}Sb are labeled, as are those from other impurities. The ^{182}Ta peaks were not observed in our earlier runs and apparently result from an (n, γ) reaction on ^{181}Ta, which somehow was introduced into our ^{117}Sn target before this last highest-resolution run. (b) Recorded with a 7 cm^3 Ge(Li) detector at MSU following an ^{115}In(α, 2n)^{117}Sb reaction. (c) Portions of spectra recorded with a 2.5 cm^3 Ge(Li) detector at LASL following a ^{117}Sn(p, n)^{117}Sb reaction (linear scales).

of the stronger γ-rays as internal standards. Some typical γ-ray singles spectra are shown in fig. 1.

A list of the energies and relative intensities of the ^{117}Sb γ-rays that were observed is given in table 2. Some well-defined γ-rays from the decay of other Sb isotopes are also included for reference. The energies assigned are mean values taken from a number of different measurements recorded under different conditions. The corresponding uncertainties in energies are based on the reproducibility of both the standard energies and the unknown decay energies from the calibration curves, the

TABLE 2
Energies and relative intensities of gamma-rays observed in ^{117}Sb spectra

Measured γ-ray energy (keV)	Relative intensity [a]	Parent [b]
26 (K X-rays)	$23\pm6\times10^3$	Sb isotopes (primarily ^{117}Sb)
158.5±0.2	$30\pm5\times10^3$	^{117}Sb
196.8±0.5		^{120g}Sb
253.7±0.3		^{118m}Sb
511.0($\gamma^{\pm}$)		Sb isotopes (primarily ^{117}Sb)
553.1±0.3	23±3	^{117}Sb
565.0±0.4		^{122}Sb
846.2±0.7	15±2	^{117}Sb
861.7±0.5	≡100	^{117}Sb
931.8±0.7		^{116g}Sb
1004.5±0.5	78±10	^{117}Sb
1020.6±0.5 [c]	33±6	^{117}Sb
1021.0±0.5 [c]	36±6	^{117}Sb
1022.7±0.8		^{120g}Sb
1050.7±0.3		^{118m}Sb
1092.1±0.8		^{116m}Sb
1156.7±0.4	7±3	^{117}Sb?
1171.2±0.9		$^{120m+g}$Sb
1203.9±0.4 (2225.9DE)		^{116}Sb
1229.8±0.3		^{118m}Sb
1287.6±0.3	9.2±2.0	^{117}Sb
1293.9±0.4		$^{116m+g}$Sb
1339.5±1.0	3±1	^{117}Sb
[1368.5±0.4 [d])		^{24}Na]
1420.1±0.4	5.7±2.0	^{117}Sb
1446.4±0.5	18±5	^{117}Sb
1578.0±0.3	6.2±2.0	^{117}Sb
[1731.9±0.12 [d]) (2753.92DE)		^{24}Na]
2225.9±0.4		^{116g}Sb

[a]) Relative intensities are listed only for ^{117}Sb γ-rays.

[b]) Determined from the following known half-lives: ^{116g}Sb (60 min), ^{116m}Sb (15 min), ^{117}Sb (2.8 h), ^{118m}Sb (5.1 h), ^{120g}Sb(5.8 d), ^{120m}Sb (15.9 min), ^{122}Sb (2.8 d) and ^{24}Na (15.0 h).

[c]) This doublet was resolved with the aid of coincidence spectra; the 1021.0 keV γ-ray is in coincidence with the 158.5 keV γ-ray, whereas the 1020.6 keV γ-ray was not found to appear in coincidence spectra.

[d]) Observed in sources that had aged for longer than three half-lives of ^{117}Sb.

sizes of the photopeaks relative to the underlying background and the quoted errors of the standard energies listed in table 1.

The relative intensities obtained are also averages from a number of measurements. Relative photopeak efficiency curves for the Ge(Li) detectors were obtained in two ways. First, a set of standard γ-ray sources whose relative intensities had been measured with NaI(Tl) detectors was used. Second, a set of points was obtained from sources emitting several γ-rays whose relative intensities were well known from established decay schemes. The efficiency curves resulting from the two methods were in very good agreement. The uncertainties in γ-ray intensities listed in table 2 include uncertainties in the peak areas and in the efficiency curves.

A 2.5 cm × 3.8 cm ø NaI(Tl) detector with a thin Be window was used to measure the ratio of the intensities of the K X-rays and the 158.5 keV γ-rays following ^{117}Sb decay.

A basic cause of experimental difficulties encountered in the study of ^{117}Sb decay is that the 158.5 keV γ-ray is $\geqq$ 300 times as intense as any of the other γ-rays following ^{117}Sb decay. This means that the higher-energy γ-rays are weak enough that they can be concealed easily by the more intense γ-rays from almost any of the other radioactive Sb isotopes that may be present as contaminants. Some of these stronger γ-rays from Sb isotopes other than ^{117}Sb are identified in fig. 1 and listed in table 2. Graded lead absorbers were used with strong sources in order to obtain an adequate number of counts in the higher-energy region of the spectra. The relative intensities of the higher-energy photons were determined after corrections for the absorbers had been made.

The weak 553.2±0.3 keV γ-ray seen in fig. 1 was found to decay with the half-life of ^{117}Sb and was suspected to be identical with the 553 keV transition reported[10-15]) to depopulate the 711 keV state of ^{117}Sn following the decay of ^{117}In. To confirm this, we obtained clear coincidence evidence described in subsect. 3.2 and also carefully measured the energy of the 553 keV γ-ray following the decay of ^{117}In. In ten distinct calibration experiments, the energy observed was 553.1±0.2 keV compared with 553.2±0.3 keV for the γ-ray following ^{117}Sb decay. We conclude that these photons arise from the same transition in ^{117}Sn.

3.2. COINCIDENCE RESULTS

Coincidence experiments were performed at Los Alamos with a Ge(Li)-Ge(Li) spectrometer. The two detectors employed had active volumes of 30 cm^3 and 45 cm^3 and resolutions of approximately 2.7 keV FWHM at 661.6 keV. The detectors were oriented with their axes collinear, but the sources were moved slightly off axis in order to reduce the coincidence count rate from annihilation radiation.

Because of the 2.8 h half-life, several freshly prepared sources were used in succession. Each source was counted for approximately two half-lives. Over 7×10^5 coincidence events were accumulated over a 2d period. During the experiment, the average count rate from random events was found to be negligible.

The data were recorded in a two-dimensional mode, stored on magnetic tape and analysed with the aid of a computer. The pulses from the detectors were passed through amplifiers that employed pole-zero cancellation to minimize the resolution deterioration due to high count rates. The bipolar signals from these amplifiers were used to drive the logic circuitry, while the unipolar pulses were analysed by two 1600-channel analog-to-digital converters. Crossover timing was employed, and the resolving time (2τ) of the coincidence circuit was approximately 120 nsec.

The high resolution of the two detectors allowed the coincidence relationships to be determined unambiguously. Gate regions were selected on each side of the coincidence matrix. The proper coincidence relationships were identified by subtracting appropriately normalized spectra coincident with adjacent background regions from the spectra gated by the γ-rays of interest; this allowed us to reduce the effects caused by the underlying Compton distributions.

TABLE 3

Gamma-gamma coincidence relationships observed in the decay of ^{117}Sb

γ-ray in gate (keV)	Coincident γ-ray (keV)
158	511, 553, 846, 862, 1021, 1288, 1339 [a], 1420
511	158, 511, 669 [b]
553	158
847	158
862	158
1021	158

[a]) Very low intensity; existence not conclusive.
[b]) Sum peak.

The results of the coincidence experiment are summarized in table 3. The particular spectrum in coincidence with the 158.5 keV photons is shown in fig. 2.

4. Decay scheme of ^{117}Sb

The decay scheme that we were able to deduce from the foregoing measurements is shown in fig. 3. Transition energies and excited-state energies are given in keV, the β^+ energy coming from the work of McGinnis [10]). The β^+/ε ratio for decay to the ^{117}Sn 158.5 keV state is a calculated value, obtained using the method of Zweifel [26]). All transition intensities for β^+ and ε-decay and for the (total) electromagnetic transitions are given in percent of the total ^{117}Sb disintegrations.

Only the 158.5 keV transition has been reported previously in published ^{117}Sb decay-scheme studies [10,19,20]). The energies of the first and second excited states of ^{117}Sn have been carefully measured in the recent study of ^{117m}Sn decay by Bocquet *et al.* [9]). Their measurements indicate energies of 158.6±0.1 and 314.6±0.1 keV. Precision has been extended in the measurement of the energy of the first excited state by Bäcklin *et al.* [27]), who report 158.50±0.10 keV. Excellent agreement is seen with

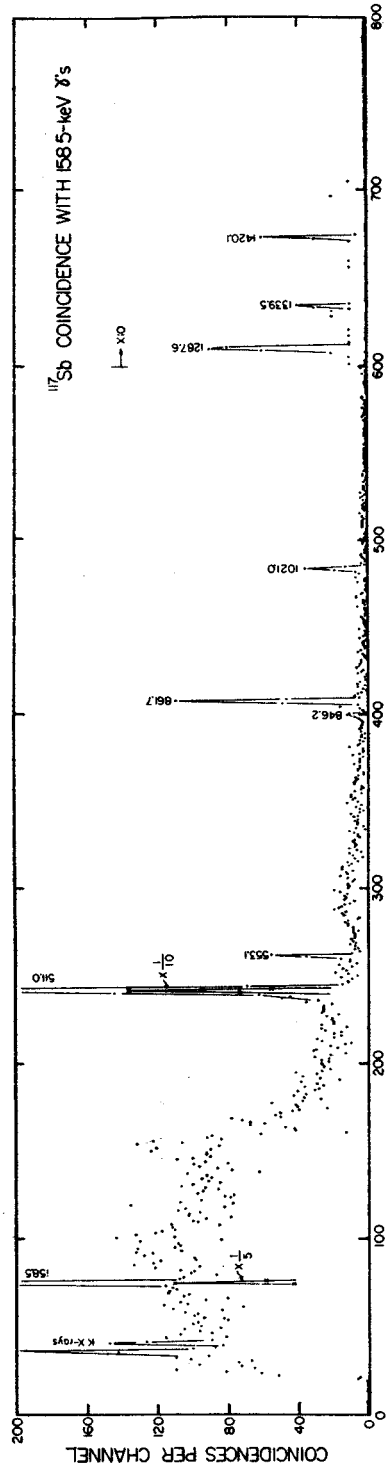

Fig. 2. Spectrum of γ-rays in coincidence with the 158.5 keV γ-ray. The active volumes of the gate and signal Ge(Li) detectors were 45 and 30 cm^3, respectively. Coincident events with the background regions of each side on the 158.5 keV photopeak have been normalized and subtracted to correct for the underlying Compton background.

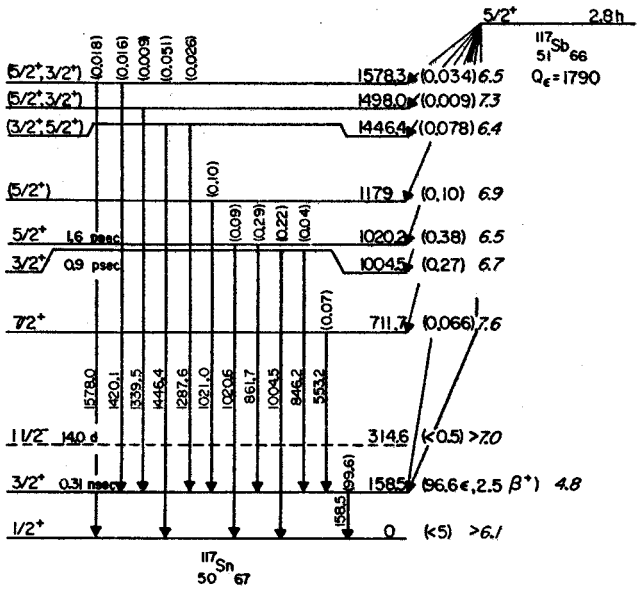

Fig. 3. Proposed decay scheme of ^{117}Sb. The intensities listed are transition intensities and are given in percent of the total ^{117}Sb disintegrations.

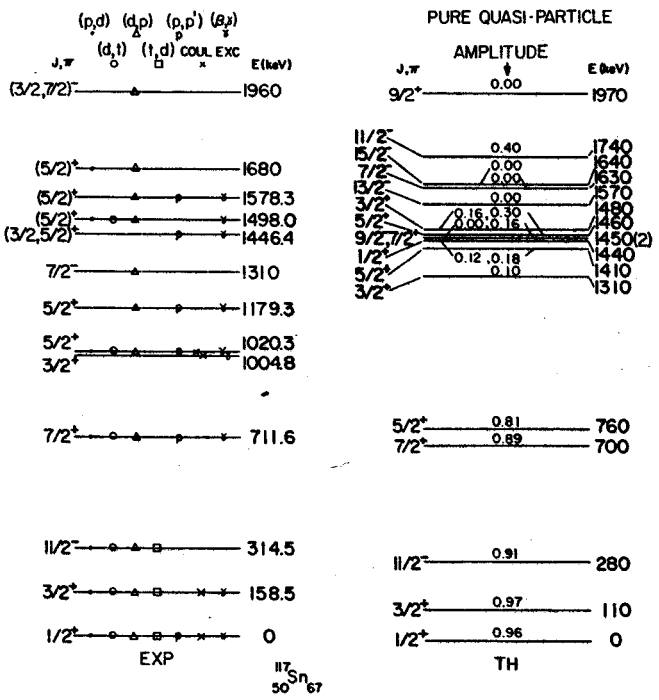

Fig. 4. Levels of ^{117}Sn observed in this and other recent studies (left) compared with the calculated levels of Sorensen [31]) (right). The quasi-particle amplitudes are listed for each calculated state.

our measurement of 158.5 ± 0.2 keV for the energy of the γ-ray depopulating the first excited state. This state has been found [8]) to have a mean life of 0.31 ± 0.03 nsec, with the 158.5 keV transition being an *l*-forbidden M1 with an upper limit of 0.4 % E2 admixture [7]). The M1 transition probability is reduced by a factor of 15 from the single-particle estimate [17]).

We observed seven γ-rays in coincidence with the 158.5 keV γ-ray, as shown in fig. 2. Each of the seven states indicated by these coincidences has been populated by one or more reactions, which we show in fig. 4; therefore these states are included with reasonable certainty in our level scheme. The cross-over transition was observed for four of the seven states. We saw no evidence for the population by ^{117}Sb of the $\frac{11}{2}^-$ isomeric state at 314.6 keV and can place an upper limit of 0.5 % on any such population.

The 711.7 keV state of ^{117}Sn has been observed by a number of workers [10-15]) to be the state that is populated by the β^- decay of the 44 min $\frac{9}{2}^+$ ground state of ^{117}In. Now, the ground state of ^{117}Sn has a measured [28]) spin of $\frac{1}{2}$ and a magnetic moment of -0.99983 n.m., which strongly suggests an $s_{\frac{1}{2}}$ state. Based on this assignment, coincidences and angular distributions between the 158.5 and 553.2 keV γ-rays indicate unique spins [14,15]) of $\frac{1}{2}^+$, $\frac{3}{2}^+$ and $\frac{7}{2}^+$ for the 0, 158.5 and 711.7 keV states, respectively. We observed the 553.2 keV γ-ray following the decays of both ^{117}In and ^{117}Sb as mentioned before and following the decay of the latter in coincidence with the 158.5 keV γ-ray. The absence of a crossover transition to the ground state is, of course, consistent with the $\frac{7}{2}^+$ assignment for the 711.7 keV state. It is also interesting to note that Walters *et al.* [29]) working from the decay of ^{117}In have recently observed a 394 keV γ-ray leading from the 711.7 keV state to the 314.6 keV isomeric state and report its intensity to be $\approx 10^{-4}$ of the intensity of the 553.2 keV γ-ray. This is consistent with our finding no evidence for the population of the $\frac{11}{2}^-$ isomeric state from the decay of ^{117}Sb, for the intensity of the 394 keV γ-ray would be well below our limits of detection.

The states at 1004.5 and 1020.2 keV were placed on the basis of their crossover and cascade transitions, the latter being observed in coincidence with the 158.5 keV γ-ray. It should be noted that part of the 1021 keV photopeak was found to be in coincidence with the 158.5 keV γ-ray, indicating two γ-rays at almost this same energy. This makes our intensity determination for the 1020.6 keV transition somewhat less precise than those for most of the other transitions. Accordingly, the energy of the 1020.2 keV state was determined from the sum of the energies of the coincident 158.5 and 861.7 keV γ-rays.

Coulomb excitation of ^{117}Sn has also been seen to populate the 1004.5 and 1020.2 keV states, which decay with mean lives of 0.9 ± 0.3 psec and 1.6 ± 0.5 psec, respectively [16]). From the Coulomb excitation studies, the states were assigned $\frac{3}{2}^+$ and $\frac{5}{2}^+$. After correcting for the 1021.0 keV γ-intensity, our results agree with the relative intensities of cascade to crossover γ-rays from these two levels as observed following the Coulomb excitation. Although superficially one might expect the

846.2 keV γ-ray to compete a little more evenly with the 1004.5 keV γ-ray, both are retarded over the single-particle estimates for M1 transitions, and it is difficult to make quantitative comparisons or predictions without further knowledge about the internal structure of the 1004.5 keV state. The $\frac{3}{2}^+$ assignment for this state is thus quite satisfactory. We also adopt the $\frac{5}{2}^+$ assignment for the 1020.2 keV state. The relative intensities of the 861.7 and 1020.6 keV γ-rays are approximately what one would expect for an M1 and E2 transition, respectively.

The previous studies [10,19,20]) of ^{117}Sb decay tentatively gave it a ground-state assignment of $\frac{5}{2}^+$, thus indicating a $d_{\frac{5}{2}}$ quasi-particle state for its 51st proton. This assignment is consistent with the other nearby odd-mass Sb isotopes, which also appear to have $\frac{5}{2}^+$ ground states. In ^{117}Sb decay to ^{117}Sn, this assignment was suggested by the low log ft value of 4.8 for population of the $\frac{3}{2}^+$ first excited state and the absence of observable population to the $\frac{1}{2}^+$ ground state. The weakness of the electron-capture transition to the 711.7 keV $\frac{7}{2}^+$ state (log ft = 7.6), even though it apparently is an allowed transition, could be ascribed to the fact that it involves an l-forbidden decay of a $d_{\frac{5}{2}}$ proton to a $g_{\frac{7}{2}}$ neutron – but the $g_{\frac{7}{2}}$ neutron subshell is already filled in ^{117}Sb; therefore a multi-particle re-arrangement may be necessary in addition to the fact that it is an l-forbidden transition. Recently the ground-state spin of ^{117}Sb has been measured [30]) to be $\frac{5}{2}$, which further corroborates the $d_{\frac{5}{2}}$ assignment.

Our findings on the decay of ^{117}Sb to the 1004.5 keV $\frac{3}{2}^+$ and 1020.2 keV $\frac{5}{2}^+$ states lend further support to the assignments for all three states. Both log ft values are consistent with allowed transitions. Although one cannot completely rule out first-forbidden transitions, they would appear to be quite unlikely, especially since these two daughter states are probably not simple one-quasi-particle states (see sect. 5). Also, there are no likely odd-parity shell-model states available for the ground state of ^{117}Sb, and even if one could concoct such a state to populate the $\frac{3}{2}^+$ and $\frac{5}{2}^+$ states by first-forbidden transitions, he would immediately find contradictions in the populations of the lower-lying states. A similar argument holds for possible odd-parity assignments for the 1004.5 and 1020.2 keV states; attempts at such assignments lead to contradictions in the remainder of the decay scheme.

Schneid *et al.* [1]) observed a state at 1.9 MeV with a (d, p) reaction and one at 1.18 MeV with a (d, t) reaction. Yagi *et al.* [2]) observed one at 1.17 MeV with a (p, d) reaction. In all three experiments, this state was deduced to be $\frac{5}{2}^+$. Yagi *et al.* [2]) may also have seen this state in the inelastic scattering of protons; however, it was not completely resolved from closely spaced surrounding states, and they quoted its energy as 1.22 MeV. The 1021.0 keV component of the 1021 keV photopeak, which we observed to be in coincidence with the 158.5 keV γ-ray, appears to depopulate a level at 1179 keV. Although our own results are not conclusive as to the spin and parity of this level, it could very well be the same $\frac{5}{2}^+$ state seen in the reactions studies. The log ft value of 6.9 is consistent with this assignment, and, considering the low intensity of the 1021.0 keV γ-ray (apparently M1), it is quite reasonable

that we did not see the even weaker ground-state transition, which would, with this assignment, be an E2. Thus, we tentatively assign the 1179 keV state $\frac{5}{2}^+$.

We could not make definite assignments for the states at 1446.4, 1498.0 and 1578.3 keV. The placement of states at these energies, however, is fairly certain because of the coincidence relationships with the 158.5 keV γ-ray. Because each of these states is fed by what may well be an allowed transition, the first choice of spins and parities would be $\frac{3}{2}^+$, $\frac{5}{2}^+$ or $\frac{7}{2}^+$. The value $\frac{7}{2}^+$ can be ruled out immediately for the 1446.4 and 1578.3 keV states because they decay to the $\frac{1}{2}^+$ ground state. It should be noted that a number of $\frac{5}{2}^+$ and/or $\frac{3}{2}^+$ states have been seen at approximately these excitations in the aforementioned nuclear reactions (cf. fig. 4). Although the assignments were not so definite as for the lower-lying states, there did not appear to be any $\frac{7}{2}^+$ states. On the basis of γ-ray branching, there might be a slight preference for the $\frac{3}{2}^+$ assignment for the 1446.4 keV state, but, on the other hand, the γ-ray branching from the 1578.3 keV state is not explainable on the basis of a naïve single-particle analysis; therefore one again should know more about the internal structures of these states before making serious deductions based on the γ-ray branching. On the basis of the reactions assignments [1,2]), aided by the observed γ-rays and the deduced log ft values, we list the possibilities ($\frac{3}{2}^+$, $\frac{5}{2}^+$) for the 1446.4 keV state and ($\frac{5}{2}^+$, $\frac{3}{2}^+$) for the other two.

5. Discussion of the states in ^{117}Sn and other odd-mass Sn isotopes

In fig. 4 we also compare the experimentally observed levels in ^{117}Sn with the levels predicted by Sorensen [31]). His intermediate-coupling calculation used wave functions that were linear combinations of pure quasi-particle, quasi-particle plus single phonon and (with small amplitudes) quasi-particle plus two-phonon configurations. In this it was an improvement over the earlier Kisslinger and Sorensen [32]) calculations. The magnitude of the pure quasi-particle amplitude is listed with each state in fig. 4.

The lowest five predicted states are seen to be fairly pure quasi-particle states, and they correspond to all the available single-particle states between $N = 51$ and $N = 82$, namely $s_{\frac{1}{2}}$, $d_{\frac{3}{2}}$, $h_{\frac{11}{2}}$, $g_{\frac{7}{2}}$ and $d_{\frac{5}{2}}$. For the heavier Sn isotopes, the $g_{\frac{7}{2}}$ and $d_{\frac{5}{2}}$ states are found to be strongly mixed and shifted, and even in ^{117}Sn it can be seen that particularly the $d_{\frac{5}{2}}$ state is becoming fragmented with a good portion of its amplitude going to the $\frac{5}{2}^+$ state predicted to lie at 1460 keV. This leaves the 760 keV $\frac{5}{2}^+$ state with considerable collective character.

The observed $\frac{1}{2}^+$ ground state, 158.5 keV $\frac{3}{2}^+$ state and $\frac{11}{2}^-$ isomeric state show every indication of being the rather pure quasi-particle states predicted. The 158.5 keV l-forbidden M1 transition and its lack of appreciable E2 admixing, for example, confirms the single-particle nature of the states it connects [7,8]). And the 156.1 keV M4 transition seen in the decay of ^{117m}Sn appears to proceed at the expected single-particle rate, although this, of course, is less a test of collective character than a test of spurious single-particle admixtures [9]).

The 158.5 and 314.6 keV states also were strongly excited by the ^{116}Sn(t, d)^{117}Sn reaction [18]) even more strongly than the ground state. This corroborates the single-neutron character of these states. Although the 158.5 keV state was reached by Coulomb excitation [17]), the B(E2) was hindered by a factor of 15, thus confirming the lack of appreciable collective character in this state.

The 711.6 keV $\frac{7}{2}^+$ state would appear also to be a fairly pure single-quasi-particle state. The principal evidence for this is the large log ft value for ^{117}Sb electron-capture decay to it, as discussed in sect. 4. If the state were appreciably collective in nature, the arguments given there about particle re-arrangements to open the $g_{\frac{7}{2}}$ neutron subshell would no longer be particularly valid, and the decay should not be quite so hindered. It is interesting to contrast this state with the $\frac{5}{2}^+$ state predicted to lie at 760 keV. The experimental state at 1020.2 keV probably corresponds to the latter and contains most of the $d_{\frac{5}{2}}$ quasi-particle amplitude; however, it does not appear to be a good single-quasi-particle state. First, it lies considerably higher than the predicted state, and this alone would suggest an appreciable amount of core excitation. This is also borne out by the fact that the state was readily reached by Coulomb excitation [17]).

The considerable difference between the $\frac{7}{2}^+$ and $\frac{5}{2}^+$ states is all the more interesting when we compare their predicted behavior in the other odd-mass Sn isotopes. In fig. 5a we have plotted the known states in these isotopes, and in fig. 5b we have added Sorensen's predictions [31]) for comparison. As mentioned above, both the $\frac{7}{2}^+$ and the $\frac{5}{2}^+$ states were predicted to be strongly mixed and coupled to the core in the heavier isotopes. However, both states are also predicted to drop in energy with decreasing N, and in so doing they are expected to become much purer single-quasi-particle states. Just below ^{117}Sn they drop quite rapidly, and the $\frac{7}{2}^+$ state becomes the 20 min 79 keV isomeric state in ^{113}Sn and the ground state at ^{111}Sn [ref. [34])]. The $\frac{5}{2}^+$ state is predicted to follow a similar trend; this makes its behavior in ^{117}Sn all the more intriguing.

The proximity of the 1004.5 keV $\frac{3}{2}^+$ and 1020.2 keV $\frac{5}{2}^+$ levels suggests that the peaks seen in (d, p) and (d, t) [ref. [1])] and in (p, d) and (p, p′) [ref. [2])] reactions near 1 MeV may need to be divided in some way between these two states. Since one (or both) member(s) of this doublet is (are) apparently strongly populated in each of these reactions, a re-interpretation of the implications of some of these data may be required. The 1004.5 keV $\frac{3}{2}^+$ level with a mean life of 0.9 ± 0.3 psec apparently corresponds to the 922 keV $\frac{3}{2}^+$ level of ^{119}Sn, which has a mean life [17]) of 1.4 ± 0.4 psec. The state in ^{119}Sn is the one most strongly populated by Coulomb excitation, and, of course, the ^{117}Sn state was one of the two states near 1 MeV strongly populated by Coulomb excitation. Thus, the 1004.5 keV state is mostly collective, as predicted.

Rather little can be said about the four remaining states that were observed in ^{117}Sb decay. Especially, we note that there are far more $\frac{5}{2}^+$ and/or $\frac{3}{2}^+$ states observed experimentally below 1970 keV than are accounted for by the theory. This makes any interpretation of the structures of the four upper states rather treacherous.

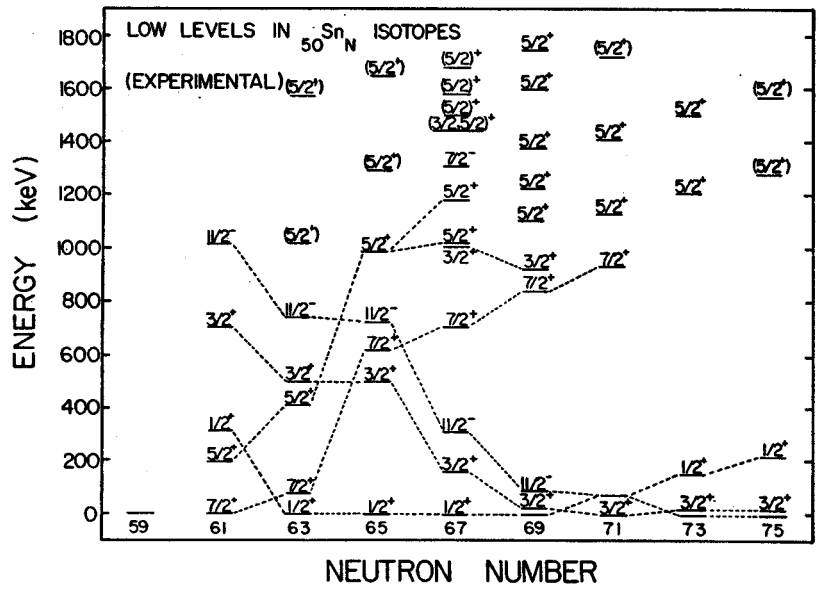

a

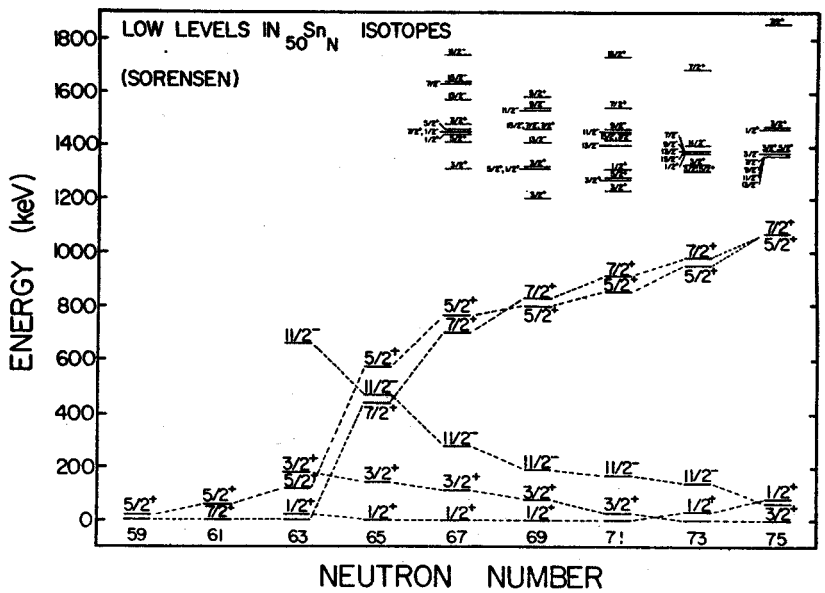

b

Fig. 5a. Experimental levels in the odd-mass Sn isotopes demonstrating the effects of changing neutron number on the positions of the states. Where possible, the data were taken from the spectroscopic information listed in ref. [21]); these were supplemented for the higher-lying states from reactions data in ref. [1]) and for ^{111}Sn from the work of Cavanagh *et al.* [33]). (b) Calculated [31]) levels in the odd-mass Sn isotopes. The small lettering for the higher-lying levels is merely for the sake of clarity. In this paper we are primarily concerned with the behavior of the lower levels.

The authors wish to thank Dr. C. R. Gruhn for his able assistance in the Ge(Li) detector fabrication program at Michigan State University and Dr. W. P. Johnson for aid in operating the Michigan State University cyclotron. We are also grateful to Mr. J. W. Starner and Dr. E. B. Shera for helpful discussions and assistance with data accumulation at Los Alamos Scientific Laboratory. Finally, we wish to thank Dr. W. B. Walters, Massachusetts Institute of Technology, for helpful discussions and for communicating some of his findings to us before publication.

References

1) E. J. Schneid, A. Prakash and B. L. Cohen, Phys. Rev. **156** (1967) 1316
2) K. Yagi, Y. Saji, T. Ishimatsu, Y. Ishizaki, M. Matoba, Y. Nakajima and C. Y. Huang, Nucl. Phys. **A111** (1968) 129
3) J. M. Cork, A. E. Stoddard, E. C. Brangan, W. J. Childs, D. W. Martin and J. M. LeBlanc, Phys. Rev. **84** (1951) 596
4) J. W. Mihelich, Phys. Rev. **87** (1952) 646
5) R. K. Golden and S. Frankel, Phys. Rev. **102** (1956) 1053
6) A. C. Li, M. Schmorak and A. Schwarzschild, Bull. Am. Phys. Soc. **6** (1961) 229
7) W. D. Hamilton, Z. Grabowski and J. E. Thun, Nucl. Phys. **29** (1962) 21
8) M. Schmorak, A. C. Li and A. Schwarzschild, Phys. Rev. **130** (1963) 15
9) J. P. Bocquet, Y. Y. Chu, G. T. Emery and M. L. Perlman, Phys. Rev. **167** (1968) 1117
10) C. L. McGinnis, Phys. Rev. **97** (1955) 93
11) J. L. Need and B. Linder, Phys. Rev. **129** (1963) 1298
12) C. W. Tang, G. E. Gordon and C. D. Coryell, MIT-LNS Progr. Rept. (1963) p. 36
13) C. D. Coryell, G. E. Gordon, J. W. Irvine, Jr. and G. Scatchard, MIT Semi-Annual Progr. Rept. (NYO-10065) (1 Nov. 1963) p. 28
14) R. V. Mancuso and R. G. Arns, Nucl. Phys. **68** (1965) 504
15) R. V. Mancuso and R. G. Arns, Nucl. Phys. **68** (1965) 513
16) R. L. Robinson, P. H. Stelson, F. K. McGowan, J. L. C. Ford, Jr. and W. T. Milner, Nucl. Phys. **74** (1964) 281
17) P. H. Stelson, W. T. Milner, F. K. McGowan and R. L. Robinson, Bull. Am. Phys. Soc. **12** (1967) 19
18) P. D. Barnes, E. R. Flynn, G. J. Igo and R. Woods, Bull. Am. Phys. Soc. **12** (1967) 546
19) K. A. Baskova, S. S. Vasil'ev, M. A. Khamo-Leila and L. Ya. Shavtvalov, ZhETF (USSR) **47** (1964) 1162
20) R. W. Fink, G. Andersson and J. Kantele, Ark. Fys. **19** (1961) 323
21) C. M. Lederer, J. M. Hollander, and I. Perlman, Table of Isotopes, 6th ed. (John Wiley and Sons, New York, 1967)
22) R. J. Howerton, D. Graff, W. J. Cahill and N. Chazan, UCRL-14001 (1967)
23) J. B. Marion, University of Maryland Technical Report 653 (1957)
24) G. Murray, R. L. Graham and J. S. Geiger, Nucl. Phys. **63** (1965) 353
25) J. S. Geiger, R. L. Graham, I. Bergström and F. Brown, Nucl. Phys. **68** (1965) 352
26) P. F. Zweifel, Phys. Rev. **107** (1957) 329
27) A. Bäcklin, B. Fogelberg and S. G. Malmskog, Nucl. Phys. **A96** (1967) 539
28) I. Lindgren, in Alpha-, beta- and gamma-ray spectroscopy, ed. by K. Siegbahn (North-Holland Publ. Co., Amsterdam, 1964) appendix 4
29) W. B. Walters, MIT, private communication
30) G. J. Garret, A. D. Jackson, Jr. and E. H. Rogers, Bull. Am. Phys. Soc. **12** (1967) 509
31) R. A. Sorensen, Nucl. Phys. **25** (1961) 674
32) L. S. Kisslinger and R. A. Sorensen, Mat. Fys. Medd. Dan. Vid. Selsk. **32**, No. 9 (1960)
33) P. Cavanagh, C. F. Coleman, A. G. Hardacre and J. F. Turner, Proc. Conf. on nuclear physics, Gatlinburg, Tennessee, (September 12–17, 1966) ed. by R. L. Becker (Academic Press, New York, 1967) p. 129
34) G. Graeffe and G. E. Gordon, Nucl. Phys. **A114** (1968) 321

Reprinted from THE PHYSICAL REVIEW, Vol. 176, No. 2, 484–489, 10 December 1968
Printed in U. S. A.

Energy-Loss Straggling of Protons in Silicon*

J. J. KOLATA AND T. M. AMOS

Michigan State University, East Lansing, Michigan

AND

HANS BICHSEL

University of Southern California, Los Angeles, California

(Received 1 August 1968)

The energy-loss straggling distributions for protons incident on a 200-μ silicon surface-barrier detector were measured in the energy region between 5 and 42 MeV. Experimental results were compared to the predictions of the Vavilov theory and found to be in excellent agreement at the higher energies. However, a systematic difference between theory and experiment was observed for proton energies less than 20 MeV, the discrepancy increasing with decreasing incident proton energy. This effect is due to appreciable variation of proton energy over the thickness of the detector. Tschalär's distribution functions, which specifically consider this variation, yield good fits to the data for energy losses as much as 80% of the incident proton energy.

I. INTRODUCTION

THE energy lost by a charged particle in a thin absorber is subject to fluctuations, because of the statistical nature of the energy-loss process. Thus, the energy Δ deposited in such an absorber by a monoenergetic beam of charged particles will be characterized by a distribution function $\phi(\Delta)$ known as the energy-loss straggling distribution. For moderately thick absorbers, that is, for those in which the mean energy loss $\bar{\Delta}$ is much greater than the maximum energy ϵ_{max} which can be transferred to an electron in a single collision, Bohr[1] showed that the distribution function is Gaussian. Landau[2] investigated the opposite extreme in which $\bar{\Delta}$ is much less than ϵ_{max}, and found that the distribution function in this case is highly asymmetric with a pronounced high-energy tail.

Symon[3] and Vavilov[4] have derived theories depending on ϵ_{max} which predict distributions intermediate between the Gaussian and the Landau forms. The parameter describing their distributions is the ratio $\kappa=\xi/\epsilon_{max}$, where the parameter ξ is directly related to $\bar{\Delta}$ and is defined in Ref. 5. For $\kappa\ll1$, the predicted distribution is of the Landau type, while for $\kappa\gg1$ it becomes Gaussian.

Previous work at isolated values of κ in the intermediate region[6,7] and a systematic survey[8,9] of the Landau transition region ($\kappa<0.1$) have shown good agreement between the predictions of Vavilov or Symon and experiment. We have investigated the Gaussian transition region ($\kappa>1$), obtaining data for protons incident on silicon in the range $0.4\leq\kappa\leq30.4$.

II. EXPERIMENTAL METHOD

A. Beam Line

Figure 1 is a schematic diagram of the elements of the beam line. A proton beam from the Michigan State University isochronous cyclotron was focused by a set of quadrupole doublets on the object slit S1 of an energy analysis system. To facilitate rapid variation of the energy of the incident beam in small steps, a degrader was placed 15 cm in front of this slit. The degrader, an aluminum wedge 7.5 cm long by 2.5 cm wide, had a maximum thickness of 0.9 cm and tapered to a sharp edge. It could be remotely positioned in the path of the beam. In this way, we were able to rapidly change the energy of the beam in steps of 2 MeV over the energy region from 20 to 42 MeV with a primary beam of 42.4±0.1 MeV, and from 4 to 26 MeV with a primary beam of 28.4±0.1 MeV. The lowest energy obtainable in the first case was determined by loss of beam intensity due to multiple scattering and energy straggling effects in the degrader.

* Work supported in part by the National Science Foundation and by Public Health Research Grant No. CA 08150 from the National Cancer Institute.

[1] N. Bohr, Phil. Mag. 30, 581 (1915).
[2] L. Landau, Zh. Eksperim. i Teor. Fiz. 8, 201 (1944).
[3] K. R. Symon, thesis, Harvard University, 1948 (unpublished).
[4] P. V. Vavilov, Zh. Eksperim. i Teor. Fiz. 32, 320 (1957) [English transl.: Soviet Phys.—JETP 5, 749 (1957)].
[5] M. J. Berger and S. M. Seltzer, Natl. Acad. Sci.—Natl. Res. Council, Publ. 1133; U.S. At. Energy Comm. NAS-NS 39, 188 (1964).
[6] T. J. Gooding and R. M. Eisberg, Phys. Rev. 105, 357 (1957).
[7] G. J. Igo, D. D. Clark, and R. M. Eisberg, Phys. Rev. 89, 879 (1953).
[8] H. D. Maccabee and M. R. Raju, Nucl. Instr. Methods 37, 176 (1965).
[9] H. D. Maccabee, M. R. Raju, and C. A. Tobias, Phys. Rev. 165, 469 (1968).

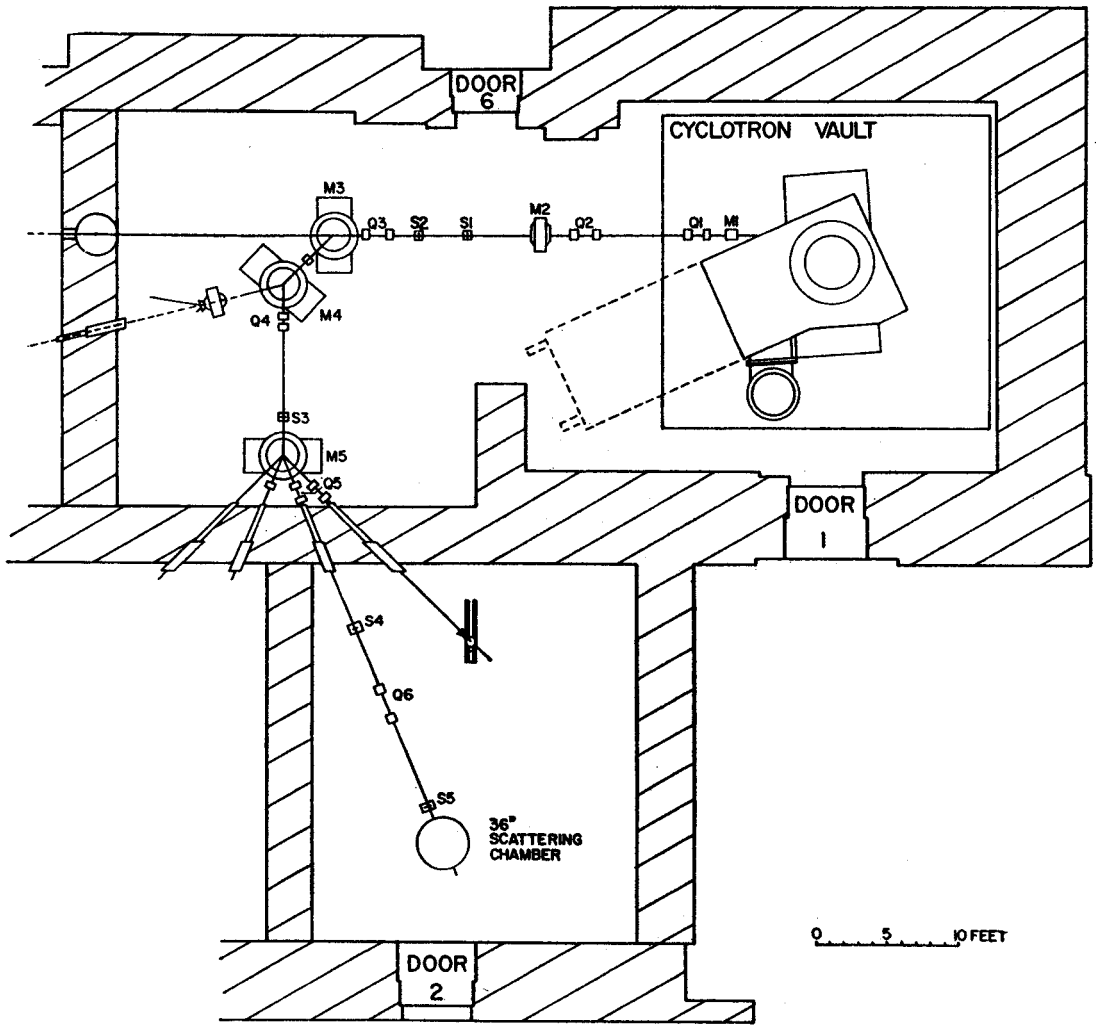

FIG. 1. Scale drawing of the beam transport system. The locations of the defining apertures (S1–S5), quadrupole doublets (Q1–Q6), and bending magnets (M3–M5) are indicated.

The degraded beam was transmitted through the object slit S1 and the divergence limiting slit S2, bent through 90° by the energy analyzing magnets M3 and M4, and focused on the image slit S3. The properties of this beam transport system have been investigated previously. In particular, the energy resolution of the transmitted beam as a function of slit openings,[10] and the energy of the analyzed beam as a function of magnet field strength[11] have been calculated. The slit widths used were 0.25 by 0.25 cm for the object and image slits, and 0.30 by 0.30 cm for the divergence slit. With these settings, the energy resolution of the transmitted beam is 8 parts in 10^4 full width at half-maximum (FWHM). The magnetic field at M3 was monitored throughout the experiment by a NMR field probe, and the measured field strengths were used to calculate the transmitted beam energy to within ±0.1 MeV.

The analyzed beam was deflected into the experimental area by magnet M5, and was focused first on a 0.95-cm-square slit S4, and then on a 0.3-by-0.5-cm defining aperture in the scattering chamber.

B. Detector and Electronics

A 200-μ totally depleted silicon surface-barrier detector with an active region 0.7 cm in diam was placed in the direct beam line 30 cm from the defining aperture at the entrance to the scattering chamber, and oriented to be perpendicular to the beam to within ±0.5°. The thickness of the detector was determined

[10] G. H. Mackenzie, E. Kashy, M. M. Gordon, and H. G. Blosser, IEEE Trans. Nucl. Sci. 14, 450 (1967).
[11] J. L. Snelgrove and E. Kashy, Nucl. Instr. Methods 52, 153 (1966).

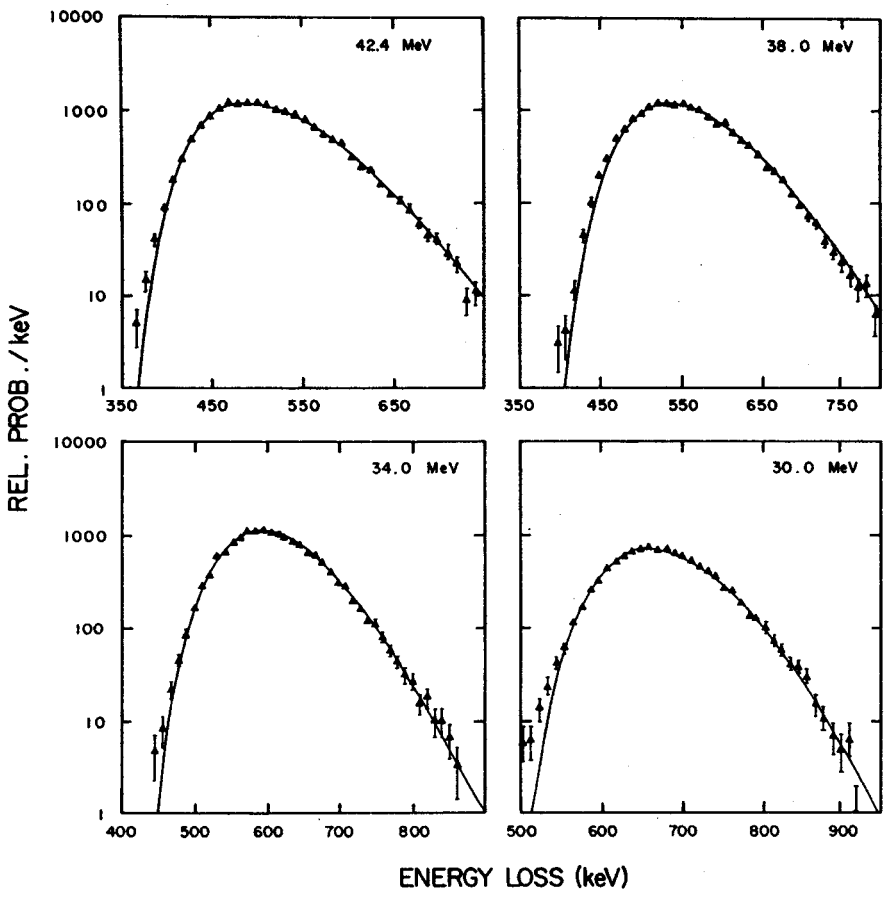

FIG. 2. Straggling distributions for 30.0- to 42.4-MeV protons. Error bars indicate statistical uncertainties only. The solid curves are the predictions of the Vavilov theory.

to be 45.6±0.4 mg/cm² by fitting the mean proton energy loss from 5 to 12 MeV to the range-energy table for silicon.[12] In a preliminary analysis assuming this thickness, the measured mean energy loss agreed with the table to within ±0.5% from 12 to 42 MeV.

The signals from this detector were amplified by a charge sensitive FET preamplifier followed by a shaping amplifier with 2-μsec time constants. The resulting pulse-height spectra were analyzed, using a conventional 1024-channel analyzer. The best energy resolution obtained was 16.4-keV FWHM, measured with a 4-MeV proton beam which stopped in the detector.

The gain and zero point of the detector-amplifier-analyzer system were monitored by inserting test pulses from a precision pulser into the preamplifier. The data were partially analyzed during the course of the experiment using the SDS Sigma 7 computer at the cyclotron laboratory, as an additional check against drifts.

The beam current extracted from the cyclotron was adjusted to give a count rate in the detector of less than 1000 counts/sec, in order to avoid pulse pile-up problems. The current required to maintain this rate varied from less than 10 nA for minimum degradation, to more than 1 μA for maximum degradation, in which case multiple scattering and energy-loss straggling effects in the degrader cause large beam losses.

III. ANALYSIS AND RESULTS

Energy-loss spectra for protons in the detector described are shown in Figs. 2–5. The error bars shown indicate statistical uncertainties only. The solid curves are the predictions of the Vavilov theory, as calculated by a FORTRAN program originally written by Seltzer and Berger[5] and modified by one of us (J.K.) for the Sigma 7 computer. The theoretical distributions obtained have been normalized to the experimental data, using a least-squares fitting criterion. In addition, they have been corrected for the finite resolution of the detection system and the energy spread in the incident beam. The detector resolution (16.4 keV) and the beam width (8 parts in 10^4) were added in quadrature, and the resultant Gaussian resolution function was folded into the theoretical distributions. This correction

[12] H. Bichsel and C. Tschalär, Nucl. Data 3A, 343 (1967).

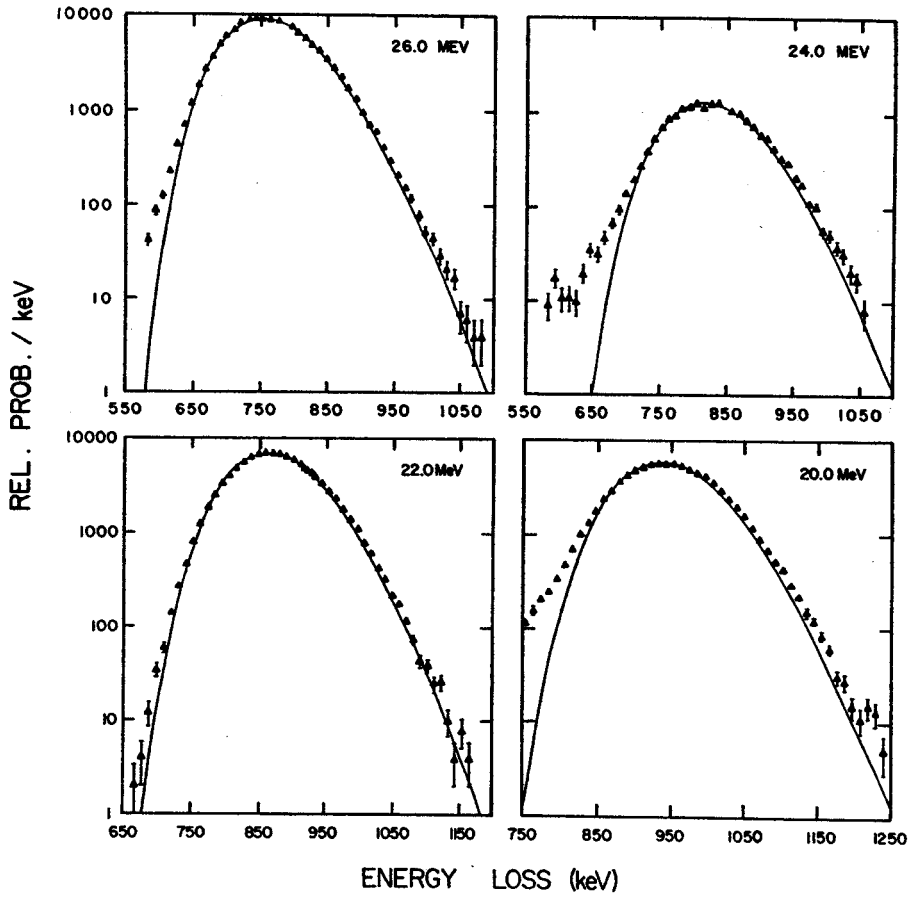

FIG. 3. Straggling distributions for 20.0- to 26.0-MeV incident proton energy.

was small compared to the total width of the distribution. For example, the full width at half-maximum of the resolution function was 34.5 keV for the data taken at 38 MeV. The corresponding correction to the width of the theoretical distribution was 2.9%, increasing it from 137- to 141- keV FWHM.

The agreement between theory and experiment is excellent for incident proton energies greater than 30 MeV; the Vavilov theory correctly predicts the shape of the distribution to 1% of the peak value. At 30 MeV and below, the probability of small energy losses seems to be enhanced above the theoretical prediction in some cases. This is not a systematic discrepancy, as can be seen by comparing the data taken at 22 MeV with the 24- and 26-MeV data, and again from the 14-, 16-, and 18-MeV data. A possible explanation of this effect is that it is due to protons which pass through the edge of the detector and thus deposit a smaller fraction of their energy in the sensitive volume of the detector. The probability that this will occur depends on the size of the beam spot at the detector, that is, on the focusing properties of the beam transport system. During the initial setup, the 42.4-MeV proton beam was focused on a scintillator at the location of the detector, prior to its insertion into the beam line. Settings for the focusing magnets were then computed as a function of proton energy to be used for the lower-energy runs. It is possible that small cumulative errors in these computed settings could have caused an increase in the beam size below 30 MeV, thus enabling some protons to escape from the edges of the detector.

An additional effect is observable in the data taken at 20 MeV and below, where there seems to be a systematic difference between theory and experiment. The predicted widths are smaller than those observed, and the magnitude of the discrepancy increases with decreasing proton energy. This is a result of the approximation, made in the derivation of the Vavilov theory, that the energy of the incident particle does not change significantly over the thickness of the target. Recently, Tschalär[13,14] has developed a theory of straggling for large energy losses, which does not make this approximation. We have fitted Tschalär's distributions to the

[13] C. Tschalär, Nucl. Instr. Methods 61, 141 (1968); and Rutherford Laboratory Report No. RHEL/R164 (unpublished).

[14] C. Tschalär and H. Bichsel, Nucl. Instr. Methods 62, 208 (1968).

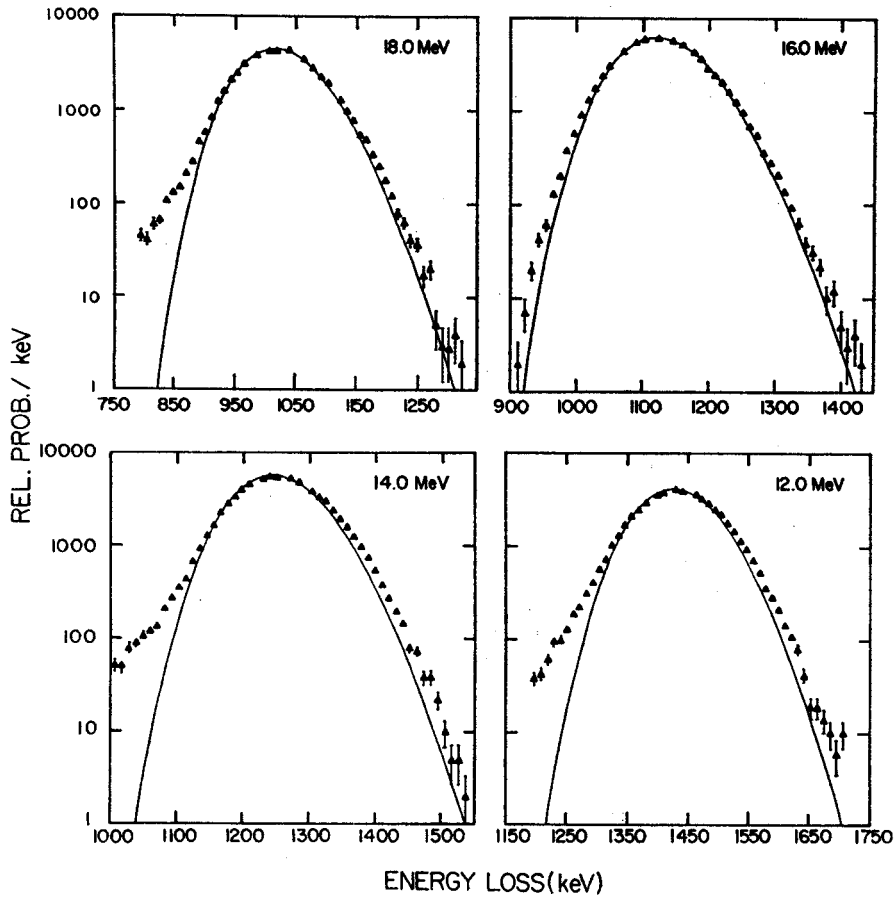

FIG. 4. Straggling distributions for 12.0- to 18.0-MeV incident proton energy.

data taken at 5.0 and 7.0 MeV, the energy lost in the detector being 76 and 34% of the initial energy, respectively. The results are shown in Fig. 5. We conclude that the method of Tschalär can predict straggling distributions accurately for very large energy losses, of the order of 80% of the initial energy. In addition, our data indicate that the variation of the proton energy over the target thickness can produce noticeable deviations from the Vavilov distribution for energy losses as small as 5% of the initial energy.

It should be noted that in all the comparisons between theory and experiment we have neglected several processes which could possibly affect the distributions. The first is the increase in effective target thickness due to multiple scattering in the detector.[14,15] This effect will be most important at the lower energies. For example, at 5.06 MeV, with a residual energy of about 1.33 MeV, the rms deviation is approximately 4°, while at 38.0 MeV it is less that 1°. The corresponding corrections to the path length are 0.2% and less than 0.01%, respectively. We have also neglected the effect of the loss of high-energy electrons, or δ rays, produced near the surface of the detector, and the possibility of energy-loss fluctuations due to nonstatistical effects such as channeling. Finally, the distributions of Vavilov and Tschalär are calculated on the assumption that the atomic collision cross section follows a $1/\epsilon^2$ law. Indications of the changes to be expected from a more realistic collision spectrum can be found in Ref. 16. For the relatively large energy losses of the present experiment, the changes are expected to be small.

IV. CONCLUSION

The Vavilov theory for energy-loss straggling of charged particles in matter has been tested for protons incident on a 200-μ silicon detector in the energy region from 5.0 to 42.4 MeV. This corresponds to a range in the parameter κ of 30.4 to 0.44, which covers the transition region to a Gaussian distribution. There is excellent agreement between theory and experiment for proton energies greater than 20 MeV. Below this energy, a systematic energy-dependent discrepancy appears which has been shown to be due to the variation of proton energy over the thickness of the target. The method of Tschalär, which takes this effect into consideration, yields good fits to the observed distributions for energy losses as much as 80% of the incident proton energy.

[15] H. Bichsel and E. A. Uehling, Phys. Rev. 119, 1670 (1960).

[16] A. M. Kellerer, Proceedings of the Conference on Microdosimetry, pp. 57–77, 1967 (unpublished).

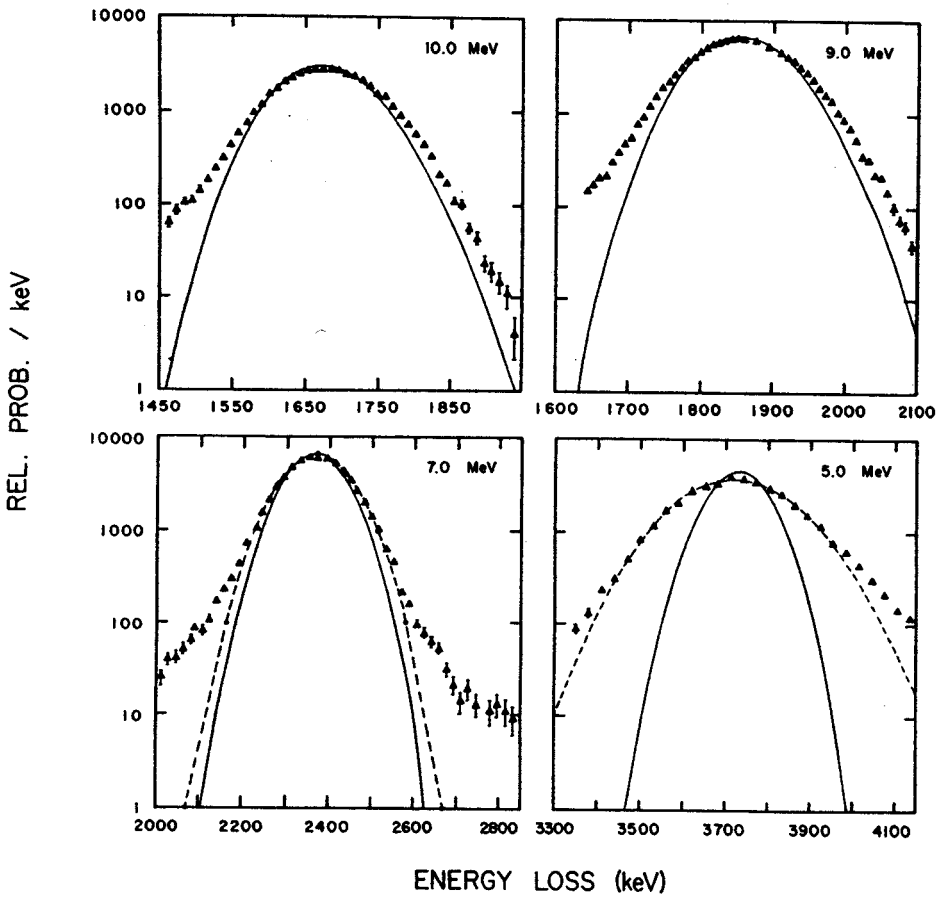

FIG. 5. Straggling distributions for 5.0- to 10.0-MeV incident proton energy. The solid curves are the predictions of the Vavilov theory. The dashed curves are the predictions of Tschalär, which take into account the variation of the proton energy over the detector thickness.

ACKNOWLEDGMENTS

The authors are indebted to Dr. A. Galonsky for his advice and encouragement in the course of this work, and to Dr. Martin Berger for supplying the program to calculate the Vavilov distribution.

THREE-QUASIPARTICLE MULTIPLET IN Pr^{139}

Wm. C. McHarris
Department of Chemistry* and Cyclotron Laboratory,† Department of Physics,
Michigan State University, East Lansing, Michigan 48823

and

D. B. Beery‡ and W. H. Kelly
Cyclotron Laboratory,† Department of Physics, Michigan State University, East Lansing, Michigan 48823
(Received 24 February 1969)

Nd^{139m} in its ϵ decay preferentially populates a multiplet of six high-lying, high-spin, odd-parity states in Pr^{139}. We interpret this as $(\pi d_{5/2})^2(\nu d_{3/2})^{-2}(\nu h_{11/2})^{-1} \rightarrow (\pi d_{5/2})(\nu d_{3/2})^{-1} \times (\nu h_{11/2})^{-1}$, with the Pr^{139} states being three-quasiparticle states.

Well-characterized three-particle states in nuclei are comparitively rare, and recognizing them most often has depended on the isomeric properties of a few high-spin states. Consequently, the excitation of a multiplet of such states in one nucleus, each state decaying to a number of lower lying states, has many interesting theoretical implications. Here we report our identification of the relatively unique population of a multiplet of six high-spin, negative-parity levels in Pr^{139} by the electron-capture decay of Nd^{139m}. We interpret this as the configuration of Nd^{139m} being peculiarly suited for populating three-quasiparticle states.

The two isomers of Nd^{139} follow the trend of $N = 79$ isomers, there being a 30-min $\frac{3}{2}^+$ ground state and a 5.5-h $\frac{11}{2}^-$ metastable state. Because the spacing between them is fairly small (231.2 keV) and the energy available for electron-capture decay is large ($\approx$3 MeV), only 12.7% of the decay of the $\frac{11}{2}^-$ state proceeds via the $M4$ isomeric transition, and the two isomers decay almost independently. We prepared the isomers by the $Pr^{141}(p, 3n)Nd^{139m+g}$ reaction, using a 29-MeV proton beam from the Michigan State University sector-focused cyclotron, and have studied the γ-ray spectra following their decay with Ge(Li) and NaI(Tl) detectors in various singles, coincidence, and anticoincidence configurations. The resulting decay scheme of Nd^{139m} is given in Fig. 1; the details on how this was constructed and the decay scheme of Nd^{139g} will be presented in another publication.[1]

The decay of Nd^{139g} is more or less straightforward and much like the decay of many similar nuclei in this region,[2] which have most of their decay going directly to the ground state of the daughter nucleus. However, it can easily be seen

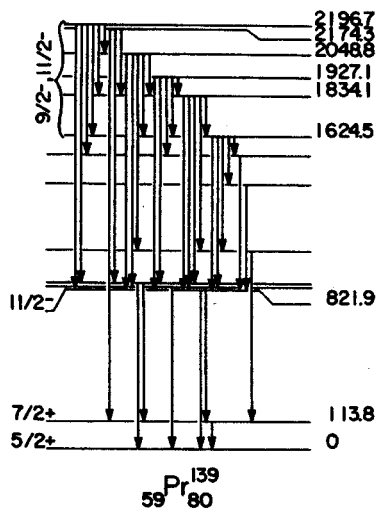

FIG. 1. Simplified level scheme of Pr^{139} showing the states that are populated in the decay of Nd^{139m} and the γ-ray transitions that de-excite them. Energies and spin-parity assignments are listed only for states pertinent to the present discussion. For more details about this scheme and its construction and for the Nd^{139g} decay scheme, see Ref. 1.

that the decay of Nd^{139m} is not so straightforward. In particular, 80.7% of its decay goes to six high-lying states at 1624.5, 1834.1, 1927.1, 2048.8, 2174.3, and 2196.7 keV in Pr^{139}, with only ≈6.5% going directly to lower lying levels. The logft values for decay to these six states lie between 5.6 and 6.3, whereas for decay to an $\frac{11}{2}^-$ state at 821.9 keV, the value is 7.0. Further, the six states appear to have some common internal structure that is significantly different from the lower states—this is demonstrated by the many enhanced low-energy γ transitions within the multiplet and the scarcity of transitions to the lower states.

We measured the half-life of the 821.9-keV state to be 40 ± 2 nsec,[3] which means that the $M2$ (708.1-KeV)[4] and $E3$ (821.9-keV) transitions deexciting it have partial half-lives of ≈42 and ≈600 nsec, compared with straightforward single-particle estimates[5] of 1.2×10^{-9} and 1.3×10^{-6} sec, respectively. Thus, the $M2$ is retarded to approximately the same degree that many $M2$'s are retarded, and the $E3$ is somewhat enhanced—this is now the fourth enhanced $E3$ that has been found in this same nuclear region.[6] The implication is that these are good single-particle transitions and the 821.9-keV state is essentially a $\pi h_{11/2}$ state.

The problem, then, is in the determination of the nature of the multiplet of six high-lying states. Logft values by themselves are not overly trustworthy as indicators of the types of β decay, but it is much more common for the values for allowed decay to be too high than for those for first-forbidden decay to be too low.[7] The conclusion is that the multiplet consists of high-spin, negative-parity states—various γ-ray branchings allow this to be narrowed down for most of the states to $\frac{9}{2}^-$ or $\frac{11}{2}^-$. But how can such states be constructed; especially, how can they be constructed so as to be favored for population over the 821.9-keV $\frac{11}{2}^-$ state?

In Fig. 2 we present a simple stylized version of our answer. The ground state of Nd^{139}, with three holes in the $N=82$ shell and two protons outside the $(g_{7/2})^8$ subshell, undoubtedly has as the major component of its wave function the configuration $(\pi d_{5/2})^2(\nu d_{3/2})^{-3}$. Its β^+/ϵ decay can be represented as converting a $d_{5/2}$ proton into a $d_{3/2}$ neutron, resulting in $(\pi d_{5/2})(\nu d_{3/2})^{-2}$, the ground-state configuration of Pr^{139}. This representation is consistent with the logft value of 5.1. Nd^{139m}, as demonstrated by the reduced transition probability of the $M4$ transition[8] and the systematics of $N=81$ and $N=79$ isomers, differs from Nd^{139g} only in the promotion of an $h_{11/2}$ neutron to the $d_{3/2}$ orbit, resulting in $(\pi d_{5/2})^2(\nu d_{3/2})^{-2}\times(\nu h_{11/2})^{-1}$. Upon converting a $d_{5/2}$ proton into a $d_{3/2}$ neutron we get $(\pi d_{5/2})(\nu d_{3/2})^{-1}(\nu h_{11/2})^{-1}$, a "three-quasiparticle state." This can be contrasted to direct population of the 821.9-keV state, which would require the transformation of a $d_{5/2}$ proton into an $h_{11/2}$ neutron, either directly or perhaps through an intermediate $d_{3/2}$ state, and a simultaneous promotion of the remaining $d_{5/2}$ proton to the $h_{11/2}$ orbit. Hence the relatively large logft value of 7.0.

Although the above interpretation qualitatively explains most of the γ-ray branchings between members of the negative-parity multiplet, there are several places involving very highly hindered transitions where it runs into difficulties. We

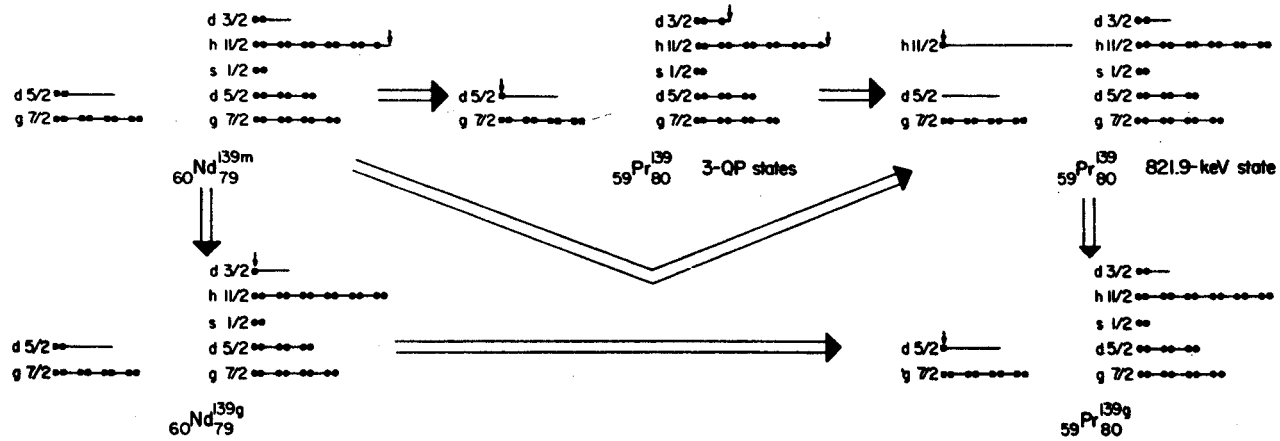

FIG. 2. Symbolic shell-model representations of some important transitions between Nd^{139} and Pr^{139} states. We have given a stylized picture of the proton (squares) and neutron (circles) states between 50 and 82 nucleons. The arrows point to the nucleons or holes of prime interest in each state.

take this to mean that small admixtures in the states are very important in determining these transition rates, but it is instructive to consider specifically one of the more extreme examples —the 1011.9-keV γ (2.9%) from the 1834.1-keV state to the $\frac{11}{2}^-$ 821.9-keV state versus the unobserved (<0.5%) 1834.1-keV γ to the $\frac{5}{2}^+$ ground state. With an $\frac{11}{2}^-$ assignment for the 1834.1-keV state one would not expect to see the 1834.1-keV γ, but with a $\frac{9}{2}^-$ assignment the arguments are not so clear. Single-particle estimates[5] for the $t_{1/2}$'s of the 1011.9-keV ($M1$) and 1834.1-keV ($M2$ or $E3$) γ's are 2.4×10^{-14} and 8×10^{-12} or 4×10^{-9} sec, respectively. According to our above description the missing $M2$ or $E3$ would involve an apparently very simple $\nu d_{3/2} - \nu h_{11/2}$ transition (the $M2$ would be l forbidden); there may also be some hindrance from uncoupling and recoupling the states. On the other hand, the observed 1011.9-keV $M1$ γ requires the more complex simultaneous changes $\nu d_{3/2} - \nu h_{11/2}$ and $\pi d_{5/2} - \pi h_{11/2}$, each of which is twice l forbidden. However, l forbiddenness loses much of its meaning in multiparticle transitions and would depend on the relative phases of the transforming states; also, core polarization in multiparticle states tends to obviate the l selection rules.[9] Still, multiparticle γ decay is formally absolutely forbidden, and although there are known cases where such transitions take place at enhanced rates (e.g., the 63-keV $E1$ γ in Bk^{250} following Es^{254} α decay[10]), these are not common. When such involved rearrangements are compared, clearly the single-particle estimates lose all meaning, and minute admixtures could easily be the deciding factors.

In this multiplet of three-quasiparticle states we thus have two different and potentially very rewarding sources of information: (1) The enhanced transitions between the various members of the multiplet. These should give information on the gross features of the states and should allow one to perform calculations on states at several MeV that normally can be done only near the ground state. (2) The very retarded transitions to states not in the multiplet. These should allow one to determine some of the admixtures in the states.

It is worth noting that here we have a somewhat unique mechanism for populating three-quasiparticle "multiplets" in a number of nuclei. The requirements are a high-spin nucleus, such as the $h_{11/2}$ isomers, and one with sufficient decay energy to populate states above the pairing-energy gap in its daughter nucleus. Additionally, the parent nucleus must be hung up with respect to decay by other modes, e.g., an isomeric transition, if present, must be of low enough energy to allow the ϵ decay to compete. Finally, the nucleus must have a relatively unique intrinsic configuration that forces the preferred decay path to be into the three-quasiparticle states. Such arrangements would appear to be present only for β^+/ϵ decay; further, they are likely to occur only below $N=82$—specifically, at $N=79$ and $N=77$, with the possibility of $N=75$ depending on the relative spacing of the $h_{11/2}$ and $s_{1/2}$ states. (Below $N=50$ the correct configuration occurs at Kr^{83} and Sr^{85}, but these are too close to β stability for populating high-lying states. Below $N=126$ the configuration is projected to occur around Pu^{211}, a region that is not even particle stable.) Nd^{139m} appears to be the nucleus closest to β stability with the requisite properties, although among currently known nuclei other possible candidates are $Sm^{141(m)}$ and $Nd^{137(m?)}$. These additional cases are now being investigated.

---

*Work supported in part by the U. S. Atomic Energy Commission.

†Work supported in part by the U. S. National Science Foundation.

‡Present address: Manchester College, North Manchester, Ind. 46962.

[1]D. B. Beery, W. H. Kelly, and W. C. McHarris, to be published.

[2]Ce^{135}: A. Abdul-Malek and R. A. Naumann, Phys. Rev. 166, 1194 (1968); Ce^{137}: D. B. Beery, W. H. Kelly and W. C. McHarris, to be published; Nd^{141}: D. B. Beery, W. H. Kelly, and W. C. McHarris, Phys. Rev. 171, 1283 (1968); Sm^{143}: D. de Frenne, K. Heyde, L. Dorikens-Vanpraet, M. Dorikens, and J. Demuynck, Nucl. Phys. A110, 273 (1968).

[3]D. B. Beery, W. C. McHarris, J. J. Kolata, and W. H. Kelly, Bull. Am. Phys. Soc. 13, 1467 (1968).

[4]This multipolarity was determined from the conversion electron data of K. Ya. Gromov, A. S. Danagulyan, L. N. Nikityuk, V. V. Murav'eva, A. A. Sorokin, M. Z. Shtal', and V. S. Shpinel', Zh. Eksperim. i Teor. Fiz. 47, 1644 (1964) [translation: Soviet Phys.—JETP 20, 1104 (1965)]; and J. Gilat and W. J. Tretyl, University of California Lawrence Radiation Laboratory Report No. UCRL-17299, 1967 (unpublished), p. 20.

[5]S. A. Moszkowski, Phys. Rev. 89, 474 (1953); also in A. H. Wapstra, G. J. Nijgh, and R. van Lieshout, Nuclear Spectroscopy Tables (North-Holland Publishing Company, Amsterdam, The Netherlands, 1959).

[6]J. R. Van Hise, G. Chilosi, and N. J. Stone, Phys. Rev. 161, 1254 (1967).

[7]C. E. Gleit, C.-W. Tang, and C. D. Coryell, Nuclear Data Sheets, compiled by K. Way et al. (Printing and Publishing Office, National Academy of Sciences—Na-

tional Research Council, Washington, D.C., 1963).
[8]R. E. Eppley, W. C. McHarris, D. B. Beery, and W. H. Kelly, to be published; K. Kotajima and H. Morinaga, Nucl. Phys. 16, 231 (1960).
[9]M. Gmitro, J. Hendeković, and J. Sawicki, Phys. Rev. 169, 983 (1968).
[10]W. C. McHarris, F. S. Stephens, F. Asaro, and I. Perlman, Phys. Rev. 144, 1031 (1966).

SYNCHROCYCLOTRON IMPROVEMENT PROGRAMS*

H. G. Blosser
Michigan State University
East Lansing, Michigan

Abstract. A number of groups are engaged in improvement of synchrocyclotrons in order to increase beam current and improve extraction efficiency and beam precision. This paper reviews the major problems involved in such improvements and the solutions contemplated by the several groups. Goals are beams of 10μa or more with extraction efficiency of at least 50% and a tenfold gain in spatial and energy definition of the beams.

Introduction

The synchrocyclotron (SC) was originally conceived as a remedy for an intolerable limitation of the classical Lawrence cyclotron, namely the energy limitation. Exploiting the principal of phase stability, the SC's were able to increase the proton energy available to experimenters by nearly a hundred fold as compared with the classical cyclotron—the important new phenomena which were uncovered in this bold advance of the energy frontier eventually developed into a whole new area of physics, usually referred to simply as "high energy" physics. The birth of the SC was though also the birth of the synchrotron and for economic reasons the SC was soon itself at an energy maximum and the energy frontier shifted to the much less costly synchrotron (which has in turn now lead to another hundred fold increase in available proton energy).

In this process of rapid development of high energy physics the exploratory experiments for which the SC's were originally intended have long since been done and almost universally today's important questions of physics in the energy range of the SC's demand detailed, precise measurements of intricate phenomena. Unfortunately the innovation which allowed the SC to bypass the energy limitation of the classical cyclotron at the same time led to less defined, poorer duty cycle beams or just the opposite of what is needed for precision experiments. Meanwhile the Lawrence cyclotron, neglected for a decade or more, suddenly in the late 1950's again blossomed into a forefront instrument of the physicists' repertoire due to the introduction of sector focusing and other improvements. Such cyclotrons have now evolved into devices of superlative precision with maximum energy pushing steadily higher thru the range of the SC's. The double pressure of the need for precise experiments and the need to stay competitive with the new CW machines have faced SC laboratories with a pressing need to improve their machines or accept obsolescence.

Motivations for improving the SC's are strong. 1) The hardware is monumental—the magnet of the Dubna SC for example contains ~twice as much iron as the Brookhaven AGS. 2) The machines are already spendidly instrumented for physics by virtue of having in progress going research programs—typically the cost of the associated instrumentation for such a facility is at least as great as the cost of the machine. 3) The laboratories are already staffed with research groups of proven merit—no other factor is so important to ultimate productivity. In spite of these compelling arguments a number of laboratories, faced with the even more compelling argument of no funds, are moving to close down their SC's. At a fortunate few locations (Cern, Columbia, Harwell and Dubna) improvement programs have been definitely approved and a number of other laboratories are still in the status of hoping for approval.

On a technical level the various approved and contemplated improvement programs display a considerable diversity in approach. In part this reflects different boundary conditions at the various laboratories such as how long a shut down is tolerable, how much money can be obtained, etc. Also, to a substantial degree the diversity of the planned programs reflects a judgment on the part of the groups involved as to what problems are most easily solvable, the answer to which of course depends considerably on the previous experience of a particular group. It is particularly interesting to note that all the presently proposed modifications contemplate retaining the FM cycle whereas persons with a background in CW cyclotrons usually feel that the best SC conversion would be a shift to full CW operation. In order that the reader can weigh the CW approach vs. various versions of FM conversions I include in this review a small amount of material on CW conversions even though none such is proposed by any of the SC groups presently working on conversions.

I have elected to organize the paper on a functional basis rather than a project basis i.e. the several sections deal with central region, acceleration system, magnet and extraction rather than with Cern, Columbia, Dubna, Harwell, etc.—the discussion is thus able to deal with a given problem in a unified way but at

the expense of fragmenting the description of the program at a particular laboratory. The disadvantage is offset by the availability of excellent internal reports on the projects from several of the laboratories[1,2,3] and, in the case of Columbia and Dubna, by papers at this conference.

Central Region

Several of the most severe difficulties in synchrocyclotrons, including the crucial problem of low extraction efficiency, are the direct result of the type of ion source normally employed, the so-called open source. Such a source, particularly when operated with an admixture of heavy gas such as Argon, yields ions originating from a broad region in the center of the machine frequently up to 20 cm in diameter. This distribution of initial conditions is directly reflected in the distribution of radial betatron amplitudes—radial amplitudes extend to 10 cm and, as will be discussed in a later subsection, efficient extraction of such a spreadout beam is extremely difficult. To escape this difficulty, conversion programs establish as a high priority goal a shift to a closed, Oak Ridge type, ion source[4] such as have been in common use in CW cyclotrons for some twenty odd years. In such a source a collimated plasma is maintained within a hollow electrode called the chimney; ions are pulled out of this plasma by means of an extraction field acting on a small slit in the side of the housing. Proton currents of up to 100 mA can be obtained from a slit 1 x 10 mm in size[5]—the initial position of the ions thus being fixed with splendid precision.

Revisions of the ion source proper involved in changing to a closed source are actually a rather trivial matter requiring an expenditure of only a few thousand dollars in the typical circumstance. This change though, then necessitates a major change in the acceleration system since ions must receive enough acceleration on the first turn to pass around the source chimney. An increase in the accelerating voltage is required from the 10 kv now typical to around 30 kv, together with installation of an electrode system to concentrate the field in the vicinity of the source so that particles are accelerated by the full voltage even on the first turn. Fig. 1 shows a possible revised central region for the Cern SC showing source, dee, defining electrodes and typical trajectories.

A second crucial problem in the central region of an SC is that of axial focusing. Since the duty cycle of the acceleration process, even in converted machines, will be very low, of order 1 in 100, achieving a given final current, say 10μA, requires an instantaneous average current 100 times higher or ~1ma. The SC's also typically have higher magnetic field and much lower energy gain per turn than CW machines—all of these factors combine to yield a vastly higher charge density than in CW machines and, as was originally pointed out by MacKenzie[6], the self repulsion of this high density charge layer is the most important single phenomena in determining the final beam current of an SC.

The most serious effect of these large space charges forces is to cause the beam to expand axially and exceed the aperture—to offset this axial defocusing designers work to maximize the offsetting axially focusing forces provided by the magnetic field and the accelerating structure. The origin of the principal contributions to this restoring force have been calculated by Holm[1] and are shown in Fig 2. The solid curves are the contribution from the accelerating gaps due to so-called first order electric focusing; this contribution can be either focusing or defocusing depending on the phase of the particle relative to the RF. (The curves are labeled in accord with the usual CW cyclotron convention, namely 0° phase is peak energy gain.) At low energies the electric focusing is extremely strong reflecting the ΔE/E dependence typical of acceleration system focusing effects.

Magnetic focusing effects as is well known divide into two contributions, usally called respectively gradient focusing and flutter focusing. The smooth approximation of Symon[7] indicates the effect of the two contributions i.e.

$$Q_z^2 = -k + F(1+2\tan^2\alpha) \qquad (1)$$

where

$$k = \frac{r}{\langle B\rangle}\frac{d\langle B\rangle}{dr},\quad F = \frac{\langle B^2\rangle}{\langle B\rangle^2} - 1,$$

and $\langle \ldots \rangle = \frac{1}{2\pi}\int_0^{2\pi} \ldots d\theta$

The angle α describes the spiral of the field, α = 0° corresponding to radial sectors, and α = 90° corresponding to the phonograph record. If the field has a simple one harmonic form i.e.

$$B(r,\theta) = B(r)\left(1 + f(r)\tan N(\theta - \phi(r))\right) \qquad (2)$$

then eq. (1) reduces to:

$$Q_z^2 = \frac{-r}{B}\frac{dB}{dr} + \frac{f^2}{2}\left(1+2r^2\left(\frac{d\phi}{dr}\right)^2\right) \qquad (3)$$

Frequently the logarithmic frequency derivitive, K, is used to specify a field shape. This parameter is related to k by the relation:

$$K = \frac{E}{\omega}\frac{d\omega}{dE} = 1 - \frac{k}{k+1}\frac{c^2}{\omega z} \qquad (4)$$

For azimuthally symmetric fields such as in the normal cyclotron, f(r) = 0 in eq.(1) and only the first term (the gradient focusing term) contributes to the focusing force. In Fig. 2 the gradient focusing term is shown for two typical fields; one (K=2) is typical of field shapes in SC's as they now exist, the other (K-5) being a likely shape for a deliberately strengthened central cone. Generally flutter focusing in the central region tends to be less effective than gradient focusing since azimuthal variations in the field must approach zero as $(r/g)^N$ where g is the air gap of the magnet. Never-the-less if g and N are both sufficiently small the term can be important. The Columbia Univ. conversion program for example contemplates placing iron sectors in the dees thereby permitting the g near the center to be 1"—with N=3 a flutter such as shown in Fig. 3 results[8]. The very rapid vise of this curve plotted on the scale of Fig. 2 produces the dotted curve i.e. an effect almost identical to that of the K=5 gradient term. (The gradient term has of course the important advantage that it is completely compatible with a normal magnet gap and therefore the delicate problem of supporting iron inside the accelerating electrodes does not arise).

Combining the various focusing forces shown in Fig. 2 yields a resultant force which for positive phases is strong at small radii, passes thru a minimum and then is again strong. (The strong initial defocusing of negative phases essentially eliminates such particles from the beam and so negative phases can be neglected.) The defocusing space charge force is, in contrast with the applied external forces, approximately independent of radius due to the offsetting effects of the azimuthal length of the charge distribution increasing linearly with radius and the radius gain per turn decreasing inversely with radius. As a result, for a given phase, the beam in the region of minimum restoring force will expand, losing particles to the dee, until the focusing force exceeds the repulsive force. Since the focusing strength passes thru a local broad minimum in this vicinity, the uniform charge approximation to the space charge force given by Blosser and Gordon[9] should be a good description of the situation—Holm has elegantly applied this expression to the situation[10], doing the appropriate integrals over the phase distribution to take account of both the phase dependence of the focusing force and the phase dependence of the capture process (discussed in a following paragraph) and also including corrections for edge effects. Depending on the choice of K, and very sensitively on the range of phases accepted at the center (also discussed in a following paragraph), Holm's formulas predict internal beam currents for the Cern conversion as indicated in Table I.

The remaining important central region consideration in an FM machine is the question of capture of particles into the stable region of the acceleration phase space. Fig. 4 shows a normal synchrotron oscillation bucket with the initially populated area indicated by the cross hatched area[11]. Other parts of the bucket cannot contribute to the capture process since (a) particles to the right of the 90° line would have to initially leave the source against a decellerating voltage and (b) particles above the line AB will return to zero energy on the first synchrotron oscillation. Fortunately nearly all of the capture region occurs in the area of positive focusing, the gray area of the figure—only the overlaping section of the two regions can contribute to the useful beam.

The rough triangular shape of the capture region in combination with the strong vertical focusing near 90° places a major premium on extending the region of useful phase as close as possible to the 90° line. Obviously one cannot however go all the way to ϕ =90°, since at this limit the initial energy gain vanishes and particles fail to clear the ion source on the first turn. Looking again at Fig. 1 it is in fact clear that for the situation therein, phases appreciably beyond 60° fail to clear the source. Other geometries[12] may allow this limit to be extended to 70°—the entries in Table I show clearly how important this point is in determining the total current.

Question has been raised in the litterature[13] as to whether particles completing an initial phase oscillation will significantly add to the charge density seen by later particles and thus reduce the expected currents. In a conventional open source SC this effect is undoubtedly important since the large radial oscillations allow particles of many different energies to overlap. On the other hand in the limit of zero radial oscillation, which the revised SC's should closely approximate (expected radial amplitudes of a few mm) there is never an actual spatial overlap of particles from a previous phase oscillation with particles then leaving the source since the E, ϕ phase is in this limit a unique, one-to-one map of a rotating r, θplane and clearly from Fig. 4 no overlap ever occurs in the E, ϕplane. The effect of returning particles can then at most be in the category of edge effect contributions to the space charge force. If this

force is computed to begin with in the infinite sheet approximation[9], as is usually the case, then such edge effects are automatically already included. The distinct spatial position of particles with different E or ϕ is illustrated in Fig. 5.

Finally, a brief comment as regards the central region of a possible CW conversion. The comment can be brief since such a conversion would involve essentially no central region difficulty. The voltage would be much higher, thus giving more latitude for clearing the source and the current and space charge effects would be more than a hundred times less for equivalent total beam. The physical layout of the central region would be about the same as that shown in Fig. 1, the focusing forces much the same as Fig. 2, but in each case with much less stringent requirements to satisfy. The design could in fact be almost directly taken over from some one of the very successful low energy cyclotrons, the boundary conditions being essentially identical. Hence as regards the central region, a CW conversion would be extremely simple compared to the FM situation.

Acceleration System

An empirical comparison of existing synchrocyclotrons immediately shows that machines with the highest current are those with the highest FM repetition rate and that in fact the accelerated current varies roughly linearly with rep rate from machine to machine. For so-called "narrow gap" geometries such as conversions normally contemplate, the capture process has been thoroughly studied as described in the previous section—results of such studies give a firm theoretical basis for anticipating approximately linear gain in current[11] as the rep rate is increased and so conversion plans place heavy emphasis on achieving a higher repetition frequency. Many large SC's presently derive their FM modulation cycle from the variable capacitance of large vibrating plates (called tuning forks)—due to mechanical problems no significant increase in the repetition rate of such tuning forks appears feasible and therefore a shift to a different type of modulator system is necessary. The most promising alternative is a rotating capacitor such as the Cern design[1] shown in Fig. 6, a device somewhat reminiscent of a steam turbine in that rows of blades on rotor and stator are first in line and then out of line as the rotor turns giving a capacitance variation with rep rate equal to the rotation frequency times the number of blades per circle. While such capacitors have been in use at Orsay and Dubna for a number of years, they never-the-less remain a formidable design problem due to the difficulties of designing bearings to work in vacuum in the presence of intense RF radiation and yet carry a massive, very rapidly rotating rotor. The development of appropriate devices in fact depends heavily on the technology of steam turbines—systems to produce rep rates of order 500 hz appear possible which is a tenfold increase over the 50 hz characteristic of present tuning fork systems.

A further significant gain in intensity can be obtained from careful tailoring of the waveform of the FM cycle. Fig. 7 shows for example the contemplated frequency vs. time profile for the Cern conversion compared with a typical sine curve with the same accelerating capability. The accelerating portion of the Cern frequency curve is derived from the requirements that the region of stable phase oscillations (the "bucket") shall have the same area at every frequency—for given dee voltage an f vs. t of this form accomplishes acceleration of all captured particles to the maximum energy in the shortest possible time. The sinusoidal f(t) by contrast produces a bucket of varying area—since the accelerated flux is determined by the smallest size of the bucket, the period of the sine wave for equivalent accelerative effectiveness must be adjusted such that its df/dt is never greater at a given frequency than that of the tailored curve and the period for the Fig. 7 sine wave has therefore been fixed on this basis. The programmed frequency also gains by using a very high df/dt in the non-accelerative return part of the FM cycle (the flyback). The two factors together produce a shortening of the cycle by nearly a factor of three which should produce an increase in beam by the same factor.

In order to reduce the capacitive load on the rf system, it is desirable to make the dee as small as possible; this is usually done by folding back the leading edges so that the dee as viewed from the top subtends considerably less azimuth than the normal 180°. In two dee machines such cut back dees are common[14] and lead to no undesirable effects since each accelerating gap is balanced by the gap 180° away on the opposite dee. With a single dee an unbalanced acceleration obviously results when the dee is cut-back—the first harmonic component of this unbalance acts to drive the radial focusing oscillation (the frequency of which is always near unity) and the amplitude of the radial oscillations is increased. The extent to which the oscillation is increased depends on the synchrotron oscillation—as the particles change phase

the acceleration at the two gaps of a cut-back dee change in relative as well as absolute magnitude—for some situations the radial amplitude increases by several centimeters[15] thus largely washing out the benefits derived from the closed ion source. As a result of this some projects propose to leave the dee at 180°, while others contemplate a modest trimming at large radii only, which is much less deleterious since (a) Q_r is further away from unity and since (b) the coupling involves always a $\Delta E/E$ coefficient. The Cern design for example uses a cutback which reduces the dee capacitance by nearly 25% while enlarging the radial amplitude by only about 1mm[16].

For a CW conversion the RF problems are of a very different character and apparently significantly simpler than for the FM systems. No modulator would be needed and the CW frequency would correspond to that of the low end of the RF cycle i.e. 15 to 16 MHZ. High energy gain per turn would be very important and a system with two 90° dees operating in the vicinity of 90 kilovolts is one of the most attractive options, thus yielding a maximum energy gain per turn of 250 KeV. As regards RF power the lower frequency and higher Q of the CW system would tend to offset the higher voltage leading to a power requirement not greatly different from that for an FM system operating at 30 KV.

Magnet

The complexity of magnet modifications tends to be just the reverse of that for the RF system i.e. a program such as at Cern which plans to leave the magnet as is (except for a possible small enhancement of the central cone) clearly has essentially no magnet problem—a conversion to partial isochronism such as at Columbia involves major modifications to the magnet but no critical tolerances except on imperfections—a fully isochronous conversion while superficially similar to the partially isochronous machine, involves very strict magnet tolerances which would necessitate a layer of trimming coils on the pole face.

Figure 8 shows one of the magnet arrangements which the Columbia group has studied[8] in planning the conversion of the Nevis cyclotron to partial isochronism. As mentioned, the design is unusual in that one of the sets of hill shims is mounted inside the dee; the resulting narrow gap leads to high flutter as shown in Fig. 3 and also extends the useful radius of the machine thus adding to the final energy. If the sectors are placed on the magnet pole as is more conventional, the focusing force in the center would rise slowly due to the $(r/g)^N$ dependence and one would be inclined to supplement the flutter focusing with an admixture of gradient focusing. Unfortunately this implies that the radial focusing frequency will pass thru the integral resonance $Q_r=1$; this is routine in CW cyclotrons but the lower energy gain and phase oscillations of an SC might lead to prohibitive first harmonic tolerances—this point requires careful investigation before a cone and flutter can be safely combined in an SC.

As regards CW conversions—the magnetic field is by all odds the controlling problem. There is first of all the question of whether enough flutter can be obtained to offset the strongly defocusing k term of eq. (1)—previous studies have concluded that a major loss of energy would result from such a conversion if it were attempted within the restrictions of existing magnets. These earlier studies were however conservative in their choice of spiral angle in order to avoid the laborious task of checking stability limits in the presence of a tight spiral. Stimulated by intellectual interest in this problem, an MSU group has recently completed a detailed numerical study of the question of how much spiral can be safely employed. The results of this study[18] establish that much tighter spirals can be used than were previously considered—with such spirals CW conversions can be accomplished by inserting spiral shims into an existing SC magnet with only a small loss of energy.

Fig. 9 shows the magnetic field shape assumed for the MSU CW conversion studies and the resulting Q values and phase slip. (The crucial problems of course occur near the edge of the magnet and so only this region is shown.) The magnetic field was assumed to have a pure sixth harmonic azimuthal dependence with flutter corresponding to results of a general model study by Smith[19] and with the edge shaped to match existing data for a magnet with 16 cm hill gap. The field is hence a realistic conversion possibility for a 5 meter diameter magnet.

From the fig. the axial frequency, Q_z, is seen to be of order 0.3 thruout the acceleration region which implies excellent focusing. These Q values and the threshold energy gain per turn, F(E), are moreover obtained numerically via integration of exact equations of motion rather that from approximate equations such as (1), and are therefore exact for the field shape assumed. From the figure it is seen that the useful region of field terminates at a radius of about 228 cm corresponding to an energy of 515 MeV. To reach 600 MeV, which a 5 meter magnet would readily do if operated FM, the average field would need to be raised

by 2 kilogauss and the flutter increased from 0.22 to 0.25. Smith's data show however that the flutter will decrease if the average field is raised and so hill coils would be necessary. The added complexity and cost of such coils would have to be weighed against the program advantages resulting from 600 MeV operation vs 515 MeV.

Interestingly, the spiral angle employed in the MSU conversion studies is limited by magnetic considerations rather than by stability. This arises from the fact that the perpendicular distance between ridges decreases as the spiral is increased—this causes the flutter to fall and at some definite angle the decrease in flutter begins to exceed the increasing $\tan^2\alpha$. From such considerations an α in the vicinity of 75° is found to produce maximum axial focusing force for a magnet of the type considered here. The more than adequate stability limits are evidenced in Fig. 10 which shows a 500 MeV phase plot. (In an earlier study of a 4 sector tight spiral field the reverse situation was found—i.e. stability vanished before the spiral of maximum magnetic effectiveness was reached.)

The key difficulty in a CW conversion stems not from stability or focusing but rather from field tolerances. If the accelerating system produces an energy gain of 250 kev/turn the total number of turns would be in the vicinity of 2500 and a field change of 1 in 10,000 would produce total loss of beam. This is however not a prohibitive tolerance—good magnets are now normally stable to a part in 100,000 and a few parts per million has been achieved in special situations. The problem also does not require significantly higher accuracy than has already been achieved in low energy cyclotrons—the MSU cyclotron for example with 220 turns maintains the particle phase to within 5° of the design value[20]. A ten fold increase in the turn number would cause roughly a 10 fold increase in phase fluctuations to ~50° which would be large but still acceptable. Moreover in view of the superior magnetic measuring systems now available as compared with 1964 when the MSU field was mapped, one should be able to determine the fields in an isochronized SC to considerably greater accuracy than was achieved at MSU.

The net work of circular pole face coils required in a CW conversion is also a distinct disadvantage and usually a major argument against such a conversion. Interestingly the requirements on such a coil array appear never to have been quantitatively assessed. The number of coils can be estimated from the achieved results in the smaller machines—one coil per 30 turns should control the phase to an accuracy of about 5°—one coil per 50 turns to an accuracy of about 10°—hence of order 50 coils would be required, individually powered. The coils would have more than adequate strength if they were capable when all powered together of raising or lowering the central field, by 10% (which incidentally in an optimized magnet would also imply an energy variation capability approaching 50%). If the coils are alloted 20 mm of space on each side of the gap and are assumed constructed with a 50% packing factor a total power of ~350 kw would be required. (The kw are calculated assuming the trimming currents bunch at the outside in the same way as the orbits.) Power supply costs would thus be in the vicinity of $100,000. The magnet problem for a CW conversion is hence seen to be formidable but clearly solvable—the cost factors are not significantly different from those for a partial isochronization as regards the iron—the additional cost of circular pole face coils and power supplies is substantial but still fractionally small compared to the total cost of a typical conversion.

Extraction

A major goal of all of the SC conversions is an efficient extraction system. Present systems in the large SC's yield efficiencies of order 5%—CW cyclotrons by comparison achieve efficiencies in the 50-100% range. The most significant difference in the two situations is the enormously smaller radial betatron amplitude of the CW machines. The improved SC's should however have a radial amplitude essentially the same as that of the CW machines and so intuitively one expects a much higher extraction efficiency from the revised SC's. It will never-the-less be comforting when a firm design for a high efficiency system for an SC is actually exhibited and its performance demonstrated. Such a demonstration via the computer is to be expected in the not too distant future since the various groups are working vigorously to arrive at a firm design. Given the known reliability of modern orbit tracking procedures a full numerical demonstration of performance should be equivalent to a direct experimental test although anxieties will certainly persist in the minds of many until an actual experiment is accomplished.

The studies of extraction now in progress are centered in every case on peeler-regenerator systems such as are presently in common use on SC's. Extensive numerical studies at both Berkeley[21] and Cern[22] have recently greatly clarified the understanding of such systems. The key difficulty is the $Q_r=2Q_z$ coupling resonance which occurs as a stop band in the edge region of any cyclotron field.

The effect of this coupling resonance is to periodically exchange radial and axial betatron amplitudes. Since the function of a resonant extraction system is to build up the radial amplitude so that it will clear a thick septum such as on a magnetic channel, a huge beam loss occurs when this large radial amplitude is converted to an axial amplitude.

The Berkeley and Cern studies both exhibit many detailed examples of the phenomena—so detailed in fact that considerable effort is required to assimilate the significance of the results. The phenomena has also been extensively studied in low energy cyclotrons[23]—a compact display of the key point is shown in Fig. 11 where the region of stable axial motion is plotted vs. radial position for three energies. The region of axial stability is seen to shrink as the energy increases finally reaching a point where no portion of the r, p_r plane is axially stable. These results do not obviously establish that a beam with small initial radial amplitude will behave better than one with large amplitude since the coherent amplitude induced in the extraction process must in either case be large. To circumvent this difficulty Paul is studying the possbility of inserting optical elements in the field which have unit transfer matrix for the radial motion, thus leaving it undisturbed, while the axial transfer matrix is arranged to correct the instability. Since the instability is a linear phenomenon, it can be removed by linear elements and Paul reports promising results from initial studies[24].

Lindbeck has emphasized the point that a linear instability always possesses inflowing as well as outflowing asymptotes—particles with z, p_z initally in the vicinity of an inflowing asymptote will require a much longer time to exceed any given growth threshold—this time can be sufficiently long to allow extraction to take place and in fact most of the successfully extracted particles from present systems appear to be due to such z, p_z initial conditions. Never-the-less, there appears no possibility of obtaining high efficiency extraction by an initial biasing of the phase in the z, p_z plane since in an SC the phenomena of precessional mixing[25] would totally smear out any such bias.

An attractive option not yet included in any of the conversion plans is to make the extraction system septum much thinner, either magnetically by use of current sheets or electrically by means of a high voltage deflector assembly such as in low energy machines. A system of the latter type would have less bending capibility than a magnetic system but still significant (the velocity of a 600 MeV proton is only twice that for 84 MeV). A multi-stage system of electrostatic field, followed by coil, followed by iron, such as is used on the Oak Ridge Isochronous Cyclotron[26] would be a very attractive system. Given the knife edge septum of such an arrangement there would be no need for the radial amplitude ever to exceed 1 cm and the problem of axial instability should therefore dissappear. With careful alignment the extraction efficiency would be expected to reach the 80% level achieved by the Philips group in a similar situation[27].

An essential element in a great many experiments with SC's (those that involve determining coincidences) is the duty cycle. Interestingly it is in this area, formerly deemed a major disadvantage of the SC, that the machines are most likely to outdo their modern competitors, the linear accelerator and the CW cyclotron. Basically the advantage of the SC on duty cycle arises from the ability to terminate the main acceleration process at any radius by turning the voltage off, leaving a "stacked" beam. Such a beam can then be slowly extracted by appropriate special devices—most present SC's in fact already have such an arrangement usually referred to as the slow extraction or stochastic extraction system. Space will not permit a detailed discussion here of the various slow extraction techniques but an article reviewing the question will appear elsewhere[28]. The principle conclusion of this study are (a) that multiple cycling slow extraction systems (of which the present Cern system is a typical example) will function less well in the converted machines than at present since such systems derive most of their present effectiveness from large radial amplitude and (b) that a system using a time dependent magnetic perturbation as proposed by Kim[29] should perform splendidly producing a total duty cycle (including both microscopic and macroscopic factors) in the vicinity of 80%. For comparison the CW cyclotron even with flat-topped RF, can not be expected to exceed 25% (100% macro d.c. X 25% micro d.c.) and linacs are unlikely to exceed ∿2% (5% macro d.c. X 40% micro d.c).

Finally, a few remarks on the extraction problem in a CW conversion. Referring to Fig. 9 one sees that the only possibility for a resonant extraction is at Q_r=3/2—to reach any other resonance the treshold energy gain per turn, F(E), would be excessively high. The 3/2 resonance could easily be excited by a small third harmonic field gradient leading to an amplitude growth much as in a conventional peeler-generator system except with the possibility open of extracting the beam at any of three azimuths if desired.

The fact that two Q_r=3/2 transitions occur within ~10cm of each other is an awkward point—one could (a) use the inner and give up 10cm of useful radius or (b) produce a third harmonic which is zero at the inner transition and rising rapidly at the outer transition or (c) manipulate the field to enlarge the radial separation of the two transitions. The last option is probably the best solution but a firm conclusion requires further study.

Conclusions

Both the Cern type conversion (leaving the magnet unchanged) and the Columbia type conversion (partial isochronization) appear certain to increase the internal beams of synchrocyclotrons by approximately an order of magnitude to a level of at least 10μa. At the same time the radial amplitude will be reduced by more than an order of magnitude which should allow very efficient extraction (using a thin septum and small radius gain per turn if by no other means). Combining the increase in internal beam and the increased extraction efficiency—an approximate hundred-fold increase in the external beam is implied. Assuming an extraction efficiency of 50% the expected internal currents are considered to be as high as practical due to the severe induced radioactivity and the necessity for possible maintainance operations. A CW conversion also appears practical on roughly the same budget and time scale as the planned conversions—a small decrease in energy would probably result but higher extraction efficiency should be achieved (~80%) and external beams could thus be pushed up by an addition factor of four for equivalent internal loss.

References

1. MSC Staff (Cern)—Proposal for the Improvement of the 600 MeV Synchrocyclotron-Aug. 1967 - (private comm.).

2. Columbia-Yale Staff—Proposal for a Major Modification to the Nevis Synchrocyclotron - Jan. 1967 - (private comm.).

3. Glazov, et.al.—High Current Phasotron at 700 MeV - JINR 9-3951 - 1968.

4. R. S. Livingston and R. J. Jones, Rev. Sci. Inst. 25(1954) 552. A closed source was installed on the Orsay SC in 1965. Debray, Cabrespine and Baixas - European Colloquium on AVF Cyclotron - April 1965 (private comm.).

5. R. Galiana—Informal Meeting on SC Development - Feb. 1968 - (private comm.).

6. K. R. MacKenzie—Nucl. Instr. Meth. 31(1964)139.

7. Symon, Kerst, Jones, Laslett and Terwilliger—Phys. Rev. 103(1965)1837.

8. R. Cohen—(private comm.)

9. H. G. Blosser and M. M. Gordon—Nucl. Instr. Meth. 13(1961)101.

10. S. Holm—Nucl. Instr. Meth. 64 (1968)317.

11. S. Kullander—Cern 66-27(1966).

12. S. Holm—(private comm.).

13. J. Rainwater—Rev. Sci. Instr. 37 (1966)262.

14. W. P. Johnson—Cern 63-19(1963)279.

15. J. P. Scanlon—Induced Radial Amplitudes in the Modified Cyclotron-1966 - (private comm.).

16. H. G. Blosser—Summary of Numerical Studies of Radial Amplitudes Induced in the Cern SC by Cutback Dees-Aug. 1967- (private comm.)

17. N. Vogt-Nilsen—(private comm.)

18. Blosser, Johnson and Loucks—Rev. Sci. Instr. - (submitted for publication)

19. P. F. Smith—Jour. Nucl. Energy Part C 1(1959)55.

20. Berg, Blosser, and Gordon—Nucl. Instr. Meth. 58(1968)327.

21. A. C. Paul—UCRL - 18211(1968).

22. S. Lindback—(private comm.)

23. Blosser, Gordon and Arnette—Nucl. Instr. Meth. 18, 19(1962)488.

24. A. C. Paul—(private comm.)

25. H. A. Grunder—Trans. on Nuc. Sci. NS-13-4(1966)371.

26. Hudson, Lord, and White—Trans. on Nucl Sci. NS-13-4(1966)101.

27. H. L. Hagedoorn and P. Kramer—Trans. on Nuc. Sci. NS-13-4(1966)64.

28. H. G. Blosser—Nucl Instr. Meth. (submitted for publication).

29. H. Kim—Trans. on Nucl. Sci. NS-13-4(1966)58.

*Supported by the National Science Found.

Table I. Typical estimates of max. current for improved synchrocyclotron with dee voltage of 30 KV (from ref. 1 & 10).

cos ϕ_s	K	rep rate(hz)	starting phase(deg)	current (μa)
0.1	2	830	0-45	7
0.1	2	830	0-60	14
0.1	2	830	0-75	22
0.3	2	875	0-60	9
0.3	5	1060	0-60	15
0.05	2	495	0-75	50

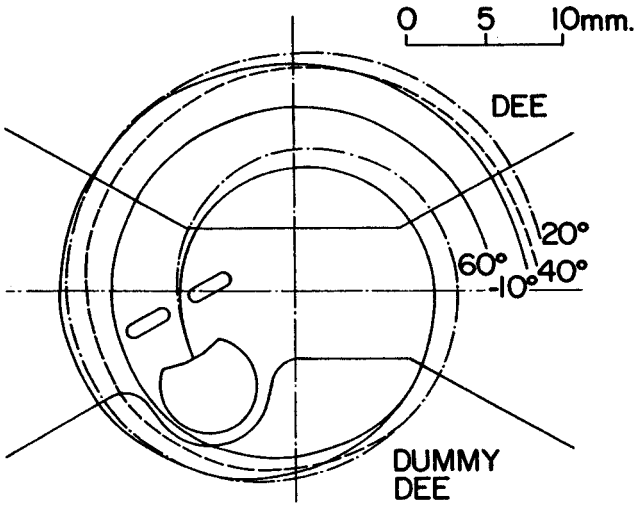

Fig. 1. Possible source, puller and dee arrangment for the Cern conversion showing orbits for four initial phases (from ref. 1).

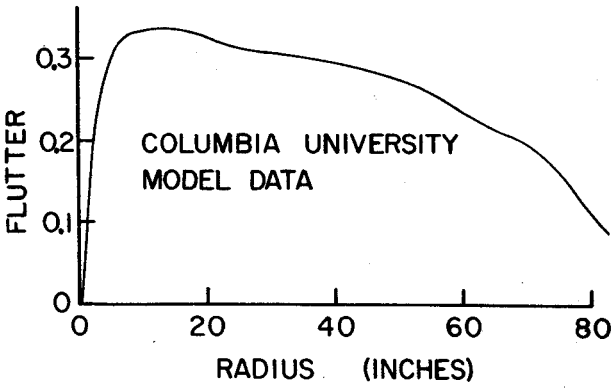

Fig. 3. Flutter coefficient, f(r), from Columbia University model study (ref. 8).

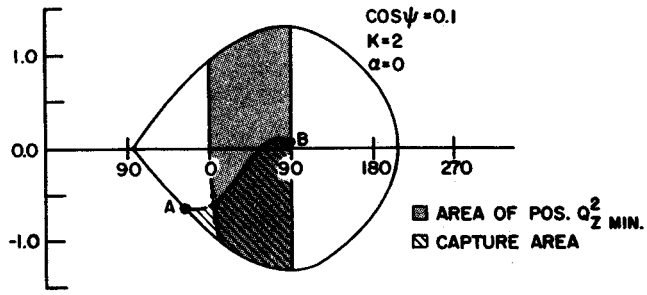

Fig. 4. Region of stable phase oscillation showing capture region (cross hatched) and region of positive axial focusing (gray). Horizontal axis is phase, vertical axis is df/dt in reduced units (from ref. 10).

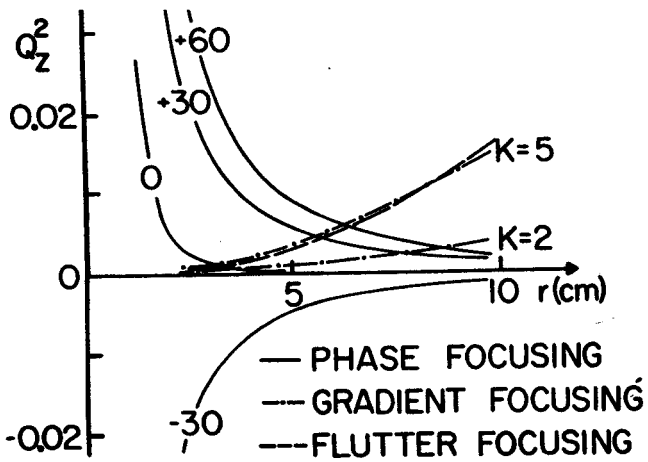

Fig. 2. Axial force coefficients ($Q_z^2=F_z/m\omega^2 z$) in the central region. Phase focusing and gradient focusing data from ref. 1, flutter focusing from ref. 8.

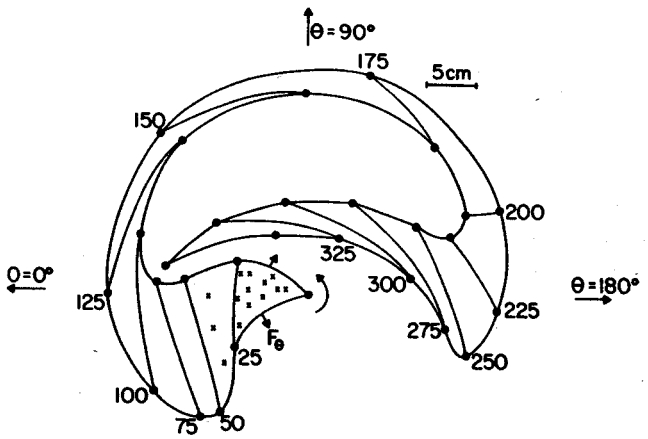

Fig. 5. Position of two typical particles after various numbers of revolutions in the central region. Coordinate system rotating with RF frequency (from ref. 1).

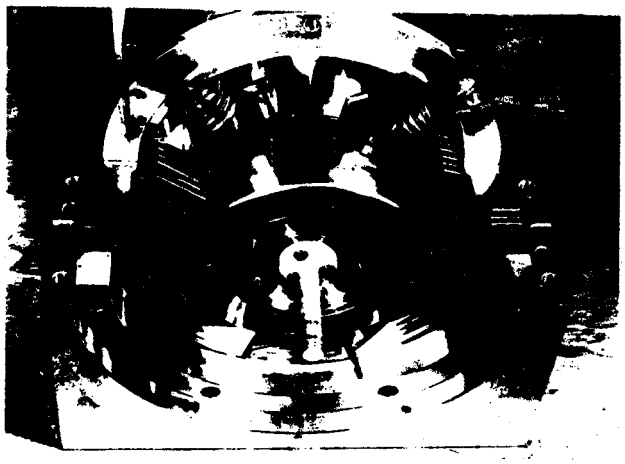

Fig. 6. Photograph of model of possible rotating capacitor for revised Cern SC (from ref. 1).

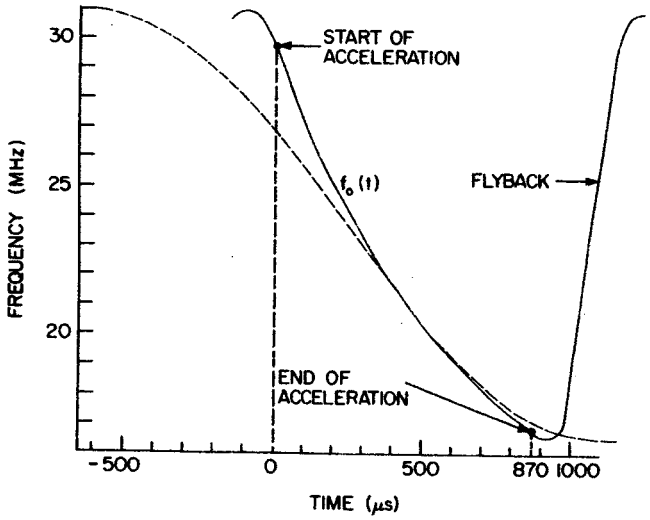

Fig. 7. Solid line-proposed frequency vs. time relation for the revised Cern SC (from ref. 1). Dashed line—half cycle of sine modulation having same minimum bucket area as solid curve.

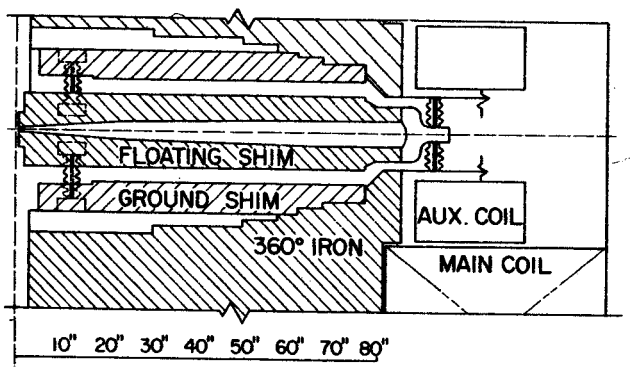

Fig. 8. Cross section view of possible sector shim arrangement for Columbia Nevis cyclotron. (from ref. 8.)

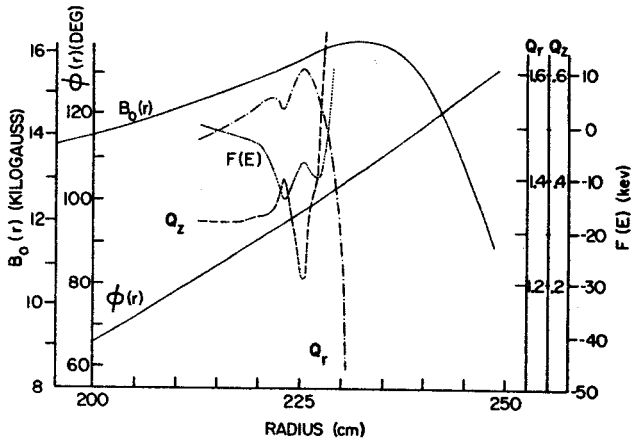

Fig. 9. Magnetic field components for MSU study of CW conversion. Field per eq. (2) with f=0.224 and N=6. F(E) is threshold energy gain per turn for acceleration to the given radius and Q_r and Q_z are radial and axial focusing frequencies. (from ref. 20)

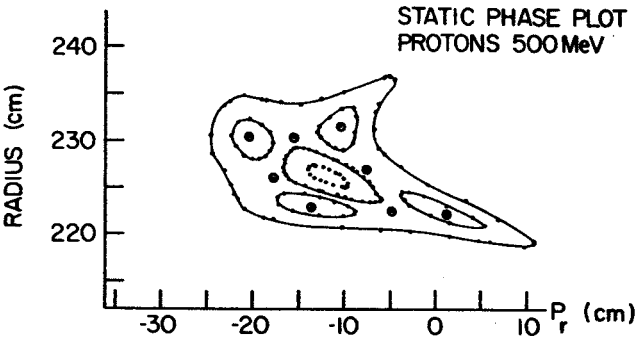

Fig. 10. Plot of radial phase space for 500 MeV protons in field of Fig. 9 (from ref. 20).

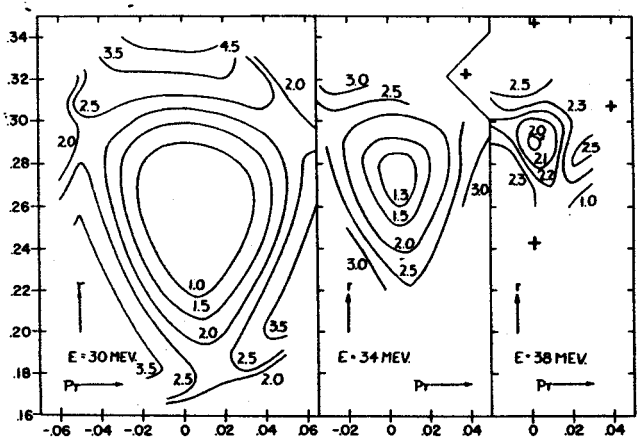

Fig. 11. Equi-trace contours for axial transfer matrix vs. position in radial phase plane for three energies in magnetic field of MSU Cyclotron. Region <2.0 is axially stable—region >2.0 is axially unstable (from ref. 25).

USE OF A SIGMA-7 IN A NUCLEAR PHYSICS LABORATORY*

W. Benenson, R. A. deForest, R. F. Au, D. L. Bayer and W. E. Merritt
Michigan State University Cyclotron Laboratory

ABSTRACT

Advanced features of the Scientific Data Systems Sigma-7 computer are being used at the Michigan State University Cyclotron Laboratory to produce a system which meets all of the needs of the laboratory. The computer is capable of large off-line tasks such as distorted wave Born approximation calculations and large on-line jobs such as 16K channel pulse height analysis and particle identification. Several off-line jobs can be time-shared with safe real-time operation using a supervisor program called JANUS.

In nuclear physics research, computers are used for data taking, data analysis, experimental control and theoretical calculations. The experience at the Michigan State University Cyclotron Laboratory with a Scientific Data Systems Sigma-7 computer has shown that a single computer can be well suited to performing all of these functions and can do them all at the same time. To achieve this a great deal of systems programming was required in the laboratory.

The foremost example of the systems programming done in the laboratory is a supervisor program called JANUS[1] conceived and written by two Michigan State graduate students. JANUS makes extensive use of the memory map, memory protection and rapid access disc to permit time-sharing of off-line tasks concurrent with safe real-time operation. An example of the power of the JANUS system occurred during a recent gamma-ray experiment in which the computer was simultaneously serving five different users; 1) the real time job which was 4096 x 4096 event logging on tape at a rate of 500 cps; 2) data analysis of a previous experiment using an oscilloscope; 3) batch plotting of spectra submitted by a variety of users; 4) a long FORTRAN job using a file monitor which holds all its results for outputting at the end of the job; 5) a FORTRAN debugging operation. The effective size of the computer for FORTRAN jobs was 128K words. The philosophy and implementation of JANUS are described in ref. 1).

HARDWARE

The central processor hardware shown in Fig. 1 consists of 32K 32-bit words of core, memory mapping and protection, floating point and 8 external interrupts. Peripheral equipment includes a 400 cpm card reader, 300 cpm card punch, 60k bpm magnetic tape transport, 600 lpm line printer, 1.5 megabyte rapid access disc, two teletypes, a large

MICHIGAN STATE UNIVERSITY CYCLOTRON
SIGMA 7 CONFIGURATION

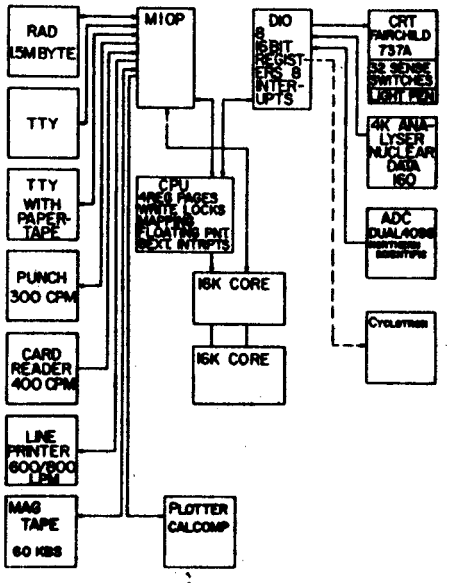

Figure 1

*Work supported in part by the National Science Foundation.

Manuscript received 13 May 1968.

screen cathode ray tube and a digital X-Y plotter. Connected to the computer are 8 16-bit registers which form part of an interface to external circuits. At present a 4K multichannel analyzer and a dual 12-bit analog to digital convertor are connected to the interface. Multiplexed channels for reading or writing in digital or analog form are being added to the interface, and the ADC's are being expanded to 4 13-bit ADC's. Computer controlled pulsers are being built for experiment simulation and continuous drift checking.

OFF-LINE USE

One feature of the off-line use that has been developed in the lab is extension of the effective memory by demand paging. In spite of the fact that this capability is available in the hardware of the computer, no use was made of it in the system providing by the manufacturer. Under demand paging, the size of programs which can be run on the Sigma-7 is not limited to the memory size (32K) but rather the number of addressable locations (effective address space). This is achieved by efficient demand paging from the disc. The memory map keeps a table of locations for each page (512 words) of memory, and pages are kept on the disc until needed. The overhead cost in time for this procedure is negligible for programs that are smaller than the real memory and grows as the programs grow. The actual computing time for a calculation may be 1 to 5 times that of the CDC 3600 at the computer center on campus, but of course the turn-around-time is so much shorter that the Sigma is in continuous demand for straight calculations. Besides large programs many small calculations are carried on daily. These are for example, beam optics calculations, kinematics, energy loss and straggling, etc. A sophisticated data analysis program has been written which uses the cathode ray tube and 32 sense switches. This program produces peak area and centroids in a form acceptable to programs which calculate excitation energies and cross section as a function of angle.

ON-LINE USE

Analog to digital converters are used for on-line data acquisition. Using halfwords as channels 16,000 channel analysis can be carried out and displayed on the screen. While taking data, the display can be used to define regions of interest. For example if counter telescope is being used, total E is plotted versus $E \times \Delta E$ and a region is chosen where the events corresponding to one type of particle will lie. A table is then stored for the allowed E and $E \times \Delta E$ for that particle. Up to five different particles can be separated and stored in 2048 channel spectra. Time and energy are also being used to separate masses[2] by plotting t^2E versus E. Routing bits are available to identify the counter from which the pulse came in the case of multicounter experiments. The computer can monitor and diagnose the behavior of the cyclotron by reading the current on a differential beam probe as a function of radius inside the machine. Equipment is being built for picking up the information needed during an experiment such as angles, pressures, scaler readings etc. Computer control of the cyclotron and external beam system has almost finished the design stage and will be implemented over the next year.

SUMMARY

At present the physicist uses the computer in almost every aspect of his experimental program. From the very beginning, when he is considering the feasibility of the idea he has had, to the very end, when he is preparing figures for the publication, the reliability of the computer enters directly into his productivity. The computer's reliability thus becomes perhaps even more important to the nuclear physics program than the reliability of the accelerator. A more serious problem has been the amount of time and effort that has been required to make the computer as useful and as flexible as it has proven to be. Much of this effort has been done on the systems level which really should be the manufacturer's responsibility. On the other hand, the education and experience obtained in this effort are an important asset in the continuing development of the computer system.

REFERENCES

1) J. O. Kopf and P. J. Plauger, Bull. Am. Phys. Soc. 13, 700(1968). P. J. Plauger and J. O. Kopf, op. cit. 13, 701(1968). J. O. Kopf and P. J. Plauger submitted to Fall Joint Computer Conference 1968.

2) C. N. Davids, S. M. Austin, Bull. Am. Phys. Soc. 13, 882(1968).

Summary of the Panel Discussion on the Use of Computers in Accelerator Experiments

Moderator:
William C. Parkinson
University of Michigan

Panellists:

Robert A. Chalmers
Lockheed Research Laboratory

Charles D. Goodman
Oak Ridge National Laboratory

Paul C. Rogers
Brookhaven National Laboratory

Walter Benenson
Michigan State University

Martin W. Sachs
Yale University

Moderator: The paper presented at this session by R. A. Chalmers illustrates that fairly complex data acquisition problems including gain stabilization of five ADC channels can be handled with a fairly small computer, an SEL 810A. The next four papers described systems based on larger computers (SEL 840A, Sigma-7, Sigma-7, and IBM 360/44, respectively), yet the data acquisition requirements do not appear to be significantly more complex. This observation suggests that nuclear physicists want their own computers to compute with.

I would like to ask the panel to state their opinions about the use of "data acquisition" computers for general computations and the need for quick computations during accelerator experiments. Is there a valid justification for general purpose computers at accelerators apart from the obvious need for complex data acquisition?

Panel: All of the panellists felt that calculations during accelerator experiments are necessary. The consensus was that an on-site computer is required unless a computer center is nearby and can provide turn-around times of a few minutes.

Question from the audience: The panel was asked whether two small computers would be better than one large one.

Panel: The panel states that there is no simple answer to that question. An objection to the two-computer approach is the high cost of peripherals. On the other hand, systems programming should be simpler, provided that neither computer is too small. The panellists thought that a two-computer system is attractive if one computer is large and the other small.

Question from the audience: Should the computer be used to set up experiments, to set amplifier gains and discriminator thresholds?

Panel: No one on the panel could think of a situation in which such an approach would be useful. It would certainly imply frequent repetition of the same experiment.

Moderator: For the sake of provoking discussion I would like to contend that the utility of light pens and CRT displays has been over-rated. What the nuclear physicist really wants is a quick, cheap, hard copy of numbers and graphical displays that he can carry away from the hectic atmosphere of the computer room to ponder over in the quiet of his office or to paste in his notebook. Would the panellists like to make any comments on this contention?

Panel: The panel believes that a means of monitoring on-line data acquisition is essential and this implies a CRT display. Different people have different preferences concerning displays vs. printed graphs for data analysis. There should be some form of interactive output, and a light pen with a CRT provides this. Light pens are good if many points have to be marked. For a few points there are good alternatives using switches or track balls.

Paul Rogers made the following closing comments:

One first ought to consider buying or copying a system. When one strikes out on ones own, he should remember that hardware usually accounts for no more than 50% of the cost of the system. A good estimate of programming speed is 6 to 8 instructions, or 6 to 8 lines of Fortran, per 8 hour day debugged and documented.

At the present time the maximum rate for data being collected and stored by on-line computer systems is on the order of 10^6 bits per second.

One must decide whether he wants to tinker or to produce physics. They are not compatible.

In summing up, the panel also expressed the opinion that the Grossingers Conference in 1962 and the Karlsruhe Conference in 1964 were useful and the panel recommended that open conferences be held at regular intervals.

LIFETIMES OF ROTATIONAL STATES FROM HEAVY-ION REACTIONS*

R. M. Diamond, F. S. Stephens, W. H. Kelly,† and D. Ward‡
Lawrence Radiation Laboratory, University of California, Berkeley, California 94720
(Received 23 January 1969)

The half-lives of several transitions in the ground-state collective bands of ^{160}Er, ^{158}Er, and ^{156}Er produced by (^{40}Ar,$4n$) reactions have been measured by a recoil-distance Doppler-shift method. These lifetimes are compared with those of several models. The mean time interval between the reaction and the population of the ground band was also determined.

The measurement of transition moments is an important method of testing nuclear models. In particular, the $E2$ moments of the $2 \rightarrow 0$ transitions in the ground-state collective bands of even-even nuclei have yielded much information on the nature of these bands. In the present work we have measured the $2 \rightarrow 0$ and several higher ground-band $E2$ moments (lifetimes) in each of three even-even Er nuclei, using a recoil-distance method. These nuclei were produced in the reactions ^{120,122,124}Sn(Ar, $4n$)^{156,158,160}Er.

The recoil-distance Doppler-shift method[1] is well suited to measure half-lives in the range 10^{-9}-10^{-12} sec.[2-5] Basically the method consists of stopping part of the excited nuclei recoiling from a thin target with a movable plunger placed closely behind the target. The fraction of the nuclei that live long enough to reach the plunger before emitting their radiation will yield a normal gamma-ray line, whereas the rest will decay in flight and yield a Doppler-shifted line. By varying the distance of the plunger from the target,

the fraction of unshifted transitions can be changed, and one can obtain the half-life of the transition if the velocity of the recoiling nucleus is also known.

The (Ar, $4n$) reaction produces a tightly collimated beam of product nuclei recoiling along the beam direction. Using a Ge(Li) detector at 0° to the beam direction, we were able to resolve completely the shifted and unshifted lines for all transitions over ~100 keV. The average recoil velocity could be obtained directly from the fractional energy difference of the shifted and unshifted lines after a correction was made for the finite solid angle of the detector (the effective angle is different from 0° for large solid angles). The lead-covered plunger was attached to a precision micrometer with which its position could be adjusted to ±0.002 mm. The targets were 1-mg/cm^2 thick metallic foils of separated tin isotopes which were supported over seven closely spaced holes, 1.5 mm in diameter, in a tantalum disk. The foils were examined under a microscope and found to be flat within about 0.01 mm.

Some typical spectra for ^{160}Er are shown in Fig. 1. We have integrated the areas under the shifted and unshifted peaks and calculated the fraction of each line that is unshifted at each distance. The analysis of these data is rather complex as account must be taken of the preceding rotational transitions and also of the 10-20 unobserved transitions that precede entry into the ground band. The (Ar, $4n$) reactions are advantageous in that almost all the feeding of the ground band occurs at high spin values. Thus the formation and decay of a given level are marked by the ground-band transitions which populate and depopulate that level. In the analysis we have used a computer program which considers three consecutive transitions at a time, e.g., $8-6-4-2$. The program makes a least-squares fit to the first set of data ($8-6$ above) varying the target location and a sequence of three arbitrary transitions to mock up whatever cascade precedes this first observed transition. Simultaneous least-squares fits to the following two sets of data ($6-4$ and $4-2$ above) are made with their two lifetimes as the only additional variables. A modified program was also used in which two components of different intensity and half-life were allowed to feed the highest state for which data were being considered. Addition of a second (slower) component turned out to be of significance in the case of ^{158}Er but of little importance for ^{156,160}Er.

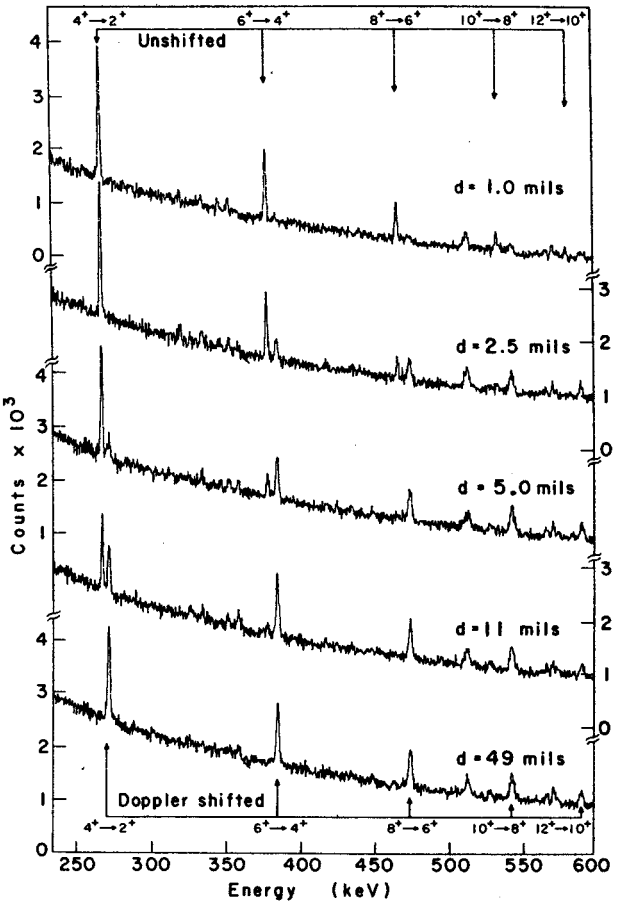

FIG. 1. Spectra from the reaction ^{124}Sn(^{40}Ar, $4n$)^{160}Er taken with the plunger set at the indicated distances from the target. The positions of the unshifted (shifted) lines are given at the top (bottom) of the figure.

A number of corrections had to be considered.[6] An important one was that due to attenuation of the angular distribution of the gamma radiation by the large hyperfine field (~40 MG) acting at the nucleus when the highly stripped target ion recoils into vacuum.[7,8] This caused a maximum correction of 6% for half-lives of the order of 3×10^{-11} sec. Small corrections for differences in absorption, efficiency, and effective solid angle between the shifted and unshifted lines were also made.

There are several sources of error. Although we do not know the absolute distance between the target and plunger to better than ±0.02 mm, this does not contribute any error to the lifetime determinations of the individual rotational transitions, as each of these is measured relative to the preceding transition. The target and plunger are neither flat nor parallel to each other within

±0.02 mm, which gives rise to instrumental limiting slopes corresponding to a mean life of ~3 $\times 10^{-12}$ sec. However, the rotational transitions are determined appreciably better than this by considering not the slope of a transition, but its separation from that of the preceding transition. In addition, there are possible errors in deducing the average velocity of the recoiling nuclei from the difference in energy of the Doppler-shifted and unshifted peaks. Seven determinations of this difference show a maximum range of ±2% from the average value, and this error cancels out completely in the ratio of two half-lives measured in the same experiment. It should be noted that the $2 \rightarrow 0$ transitions in ^{158,160}Er were determined in separate experiments using a longer recoil chamber and somewhat thinner targets. The most significant error for the fast transitions is in the peak-area integrations. The spectra are not particularly clean, and a small extraneous peak could cause a systematic error in the integration of a particular line. The uncertainty introduced by the integrations is estimated to be $\pm 0.47 \times 10^{-12}$ sec for ^{160,158}Er and $\pm 0.66 \times 10^{-12}$ sec for ^{156}Er which has somewhat poorer spectra. An error of ±5% has been set for the best transitions to account for other systematic errors and for the fact that a number of corrections (mentioned above) ranging up to a few percent in magnitude had to be made to the raw data.

Figure 2 shows a comparison of the experimental points and the computer-calculated curves for ^{160}Er. The lowest points of the fastest transitions tend systematically to be high, which probably indicates small amounts of somewhat slower feeding. The half-life values obtained are shown in Table I together with the energies of the transitions and the ratio of v/c for the recoils. Also listed are the experimental $B(E2)$ values, and these are compared with three sets of theoretical $B(E2)$ values.

Several qualitative conclusions can be drawn from the $B(E2)$ values in Table I. Within our limits of error, all these values are nearly consistent with the rigid-rotor limit; however, those for ^{160}Er probably fall below this limit for high spin values and may even show an absolute decrease for the highest spin values, whereas those for the other two nuclei probably go above this limit. In fact, the $B(E2)$ values for ^{156}Er are fitted about as well by the vibrator limit, as might be expected from the energy-level spacings in this nucleus. Since the more vibrational nuclei start with smaller $B(E2; 2 \rightarrow 0)$ values than

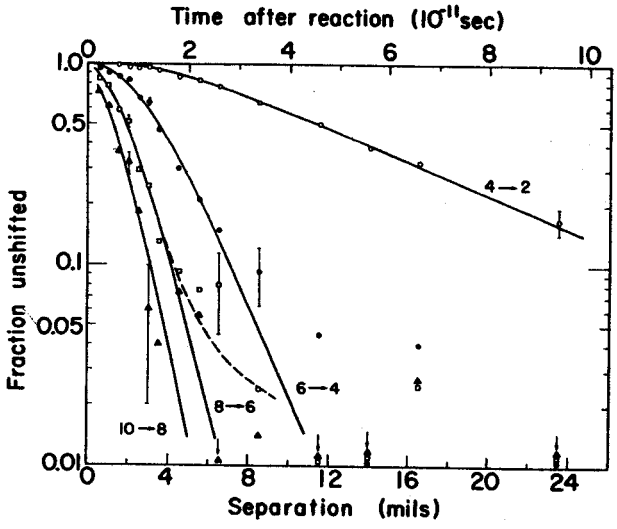

FIG. 2. The fraction of each transition which is unshifted in energy versus the separation distance of the target and plunger. The symbols represent experimental points for the ground-band transitions in ^{160}Er. The solid lines are the computer-calculated curves, and the dashed line for the $8 \rightarrow 6$ transition shows the effect of using the program which allows two components to feed the ground-state band.

the rotors, but increase more rapidly with increasing spin, there is a tendency for the $B(E2)$ values to become the same at higher spins. Thus for the three nuclei studied here the spread between the $B(E2; 2 \rightarrow 0)$ values is a factor of 2.5, but between the $B(E2; 6 \rightarrow 4)$ values it is only a factor of 1.3. This type of behavior has already been noted for the transition energies of even-even nuclei at high spin[9] and suggests that the difference between the rotational- and vibrational-type nuclei near the ground state may be disappearing with increasing angular momentum.

It is also of interest to compare the $B(E2)$ values with the predictions of the centrifugal stretching model.[10] The last column in Table I makes this comparison using the calculations of Davydov and Ovcharenko.[11] The values of μ are taken from fits to the energy levels. The experimental $B(E2)$ values do not increase as much as predicted by this model for ^{160}Er. Thus, in this nucleus centrifugal stretching is not the only change taking place with increasing angular momentum. This conclusion has previously been reached in other similar cases based on (1) the mixing of the ground- and β-bands,[12,13] (2) the Mössbauer isomer-shift work,[14,18] (3) the μ-mesonic x-ray studies,[19] and (4) theoretical calculations.[20,21] It is generally supposed that the other important

Table I. Lifetimes of collective transitions in ^{156,158,160}Er.

Nucleus	Transition	Energy (keV)	Recoil v/c(%)	$T_{1/2}$ (psec)	α_T (α_K+1.3α_L)	B(E2;I→I-2) ($e^2\times10^{-48}$ cm^4)	B(E2)$_{rot}$ [a]	B(E2)$_{vib}$ [a]	B(E2)$_{c.s.}$ [a]
^{160}Er	2 → 0	126.7	1.96	919±46	1.30	0.83±0.04	(0.83)	(0.83)	(0.83)[b]
	4 → 2	264.3	1.80	34.5±1.7	0.089	1.16±0.06	1.19	1.66	1.25
	6 → 4	376.4	1.80	5.89±0.47	0.037	1.34±0.12	1.31	2.49	1.48
	8 → 6	464.6	1.80	2.16±0.47	0.020	1.18±0.27	1.37	3.32	1.70
	10 → 8	538.1	1.80	1.24±0.47	0.014	1.05±0.40	1.40	4.15	1.91
^{158}Er	2 → 0	192.7	1.96	300±15	0.283	0.55±0.03	(0.55)	(0.55)	(0.55)[c]
	4 → 2	335.7	1.87	14.4±0.72	0.050	0.87±0.04	0.79	1.10	0.87
	6 → 4	443.8	1.87	2.80±0.47	0.026	1.14±0.19	0.87	1.65	1.11
	8 → 6	523.8	1.87	1.21±0.47	0.015	1.16±0.45	0.91	2.20	1.35
^{156}Er	2 → 0	344.4	2.20	33.2±1.7	0.047	0.33±0.02	(0.33)	(0.33)	(0.33)[d]
	4 → 2	452.9	2.20	5.42±0.66	0.022	0.53±0.06	0.47	0.66	0.61
	6 → 4	543.2	2.20	1.14±0.66	0.013	1.03±0.60	0.52	0.99	0.91

[a]These values have been normalized to the experimental 2 → 0 values.
[b]These values have been calculated for $\mu = 0.3$ and $\gamma = 10°$.
[c]These values have been calculated for $\mu = 0.4$ and $\gamma = 10°$.
[d]These values have been calculated for $\mu = 0.8$ and $\gamma = 10°$.

change occurring with increasing angular momentum is a reduction of the pairing correlations due to the Coriolis force. It is not clear how this reduction would affect the $B(E2)$ values. For ^{158}Er, however, the $B(E2)$ values from the centrifugal-stretching model fit very well and it will be of interest to see if such nuclei between rotors and vibrators do indeed stretch. For ^{156}Er, the centrifugal stretching and vibrator models give very nearly the same prediction, and in this case our data cannot really distinguish these values from those of the rigid rotor.

The decay curves, such as those in Fig. 2, also indicate the mean time interval between the reaction ($d = 0$) and the population of the ground band ($1/e$ point on the curves for the fastest rotational transitions). These mean feeding times are $(6 \pm 3)\times10^{-12}$, $(1.1 \pm 0.3)\times10^{-11}$, and $(1.6 \pm 0.3)\times10^{-11}$ sec, respectively, for ^{160}Er, ^{158}Er, and ^{156}Er. Considering that 10-20 transitions must be emitted in this time interval, these feeding times seem rather short, especially for the rotor, ^{160}Er. This subject is discussed more fully in another publication.[22] The trend between ^{160}Er and ^{156}Er is rather striking, and it will be of interest to see if this reflects a general difference between rotors and vibrators, or is just something peculiar to these three cases.

This type of half-life measurement has been shown to give sufficient accuracy to distinguish among alternative models for the collective band of even-even nuclei. It can also obviously be used to measure many other lifetimes in the range 10^{-9}-10^{-12} sec, where, in general, high precision will be less critical. We have made measurements on the reaction ^{152}Sm(^{20}Ne, $4n$)^{168}Hf and these studies appear to be feasible on reactions of this type, although the problem of side feeding has not been fully evaluated in this case. It seems clear that this method can produce much systematic information on lifetimes and feeding times following (HI, xn) reactions.

The authors would like to express their appreciation to Mr. G. Steers and Mr. T. Gee for preparing the targets, and to Mr. D. Lebeck and Mrs. R. Garrett for help with the analyses.

*Work performed under the auspices of the U. S. Atomic Energy Commission.

†Permanent address: Department of Physics, Michigan State University, East Lansing, Mich. 48823.

‡Present address: Nuclear Physics Division, Chalk River Nuclear Laboratories, Chalk River, Ontario, Canada.

[1]S. Devons, G. Manning, and D. St.-P. Bunbury, Proc. Phys. Soc. (London) A68, 18 (1955).

[2]I. F. Wright, Bull. Am. Phys. Soc. 6, 285 (1961).

[3]T. K. Alexander and K. W. Allen, Can. J. Phys. 43, 1563 (1965).

[4]T. K. Alexander, K. W. Allen, and D. C. Healy, Phys. Letters 20, 402 (1965); K. W. Allen, T. K. Alexander, and D. C. Healy, Phys. Letters 22, 193 (1966).

[5]P. G. Bizzetti, A. M. Bizzetti-Sona, S. Kalbitzer, and B. Povh, Z. Physik 201, 295 (1967).

[6]K. W. Jones, A. Z. Schwarzschild, E. K. Warburton, and D. B. Fossan, Phys. Rev. (to be published).

[7]D. Ashery, N. Bahcall, G. Goldring, A. Sprinzak, and Y. Wolfson, Nucl. Phys. A101, 51 (1967).
[8]I. Ben Zvi, P. Gilad, M. Goldberg, G. Goldring, A. Schwarzschild, A. Sprinzak, and Z. Vager, Nucl. Phys. A121, 592 (1968).
[9]F. S. Stephens, N. Lark, and R. M. Diamond, Phys. Rev. Letters 12, 225 (1964); R. M. Diamond, F. S. Stephens, and W. J. Swiatecki, Phys. Letters 11, 315 (1964).
[10]A. S. Davydov and A. A. Chaban, Nucl. Phys. 20, 499 (1960).
[11]A. S. Davydov and V. I. Ovcharenko, Yadern. Fiz. 3, 1011 (1966) [translation: Soviet J. Nucl. Phys. 3, 740 (1966)].
[12]Y. Yoshizawa, B. Elbek, B. Herskind, and M. C. Olesen, Nucl. Phys. 73, 273 (1965).
[13]G. C. Seaman, J. G. Greenberg, D. A. Bromley, and F. K. McGowan, Phys. Rev. 149, 925 (1966).
[14]J. Fink and P. Kienle, Phys. Letters 17, 326 (1965).
[15]D. Yeboah-Amankwah, L. Grodzins, and R. B. Frankel, Phys. Rev. Letters 18, 791 (1967).
[16]P. Steiner, E. Gerdau, P. Kienle, and H. J. Körner, Phys. Letters 24B, 515 (1967).
[17]U. Atzmony, E. R. Bauminger, J. Hess, A. Mustachi, and S. Ofer, Phys. Rev. Letters 18, 1061 (1967).
[18]P. Kienle, W. Henning, G. Kaindl, H. J. Körner, H. Schaller, and F. Wagner, J. Phys. Soc. Japan 24, 207 (1968).
[19]S. Bernow, S. Devons, I. Duerdoth, D. Hitlin, J. W. Kast, E. R. Macagno, J. Rainwater, K. Runge, and C. S. Wu, Phys. Rev. Letters 18, 787 (1967).
[20]T. Udagawa and R. K. Sheline, Phys. Rev. Letters 16, 325 (1966).
[21]E. R. Marshalek, Phys. Rev. Letters 20, 214 (1968).
[22]F. S. Stephens, R. M. Diamond, W. H. Kelly, J. O. Newton, and D. Ward, to be published.

Reprinted from THE PHYSICAL REVIEW, Vol. 168, No. 4, 1249–1265, 20 April 1968
Printed in U. S. A.

$M2$ Isomerism in ^{83}Rb and High-Resolution Spectroscopic Investigations of the Decay of ^{83}Sr

R. C. ETHERTON*†
Department of Physics, Michigan State University, East Lansing, Michigan
and
Department of Physics and Astronomy, Southern Illinois University, Carbondale, Illinois

AND

L. M. BEYER*† AND W. H. KELLY*
Department of Physics, Michigan State University, East Lansing, Michigan

AND

D. J. HOREN
U. S. Naval Radiological Defense Laboratory, San Francisco, California‡
(Received 17 August 1967)

The photon spectrum accompanying the electron-capture decay of ^{83}Sr has been studied with high-resolution Ge(Li) spectrometers in singles and coincidence configurations. The positron and internal-conversion-electron spectra were investigated with the MSU "orange" and $\pi\sqrt{2}$ iron-free electron spectrometers. Sixty transitions were identified. Excited states have been placed in ^{83}Rb at 5.0, 42.3, 295.2, 389.2, 423.5, 736.8, 804.8, 994.2, 1043.7, 1053.7, 1103.0, 1202.0, 1242.6, 1273.1, 1324.6, 1653.1, 1756.9, 1783.5, 1916.7, 1952.2, 2014.8, 2090.0, 2147.8, and 2179.3 keV. Internal-conversion coefficients, logft, and γ-ray branching ratios have been used to place limits upon the spins and parities of the excited states. An isomeric $M2$ transition of 42.3 keV has been identified. The ground-state spin and parity of ^{83}Sr have been shown to be $\frac{7}{2}^+$, which are the same as for all other known 45-neutron nuclei.

1. INTRODUCTION

USING shell-model configurations with the assumption that the nuclear potential is due to two-body effective interactions between nucleons, Talmi and Unna have made calculations[1] to predict the characters of the ground and first excited states of several strontium isotopes. At the same time, these authors noted the lack of experimental data for isotopes in this mass region. The present work was motivated by a desire to extend the data, as well as to test some of the results of their calculations for ^{83}Sr.

When this investigation was first started only three γ transitions of 40, 385, and 755 keV had been identified[2] as belonging to the decay of ^{83}Sr. Preliminary investigations by Maxia, Kelly, and Horen[3] have indicated that the decay of ^{83}Sr is somewhat more complex with observed transitions of 40, 375, 408, 770, 1160, 1560, and 1960 keV. Later, Reddy, Johnston, and Jha[4] presented data in agreement with Maxia *et al.* and placed levels at 40, 380, 480, 1160, 1560, 1960, and 2120 keV for ^{83}Rb. These data were all recorded with NaI(Tl) detectors.

It was soon evident from our early γ-γ coincidence data taken with NaI(Tl) detectors that the decay scheme was much more complex. We have used high-resolution Ge(Li) detectors in singles and coincidence configurations in order to perform a more complete investigation. Some 60 transitions have been identified as belonging to ^{83}Sr decay and have been fitted into a complex decay scheme. In addition, intermediate and high-resolution magnetic spectrometers have been used to measure the internal-conversion coefficients of several transitions, thus leading to additional information on the spin-parity assignments of the low-energy levels.

2. EXPERIMENTAL PROCEDURES

A. Source Preparation

The strontium-83 activity was produced from stable isotopes by means of two different nuclear reactions. The early γ-ray measurements were made using sources produced by bombarding arsenic metal with 10.4-MeV/nucleon ^{12}C ions in the Lawrence Radiation Laboratory HILAC when two of the present authors (DJH and WHK) were guests of LRL. Later sources were produced by bombarding rubidium chloride with 37- to 42-MeV protons from the Michigan State University cyclotron.

In both cases the strontium activities were separated chemically by precipitating the strontium with $SrCl_2$ carrier in chilled fuming nitric acid. Small amounts of ^{82}Sr and ^{85}Sr were present in the sources from the HILAC bombardment, whereas only the ^{85}Sr contaminant was present in the sources prepared with the cyclotron bombardments.

Two carrier-free chemical procedures were used to prepare the electron sources, all of which were cyclotron-

* Supported in part by the U. S. National Science Foundation.
† Present address: Department of Physics and Astronomy, Murray State University, Murray, Ky.
‡ Supported in part by U. S. Navy Bureau of Ships.
[1] I. Talmi and I. Unna, Nucl. Phys. 19, 225 (1960).
[2] T. Kuroyanagi, J. Phys. Soc. Japan 16, 2363 (1961).
[3] V. Maxia, W. H. Kelly, and D. J. Horen, J. Inorg. Nucl. Chem. 24, 1175 (1962).
[4] K. R. Reddy, A. S. Johnston, and S. Jha, Bull. Am. Phys. Soc. 9, 17 (1964); and private communication.

produced. The first technique[5] involved a coprecipitation of the strontium fraction with barium in chilled fuming nitric acid. The barium was then separated from the strontium by saturating a chilled 0.1 *N* HCl solution with HCl gas and precipitating only the barium.

The second carrier-free procedure involved a slightly modified version of the extraction technique originally reported by Kiba and Mizukani.[6] The RbCl target was dissolved in a few milliliters of a 0.5*M* buffer solution composed of acetic acid and ammonium hydroxide, adjusted to pH 8. The solution was transferred to a separatory funnel containing an equal volume of 0.05*M* TTA in hexone and extracted. After two extractions, the organic solution was found to contain about 90% of the ^{83}Sr produced, which was radiochemically free of rubidium activities. This solution was very convenient for the preparation of γ sources. The electron sources were obtained by back extraction of the strontium with a very small amount of 0.2*N* HNO_3. The procedure was simple, could be performed rapidly, and the purity of the sources produced appeared to be the same as those produced using the first technique.

The sources for the β-ray spectrometers were prepared from either of the above solutions by vacuum sublimation onto a 0.00025-cm aluminum foil. The $Sr(NO_3)_2$ proved to be more amenable to this technique than $SrCl_2$.

The ^{83}Sr γ spectra obtained from the sources produced using the heavy ion reactions appeared to be identical to those obtained from sources produced using the proton reactions.

B. Apparatus

The high-resolution γ-ray spectrometers consisted of Ge(Li) detectors[7] with sensitive volumes ranging from 1 to 7 cm^3. The associated electronics consisted of a low-noise vacuum tube or a field-effect transistor preamplifier and a low-noise *RC* pulse shaping amplifier coupled to a 1024-channel analyzer.

γ-γ coincidences were recorded using conventional fast-slow multiple coincidence circuits with resolving times of approximately 50 nsec. The γ detectors used for these experiments were the 7-cm^3 Ge(Li) and either a 7.6 by 7.6-cm NaI(Tl) or a split-annulus NaI(Tl) detector.[8]

The 7-cm^3 Ge(Li) and split-annulus NaI(Tl) detectors were used as an anti-Compton, a pair, and an any-coincidence spectrometer, as described in Ref. 8.

A large fraction of the conversion electron and positron data was recorded with the MSU "Orange" spectrometer.[9] The baffles and detector slit were set for a resolution of 0.8% at a transmission of approximately 5%. Most of the measurements on the 42.3-keV transition were recorded with the MSU iron-free $\pi\sqrt{2}$ spectrometer.[10] In these latter measurements, the baffles were set for a resolution of 0.2%. However, source thickness strongly limited the resolution of the low-energy lines.

3. EXPERIMENTAL RESULTS

A. γ-Ray Singles Spectrum

The γ-ray singles spectrum taken with a Ge(Li) detector of 3-cm^3 sensitive volume and resolution of 3 keV for the 662-keV ^{137}Cs photon is shown in Figs. 1(A) and 1(B). The low-energy part of the spectrum, taken with an expanded gain, is shown in Fig. 1(A), while the high-energy portion is shown in Fig. 1(B).

The energies of the observed photon transitions are listed in Table I along with their relative intensities. The energies of the more intense transitions were determined from spectra taken with ^{83}Sr sources mixed with photon emitters containing transitions of well-known energies.[11] These standard energies are listed in Table II. The technique used to determine the energy calibration curve was to least-squares-fit the peak centroids of the well-known transitions to a quadratic equation after the background had been subtracted from under the peaks. The background was obtained from a third-order least-squares fit to the counts in the channels adjacent to both sides of the peak. The deviations of the energies of the calibration transitions from the quadratic fit were never greater than $\pm$0.1 keV. The energies of the low-intensity photons were similarly determined using the strong transitions in ^{83}Sr as standards. The energies thus obtained were consistent at various gain settings. The RMS deviations from the average energies for the strong transitions listed in Table I ranged from $\pm$0.1 to $\pm$0.2 keV. The errors quoted in Table I include an estimate of $\pm$0.3 keV to account for any systematic errors that may have been present.

The relative intensities were obtained using experimentally determined efficiency curves.[12] For comparison, the relative intensities of the strong transitions measured with NaI(Tl) detectors are also listed in Table I. In general, the agreement of the two measurements was quite good.

Several very weak transitions were observed in spectra obtained using the anti-Compton spectrometer. These spectra were obtained from two different source geometries with respect to the Ge(Li) and NaI(Tl) split-annulus detectors, and are shown in Figs. 2(A) and 2(B).

[5] W. N. Sunderman and C. W. Townby, Natl. Acad. Sci.—Natl. Res. Council Publ. NAS-NS 3010 (1960).
[6] Ioshiyasu Kiba, and Ihigeru Mizukanii, Bull. Chem. Soc. Japan 31, 1007 (1958).
[7] We are grateful to Dr. G. Berzins, who made these detectors, for help in their use.
[8] R. L. Auble *et al.*, Nucl. Instr. Methods 51, 61 (1967).
[9] K. M. Bisgord, Nucl. Instr. Methods 22, 221 (1963).
[10] L. J. Velinsky, Ph.D. thesis, Michigan State University, 1965 (unpublished); Q. L. Baird, J. C. Nall, S. K. Haynes, and J. H. Hamilton, Nucl. Instr. Methods 16, 275 (1962).
[11] G. T. Ewan and A. J. Tavendale, Atomic Energy Commission, Limited (Canada) Report No. AECL2079, 1964 (unpublished) and references cited therein.
[12] R. L. Auble (private communication).

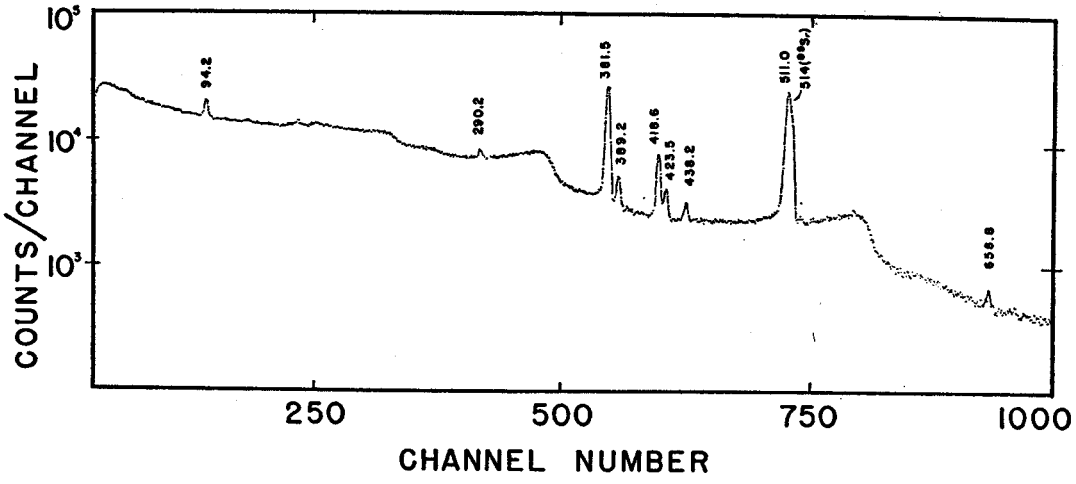

(A)

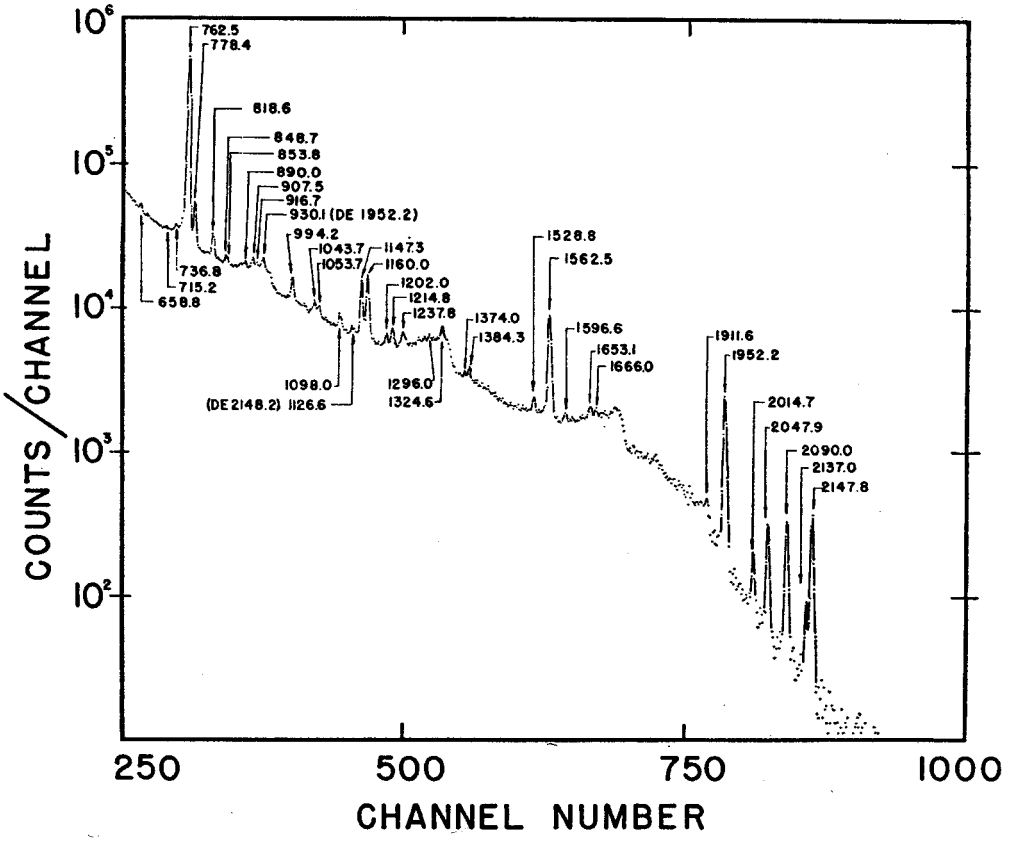

(B)

FIG. 1. Photon singles spectrum of ^{83}Sr taken with a 3-cm^3 Ge(Li) detector. (A) Low-energy region. (B) High-energy region.

In one case, the source was placed outside the annulus and the photons collimated into the Ge(Li) detector. In the second case, the source was inserted into the well of the annulus and a 5.1 by 5.1-cm NaI(Tl) detector was mounted in the tunnel above the source to increase the total solid angle subtended by the NaI(Tl) detectors. In this second case, more real coincidences due to γ cascades in the source were subtracted from the spectrum than in the first case. Therefore, in addition to improving peak to Compton ratios, those transitions involved in strong coincidence cascades can also be determined easily. The energies and relative intensities of the γ rays observed in these anti-Compton spectra are listed in Table III. These intensities are given rela-

TABLE I. Energies and relative intensities of transitions from the decay of ^{88}Sr.

Energy keV	Relative photon intensity[a] Ge(Li)	NaI(Tl)	Energy keV	Relative photon intensity[a] Ge(Li)	NaI(Tl)
(K x ray)		376.0	805 ±2.0[b]	0.1	
42.3±0.1[c]		5.2	818.6±0.5	2.4	
94.2±0.5	1.0	1.0	848.7±1.0	0.4	
290.2±0.5	1.4	1.2	853.8±0.5	0.4	
381.5±0.5[d]	60		889.0±0.5	0.4	
389.2±0.5	4.0	53	907.5±0.5	0.5	
418.6±0.5	17.8		916.7±1.0	0.1	
423.5±0.7	4.6	18	944.2±1.0	0.1	
438.2±0.5	2.7		994.2±0.5	1.5	
511.0[e]	163.2		1020 ±1.0[f]	0.1	
540.6±1.0	0.1		1036.8±1.0	0.2	
644.5±1.0	0.1		1043.7±1.0	0.5	
652.8±1.0	0.1		1053.7±0.7	0.6	
658.6±1.0	0.4		1098.0±0.5	0.6	
674.0±1.0	0.1		1147.3±0.5	3.8	
714.2±1.0	0.2		1160.0±0.5	4.5	7.8
732.0±1.0	0.2		1202.0±0.5	0.4	
736.8±0.5	0.5		1214.8±0.5	0.4	
753 ±2.0[f]	0.1		1237.6±1.0	0.5	
762.5±0.5	≡100	≡100	1242.6±1.0	0.3	
778.4±0.5	5.5		1273.1±1.0	0.1	
1284.6±1.0	0.1		1757 ±2.0[b]	0.1	
1296.0±1.0	0.4		1778 ±2.0[b]	0.08	
1324.6±1.0	0.5		1796 ±2.0[b]	0.14	
1374.0±1.0	0.2		1874 ±2.0[b]	0.1	
1384.0±1.0[b]	0.5		1911.6±1.0	0.14	
1528.8±1.0	0.2		1947 ±1.0[b]	0.1	
1562.5±0.5	5.5	4.5	1952.2±0.5	2.6	2.7
1596 ±2.0[b]	0.1		2014.7±0.7	0.1	
1653.1±1.0	0.3		2047.9±0.7	0.3	
1666.0±1.0	0.1		2090.0±0.7	0.3	
1710 ±2.0[b]	0.3		2137.0±1.0	0.1	
1722 ±2.0[b]	0.2		2147.8±0.7	0.5	
1749 ±2.0[b]	0.1				

[a] A 10% error in relative intensities is estimated.
[b] Seen in anti-Compton spectra only.
[c] $\pi\sqrt{2}$ β-ray spectrometer measurement.
[d] Doublet.
[e] Annihilation quanta. Total relative intensity determined with total annihilation.
[f] Seen in coincidence spectra only.

tive to the intensity of the 1952.2-keV transition which, as will be seen later, is not in coincidence with any photons.

B. γ-γ Coincidence Studies

γ-γ coincidence experiments were performed for all of the strong transitions and many of the weak ones.

TABLE II. Calibration energies.[a]

Source	Energy, keV[b]
^{131}I	80.164
^{132m}Te	159.00
^{131}I	284.307
^{131}I	364.467
Annihilation	511.006
^{137}Cs	661.595
^{60}Co	1173.226
^{60}Co	1332.483
ThC'' (DE)	1592.46
^{88}Y	1836.2
ThC''	2614.47

[a] Reference 11.
[b] Errors in these energies are ≤0.1 keV except for ^{88}Y, which is ±0.3 keV.

Initially, these were made using two 7.6 by 7.6-cm NaI(Tl) scintillation detectors. The energy resolutions of these detectors were approximately 8% for the

TABLE III. Energies and relative intensities of photons in the decay of ^{88}Sr observed in the anti-Compton and "any γ-γ" coincidence experiments.

Energy keV	Relative intensity Anti-Compton Collimated[a]	Uncollimated[b]	Any γ-γ coincidence
290.2	1.1		
381.5	48.0	24.2	210
389.2	3.9	1.3	27.5
418.6	13.7	6.8	50.3
423.5	3.7	1.8	12.8
438.0	2.3	0.3	7.5
511.0			256
658.6	0.33		5.8
714.2	0.15		2.2
732.0	0.16		3.0
736.8	0.48	0.2	6.6
762.5	90.0	63.9	≡100
778.4	4.5	1.2	31.8
805		0.1	
818.6	1.8	0.67	15.5
848.7	0.34	0.1	5.5
853.8	0.44	0.2	2.6
889.2	0.38		3.5
907.5	0.57	0.29	11.4
916.7	0.24		8.8
944.2	0.55	0.1	6.8
994.2	1.3	0.43	12.5
1036.6	0.14	0.06	2.7
1043.7	0.86	0.37	6.8
1053.7	0.5	0.33	5.7
1098.0	0.63	0.22	4.0
1147.3	3.3	1.2	34.3
1160.0	3.9	3.9	3.2
1202.0	0.56	0.42	
1214.8	0.7	0.2	6.8
1237.6	0.46	0.45	
1242.6	0.26	0.29	
1296.0	0.3	0.4	3.5
1324.6	0.73	0.37	7.5
1374.0	0.20	0.04	
1384.0	0.57	0.14	5.4
1528.8	0.30	0.05	3.0
1562.5	5.0	1.7	39.3
1596		0.07	
1653.1	0.21	0.22	
1666.0	0.16	0.05	2.3
1710		0.26	
1722		0.18	
1749		0.10	
1757		0.10	
1778		0.08	
1796		0.14	
1874	0.05	0.08	
1911.6	0.14	0.14	
1947		0.1	
1952.2	≡2.6[c]	≡2.6[c]	
2014.7	0.11	0.14	
2047.9	0.34	0.31	
2090.0	0.41	0.37	
2137.0	0.11	0.09	
2147.8	0.57	0.55	

[a] Source outside annulus tunnel.
[b] Source inside annulus tunnel, immediately adjacent to the Ge(Li) detector.
[c] Adjusted to equal relative intensity of the 1952.2 photon in singles.

662-keV photon of ^{137}Cs. Later, the coincidence experiments were repeated using either a 7.6 by 7.6-cm NaI(Tl) crystal or the split-annulus NaI(Tl) crystal

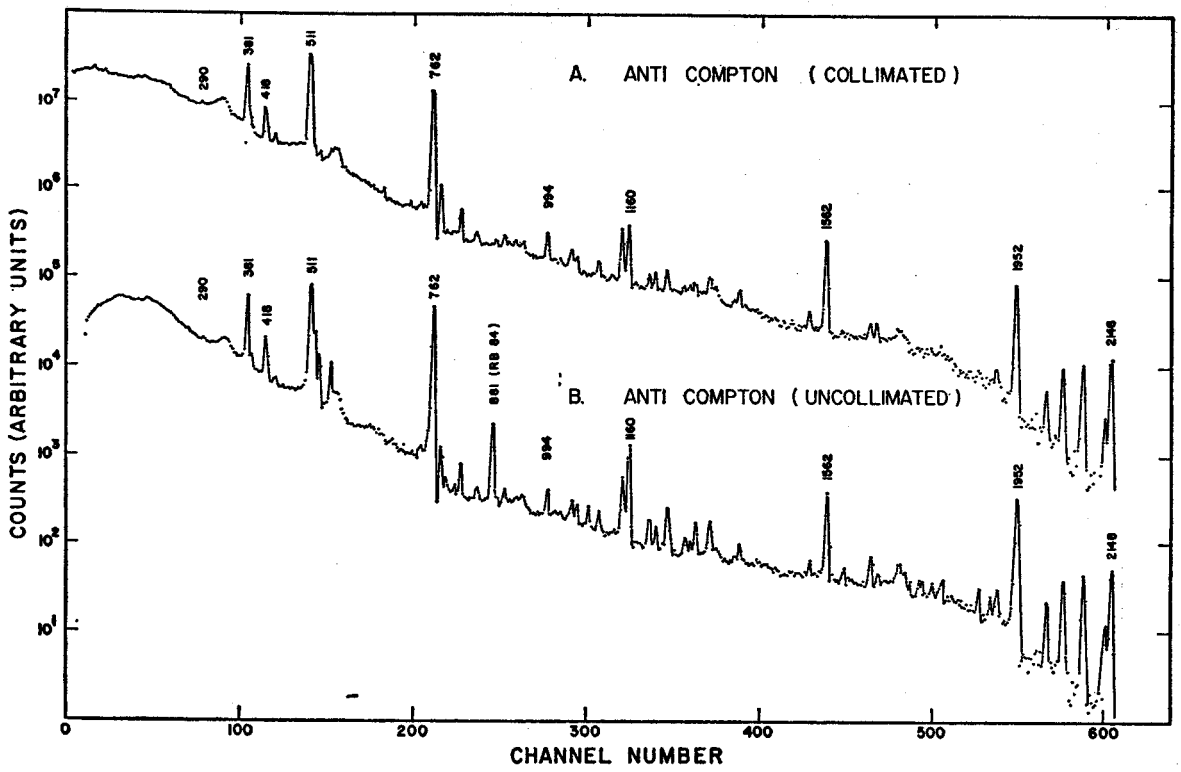

FIG. 2. Anti-Compton photon spectra of ^{88}Sr taken with a 7-cm^3 Ge(Li) and the split-annulus NaI(Tl) detectors. Spectrum A was recorded with the source placed external to the annulus with the γ rays collimated into the Ge(Li). Spectrum B was recorded with the source placed adjacent to the Ge(Li) detector.

as the gate detector and a 7-cm^3 Ge(Li) detector for display on the 1024-channel analyzer. The energy resolution of the 7-cm^3 Ge(Li) detector was 4.5 keV for the 662-keV photon of ^{137}Cs. The results of both studies were consistent and only those data taken with the germanium detector will be discussed here.

In order to complement the anti-Compton data, a coincidence spectrum with the NaI(Tl) annulus–Ge(Li) system was recorded using an integral gate. This is called the "any γ-γ coincidence experiment." For this measurement, the source was sandwiched between 0.35 cm of copper to produce total annihilation and then placed 2 cm above the Ge(Li) detector. A 2.2-cm-thick cylindrical iron shield was placed around the Ge(Li) detector to reduce crystal-to-crystal scattering. The coincidence spectrum recorded from this con-

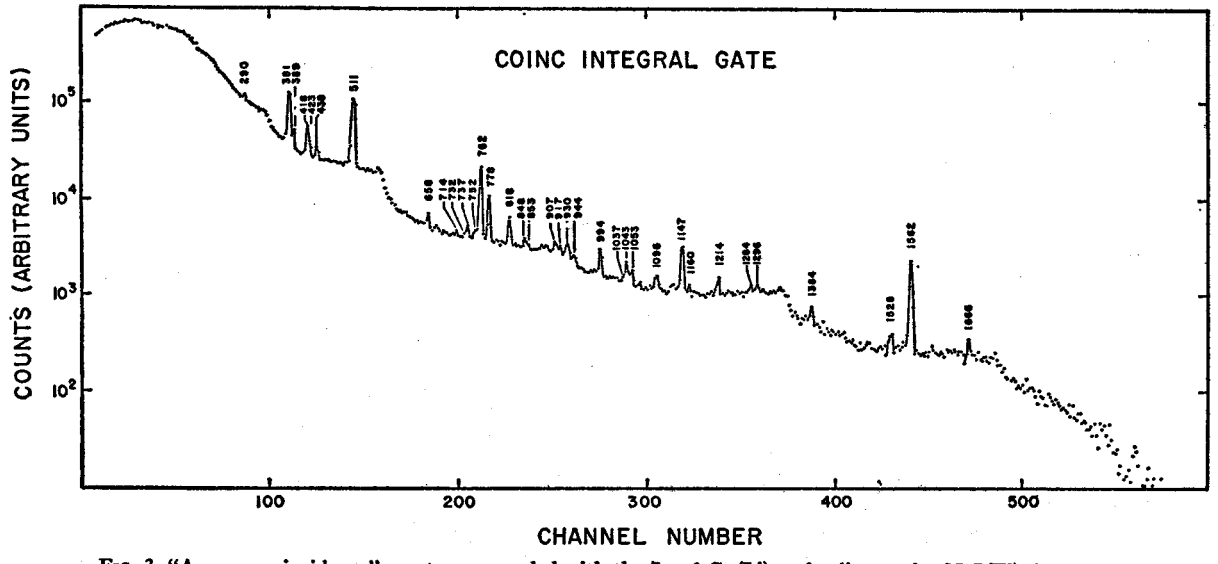

FIG. 3. "Any γ-γ coincidence" spectrum recorded with the 7-cm^3 Ge(Li) and split-annulus NaI(Tl) detectors.

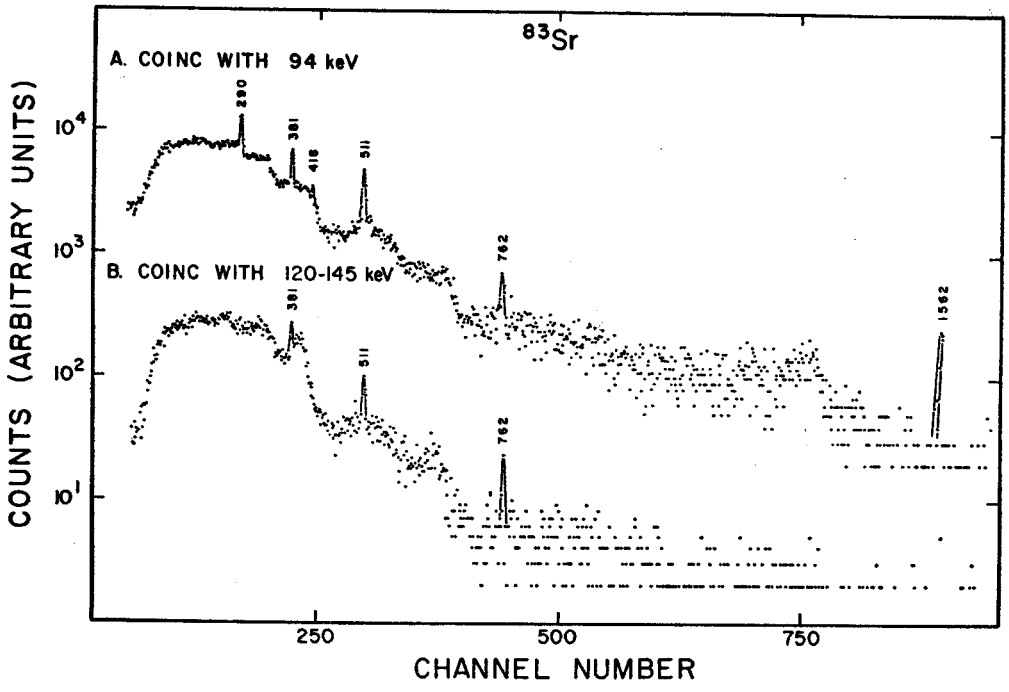

FIG. 4. Photon spectrum in coincidence with the 94.2-keV photon taken with the 7-cm³ Ge(Li) detector. The coincidence gate detector was a 3.8 by 2.5-cm NaI(Tl) crystal with a 0.013-cm beryllium window. For comparison, spectrum B was recorded with the NaI(Tl) detector gating on the region above the 94.2-keV photon.

figuration is shown in Fig. 3. The energies and relative intensities of the photons observed in this coincidence spectrum are also listed in Table III. Almost all of the photons were noticeably enhanced relative to the 762.5-keV γ ray, indicating that this photon is not in as strong coincidence as many of the others.

Additional coincidence spectra were recorded in separate experiments with the coincidence gates set on

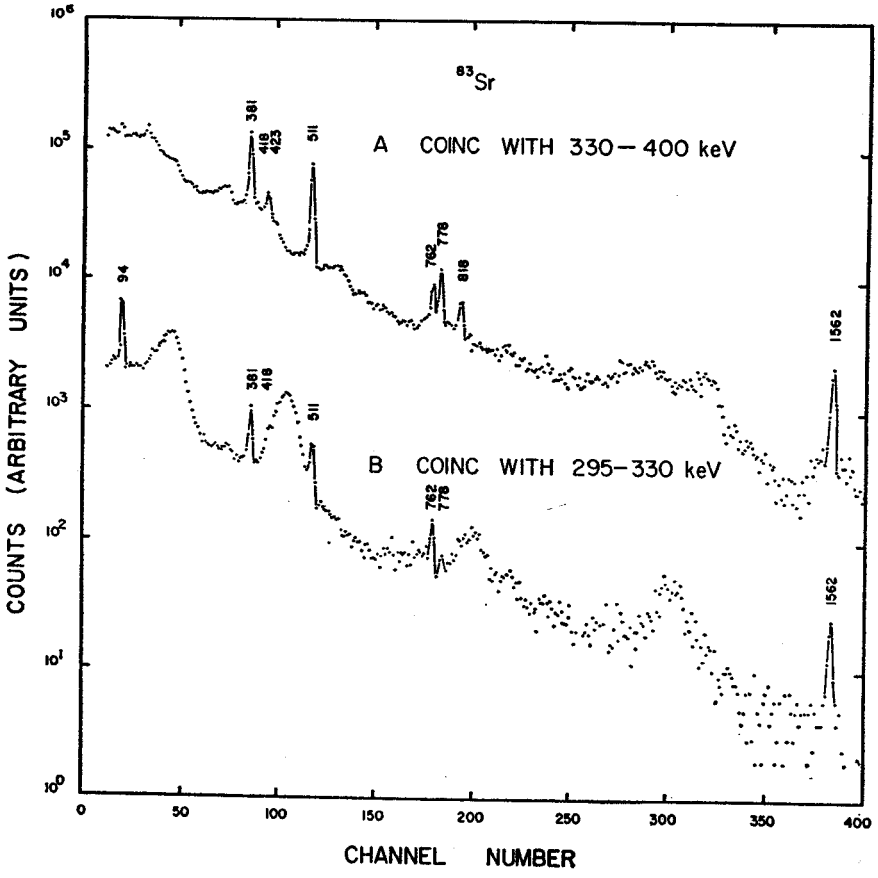

FIG. 5. Photon spectra in coincidence with segements of the 295–400-keV region taken with the 7-cm³ Ge(Li) and 7.6 by 7.6-cm NaI(Tl) detectors. Spectrum B was recorded with the NaI(Tl) detector gated on 295–330 keV and includes part of the 290.2-keV photopeak. Spectrum A was recorded with the NaI(Tl) detector gated on the low-energy side of the 381-, 418-, and 423-keV photopeak.

the peaks with energies of 94.2, 381.5, 418.6, 762.5, 1147.3, 1160.0, and 1562.5 keV. For comparison, coincidence spectra were also recorded for coincidence gates set on the Compton regions below and above these peaks. Also, the 600–735-keV and 800–1100-keV regions of the spectrum were divided into six segments of 50- to 100-keV width and coincidence gates set on each segment.

Three different NaI(Tl) detectors were used to provide the coincidence gates. A 3.8 by 2.5-cm NaI(Tl) detector with a 0.013-cm beryllium window was used for the coincidence gates set on the 94.2-keV photopeak and the Compton region directly above it. A 7.6 by 7.6-cm NaI(Tl) detector was used for the coincidence gates set to the 381.5, 762.5, and 1562.5-keV photopeaks. The split-annulus NaI(Tl) detector was used for all of the other coincidence gates. The results of all these measurements are shown in Figs. 4–11, inclusive. Many of the spectra have been gain shifted by the computer for ease of comparison and presentation. These spectra have not been corrected for chance coincidences; however, the gross true-to-chance ratio was monitored and in every experiment it was 25 to 1 or greater.

In order to identify the states populated by positron decay, a triple coincidence experiment was performed using the NaI(Tl) split annulus and the 7-cm^3 Ge(Li) detectors. The source was placed into the well of the split annulus and immediately above the Ge(Li) detector. The pulses from each half of the split-annulus were used to provide a coincidence gate on the 511-keV photopeak. The coincidence spectrum recorded from this configuration is shown in Fig. 12(B). In order to distinguish those photons depopulating the states fed by the positron decay from the double escape peaks of the high-energy photons, the experiment was repeated

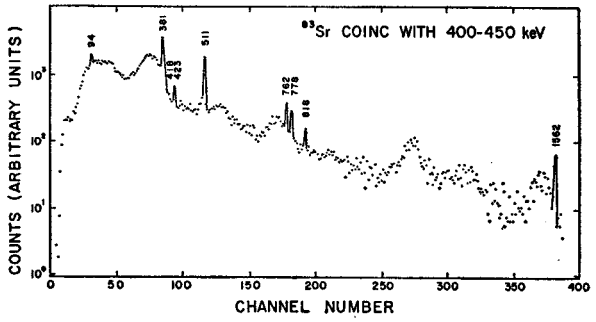

FIG. 6. Photon spectrum in coincidence with the 400–450-keV region taken with the 7-cm^3 Ge(Li) and the NaI(Tl) split-annulus detectors.

with the source placed external to the split-annulus detector and the photons collimated into the Ge(Li) detector. This spectrum, which contains only the double escape peaks, is shown in Fig. 12(C).

Note that the double escape peak of the 1562.5-keV photons was greatly reduced in the spectrum obtained with the source in the annulus [Fig. 12(B)]. This was caused by the 511-keV annihilation quanta from the 1562.5-keV photons summing with the coincident 94.2-, 290.2-, and 389.2-keV photons. These photons were very efficiently detected in the split annulus and the summing produced pulses corresponding to energies appreciably greater than 511 keV and therefore the gate requirement was no longer satisfied. The intensity of photons in cascades that are in coincidence with the positrons will be reduced similarly in the coincidence spectrum.

In almost every case, the coincidence gates necessarily included two or more γ rays because of their close energy spacings, and, in addition, many underlying Compton photons. This makes the interpretation of

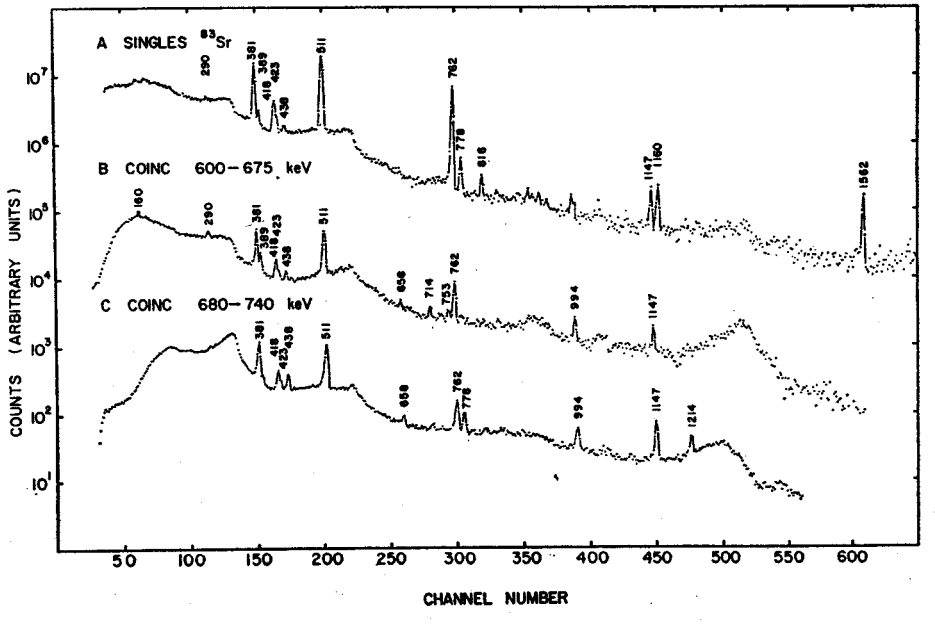

FIG. 7. Photon spectra in coincidence with segments of the 600–740-keV region taken with the same detection system as used for Fig. 6. A singles spectrum is given for reference. The spectra have been adjusted to have the same energy scales with the MSU CDC 3600 computer.

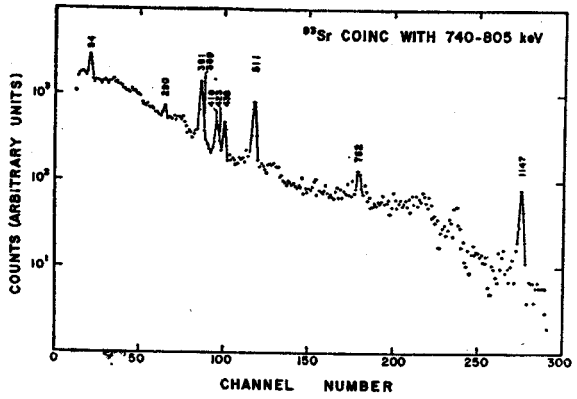

FIG. 8. Photon spectrum in coincidence with the 762.5-keV peak taken with the same detectors as used for Fig. 5.

most of the coincidence data difficult. However, a consistent interpretation can be obtained by quantitative comparisons of the different coincidence spectra. A summary of the coincidences seen in these experiments is presented in Table IV. It is possible to establish, by the comparison of spectra recorded with adjacent coincidence gates, that some of the peaks appearing in the coincidence spectra are the result of coincidences with Compton photons or sum peaks in the gate interval. These are listed in Table IV under the heading "Compton or sum coincidence". The appearance of the 511-keV peak in all of the coincidence spectra of the coincidence gates between 900–1200 keV can be accounted for by sum coincidences. These arise from one of the 511-keV annihilation quanta summing with any of the coincident 381.5-, 418.6-, 423.5- or 762.5-keV photons or their Compton photons in the NaI(Tl) annulus detector.

Comparisons of the coincidence spectra obtained from gates at 680–740 keV, 740–805 keV, 815–880 keV and 1100–1200 keV [Figs. 7(C), 8, 9(B), and 10] reveal that the 762.5-keV transition is in coincidence with the 1147.3-keV photons. Further, the peak at 438.2 keV is

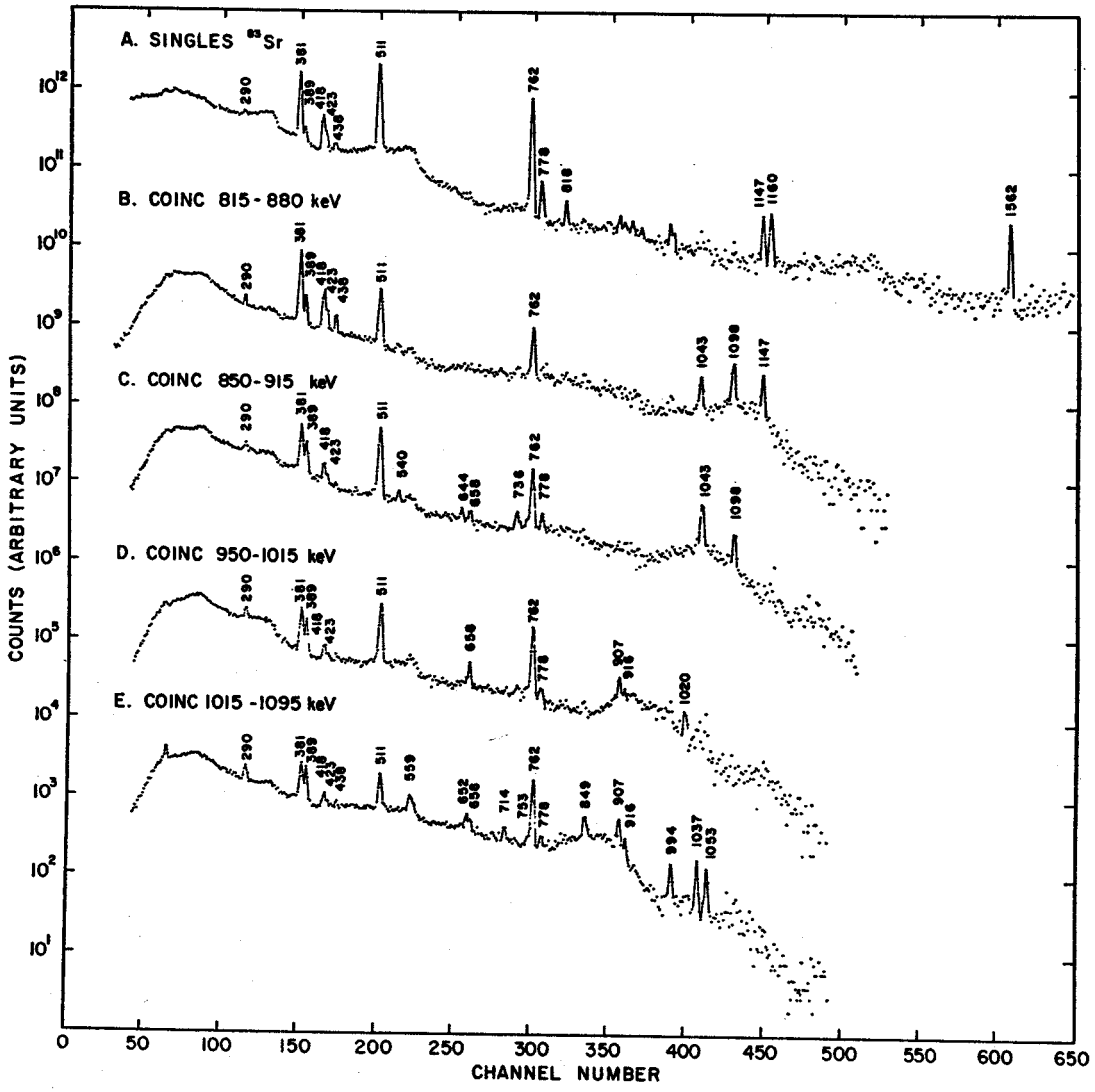

FIG. 9. Photon spectra in coincidence with various segments of the 800–1100-keV region. Spectrum A is a singles spectrum for reference. The detectors were the same as for Fig. 6. The energy scales have been adjusted as in Fig. 7.

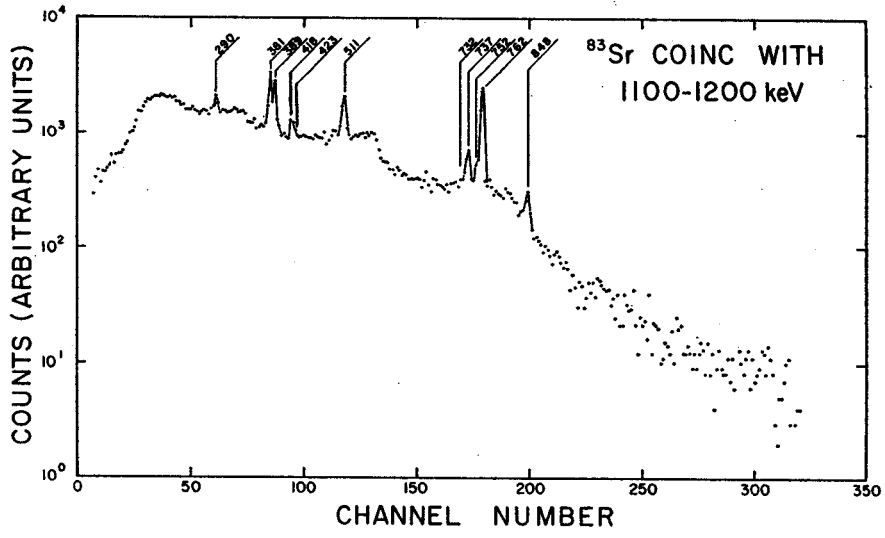

FIG. 10. Photon spectrum in coincidence with the 1147–1160-keV doublet. The detectors were the same as used for Fig. 5.

concluded to be in coincidence with the 762.5-keV γ, since the 762.5-keV peak is observed to grow as the coincidence gate is moved from 295–400 to 400–450 keV [Figs. 5(B), 5(A), and 6].

The ratio of the intensity of the 381.5-keV photon with the combined intensities of the 418.6- and 423.5-keV photons recorded in the coincidence spectra obtained with the coincidence gates at 330–400, 400–450, 740–805, and 1100–1200 keV [Figs. 5(A), 6, 8, and 10] are very informative and were crucial in the construction of the decay scheme. These ratios were 4.2, 5.2, 2.3, and 4.0, respectively, in comparison to 2.7 in the singles spectrum. Furthermore, the 418.6- and 423.5-keV photons always appeared in the coincidence spectra together and in the same intensity ratio as in singles. These ratios can be explained only with the conclusion that the 381.5-keV peak actually consists of two photons very close in energy, with one of them in coincidence with the other as well as with the 418.6- and 423.5-keV photons. The relative intensities of the two 381.5-keV photons have been calculated from the coincidence data to be 23.5 for the one in coincidence with the 418.6- and 423.5-keV photons and 36.5 for the other. No noticeable broadening of the 381.5-keV peak was observed. An upper limit of 0.2 keV is placed for the energy difference of the doublet.

The 42.3-keV transition was not observed to be in

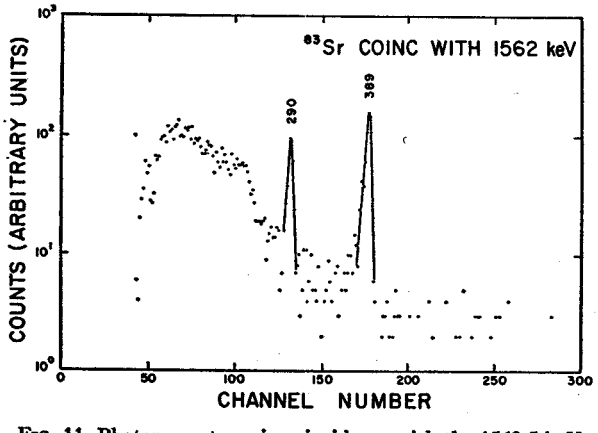

FIG. 11. Photon spectrum in coincidence with the 1562.5-keV peak. The detectors were the same as used for Fig. 5.

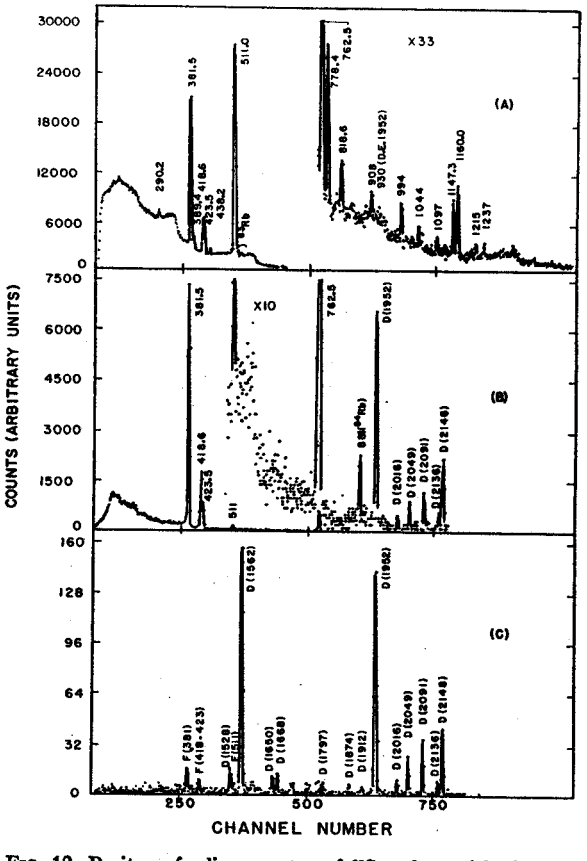

FIG. 12. Positron feeding spectra of ^{83}Sr taken with the same detectors as used for Fig. 6. Spectrum A is a singles spectrum which is shown for reference. Spectrum B is the positron feeding *and* double escape spectrum obtained with the γ rays collimated into the Ge(Li) detector from an external source. Spectrum C is the double-escape spectrum recorded with the pair spectrometer as described in Ref. 8.

TABLE IV. Coincidence summary.

Gate interval in keV	γ in gate in keV	Coincidence with γ in keV	Compton or sum coincidences	Figure No.
87–112	94.2	290.2, 1562.5	381.5, 418.6, 423.5, 511.0, 762.5	4(A)
120–145	None		381.5, 418.6, 423.5, 511.0, 762.5	4(B)
295–330	290.2	94.2, 1562.5	381.5, 418.6, 511.0, 762.5, 778.4	5(A)
340–400	381.5, 389.2, 418.6, 423.5	381.5, 418.6, 423.5, 511.0, 778.4, 818.6, 1562.5	94.2, 762.5	5(B)
400–450	381.5, 389.2, 418.6, 423.5, 438.2	381.5, 418.6, 423.5, 511.0, 762.5, 778.4, 818.6, 1562.5	94.2	6
600–675	644.5, 652.8, 658.6, 674.0	381.5, 418.6, 423.5, 658.6, 714.2, 753.2, 762.5, 994.2	290.2, 389.2, 511.0, 1147.3	7(B)
680–740	674.0, 714.2, 732.0, 736.8, 753.2, 762.5	381.5, 418.6, 423.5, 438.2, 511.0, 658.6, 714.2, 762.5, 778.4, 994.2, 1043.7, 1147.3, 1214.8		8
740–805	732.0, 736.8, 753.2, 762.5, 778.4, 818.6	381.5, 418.6, 423.5, 438.2, 511.0, 762.5, 778.4, 1147.3		8
815–880	818.6, 848.7, 853.8, 989.2	381.5, 418.6, 423.5, 438.2, 762.5, 1043.7, 1098.0, 1147.3	290.2, 389.2, 511.0	9(B)
850–915	848.7, 853.8, 889.2, 907.5 916.7	381.5, 418.6, 423.5, 540.2, 644.5, 658.6, 732.0, 736.8, 762.5, 778.4, 1043.7, 1098.0	290.2, 389.2, 511.0	9(C)
950–1015	944.2, 994.2, 1020.1	381.5, 418.6, 423.5, 658.6, 762.5, 778.4, 907.5, 994.2, 1020.1, 1053.7	290.2, 389.2, 511.0	9(D)
1015–1095	1020.1, 1037.8, 1043.7, 1053.7, 1098.0	381.5, 418.6, 423.5, 559, 652, 658, 714.2, 753.2, 762.5, 778.4, 848, 907.5, 916.7, 994.2, 1037.8, 1053.7	290.2, 389.2, 511.0	9(E)
1100–1200	1098.0, 1147.3, 1160.0, 1202.0, 1214.8	318.5, 418.6, 423.5, 732.0, 736.8, 753.2, 762.5, 848.7	290.2, 389.2, 511.0	10
1525–1600	1528.8, 1562.5	94.2, 290.2, 389.2		11

prompt coincidence with any of the other photons, x rays, or positrons.

C. Conversion Coefficients and the Positron Spectra

1. 42.3-keV Transition and the Search for an Isomer in ^{83}Sr

It is well known that the isotopes ^{87}Sr and ^{85}Sr possess isomeric states which arise from the filling of the $p_{1/2}$ and $g_{9/2}$ shells in this region. In addition, Talmi and Unna[1] predict a similar type structure for ^{83}Sr, suggestive of an isomeric state. From the lack of observed transitions in prompt coincidence with the 42.3-keV photon, a question arises as to whether this transition might be in the parent. In order to clarify this point, its K, L, and M conversion electron spectra were recorded with the $\pi\sqrt{2}$ β spectrometer and the results

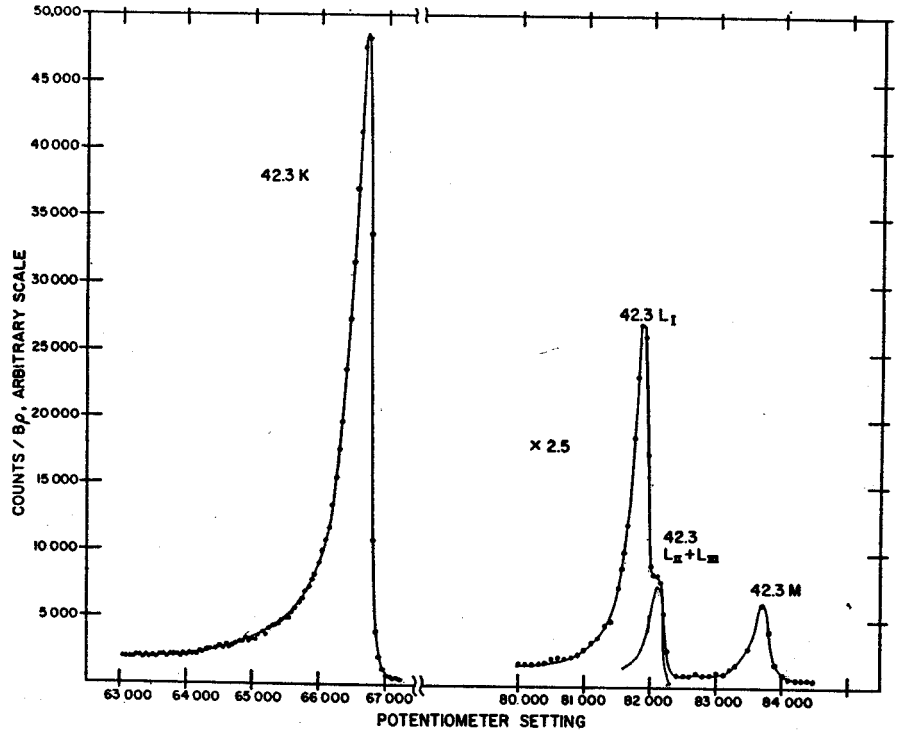

FIG. 13. The K, L, and M conversion electron lines of the 42.3-keV transition in ^{83}Rb. This spectrum was recorded with the MSU $\pi\sqrt{2}$ iron-free spectrometer.

TABLE V. Experimental results of the internal-conversion electron measurements on the 42.3-keV transition.

E_γ (keV)	E_K-E_{LI} (keV)	E_K-E_M (keV)	α_K	K/L	$L_I/(L_{II}+L_{III})$	K/M
42.3±0.05	13.20±0.03	15.0±0.1	29.3±3.5	5.5±0.1	2.8±0.2	30±2

are shown in Fig. 13. The measured K-L and K-M energy differences were compared with x-ray binding energies and were found to deviate by only 0.07 keV from the values for rubidium as is shown in Tables V and VI. Hence, we conclude the 42.3-keV transition is in rubidium. Several other experiments were performed to specifically search for an isomeric state in ^{83}Sr, but no positive evidence was found for the existence of the isomer. The fast chemical procedures described in Sec. 2A have been utilized to place an upper limit of 2 min on the half-life of any existing short-lived isomeric state in ^{83}Sr. This limit is based on the assumption that an isomeric transition or states fed directly by the β decay of the isomer would be seen in the γ spectra.

The measured K/L, $L_I/(L_{II}+L_{III})$, and K/M ratios for the 42.3-keV transition are also listed in Table V, and the theoretical predictions for various multipolarities[13] are listed in Table VII. The K internal-conversion coefficient α_K has also been obtained with the orange spectrometer by comparison with that obtained for the 381.5-keV transitions and is in good agreement with the $M2$ multipolarity indicated by the above results. The K/M ratio is also in good agreement with the recent calculation of Bhalla for a pure $M2$ transition.[14] The knowledge of this multipolarity was found to be an essential element in the decay scheme construction because of the strength of the transition and its location in the scheme.

The measured value of the transition energy was determined with the $\pi\sqrt{2}$ electron spectrometer as 42.3 ±0.05 keV.

TABLE VI. Electron binding energies, demonstrating that the 42.3-keV photon is a transition in rubidium.[a]

Nucleus	E_K-E_{LI} (keV)	E_K-E_M (keV)
Sr	13.89	15.80
Rb	13.13	15.0

[a] Reference 19.

TABLE VII. Theoretical internal-conversion coefficients for 42.3-keV transition in rubidium, as a function of multipolarity.[a]

α_K				K/L				$L_I/(L_{II}+L_{III})$			
$E1$	$E2$	$M1$	$M2$	$E1$	$E2$	$M1$	$M2$	$E1$	$E2$	$M1$	$M2$
1.06	16.2	1.52	32.9	9	3.2	8.6	5.6	3.4	0.36	13.4	3.4

[a] Reference 13.

[13] M. E. Rose, *Internal Conversion Coefficients* (Interscience Publishers, Inc., New York, 1958).
[14] C. P. Bhalla (private communication).

2. 762.5-keV Transition

The absolute conversion-coefficient measurements can be performed very satisfactorily by making an absolute measurement of a single transition, then comparing electron and photon relative intensities of the remaining transitions. The 762.5-keV K-conversion line, shown in Fig. 14, has been chosen as the standard line, and its absolute α_K measured via the mixed source technique. The internal-conversion line of the 661.6-keV transition in ^{137m}Ba has been used in conjunction with relative photon intensity measurements performed with a 7-cm^3 Ge(Li) detector having 4.5-keV resolution (full width at half-maximum). The relation

$$\alpha_K(762.5)=\alpha_K(661.6)\frac{I_e(762.5)}{I_e(661.6)}\frac{I_\gamma(661.6)}{I_\gamma(762.5)},$$

with the measured quantity[15] $\alpha_K(661.6)=0.0894$, yields the desired result directly.

As shown in Table VIII, the measured value of $\alpha_K=(9.5\pm0.5)\times10^{-4}$ for the 762.5-keV transition in ^{83}Rb agrees well with that expected for a pure $E2$ transition. However, an appreciable $M1$ admixture cannot be excluded. The K/L ratio, although not a very sensitive test of the multipolarity in this case, was unattain-

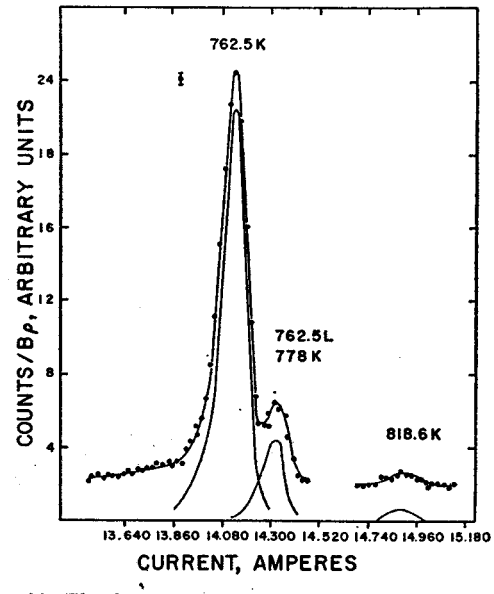

FIG. 14. The internal-conversion electron spectrum of ^{83}Sr, spanning the 740–830-keV region, recorded with the "orange" spectrometer.

[15] J. S. Merritt and J. G. V. Taylor, Anal. Chem. 37, 351 (1965); Nucl. Sci. Abstr. 19, No. 16860 (1965).

TABLE VIII. Multipole order of transitions in ^{83}Rb, based on measured values of the internal-conversion coefficients.

E_γ (keV)	Relative electron intensity $I_{(762K)}\equiv 100$	Relative γ-ray intensity $I_{(762\gamma)}\equiv 100$	α_K[a] (expt)	α_K[a] (theoretical) $E1$	$E2$	$M1$	$K/(L+M)$ (expt)	K/L (theoretical) $E1$	$E2$	$M1$	Multipole order
94.2	K 230	1.0	2.2±0.2(−1)	1.0(−1)	1.0(0)	1.5(−1)			6.5	8.7	$M1$, ≤10%$E2$
290.2	K 21, $L+M$ 2.1	1.4	1.4±0.2(−2)	3.9(−3)	1.8(−2)	7.9(−3)	10±2		8.6	9.0	35%$M1$, 65%$E2$
381.5[b]	K 440, $L+M$ 60	23.5, 36.5 / 60.0[c]	7.1±0.3(−3)	1.9(−3)	7.2(−3)	4.1(−3)	7.4	9.6	8.9	9.2	$E2$, <10%$M1$[b]
389.2	K 27, $L+M$ 3.2	4.0	6.5±0.5(−3)	1.8(−3)	6.7(−3)	3.9(−3)	8±2				$E2$, 20%$M1$
418.6	K 26	17.8	1.4±0.2(−3)	1.5(−3)	5.3(−3)	3.3(−3)					$E1$
423.5	K 7.8	4.6	1.6±0.4(−3)	1.4(−3)	5.1(−3)	3.2(−3)					$E1$
438.2	K 7.7	2.7	2.7±0.4(−3)	1.3(−3)	4.6(−3)	2.9(−3)					$M1$
762.5	K 100	100	9.5±0.5(−4)	3.6(−4)	9.3(−4)	8.8(−4)			8.7	9.3	$E2$(+$M1$)
778.4	K 5.5	5.5	9.6±2 (−4)	3.4(−4)	8.8(−4)	7.9(−4)					$M1$, $E2$
818.6	K 2.7	2.4	1.1±0.4(−3)	3.1(−4)	7.8(−4)	7.0(−4)					$M1$, $E2$

[a] The number in parentheses are the appropriate powers of 10, i.e., 2.2±0.2(−1) means (2.2±0.2)×10^{-1}.
[b] The 381.5-keV transition is a doublet, as described in Sec. 3B.
[c] The division of intensities of the 381.5-keV doublet are based on the coincidence results described in Sec. 3B.

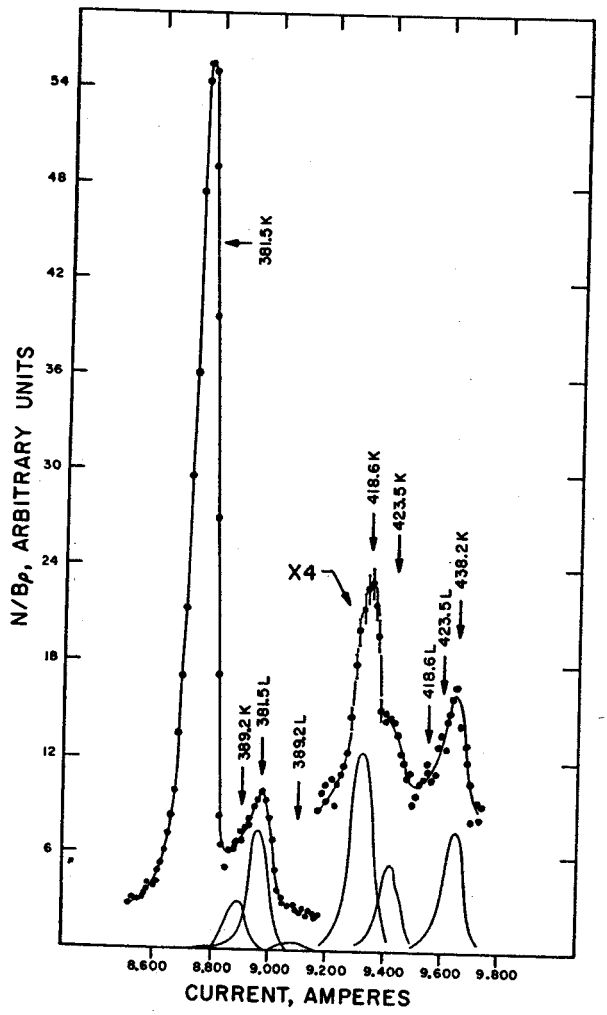

FIG. 15. The internal-conversion electron spectrum of ^{83}Sr spanning the 350–440-keV region. This was recorded with the "orange" spectrometer.

able because of the incomplete resolution of the 762.5-keV L and the 778.4-keV K lines in the internal-conversion spectrum.

3. 381.5-keV Transitions

The conversion electron spectrum encompassing the region from 350 to 440 keV is shown in Fig. 15. The peak corresponding to a 381.5-keV transition has been shown in Sec. 3B to be a cascading doublet on the basis of coincidence results, the upper member having about 60% of the intensity of the lower one. Thus, the α_K obtained for this peak must be considered as composite and was determined independently by both the mixed source technique and by comparison with the 762.5-keV α_K measurement described above. The former yields the result $\alpha_K=(7.2\pm0.3)\times10^{-3}$. Assigning $\alpha_K=9.5\times10^{-4}$ for the 762.5-keV transition, the value $\alpha_K=(7.0\pm0.3)\times10^{-3}$ was obtained for the composite peak when comparing relative electron and photon intensities. A simple average has been taken as the final value. Both values are in good agreement with the 7.2×10^{-3} theoretical $E2$ value,[13] as shown in Table VIII. Within the limits of the data, either both of the 381.5-keV transitions are $E2$ with an upper limit of 10% $M1$ or, if one is pure $E2$, the other transition may be mixed.

The measured $K/(L+M)$ ratio of 7.4±0.5 for the 381.5-keV transitions has been obtained by the standard stripping process, whereby counts from the unresolved 389-keV K line were removed. The theoretical K/L ratio[13] for an $E2$ transition is 8.9. Application of the semiempirical method of Chu and Perlman[16] to the M shell yields a value of 1.7×10^{-4} for the total M conversion coefficient. However, it has been shown[17] that the ratio of $M_{\text{Chu}}/M_{\text{exp}}$ may be as much as 1.7 in this

[16] Y. Y. Chu and M. L. Perlman, Phys. Rev. 135, B319 (1964).
[17] O. Dragoun and P. Johns, Phys. Letters 24B, 146 (1967).

mass region. Even if this is the case for this transition, the measured $K/(L+M)$ ratio can be considered to be in agreement with that expected for an $E2$ transition.

4. Remaining Internal-Conversion Coefficients

The K conversion lines corresponding to the 389.2-, 418.6-, 423.5-, and 438.2-keV transitions have been analyzed as shown in Fig. 15, using standard stripping techniques. The results of the analyses and the assigned multipolarities are given in Table VIII. The K conversion line of the 381.5-keV transitions was used for the standard line shape. The 438.2-keV K line is not completely resolved from the 418.6- and 423.5-keV L lines. However, the theoretical K/L ratio of 10 for these latter two transitions indicates that the majority of the intensity of this line arises from the 438.2-keV K conversion line.

Figure 16 shows the K conversion line of the 94.2-keV transition and the K and L lines of the 290.2-keV transition. A summary of the results and assigned multipolarities are also given in Table VIII. The 94.2-keV transition is not strong enough to allow a reliable K/L measurement, although a lower limit of 8 can be derived from the data.

The conversion electron spectrum from 740 to 870 keV is shown in Fig. 14. The intensity of the 778.4-keV electron line was obtained by subtracting from the total counts in the 762.5-L and 778.4-K composite line, an amount for the 762.5-keV L line based on the assumption that it is a pure $E2$ transition. The resulting α_K, listed in Table VIII, for the 778.4-keV transition, indicates an $M1+E2$ mixture, but little can be said about the mixing ratio within the experimental accuracy of the measurement.

5. Positron Spectra

The positron spectra have been measured with the orange spectrometer. The detector slit was opened wide to produce a higher positron count rate relative to counts registered from positrons annihilating in the material surrounding the detector. Under these circumstances the resolution was 2%.

The analysis of the Fermi-Kurie plot is shown in Fig. 17 and indicates branches with end-point energies at 1227±8, 803±15, and 465±50 keV. The stripping procedure was accomplished by making successive first-order least-squares fits to the high-energy fraction of the Fermi-Kurie plots. The resulting analysis indicates that there are 84.7, 9.2, and 6.1% of the positrons contained in the high-, intermediate-, and low-energy groups, respectively.

4. PROPOSED DECAY SCHEME

A decay scheme consistent with all our data has been constructed from the results of the coincidence studies, energy sums, and relative intensities of the transitions.

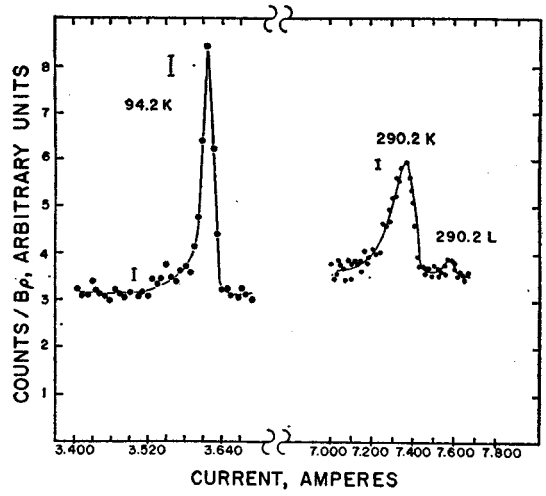

FIG. 16. The internal-conversion lines of 94.2- and 290.2-keV transitions in the decay of ^{83}Sr. Different sources were used for the two lines. The 290.2-K conversion line was recorded using a source thick enough to cause line broadening. These were recorded with the "orange" spectrometer.

This scheme is shown in Fig. 18. In general, a comparison of the energy sums of competing cascades and crossover transitions shows agreements to better than 0.5 keV for sums involving transitions having relative intensities greater than 0.5 (relative to 100 for the 762.5-keV transition) and usually to better than 1.0 keV for those involving the weaker photons.

The logft values listed in the decay scheme were determined from the relative intensities into and out of each state and from the x-ray and positron intensities. The positron branching ratios were determined from the Fermi-Kurie plots of the positron spectrum and from the triple coincidence experiments. The positron end points given in the decay scheme were obtained by assuming the 1227-keV branch is to the ground state and subtracting the state energies from this value. Explicit searches were made for positron feeding to the 736.8-keV state in triple-coincidence experiments with the positron annihilation radiation. No such feeding was found.

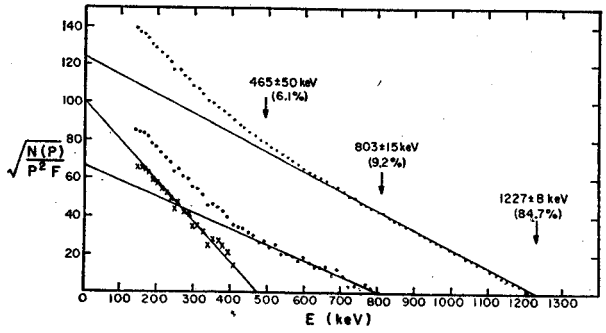

FIG. 17. The Fermi-Kurie analysis of the positrons emitted in the decay of ^{83}Sr. These data were recorded with the "orange" spectrometer.

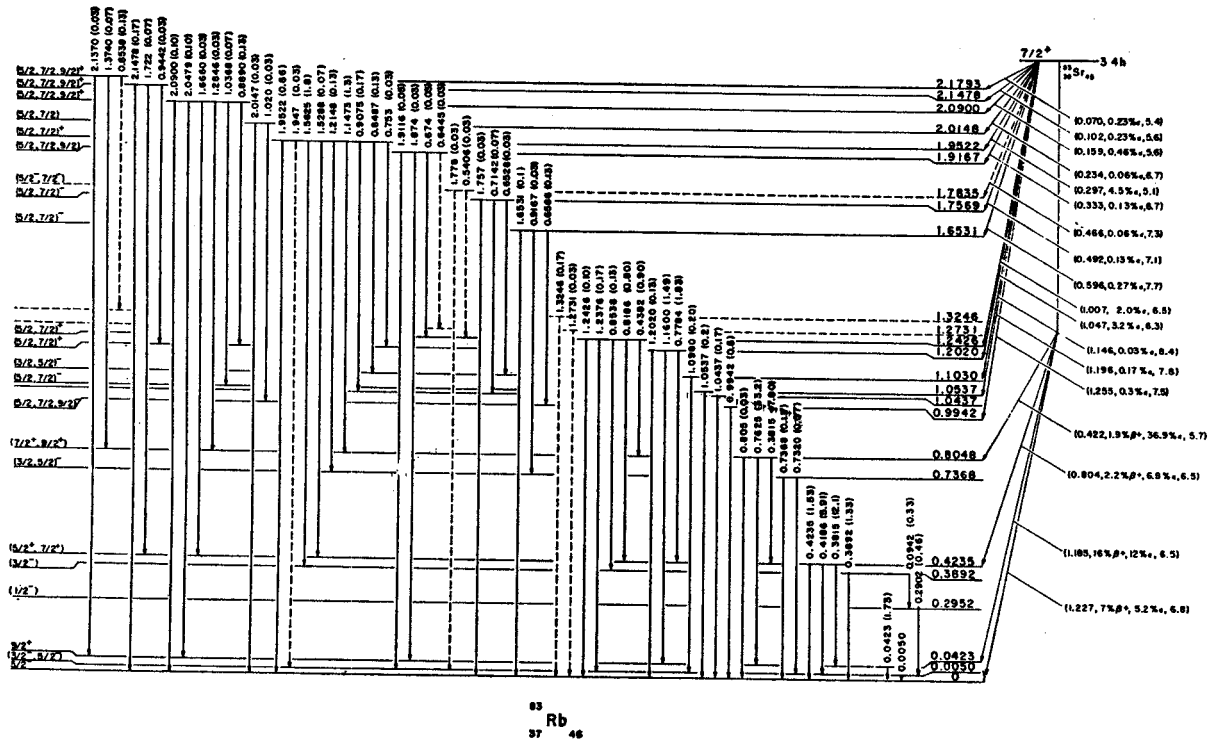

FIG. 18. The proposed decay scheme for ^{83}Sr. Energies are in MeV. The relative intensities given for the photons are in the units of percent per decay of the ^{83}Sr parent.

A. Evidence for the 42.3-keV State

The placement of a state at 42.3 keV was dictated by the relative intensity of the 42.3-keV transition and its long lifetime. The total internal-conversion coefficient has been measured to be 33, which gives a total of 188 units for this transition (relative to 100 for the 762.5-keV photon), making the 42.3-keV transition the strongest in the decay scheme.

B. Evidence for the 423.5-, 804.8-, and 5.0-keV States

A state was placed at 423.5 keV as a result of the relationships of the 381.5- and 423.5-keV photons in the coincidence spectrum. It is supported by several observed coincidence cascades that are listed in Table IV.

It was not possible to account for the relative intensity of the 42.3-keV transition without having the 762.5-keV photon feeding the 42.3-keV state. Furthermore, a very low intensity photon of about 805 keV was observed in the anti-Compton spectrum described in Sec. 3A. Therefore, a state was placed at 804.8 keV, which is the energy sum of the 42.3- and 762.5-keV transitions.

The 381.5-keV peak was shown in Sec. 3B to consist of two γ rays very close in energy and in coincidence with each other. The second 381.5-keV γ ray is therefore placed as depopulating the 804.8-keV state to the 423.5-keV state.

At this point, it was not possible to complete the construction of the decay scheme in a way that is consistent with the coincidence data without postulating the existence of a state at 5.0 keV. The previously mentioned intensity ratios of the 418.6- and 423.5-keV doublet imply that these transitions originate from the same state. In addition, there are other doublets with 5-keV energy differences, namely, the 732.0–736.8-, 1237.6–1242.6-, and 1947–1952.2-keV pairs. The 732.0–736.8-keV doublet also always occurred together and in the same intensity ratio in both singles and the coincidence spectra.

An effort was made to detect photons at 5.0-keV with a proportional counter and with a thin-window, high-resolution Si(Li) detector; but, because of the highly converted nature of low-energy transitions and the large background caused by the other photons and positrons, the results were inconclusive.

A careful search was made in both the photon and internal-conversion spectra for a transition of 37 keV which would fit between the 42.3- and 5.0-keV states. An upper limit of 1% can be placed on the intensity for such a 37-keV transition relative to the intensity of the 42.3-keV photon.

The triple-coincidence spectra (Fig. 12) support the placement of the states at 423.5 and 804.8 keV. Only the 381.5-, 418.6-, 423.5-, and 762.5-keV transitions are seen to be in prompt coincidence with the positrons. The positron branching ratios calculated from early

triple-coincidence data obtained from NaI(Tl) detectors were, in units relative to the 762.5-keV photons, 4.0±0.8 for the 804.8-keV state and 7.2±1.5 for the 423.5-keV state. These agree, to within the experimental error, with those obtained from the Fermi-Kurie plots, which were 5.2±1.0 for the 804.8-keV state and 7.9±1.5 for the 423.5-keV state. These values are consistent with those calculated using the proposed decay scheme and relative photon intensities and theoretical K/β^+ and E_K/E_L ratios.[18,19]

C. Evidence for States at 295.2 and 389.2 keV

The coincidence spectra show that the 1562.5-keV photon is in coincidence with the 94.2-, 290.2-, and 389.2-keV transitions and that the 94.2-keV photon is in coincidence with the 290.2-keV photon. The 389.2-keV photon was not observed to be in coincidence with either the 94.2- or 290.2-keV photons. The energy difference of 4.8 keV between the 389.2±0.5-keV and the sum of the 94.2±0.5- and the 290.2±0.5-keV photons is too large to be accounted for by the experimental errors of the energy measurements of these three photons; therefore the 389.2-keV photon cannot be a crossover transition for just the 94.2- and 290.2-keV photons alone. These coincidence data can be explained easily with the inclusion of the unobserved 5.0-keV transition in cascade with the 94.2- and 290.2-keV photons. Hence, states were placed at 295.2 and 389.2 keV.

The evidence for the placement of the state at 295.2 keV instead of at 99.2 keV is very weak. [*Note added in proof.* In a preliminary report, S. Morinobu *et al.*[20] presented data obtained from experiments similar to those reported herein. Their data are in substantial agreement with ours. They have also measured the half-life of the 42.3-keV state to be 7.8±0.7 msec., which is in agreement with the $M2$ assignment to the 42.3-keV transition. In a delayed-coincidence experiment on the 290–94-keV cascade, they found the half-life of the 94-keV transition to be 1.2 nsec. This establishes the order of the 290–94-keV cascade, which was found to be ambiguous in our experiments. This order is opposite to that given in the decay scheme shown in Fig. 18. S. Morinobu *et al.*[20,21] have also performed angular correlation experiments on the 1562–94-, 1562–290-, 1562–389-, and 1147–762-keV cascades. Their correlation coefficients are consistent with our spin assignments to the states involving these transitions.] The intensities of the 94.2- and 290.2-keV transitions are equal to within the experimental errors. According to the energy sum and relative intensities, the very weak 1796-keV transition fits nicely between the states at 2090.2 and 295.2 keV. However, the 1796-keV photon was seen only once and then in an anticoincidence spectrum that was taken over a very long time. Therefore, this transition is not placed in the scheme.

D. Evidence for States at 1202.0, 1242.6, and 1952.2 keV

The anti-Compton and the "any γ-γ" coincidence spectra indicate that the 1160.0-, 1202.0-, 1237.6-, 1242.6-, 1947-, and 1952.2-keV transitions are not in prompt coincidence with any other photons and therefore they probably populate the 42.3, 5.0 keV, or ground state. Numerous coincidence relationships and energy sums support the placement of states at 1202.0, 1242.6, and 1952.2 keV.

E. Remaining States

The remaining states account for a very small fraction of the decays of ^{83}Sr and were placed on the basis of the coincidence data and, in a few cases, upon the existence of an energy sum alone. Those transitions not observed in coincidence and not satisfying an energy sum were left out of the decay scheme. These were the 1296.0-, 1384.3-, 1596-, 1710-, 1749-, and 1796-keV photons.

5. SPIN AND PARITY ASSIGNMENTS

A. 42.3-keV State

The ground-state spin and parity of ^{83}Rb have been determined[22,23] by atomic-beam methods to be $\frac{5}{2}^-$. Since it was shown in Sec. 3C1 that the 42.3-keV transition has multipolarity $M2$, the spin and parity of the state at this energy is limited to $\frac{1}{2}^+$ or $\frac{9}{2}^+$. Although the $\frac{1}{2}^+$ assignment was considered, it did not lead to a consistent interpretation of all the data. On the other hand, the $\frac{9}{2}^+$ assignment, which might be expected on the basis of shell-model systematics, does lead to consistency. Hence, we tentatively assign spin and parity of $\frac{9}{2}^+$ to the 42.3-keV state.

B. 5.0- and 423.5-keV States of ^{83}Rb and the Ground State of ^{83}Sr

The 423.5-keV state decays via an $E1$ transition (423.5 keV) to the $\frac{5}{2}^-$ ground state, and by an $E2$ ($+M1$?) transition (381.5 keV) to the $\frac{9}{2}^+$ 42.3-keV state. Hence, the 423.5-keV state must have spin and parity $\frac{5}{2}^+$ or $\frac{7}{2}^+$. Any $M1$ admixture in the 381.5-keV transition would limit the choice to $\frac{7}{2}^+$.

From shell-model considerations and the systematics of the odd-A strontium isotopes, it is expected that

[18] M. L. Perlman and M. Wolfsberg, Brookhaven National Laboratory Report No. BNL 485(T-110), 1958 (unpublished).
[19] A. H. Wapstra, G. J. Nijgh, and R. Van Lieshout, *Nuclear Spectroscopy Tables* (North-Holland Publishing Co., Amsterdam, 1959), p. 58.
[20] S. Morinobu, I. Katayama, H. Adachi, M. Ishii, and H. Ikegami, Contributions to International Conference on Nuclear Structure, 1967, Tokyo, Japan, contribution No. 4.124, p. 169 (unpublished).
[21] S. Morinobu (private communication).
[22] J. B. Hobson, J. C. Hubbs, W. A. Nierenberg, H. B. Silsbee, and R. J. Sunderland, Phys. Rev. 104, 101 (1956).
[23] J. C. Hubbs, W. A. Nierenberg, H. A. Shugart, H. S. Silsbee, and R. J. Sunderland, Phys. Rev. 107, 723 (1957).

^{83}Sr will have spin and parity of $\frac{1}{2}^-$, $\frac{7}{2}^+$ or $\frac{9}{2}^+$. The logft values for the β transitions to the 42.3- and 423.5-keV states appear to be allowed, or possibly first forbidden. Hence, the spin and parity of $\frac{1}{2}^-$ is ruled out for the ground state of ^{83}Sr.

The $E1$ character of the 418.6-keV transition between the 423.5- and 5.0-keV levels implies the latter has negative parity with spin $\frac{3}{2}$ or greater, but less than $\frac{9}{2}$. As previously noted, an upper limit of 1% on the intensity of a 37.3-keV photon relative to that of the 42.3-keV photon has been set. If the 5-keV state had spin and parity of $\frac{7}{2}^-$ or $\frac{9}{2}^-$, this would suggest that an $E1$ transition between the 42.3- and 5.0-keV states would be retarded by a factor of 10^{11}, assuming that both it and the 42.3-keV $M2$ transitions were single particle. Furthermore, such an upper limit for the relative intensity of a 37.3-keV photon relative to that of the 42.3-keV photon would seem to rule out the possibility of an $M2$ transition between the states in question. Hence, we conclude that the spin and parity for the 5-keV state is $\frac{3}{2}^-$ or $\frac{5}{2}^-$, with the $\frac{3}{2}^-$ assignment being preferred. This then fixes the spin and parity of the 423.5-keV state as $\frac{5}{2}^+$, and from the logft value of 5.7 for the decay to this level, the ground state of ^{83}Sr is inferred as $\frac{7}{2}^+$.

C. 295.2- and 389.2-keV States

The $M1+E2$ character of the 290.2-keV transition, in conjunction with the spin and parity of the 5-keV state, establishes the parity of the 295.2-keV state as negative with spin $\frac{1}{2}$, $\frac{3}{2}$, or $\frac{5}{2}$. Of these possibilities, $\frac{5}{2}$ would be excluded by the high logft value (i.e., ≥ 9) for the decay to this level. Moreover, the absence of a transition from the 295.2-keV state to the $\frac{5}{2}^-$ ground state, as well as the absence of other transitions to this level (except for the 94.2-keV transition), would make a $\frac{3}{2}^-$ assignment difficult to comprehend. This, with the lower limit for the logft value for decay to this level, leads us to suggest spin and parity of $\frac{1}{2}^-$ for the 295.2-keV state.

The measured and assigned spins and parities for the ground and 295.2-keV states, respectively, in conjunction with the $E2$ and $M1+E2$ transitions from the 389.2-keV state to these levels, then determine the spin and parity of the 389.2-keV state as $\frac{3}{2}^-$. This assignment would be consistent with the logft value (i.e., >8) for the decay to this state.

D. 804.8-keV State

The $E2$ character of the transitions from the 804.8-keV state to the 42.3- and 423.5-keV states restricts the spin and parity to $\frac{5}{2}^+$, $\frac{7}{2}^+$, or $\frac{9}{2}^+$. These are consistent with the allowed logft value for the β decay to this level. From the absence of observed transitions to levels with spins $\frac{1}{2}$ and $\frac{3}{2}$, it would appear that $\frac{7}{2}^+$ or $\frac{9}{2}^+$ is most probable for the 804.8-keV state. Any $M1$ admixture in the 381.5-keV transition to the $\frac{5}{2}^+$ 423.5-keV state would eliminate the possiblity of $\frac{9}{2}^+$.

E. 1202.0-keV State

The $M1+E2$ character of the 778.4-keV transition, in conjunction with the allowed logft value for the β decay to the 1202.0-keV state, would restrict its spin and parity to $\frac{5}{2}^+$ or $\frac{7}{2}^+$. The fact that this level is observed to decay only to states with spins and parities of $\frac{5}{2}\pm$ and $\frac{9}{2}^+$ suggests that the spin and parity of the 1202.0-keV state is $\frac{7}{2}^+$.

F. 1242.6-keV State

The $M1$ character of the 818.6-keV transition, in conjunction with the allowed logft value for the capture decay to the 1242.6-keV level, would restrict its spin and parity to $\frac{5}{2}^+$ or $\frac{7}{2}^+$. The γ-ray branching from this level would seem to favor the $\frac{5}{2}^+$ assignment.

G. 1952.2-keV State

The logft value of 5.1 for the capture decay to the 1952.2-keV state implies that it should have spin and parity $\frac{5}{2}$, $\frac{7}{2}$, or $\frac{9}{2}^+$. Of these, the γ-ray branchings to levels with spins and parities of $\frac{3}{2}^-$, $\frac{5}{2}^-$, $\frac{5}{2}^+$, and $\frac{7}{2}^+$ would tend to favor a $\frac{5}{2}^+$ assignment to the 1952.2-keV state.

H. 2090.0-keV State

Here also the logft value of 5.6 would imply $\frac{5}{2}$, $\frac{7}{2}$, or $\frac{9}{2}^+$ for the spin and parity of the 2090.0-keV state. The photon branchings to levels with spins and parities $\frac{5}{2}^-$, $\frac{5}{2}^+$, $\frac{7}{2}^+$, and $\frac{9}{2}^+$ would seem to favor a $\frac{7}{2}^+$ assignment.

I. 2179.2-keV State

The allowed logft value and the observation of only γ-ray branches to levels with spins and parities $\frac{7}{2}^+$ and $\frac{9}{2}^+$ would seem to favor a $\frac{9}{2}^+$ assignment for the 2179.2-keV state.

6. DISCUSSION

The calculations of Talmi and Unna[1] predict the ground state of $_{38}{}^{83}Sr_{45}$ as $\frac{9}{2}^+$, with excited states of spin-parity $\frac{1}{2}^-$ at 170 keV and $\frac{7}{2}^+$ at 320 keV. Even though the odd-mass strontium isotopes ^{85}Sr and ^{87}Sr have similar level structures, the other 45-neutron even Z nuclei ^{77}Ge, ^{79}Se, and ^{81}Kr have $\frac{7}{2}^+$ ground states.[24] The $\frac{7}{2}^+$ assignment for ^{83}Sr, which has been inferred from this study, is thus consistent with the systematics in this region. The state possibly corresponds to a $(p_{1/2})^{-2}$ $(g_{9/2})^{-3}{}_{7/2}$ shell-model configuration.

[24] *Nuclear Data Sheets*, compiled by K. Way *et al.* (U. S. Government Printing Office, National Academy of Sciences—National Research Council, Washington, D. C.).

Figure 19 compares the few known states below 525 keV in the odd-mass rubidium isotopes. In ^{83}Rb, the ground state ($\frac{5}{2}^-$), the 5.0 ($\frac{3}{2}^-$)-, the 4.23 ($\frac{9}{2}^+$)-, and 295.2($\frac{1}{2}^-$)-keV states probably arise from shell-model proton configurations $(f_{5/2})^{-1}$, $(p_{3/2})^{-1}$, $(g_{9/2})^1$, and $(p_{1/2})^1$, respectively. However, the extremely close spacing of these levels may indicate an appreciable amount of a more complex configuration mixing. The low-lying $\frac{3}{2}^-$ state is expected since the $(p_{3/2})^{-1}$ and $(f_{5/2})^{-1}$ configurations are in competition for the ground state of the rubidium isotopes,[24] the former apparently prevailing for ^{81}Rb and ^{87}Rb, the latter for ^{83}Rb and ^{85}Rb. The $\frac{9}{2}^+$ states in ^{81}Rb and ^{85}Rb probably correspond to the same type configuration assigned for ^{83}Rb. The $\frac{9}{2}^+-\frac{5}{2}^-$ energy-level separation is changing very rapidly in this series of nuclei, the $\frac{9}{2}^+$ state actually being the lower state in ^{81}Rb. This trend may suggest that the 2970-keV state in ^{87}Rb is $\frac{9}{2}^+$, an assignment which is consistent with the logft value of the β transition to the level.[24] Very little is known about the level schemes of these other odd-mass rubidium isotopes, suggesting the need for further investigations in this region before systematic trends of the single-particle levels can be established.

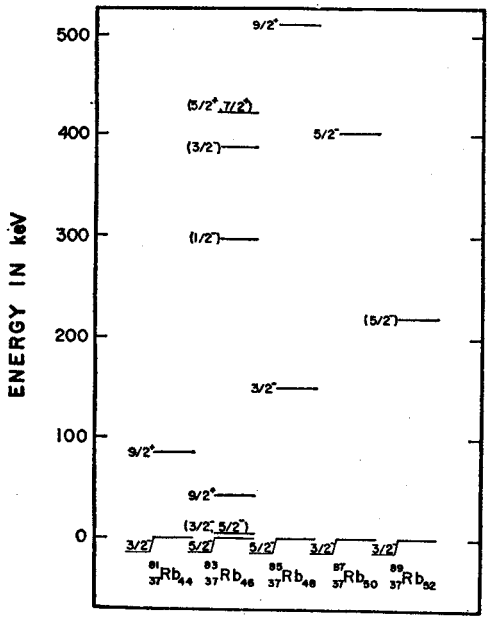

FIG. 19. Comparison of the low-energy levels of the odd-mass rubidium isotopes.

It is conceivable that some of the higher-energy states in ^{83}Rb could arise from more complicated shell-model configurations, as well as collective excitations. It is interesting to consider that the strongly excited 423.5- and 804.8-keV states can be attributed to the latter phenomenon. This can be done from two slightly different points of view, although there are objectionable features to both interpretations. First, it is noted that the 804.8-, 423.5-, and 42.3-keV states are connected by two relatively pure $E2$ transitions of comparable energy, hence suggestive of a vibrational structure built on the 42.3-keV ($\frac{9}{2}^+$) single-particle state. The other point of view, based on the core coupling model of de-Shalit,[25] assumes the 804.8- ($\frac{7}{2}^+$) and 423.5-keV ($\frac{5}{2}^+$) states are part of a multiplet of states produced by coupling of the 2^+ core excitation with the $\frac{9}{2}^+$ particle state. However, transitions between members of the multiplet should be predominantly $M1$, whereas an upper limit of 40% can be placed on the $M1$ contribution of the observed transition. In either event, if the 804.8-keV state is truly of collective nature, the $E2$ transition probability of the 762.5-keV transition should be enhanced over the Weisskopf single-particle estimate.[19] A measurement of the lifetime of the state might serve to test the hypothesis.

Finally, one might expect similar collective states built on the ground and 5.0-keV states in much the same manner as they seem to be built on the $\frac{9}{2}^+$ state. The 389-keV level may have such a composition. However, most of the states formed in this manner may be inaccessible to the β-decay process, since it requires a $g_{9/2}$ neutron to be transformed into an $f_{5/2}$ or $p_{3/2}$ proton, a process which is both j- and l-forbidden. On the other hand, one might expect the decay of the $g_{9/2}$ extra core neutron in ^{83}Sr to very effectively populate levels built on the $g_{9/2}$ proton states in the ^{83}Rb daughter.

[25] A. de-Shalit, Phys. Rev. 122, 1530 (1961).

ACKNOWLEDGMENTS

The authors wish to thank Dr. R. L. Auble and Dr. G. Berzins for assistance with the data analysis. We are also grateful to Dr. G. B. Beard for the use of his high-resolution Si(Li) detector. The assistance of Dr. W. P. Johnson and Dr. H. G. Blosser with the early MSU cyclotron runs is gratefully acknowledged. Two of the authors (W. H. K. and D. J. H.) wish to express their appreciation to the staff of the Lawrence Radiation Laboratory, Berkeley, Calif., for their splendid hospitality during the early stages of this investigation, and to the U. S. Atomic Energy Commission for its support during this same time. The aid of Dr. R. M. Diamond, of LRL, with the HILAC bombardments is very much appreciated. The encouragement and assistance of Dr. S. K. Haynes and W. C. Johnston with the measurements with the $\pi\sqrt{2}$ iron-free electron spectrometer are deeply appreciated. We wish to thank Dr. J. P. Hurley and J. M. Mathiesen for the use of their Ge(Li) detectors during the early stages of this work. One of the authors (R.C.E.) wishes to thank the NSF for the Science Faculty Fellowship that he held during the early stages of this investigation. Another of the authors (L.M.B.) wishes to gratefully acknowledge the assistance of an NDEA fellowship.

JANUS: A flexible approach to realtime timesharing*

by J. O. KOPF and P. J. PLAUGER

Michigan State University
East Lansing, Michigan

INTRODUCTION

Motivation

A third generation computer seems to cause as many problems as it solves; not because it is difficult to program or too problem directed—quite the contrary. The problems arise because such a computer lends itself so willingly to *all* applications—realtime data acquisition, process control, scientific calculations, bookkeeping and conversational time-sharing. In a nuclear physics laboratory, there are enough imaginative people interested in each of these subjects that eventually all are implemented with some success. The central problem, then, is to develop an operating environment compatible with open-ended development of any or all types of computer usage. Ideally, one seeks a standard operating system providing the framework and resources to aid all such development.

In our case, the desired priority of computer usage was to be: 1. realtime data acquisition and control; 2. interactive on-line operations, especially data analysis; 3. background operation. In a nuclear physics experiment, realtime operation is normally characterized by immense buffers—which are updated at each input event, rather than transmitted as sequential data—indicating the desirability of a small resident monitor, and non-permanently dedicated interrupt routines and buffers. Event rates as high as 50,000 events/second may be expected, implying the need for a powerful computer to perform quickly the operations necessary to each event.[1,2]

The Michigan State University Cyclotron Laboratory installed a Scientific Data Systems Sigma-7 computer in January 1967. We have constructed operating system JANUS for the Sigma-7 to meet the goals outlined above. JANUS has proved to be far more powerful than we originally expected.

The SDS Sigma-7

The SDS Sigma-7 is a high-speed, integrated circuit machine with sophisticated timesharing hardware.[3] It features a 32-bit word, with displacement indexing by 8-bit bytes, half-words, words and doublewords, and direct addressing to 128k words. Timesharing hardware includes master/slave modes, rapid context switching (Exchange- and Load-Program-Status-Doubleword instructions), a powerful interrupt structure with certain functions inhibitable under program control, program traps which are independent of the interrupt structure, and mapping hardware.

The Sigma makes extensive use of scratch-pad memories; integrated flip-flop registers whose access time is insignificant compared with core memory. Thus there are 16 distinct registers, effectively accumulators. Instructions normally reference one or more of these registers. In addition, the computer treats these registers as the first 16 locations of memory: all instructions are valid for register-register operations. The computer is thus effectively a two-address machine, where one address space is a subset of the other. Furthermore, four registers may be used in a block as a decimal accumulator (31 digits plus sign), seven others may be used as index registers (post indexing), and any even-odd register pair may be used for double precision work.

The hardware also makes use of hard-wired table look-up and translation for certain functions. An example is the map. Memory is naturally divided into 512-word pages. The map consists of a scratch-pad memory of 256 bytes, one for each page of virtual memory (virtual memory is the full address space of the machine, independent of

*Supported by the National Science Foundation.

the actual core memory available). When the map is in operation, the first byte of the effective virtual address is used as an index to look up a translation byte from the map, which replaces the original byte to form the actual address used to make the memory reference. As a result, contiguous virtual pages need not be in contiguous actual memory; under a properly initialized map they act as though they are. Associated with each page is a two-bit *access process* code which can inhibit slavemode from writing, executing, or even reading words in the page. In conjunction with a rapid access disc (RAD), this hardware provides the swapping control needed for efficient timesharing.

In addition, the computer has two major means of communicating with the external world. The Input-Output Processor (IOP, of which there may be up to 8) is designed for sequential transmission of data asyncronously with the operation of the computer. The Direct I/O (DIO) provides for the transmission of one word at a time to or from the registers, under program control. JANUS normally uses the IOP for conventional I/O operations; the DIO for acquisition and control.

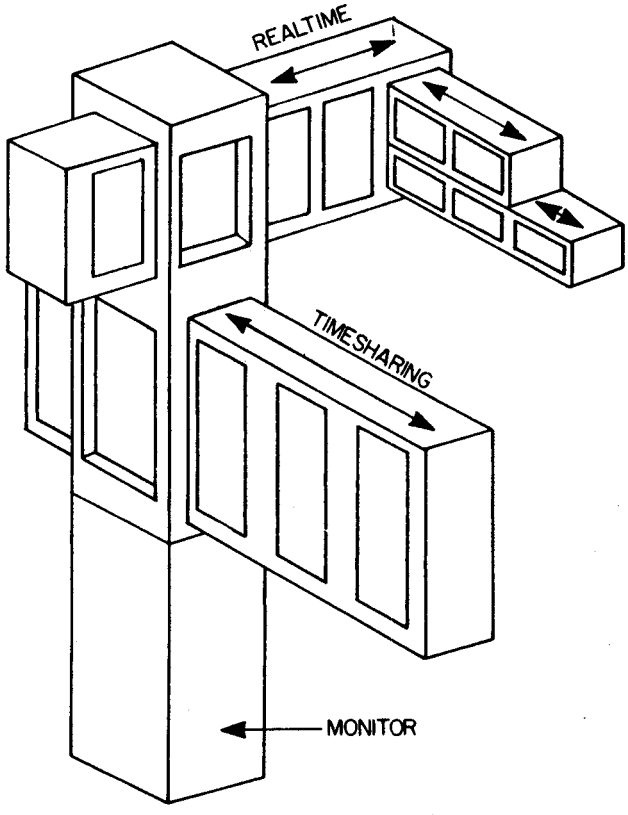

FIGURE 1—Hardware resources of the MSU Sigma-7 system. Items labelled "J" are handled by JANUS. Those labelled "S" are shared by all users on a cyclic basis. All others are loaned out on a first come, first served basis for exclusive use.

Figure 1 details the resources available on the MSU Sigma-7.

Other approaches

Before going into the details of JANUS, we should perhaps explain why we felt existing approaches were inadequate for our needs.

Conventional realtime systems are usually geared for one application, or one set of applications. One cannot randomly start and stop arbitrary functions, even though the particular resources needed may be standing idle. In particular, one cannot "batch" process (i.e. compile, load and run a series of purely computational programs) to take advantage of the usually large CPU time available between interrupts.

By dividing memory into *foreground* and *background* areas, it is possible to operate a batch system in conjunction with one or more realtime operations. Aside from the fact that either of these areas is frequently; a) unused for long periods of time or, b) inadequate for many jobs that *could* be run in full memory, there is a more sophisticated drawback. Since realtime operations must often use the same resources as the batch, a large resident monitor is needed to handle common operations and to prevent conflicts. Furthermore, since realtime operations occur on an interrupt basis, the monitor must either be reentrant to several levels or must inhibit interrupts while it is active (or a little of both). The former solution makes the resident even larger and slower—the latter interferes with fast response to realtime events.

Conventional time-sharing systems[4] can be geared to provide the random stop/start of realtime which we desire, and are better geared to adapt efficiently to dynamically changing memory availability. But the usual approach has been to take an already large foreground/background type monitor and to add a swapper, job scheduler and elaborate I/O queuing routines to the resident. The dedicable memory left over can be vanishingly small.

Figures 2 and 3 caricaturize the distinction we made between what we saw in conventional approaches to realtime timesharing and what we envisioned for JANUS.

There still remains the problem, not yet mentioned, of the hybrid job. It is often desirable to

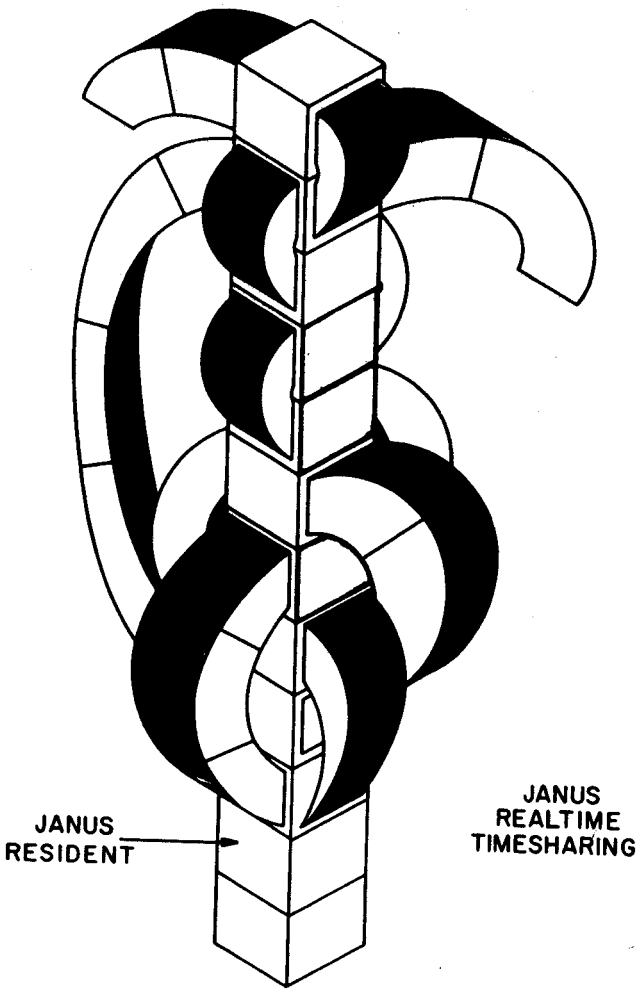

FIGURE 2—Caricature of a "conventional" realtime timesharing system. It is characterized by a large resident monitor and rather rigid frame-at-a-time use of remaining memory.

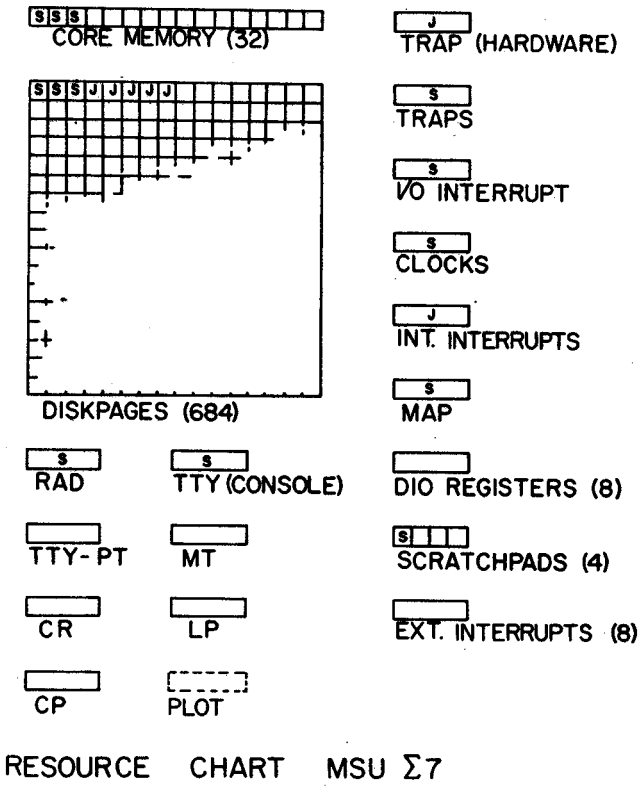

FIGURE 3—Caricature of JANUS system, with small resident and intertwined tasks having both dedicated realtime and timeshared parts.

construct programs having a small realtime part and a large problem-solving part that could happily be timeshared. The question is raised as to specifying such an animal. How is communication between the two parts effected?

We found the answers to these questions, and the inspiration for answering many more, in the definition of PL/I.[5]

Design of JANUS

Terms and philosophy

The PL/I language definition provides a vocabulary and a philosophy (we have probably corrupted both). In PL/I a piece of code containing all routines needed to perform a job, or distinct part of a job, is a *task*. A task can start one or more *subtasks* to perform asynchronous operations; it can go into a wait state until certain *events, signalled* by other tasks, occur, On can specify *on-units* to be activated when *conditions* are raised (interrupts or traps). These are the terms needed to describe what JANUS does.

Equally important is the philosophy. PL/I is a modular language with the built in attitude, "If you don't know about this option, it isn't there. I will do what you most likely want done." With only 16k words of core memory, one must necessarily begrudge the presence of excess code. This is the philosophy by which JANUS works.

It should be emphasized that JANUS does not require the PL/I compiler to operate, nor do we plan to write one. The concepts are quite useful without the compiler.

Timeshared monitors

A monitor is used to provide certain functions, such as control and I/O, which a user either does not want to implement himself, or cannot be trusted with. However, these functions may be made modular in form, and can thus be loaded from a library.

The amount of code that truly must be resident in a timesharing system is really quite small. A scheduler (JOB CHANGER) and RAD handler (SWAPPER) are, of course, required. A console teletype handler is rather important to initiate system actions and to provide a common voice-ear for all users. Other I/O handlers are not required.

If one extends the concept of a task to include all the mastermode routines required for its execution, many interesting by-products result. First, the resident requirements are drastically reduced. If no one is reading cards, no card reader handler is in memory. Second, each task can have a "tailor-made monitor." If task A never does realtime operations, it has no such handlers in its master-mode end. Third, and perhaps most important, monitor routines need not be re-entrant. Each talks only to one user.

All the resident must do is act as referee. Peripherals, indeed any nonshareable system resources (interrupts, extra register blocks, disc space) are handed out on a first come, first served basis, and passed on to the next requestor when released by the current user.

Naturally, such a scheme requires that all mastermode routines be "honest," and completely debugged, but this is a rather ordinary requirement. A malicious or naive mastermode routine can cause damage any number of ways, so JANUS assumes that no such routine exists and performs virtually no checking. While it may appear that spreading the responsibility for system integrity over many routines increases the programming load, the fact that each routine is a module with clearly defined rules of construction actually makes the coding job much easier.

Thus, JANUS is a system that timeshares monitors, in the ordinary sense, and is itself only a referee. Each monitor essentially patches together the small computer it needs to perform a specific operation, leaving all unused system resources available for other tasks. Since, in general, no one job requires more than a few private resources, another subsystem can be constructed from the remainder, and then another, until the entire system is active.

In the MSU implementation, the JANUS resident occupies 3.5k words (7 pages).

Resident and system tasks

The RAD is arbitrarily divided into approximately 680 diskpages, each holding 512 words of useable information. Each distinct page of a task or file has a unique *diskname* (16-bit) by which JANUS can locate it. The first page of every task begins at location X' C00' under the map and is called the *task control page* (TCP). All information required by JANUS to bring in a task and start it up is stored in fixed locations in the first 34 to 283 words of the TCP, depending on the size of the task. Thus, JANUS needs only know the diskname of the TCP, called the *taskname,* to bring in the whole task. With 16-bits of status information, the taskname becomes a one-word entry on the resident ring of active tasks.

Note that a task sees only 3.0k of JANUS. (Under the map, each task is executing in its own unique address space of up to 128k-words, generally independent of the available core memory. Task address spaces diverge after 6 pages: the lower 3k are common to all tasks and contain the major portion of JANUS.) The remaining resident page is the TCP of the HOUSEKEEPER task, the nonresident supervisor. Rather than maintain complete lists of resources and requests in resident, JANUS maintains only token lists, to meet short-term needs, and invokes the HOUSEKEEPER as needed to tidy up lower core.

JANUS also serves as intermediary between interrupt routines, which run unmapped in dedicated memory, and their controlling tasks, which are mapped and not necessarily in memory at any given time. The most important service provided is the MESSAGE CENTER, the *only* multiply re-entrant resident routine in the system. It will accept a one word *signal* (consisting a 16-bit taskname and an 8-bit identifier) from any source and pass it on to the specified task, pulling it out of a wait state if necessary. Great pains have been taken to ensure that no signals are lost, duplicated or rejected by JANUS.

Communication in the other direction—alerting interrupts—is generally possible through the hardware. Interrupts can be triggered under program control. But since the I/O interrupt has a software fan out to individual device handlers, JANUS provides a software device-directed trigger, or "kick," to aid communication. A pseudo-acknowledgment status word is added to a queue and the interrupt is triggered. The resident interrupt routine, after acknowledging all real interrupts, empties the queue, passing the contents to the individual routines. This feature simplifies coding of I/O handlers, since all con-

trol operations can be confined to the interrupt end of the handler.

The last major component of the resident is the console teletype handler, used by all tasks to communicate with the operator. Output is sequential in order of request and may interrupt an input. All console teletype I/O is prefix directed to the appropriate task. A prefix pool is available to provide unique prefices upon request. Prefices consist of a byte count, plus up to 3 characters.

One prefix, the ampersand (&) is reserved for directing messages to JANUS. A special task, the AMPERSCANNER, decodes these messages and takes appropriate action. The AMPERSCANNER knows where to find, or how to generate, all tasks built into the system, and thus is responsible for initiating most processes.

A third system task is the MORTICIAN, which dissects dead tasks and files, and returns their component pages to the system diskpage pool.

Other system tasks are an open-ended set of symbionts, used to perform an I/O operation with a disk file. Tasks may either do their own I/O or generate a file, and let the appropriate symbiont perform the necessary I/O operations. Symbionts do not take up any memory space unless they are actively working on a file. Only the system tasks are immortal under JANUS. All other tasks are brought into existence for a specific application and are interred when no longer needed.

Operation

Job changer

Figure 4 is a flow chart of the JOB CHANGER, which is responsible for entering and leaving tasks between time slices, and for delivering messages (signals) to tasks. The lowest priority interrupt is the job-changing interrupt. It fires when its corresponding count pulse interrupt counts to zero (or when triggered by a CPU instruction), and transfers control directly to the task monitor to perform register saving and any other slice-end functions needed before branching to the JOB CHANGER.

Similarly at slice-start, the JOB CHANGER gives the task monitor an opportunity to process signals and restore registers before continuing. A special purpose task thus has the option of streamlining both ends of the process. Note that a task also has the option of putting itself on high priority, a status such that it must be the next task executed, although this practice is discouraged.

No attempt is made to compute an "optimal" slicetime. This interval is fixed by an empirical tuning process and is currently 0.1 second.

Swapper

A flow chart of the SWAPPER algorithm is shown in Figure 5. Once the TCP of the next task is in memory, the SWAPPER works from a variable length table in the TCP to determine what pages *must* be brought in (or located in memory) to permit the task to proceed.

Since it takes an average of 28 milliseconds to read or write one page of memory to the RAD, whenever possible great effort is made to avoid actually swapping. Some of the techniques used are:

1) Storage areas are grouped together, beginning on a page boundary, so that all other pages can be flagged "read only." Thus, the SWAPPER knows not to write these pages back to the RAD.

2) Slavemode storage areas are at first write-protected, so that the task monitor can inform the SWAPPER (via the TCP table) whether or not a page has been modified.

3) Only those pages of a task which are known to be needed (or for which usage cannot be monitored) during the next timeslice are flagged "must be in next time" or "must be in everytime."

4) A four-level "usage priority" is maintained for each page of real memory (see Figures 4 and 5). After each timeslice it is set to a high value if used, reduced toward zero if not. As a result, pages are "turned" according to a weighted LRU (Least-Recently Used) algorithm. A page which must be written back has a higher weight than one which does not. Other weight criteria may also be established. This simple trick helps the JOB CHANGER and SWAPPER "learn" the best way to use memory as the system load changes.

Such great pains were taken to improve swap efficiency, in fact, that a wholly unexpected by-product was created. Slavemode memory usage could be monitored so closely that *the slave portion of a task need never be all in memory at once,* but instead pages would be brought into core upon demand. Thus a problem-solving program could be written using the full 128k address space

FIGURE 4—Flow chart for JOB CHANGER (scheduler). It operates at lowest priority interrupt level.

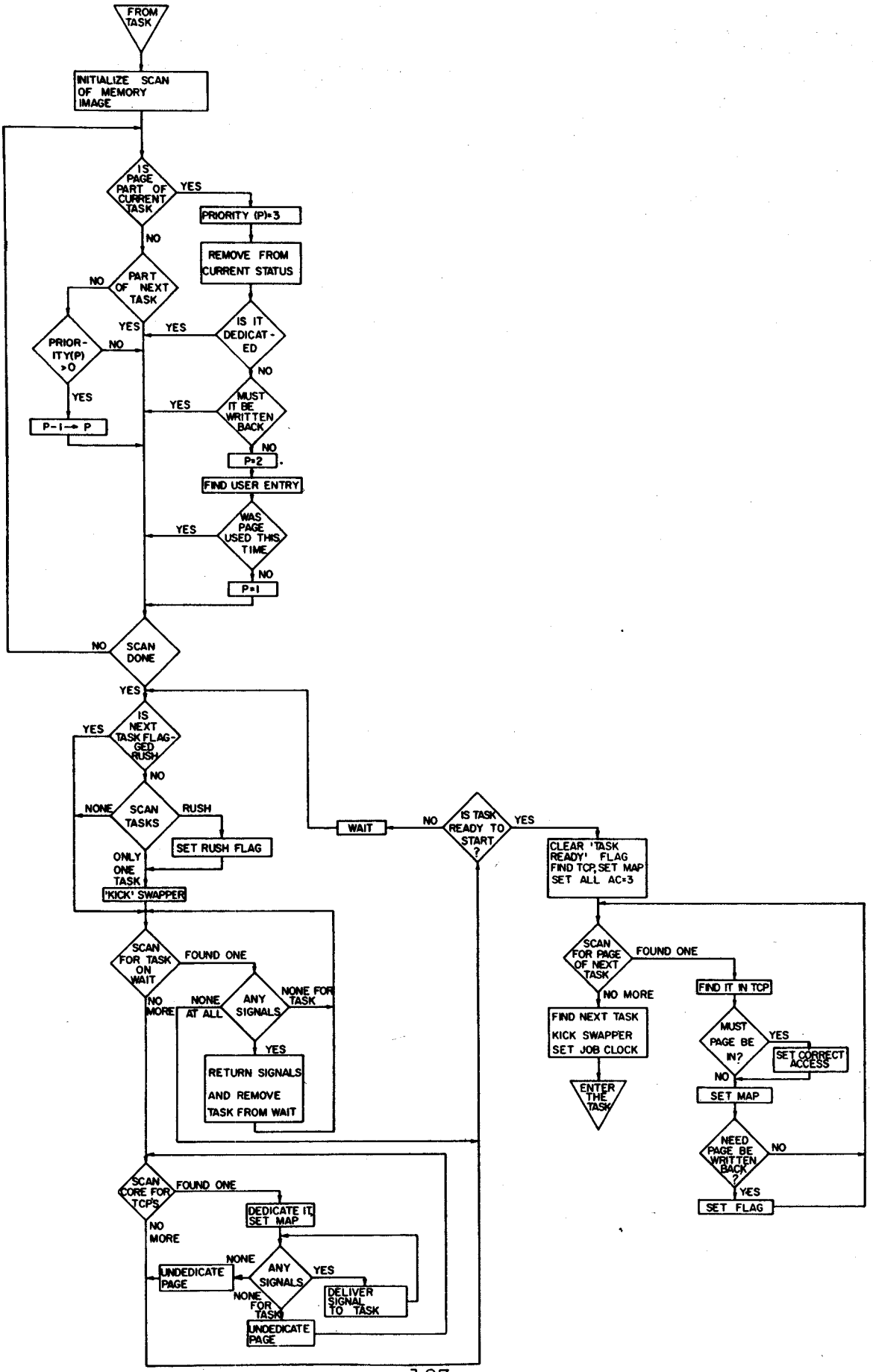

FIGURE 5—Flow chart for SWAPPER. It operates at I/O interrupt level whenever RAD operation completes or software "kick" is administered by JOB CHANGER.

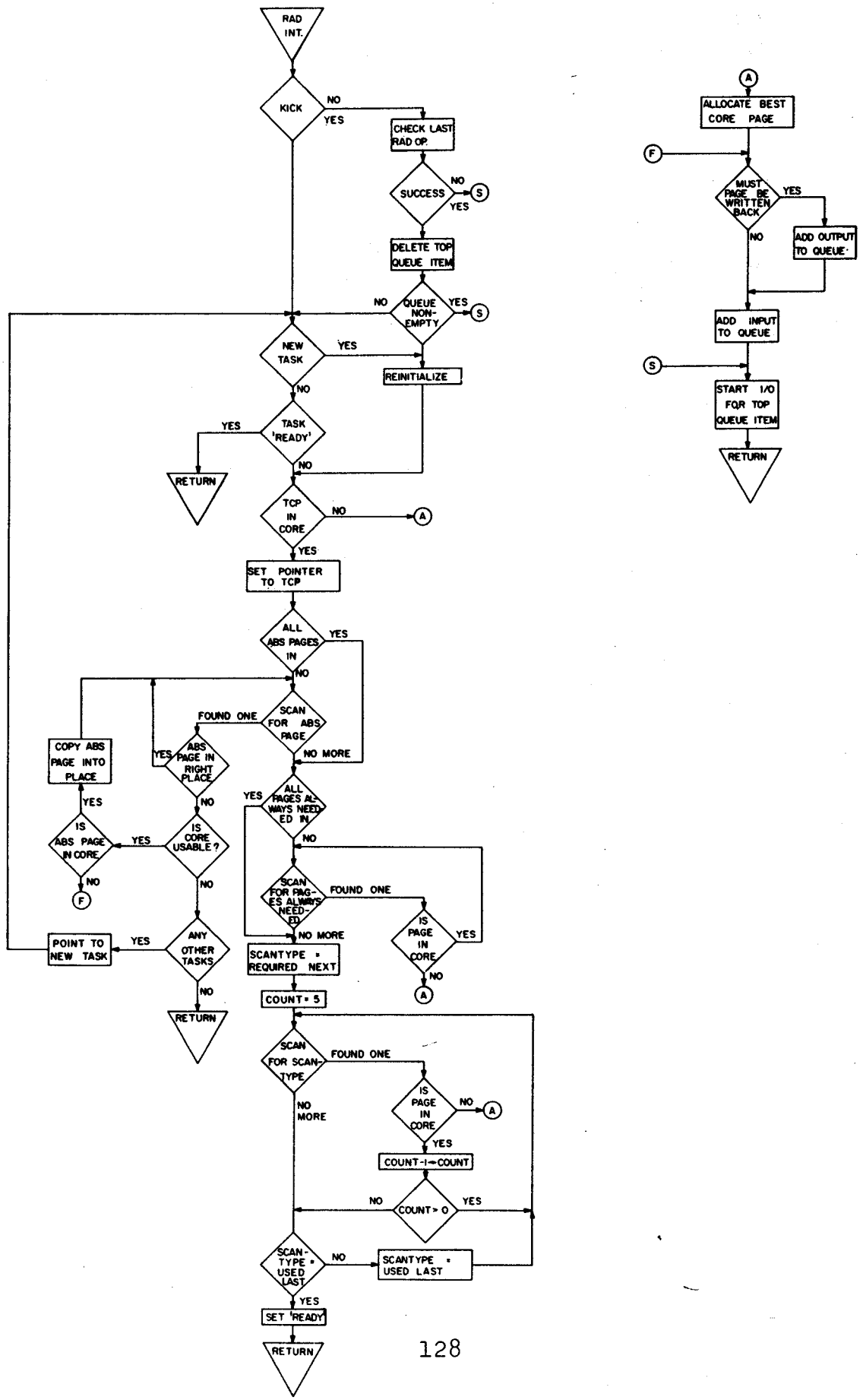

of the machine and, *with no alteration,* run on a Sigma-7 with as little as 8k of actual memory, although less efficiently than in the full machine.

Demand paging

Figure 6 is a flow chart of the demand paging algorithm. It is implemented as an optional task monitor module (a pure process control task would have no use for this feature), and occupies 250-words. Whenever an access protect violation is signalled via the Nonallowed Operation trap, the routine is entered to determine a) what page reference caused the trap and b) whether it was indeed an error or a valid reference. If the latter, the page is made available and usage is noted.

The routine is time consuming because the access protects were not originally designed for this purpose, and hardware deficiencies must be made up in software. But each page traps at most twice during each 0.1 second timeslice, and the possible gain in information weighs heavily against 28 milliseconds per page swaptime.

Except for the Execute instruction, which is infinite level, no Sigma-7 instruction can access more than five pages before reaching an exit point. With special handling for execute, this five page limit applies to all cases. Consequently, timesharing can be maintained as long as there are sufficient non-dedicated pages of memory to hold the largest task monitor, plus five slave-mode pages. The MSU Sigma-7 thus has over half its 16k memory dedicable for I/O and other realtime processes.

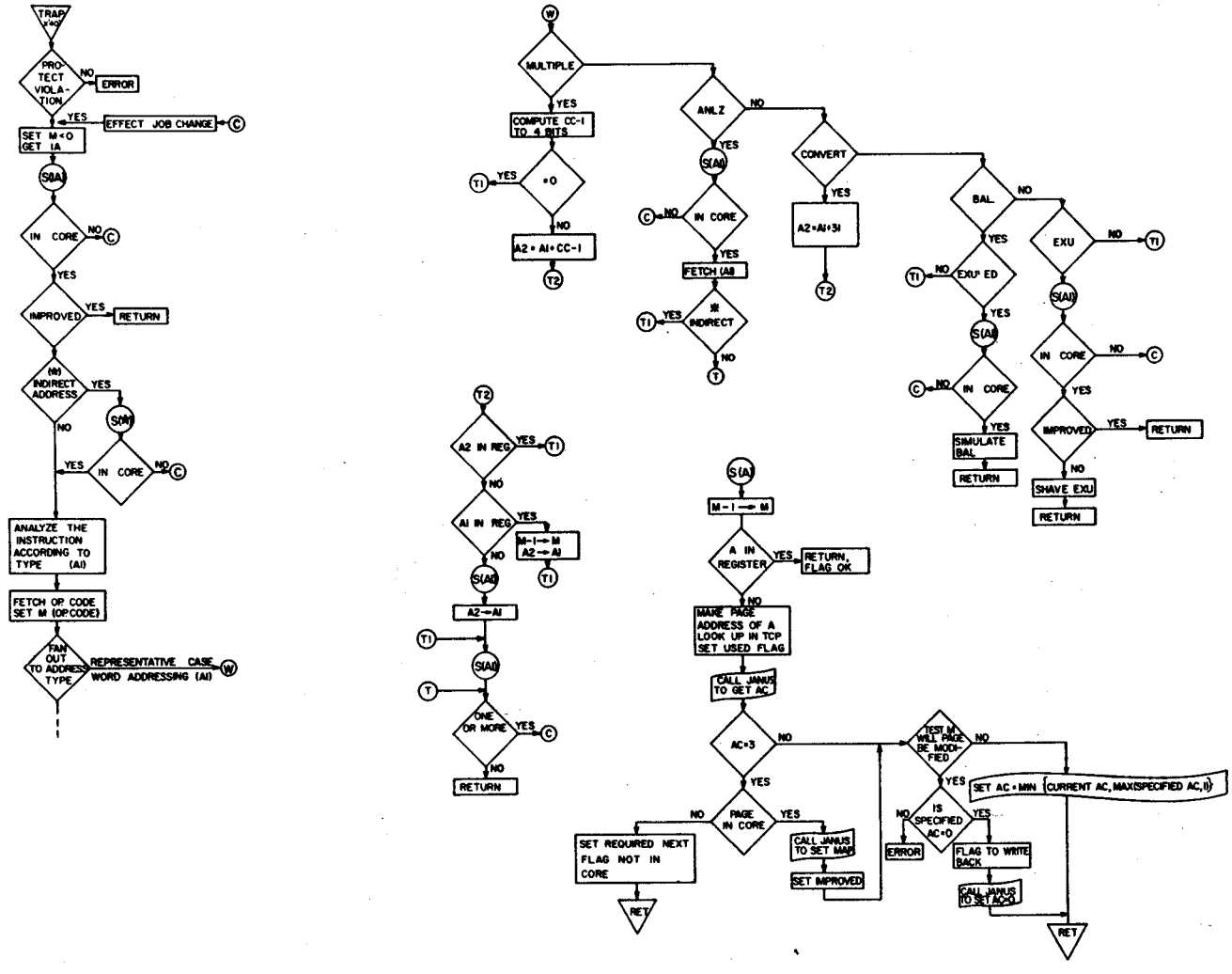

FIGURE 6—Flow chart of Demand Paging algorithm, a 250-word routine which may be included in a task monitor to permit task to occupy full 128k virtual memory. It operates whenever Nonallowed Operation trap occurs in the task.

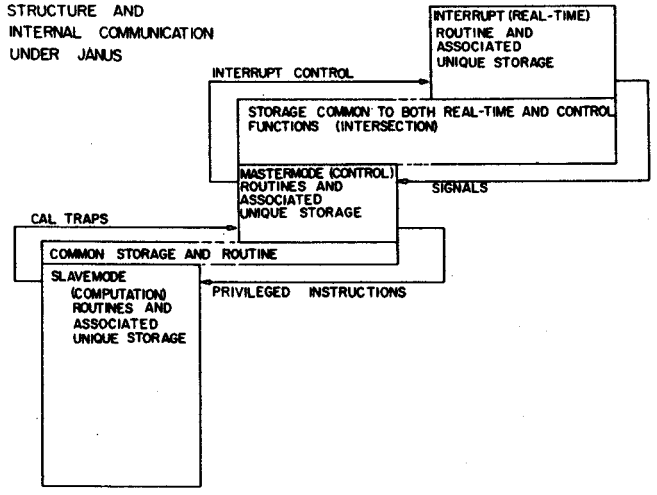

FIGURE 7—Typical realtime (I/O) driver. This illustrates optional three-part division of labor and modes of communication between parts.

Efficiency

It is difficult to measure the overall efficiency of the JANUS system, because loading changes so rapidly with even the simplest uses. Several extreme cases can be cited, however, to provide a feel for overall parameters:

1) In the case where all active tasks fit in memory at once, the SWAPPER "learns" in about 1 second that all codes should be in memory. Afterward, the time spent in the JOB CHANGER and SWAPPER (overhead) drops to less than 5% total CPU time.

2) The FORTRAN optical model code GIBELOMP, which requires approximately 35k words of slave code in a Sigma-7, registers a swap overhead (the fraction of time not spent in slave problem-solving mode) of 20% when running alone in the machine.

3) While it is possible to create pathological cases where swap overhead would exceed 99%, system processors and compiled code seldom burst over 50% overhead.

These figures are, of course, degraded as available memory decreases or external interrupt load increases.

CONCLUSION

JANUS has proved to be a viable solution to the needs outlined in the introduction. By extending the concept of realtime operations to include *all* I/O operations, a small resident is possible, permitting the use of most of memory for production. Whether that production is realtime data acquisition, computation, or a mix is irrelevant—it can proceed if the necessary resources are available. Any realtime process can interrupt the system or background processes at all times, permitting high data rates. The ability to run large computation codes with reasonable efficiency, and in a timesharing environment, is an unexpected boon.

While the concept of timesharing monitors does permit a minimal resident supervisor, it would appear to suffer from the need of writing specialized monitors for the library. However, certain facts should be kept in mind. Each monitor is no more complex than a corresponding standalone system would be—only the rules are different. Each monitor need contain only those functions necessary and sufficient for the task in question. The various functions are modular; once a specific function has been coded, it may be placed in a library for future use, rather than having to be recoded again and again. Given such a library of monitor functions, it is possible to define a system loader (actually a task maker) which can generate a tailor-made monitor. This sort of operation is not uncommon in single-user monitors, where, for example, a magnetic tape handler is included only if the programmer references it implicitly or explicitly. It is not an overly restrictive requirement that the possible set of operations to be performed be known before execution is started.

Demand paging requires some form of map with protection, as well as an external storage medium. Although there is some controversy as to the value of demand paging in a timesharing environment, JANUS demonstrates the value of the concept in situations of single user, limited memory machines. While overhead for problems which fit into core is minimal, larger problems can also be run, although at lower efficiency, at less monetary cost than would be incurred by an increase in core memory. Given demand paging, additional memory increases efficiency. Comparing an open-shop, small demand-paged computer with a closed-shop computation center, turn around time is significantly reduced, even if the actual computer running time is increased by orders of magnitude.

The Sigma-7 is an admirable machine for timesharing, but was not designed with demand paging in mind. Certain features necessary for demand paging, while capable of being implemented

by software, would be much more efficient if implemented in hardware. These include: 1. Scratch-pad registers, readable and clearable under computer control, which would automatically keep track of all pages referenced and modified. 2. A more powerful hierachy of operation modes and a different sequence of protection. A better sequence of protection might be: write permitted, write permitted from master-mode, no write permitted, and no access permitted. Master-slave modes of operation should be expanded to the point where the protection could optionally apply to master-mode thus permitting demand paging operation of such code. 3. A privileged instruction which would interpretively execute any instruction, and return the reference which would cause a trap. Other features, such as a readable map, would be of great use.

In conclusion, we feel that JANUS may well serve as a model for future computer systems, due to its flexibility and lack of constraints. As much as possible, limitations on computer usage are set by hardware, rather than by system conventions.

REFERENCES

1 J A JONES
On-line computers for research
Nucleonics p 34 Jan 1967 A survey of the field containing many references which will not be duplicated here

2 J BIRNBAUM M M SACHS
Computer and nuclear physics
Physics Today p 43 July 1968

3 *SDS Sigma-7 computer reference manual (#90009-506)*
Scientific Data Systems Santa Monica California May 1967

4 B W LAMPSON
A scheduling philosophy for multiprocessing systems
Communications of the ACM p 347 May 1968

5 *IBM System/360 operating system—PL/I language specifications (#C28-6571-4)*
IBM Corporation New York New York December 1966

1.E.4

Nuclear Physics A123 (1969) 54—64; © *North-Holland Publishing Co., Amsterdam*

COLLECTIVE 2^+ AND 3^- EXCITATIONS IN Ni AND Zn ISOTOPES VIA INELASTIC DEUTERON SCATTERING

R. K. JOLLY †, M. D. GOLDBERG †† and A. K. SENGUPTA †††

AERE, Harwell, U.K.

Received 26 July 1968

Abstract: Excitation energies and differential cross sections for inelastic scattering of 11.5 or 11.8 MeV deuterons leading to the collective 2^+ and 3^- states of ^{64,62,60,58}Ni and ^{68,66,64}Zn have been measured. The cross sections have been compared with distorted-wave Born approximation calculations for a deformable potential using complex coupling and including the contribution from Coulomb excitation. Effects of using different exit and entrance channel optical-model parameters on the cross sections for the 3^- states are discussed. In addition to spin and parity assignments, values of B(E2) and B(E3) have been extracted. In all cases studied in the present work, DWBA calculations yield values of $B(\mathrm{E2}; 0 \rightarrow 2)$ in good agreement with previous measurements if the interaction radius is chosen to be the radius of the real well.

E NUCLEAR REACTIONS ^{64,62,60,58}Ni, ^{68,66,64}Zn(d, d') E_d = 11.5 or 11.8 MeV; measured σ ($E_{d'}$, θ). Deduced 2^+, 3^- level energies, J, π, $B(\mathrm{E}\lambda)$. Enriched targets.

1. Introduction

In the past several years, fruitful attempts [1,2]) have been made to interpret data on the low-lying states of spherical nuclei in terms of some simple assumptions regarding the residual interaction. Detailed data on the collective quadrupole and octupole states in doubly even spherical nuclei are very useful for determining this interaction particularly its long-range components. Measurements of the collective quadrupole states are quite numerous [3]), but data on the collective octupole states are not as abundant, because these states are usually found at about three times the excitation energy of the quadrupole state and invariably among a host of other states.

However, recent availability of high-resolution scattering facilities and the successful application of distorted wave Born approximation (DWBA) theories to predict direct interaction inelastic scattering cross sections have stimulated considerable interest in studying collective states by this method. At Harwell, a further stimulus for such measurements was provided by the successful fabrication of position-sensitive detectors (PSD) by the Electronics Division. These detectors, when used in conjunction with a magnetic spectrometer, eliminate the need for complete dependence on time-consuming nuclear emulsion plates. Consequently, a programme

† Present address: Cyclotron Laboratory, Michigan State University.
†† On leave from Brookhaven National Laboratory.
††† Present address: Saha Institute of Nuclear Physics, CALCUTTA.

of systematic studies on the collective states of doubly even spherical nuclei was begun with the isotopes of Ni and Zn.

2. The experimental procedure

Deuterons of 11.5 or 11.8 MeV energy from the Harwell tandem Van de Graaff accelerator bombarded self-supporting targets ($\approx$ 1 mg/cm^2) of ^{58}Ni, ^{60}Ni, ^{62}Ni, ^{64}Ni, ^{64}Zn, ^{66}Zn and ^{68}Zn; and the reaction products were analysed with a Buechner magnetic spectrometer. Angular distributions of inelastic deuteron groups corresponding to quadrupole and octupole excitations in the residual nucleus were measured using two PSD appropriately placed in the focal plane of the spectrometer. Since such use of PSD has been discussed elsewhere [4]), we consider it here only briefly. The output from a PSD consists of an energy pulse E corresponding to the energy loss of the particle in the depletion layer and an EX pulse that depends both on the energy and the location X of the particle incident on the detector. For reactions induced by 11.5 MeV deuterons, the most likely products are protons, deuterons, tritons and α-particles which, for a given magnetic rigidity, have the following relationship in their absolute energies:

$$E_p = E_\alpha = 2E_d = 3E_t, \tag{1}$$

where the subscripts refer to the particle type. Let us assume that the dispersion in the energy of deuterons across the length of a PSD is small as compared to the difference between the energies of protons (or α-particles), deuterons and tritons as given by relation (1). If the depletion depth is sufficient to stop the protons, then the various particle groups are clearly separated in the full energy (E) spectrum. Thus it is possible to select the deuteron spectrum by setting a window in the appropriate region of the E spectrum and studying the EX spectrum in coincidence with the window output. For angular distribution measurements, the EX signal was treated as an X signal. Some nuclear emulsion plate exposures were made at a few chosen angles to measure the excitation energies of the collective 2^+ and 3^- groups and to identify all the peaks that were seen in the gated position spectra from the two PSD. This arrangement for identifying the peaks and measuring their excitation energies is only temporary, as work on filling the entire focal plane of the spectrograph with PSD is currently in progress. Eventually the position signal will be obtained by an analogue division of the EX signal by the E signal.

Since prior DWBA calculations had revealed a rather mild structure in the angular distributions, data were taken at 5° or 10° intervals to get the angular distribution shape with an optimum number of experimental points. In practically all the cases reported here, the angular distributions were measured with PSD though some angular distributions were also measured with plates. The inelastic cross sections were normalized by measuring a known elastic scattering cross section at the same or nearly the same energy. Any effects of target non-uniformity and deterioration in the present measurements were eliminated by using the counts from a monitor detector.

3. DWBA calculations

The details of DWBA calculations of inelastic scattering have been discussed several times in the literature [5-8]), therefore we do not discuss the underlying theory and assumptions and proceed at once to the present work.

In DWBA calculations for vibrational excitations, the cross sections are of the form

$$\left(\frac{d\sigma}{d\Omega}\right)_l = \beta_l^2 \, \sigma_l(\theta) \tag{2}$$

for an angular momentum transfer l in the inelastic collision; β_l^2 is the mean square deformation of the vibrational state. The angle-dependent factor $\sigma(\theta)$ in formula (2) was calculated using the Oak Ridge National Laboratory code JULIE [9]). The optical-model parameters used were those obtained by Perey and Perey [10]). They used a potential of the form

$$\begin{aligned} U(r) = & -V(e^x+1)^{-1} + iW' \frac{d}{dx'}(e^{x'}+1)^{-1} \\ & + \begin{cases} Ze^2/r & \text{for } r > R_c \\ Ze^2\,(3-r^2/R_c^2)/2R_c & \text{for } r \leqq R_c, \end{cases} \end{aligned} \tag{3}$$

where

$$x = \frac{r-R}{a}, \quad R = r_0 A^{\frac{1}{3}}, \quad x' = \frac{r'-R'}{a}, \quad R' = r'_0 A^{\frac{1}{3}}.$$

The Coulomb radius R_c was always set equal to the radius of the real well.

The DWBA calculations for inelastic scattering were performed using the surface-coupling collective model. The validity of this model has been proven in numerous analyses [5,11,12]). In some of these analyses [11,12]) related to deuteron scattering, it has also been demonstrated that for a correct prediction of the inelastic scattering differential cross sections one has to use complex coupling and include the contribution from Coulomb excitation. If the calculations incorporate these features, the resulting values of β_l are in reasonable agreement with those determined by other techniques such as Coulomb excitation and inelastic electron scattering. The optical potential parameters used in the DWBA calculations in the present work were from the analyses of Perey and Perey [10]) and Dickens and Perey [13]).

DWBA calculations for the 2^+ states were performed using the same optical-model parameters for the entrance and exit channels, while those for the 3^- states (on account of their relatively high excitation energies) took into account the energy dependence of these parameters as found in the case of ^{60}Ni by Dickens *et al.* [13]). The same energy dependence was assumed for the parameters of Zn. For the complex coupling and the Coulomb terms, the parameters used were the average of those for the entrance and exit channels to satisfy the requirement of symmetry between the two channels. The main effect of using different parameters for the two channels was an increase in the values of β_3 by 3 % for Zn isotopes, 4 % for ^{62}Ni and ^{64}Ni and 5 % for ^{60}Ni and ^{58}Ni. The shapes of the calculated angular distributions remained

largely unaltered except in ^{58}Ni and ^{60}Ni (see fig. 2), where the difference between the entrance and exit channel parameters was the largest. The various parameters employed in the present DWBA calculations have been listed in table 1.

TABLE 1
Deuteron optical potential parameters for Ni and Zn
$r_0 = r_{0c} = 1.15$, $a = 0.81$,
$r'_0 = 1.34$, $a' = 0.68$

Nucleus	Entrance channel		Exit channel	
	V	W'	V	W'
^{60,58}Ni	92.0	94.8	99.5	83.0
^{64,62}Ni	92.0	94.8	96.5	86.3
^{68,66,64}Zn	94.8	90	99.5	85.0

All lengths are in fm and well depths in MeV.

4. Results and discussion

Comparison between the experimental differential cross sections and the DWBA calculations is shown in figs. 1–4. The values of β_2 and β_3 obtained from such a comparison are indicated in these figures. The agreement between the shapes of the DWBA angular distributions and the experimental data is quite satisfactory.

The reduced transition probabilities $B(El, 0 \rightarrow l)$ and their ratios to single-particle estimates are related to the deformation parameters by

$$B(El; 0 \rightarrow l) = \left(\frac{3ZeR^l}{4\pi}\right)^2 \beta_l^2, \tag{4}$$

$$\frac{B(El)}{B(El)_{s.p.}} = \frac{(3+l)^2}{2l+1}\frac{Z^2}{4\pi}\beta_l^2, \tag{5}$$

where the various symbols in (4) and (5) have been defined in sect. 3. Since different analyses employ different values of the interaction radius, it is customary to compare the deformation length $\beta_l r$ derived from different measurements, where r is the interaction radius. It has been suggested [14]) that for (^{3}He, ^{3}He') where most of the cross section comes from the imaginary part of the potential, perhaps one ought to use the radius of the imaginary potential because this choice yields deformation lengths that are in better agreement with those from other measurements. Dickens *et al.*[13]) in (d, d') studies on ^{60}Ni and ^{114}Cd with 12 MeV deuterons have shown that inclusion of the imaginary term in the coupling potential increases the cross section by a factor of four. Following the above argument, therefore, one ought to use the radius of the imaginary potential for calculating the deformation lengths in (d, d') studies. Present work, however, shows that our values of $\beta_l r$ agree better with

other measurements if we use the radius of the real potential. This means that either the arguments valid for (^{3}He, ^{3}He′) are not valid for (d, d′) or else the question of choice of a proper interaction radius needs to be investigated further. We, nevertheless, chose to use the radius of the real potential in calculating the values of $\beta_l r$ and $B(El; 0 \rightarrow l)$ for the various cases studied here.

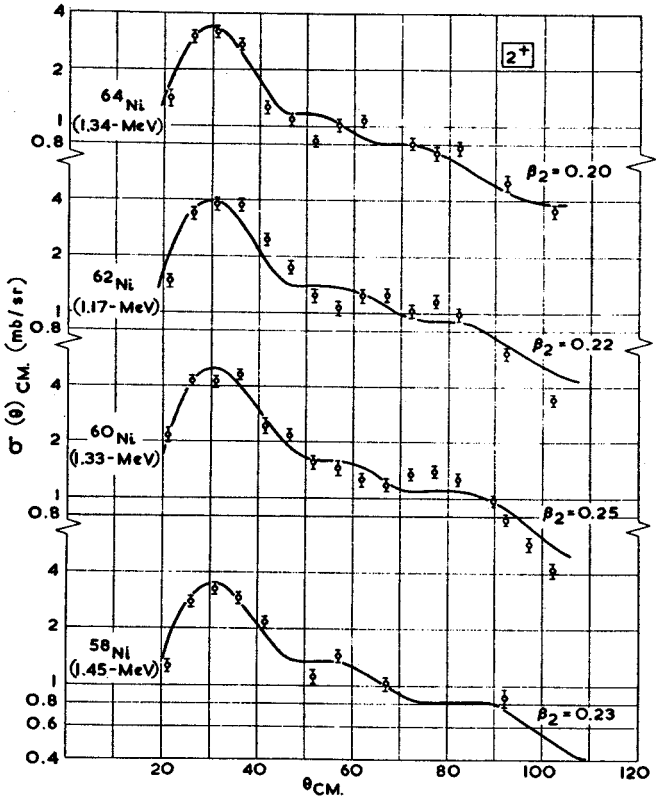

Fig. 1. A comparison between DWBA calculations (solid curves) and the experimental cross sections for the first excited 2+ states in the even isotopes of Ni. The numbers on the left-hand side of each curve (within parentheses) are excitation energies and those on the right-hand side the values of β_2 needed to fit the experimental cross sections.

The deformation parameters, lengths and reduced transition probabilities for the 2^+ and 3^- states are listed in table 2. These values for the 2^+ states are compared with those adopted by Stelson and Grodzins [3]) as "best values" from a survey of all previous measurements. The agreement is quite impressive in view of the fact that the quoted errors in our values take into account only experimental uncertainties and not those implicit in the DWBA theory.

For the collective 3^- states in ^{58}Ni, ^{60}Ni and ^{62}Ni, there are several reported measurements employing methods ranging from electron scattering to α-scattering.

The interaction radii in these analyses also vary from 1.1 to 1.5 fm. Our values of β_3 fall within the range of reported values listed in table 2. In ^{64}Ni and ^{64}Zn, we could

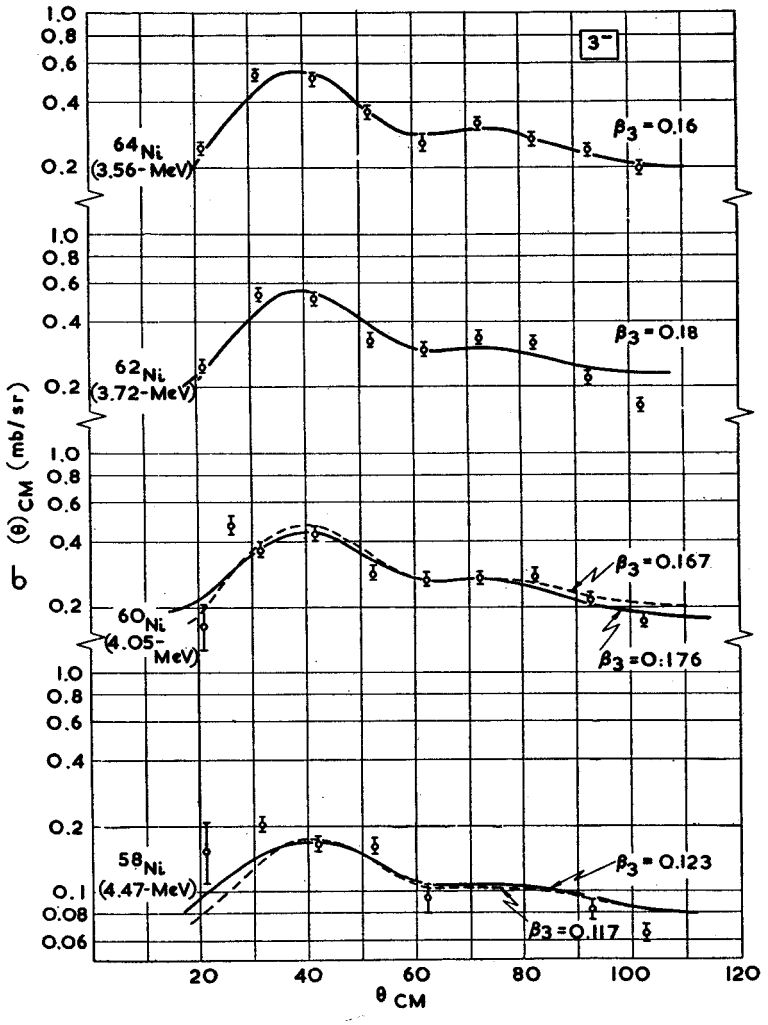

Fig. 2. A comparison between DWBA calculations and the experimental cross sections for the collective 3⁻ states in the isotopes of Ni. The solid curves are calculations using different parameters for the entrance and exit channels, while the broken curves are for the same parameters in the two channels. These two curves are indistinguishable for ^{62}Ni and ^{64}Ni, and the values of β_3 on the right refer to the calculations with different parameters for the two channels. See caption for fig. 2.

find only one previous measurement employing enriched isotopic targets. The agreement with our values of β_3 is quite good. In the other two isotopes of Zn, there are no measurements reported in the literature. It is important to point out here that energy resolution better than 100 keV is essential for an accurate determination of

TABLE 2

A comparison of the values of excitation energy, β_l, reduced transition probabilities, their ratio to single-particle estimates and the effective surface tension of the collective deformation deduced from the present work and other measurements

Nucleus	J^π	Excitation energy (MeV)	β_l	$\beta_l r_0$	$B(El; 0 \to l)$ [cm^{2l}]	$\frac{B(El)}{B(El)_{s.p.}}$	C_l (MeV)	Ref.
^{58}Ni	2^+	1.45	0.232	0.265	$(0.095\pm0.008)\times10^{-48}$	16.9	67.3	present work
		1.460	0.187	0.224	$(0.073\pm0.007)\times10^{-48}$	11		[3]
	3^-	4.45	0.123	0.142	$(0.053\pm0.004)\times10^{-73}$	4.9	1026	present work
			0.10–0.20					[5,8,14,18–23]
^{60}Ni	2^+	1.33	0.254	0.287	$(0.117\pm0.009)\times10^{-48}$	20.1	51.8	present work
		1.332	0.211	0.253	$(0.097\pm0.008)\times10^{-48}$	13		[3]
	3^-	4.05	0.176	0.202	$(0.115\pm0.009)\times10^{-73}$	9.9	460	present work
			0.17–0.24					[6,7,12,19,21–24]
^{62}Ni	2^+	1.17	0.218	0.253	$(0.091\pm0.007)\times10^{-48}$	14.8	61.9	present work
		1.171	0.193	0.232	$(0.083\pm0.007)\times10^{-48}$	11		[3]
	3^-	3.72	0.175	0.201	$(0.122\pm0.010)\times10^{-73}$	9.8	423	present work
			0.187–0.23					[21,23,25]
^{64}Ni	2^+	1.34	0.198	0.230	$(0.079\pm0.006)\times10^{-48}$	12.3	85.0	present work
		1.340	0.192	0.230	$(0.087\pm0.017)\times10^{-48}$			[3]
	3^-	3.56	0.163	0.188	$(0.113\pm0.008)\times10^{-73}$	8.5	470	present work
			0.181	0.226				[25]
^{64}Zn	2^+	0.991	0.272	0.311	$(0.168\pm0.009)\times10^{-48}$	26.5	33.8	present work
		0.995	0.252	0.302	$(0.170\pm0.015)\times10^{-48}$	22		[3]
	3^-	2.997	0.206	0.242	$(0.207\pm0.012)\times10^{-73}$	15.7	246	present work
			0.21	0.262				[24]
^{66}Zn	2^+	1.037	0.242	0.276	$(0.141\pm0.007)\times10^{-48}$	21.0	44.5	present work
		1.040	0.227	0.272	$(0.145\pm0.013)\times10^{-48}$	18		[3]
	3^-	2.819	0.207	0.237	$(0.224\pm0.015)\times10^{-73}$	15.8	230	present work
^{68}Zn	2^+	1.073	0.23	0.265	$(0.130\pm0.012)\times10^{-48}$	18.6	51.6	present work
		1.078	0.205	0.246	$(0.125\pm0.011)\times10^{-48}$	15		[3]
	3^-	2.736	0.198	0.228	$(0.220\pm0.017)\times10^{-73}$	14.6	242	present work

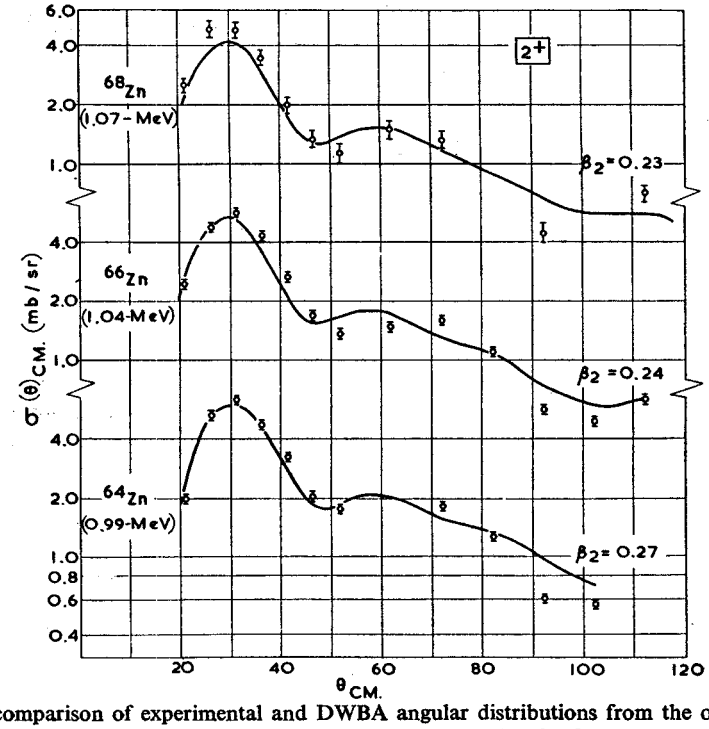

Fig. 3. A comparison of experimental and DWBA angular distributions from the one-phonon 2^+ states in the even isotopes of Zn. See caption for fig. 2.

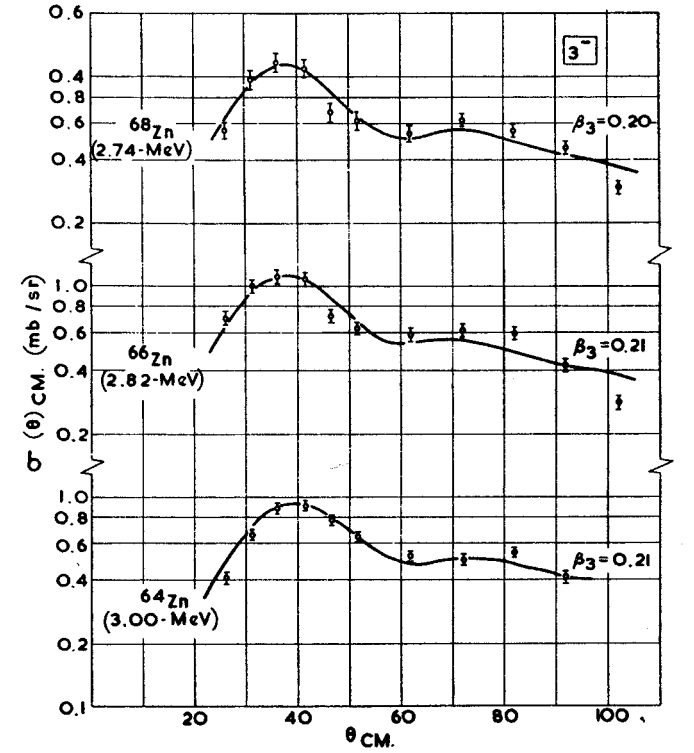

Fig. 4. A comparison of experimental and DWBA angular distributions for the collective 3^-state in the even isotopes of Zn. See caption for fig. 2 and section 3 for a discussion of the 3^- calculations in these isotopes of Zn.

β_3 for the cases studied in the present work as the 3^- level is usually surrounded by other states with cross sections that are 5–20 % of the 3^- cross section [15]). The energy resolution in the present work was ≈ 25 keV and, therefore was quite adequate for the purpose of determining β_3.

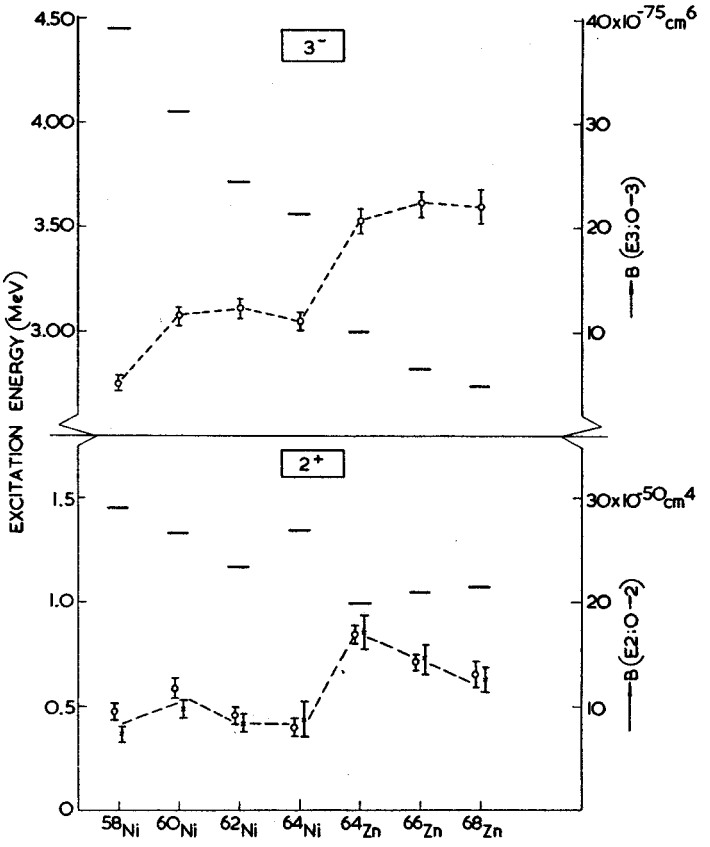

Fig. 5. Excitation energies and reduced transition probabilities for the collective 2^+ and 3^- states of even isotopes of Ni and Zn. The short horizontal lines represent level energies and the circles the reduced transition probabilities measured in the present work. The crosses are the adopted values of $B(\mathrm{E2}; 0 \rightarrow 2)$ from ref. [3]).

The values of excitation energy and $B(\mathrm{E}l)$ for both the 2^+ and 3^- states have been plotted in fig. 5 showing the comparison with the adopted values [3]) of $B(\mathrm{E2}; 0 \rightarrow 2)$. It is instructive to study the systematic trends in these quantities in terms of the collective and the shell models. Another interesting quantity from this viewpoint is the effective surface tension for vibrational deformation

$$C_l = \frac{(2l+1)\hbar\omega_l}{2\beta_l^2}, \tag{6}$$

where $\hbar\omega_l$ is the excitation energy for the collective one-phonon state. Values of C_l have been listed in table 2 and plotted in fig. 6. It is noteworthy that C_2 and C_3 do not show similar trends. The ^{58}Ni nucleide has two neutrons outside a doubly closed core of 28 protons and neutrons. Consequently, going from ^{58}Ni to ^{68}Zn, one expects an increasing "softness" against collective deformations. While C_3 shows

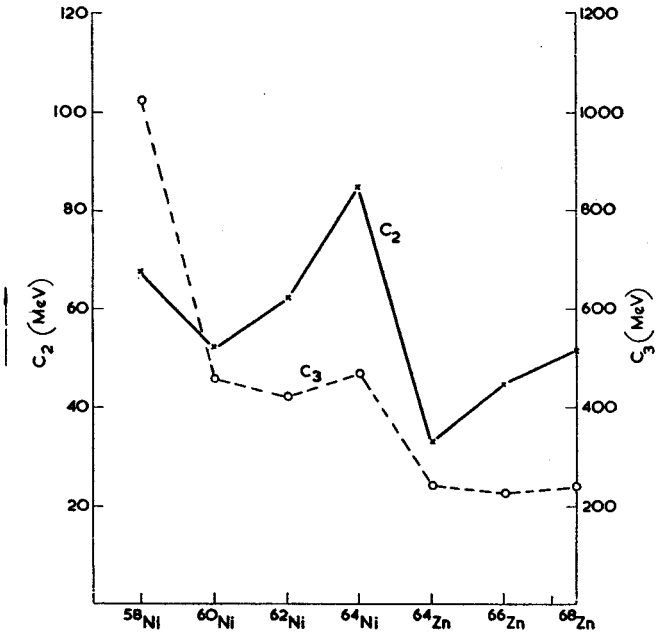

Fig. 6. The effective surface tension constants C_2 and C_3 for the even isotopes of Ni and Zn. See text for a discussion of these constants.

such a trend, the behaviour of C_2 does not. This clearly shows that a vibrational description of the 2^+ states in these nuclei is an over simplification.

The degree of agreement between our measurements of $B(\mathrm{E2}; 0 \rightarrow 2)$ and the adopted values [3]) shows that even for deformations as large as 0.25 (as in the case of Zn) the fact that explicit coupling of the ground state to the low-lying collective states has been ignored in the DWBA does not seem to matter. This supports the claim of Perey and Satchler [16]) that if one performs the DWBA calculations in a consistent manner, i.e. one extracts optical potential parameters from accurately normalized [17]) elastic scattering data and uses these parameters for inelastic scattering calculations, one obtains reasonable deformation parameters and reduced transition probabilities. Accurate normalization of the elastic scattering data is important as experience shows [12]) that poorly normalized elastic scattering data yield optical-model parameters that lead to less satisfactory predictions of inelastic scattering cross sections.

Admittedly, the number of cases investigated here is not large enough to enable a generalization of the above remarks, but there is mounting evidence in favour of the claim of Satchler and Perey as stated above. The validity of DWBA calculations as reflected in the present work and elsewhere [5-8,11,12]) makes direct-interaction inelastic scattering at appropriately chosen energies a very convenient and dependable tool for measuring the properties of one-phonon states.

The authors are thankful to Dr. A. T. G. Ferguson for reviewing this manuscript. They also feel indebted to Mr. G. V. Ansell for his assistance in testing and setting up the position sensitive detectors for present measurements. Thanks are also due to Dr. R. M. Drisko for lending the authors a copy of the DWBA code JULIE.

References

1) L. S. Kisslinger and R. A. Sorenson, Mat. Fys. Medd. Dan. Vid. Selsk. **32**, No. 9 (1960); Revs. Mod. Phys. **35** (1963)
2) S. Yoshida, Nucl. Phys. **38** (1962) 380
3) P. H. Stelson and L. Grodzins, Nuclear data, Section A. Vol. 1, No. 1, (Academic Press, New York) 1965
4) R. Bock, H. H. Duhm, W. Melzer and B. Stadlen, Nucl. Instr. **41** (1966) 190; W. W. Daehnick and Y. S. Park, Bull. Am. Phys. Soc. **12I** (1967) 461
5) E. Rost, Phys. Rev. **128** (1962) 2708
6) T. Stoval and N. M. Hintz, Phys. Rev. **135** (1964) B330
7) M. P. Fricke and G. R. Satchler, Phys. Rev. **139** (1965) B567
8) M. M. Stautberg and J. J. Kraushaar, Phys. Rev. **151** (1966) 969
9) R. H. Bassel, R. M. Drisko and G. R. Satchler, ORNL Report No. 3240 and supplement, unpublished
10) C. M. Perey and F. G. Perey, Phys. Rev. **132** (1963) 755
11) J. K. Dickens, F. G. Perey and G. R. Satchler, Nucl. Phys. **73** (1965) 529
12) R. K. Jolly, Phys. Rev. **139** (1965) B318
13) J. K. Dickens and F. G. Perey, Phys. Rev. **138** (1965) B1083
14) E. R. Flynn and R. H. Bassel, Phys. Rev. Lett. **15** (1965) 168
15) R. K. Jolly, E. K. Lin and B. L. Cohen, Phys. Rev. **128** (1962) 2292; E. K. Lin, Nucl. Phys. **73** (1965) 613
16) F. G. Perey and G. R. Satchler, Phys. Lett. **5** (1963) 212
17) J. K. Dickens and F. G. Perey, Phys. Rev. **138** (1965) B1080
18) R. Beurtey, P. Catillon, R. Chaminade, M. Crut, H. Faragi, A. Popineau, J. Saudinos and J. Thirion, Compt. Rend. **252** (1961) 1756
19) H. Crannel, R. Helm, H. Kendall, J. Oeser and M. Yearian, Phys. Rev. **123** (1961) 923
20) H. W. Broek and G. R. Satchler, Nucl. Phys. **64** (1965) 259
21) S. F. Eccles, H. F. Lutz and V. A. Madsen, Phys. Rev. **141** (1966) 1067
22) O. N. Jarvis, B. G. Harvey, D. L. Hendrie and J. Mahoney, Nucl. Phys. **A102** (1967) 625
23) M. A. Duguay, C. K. Bockelman, T. H. Curtis and R. A. Eisenstein, Phys. Rev. **163** (1967) 1259
24) G. R. Satchler, R. H. Bassel and R. M. Drisko, Phys. Lett. **5** (1963) 256
25) A. L. McCarthy and G. M. Crawley, Phys. Rev. **150** (1966) 935

DWBA AND THE 3.12 MeV STATE IN ^{60}Ni

R. K. JOLLY, M. D. GOLDBERG * and A. K. SENGUPTA **
A.E.R.E., Harwell, U.K.
W. DARCEY
University of Oxford, U.K.
R. CHAPMAN ‡ and S. HINDS ‡‡
A.W.R.E., Aldermaston, U.K.

Received 3 January 1969

The apparent inconsistency and failure of DWBA analyses applied to (d, d') angular distribution data for the 3.12 MeV state of ^{60}Ni, measured at E_d = 11.5 MeV and 14.8 MeV, are explained by (t, p) measurements which suggest that the state is a 2^+, 4^+ doublet.

It has been firmly established by several workers [1-3] that there is a state at 3.12 MeV in ^{60}Ni with spin and parity 2^+. However, DWBA analysis of ^{60}Ni(d, d') data measured by Jolly et al. at E_d = 14.8 MeV (resolution 55 keV) [4] and, more recently, at E_d = 11.5 MeV with improved energy resolution (≈ 25 keV) [5] did not agree with the accepted spin and parity assignments for this state. Indeed the (d, d') data at E_d = 14.8 MeV appeared to be consistent with a spin and parity of 3^- (fig. 1 top), while the agreement with $l = 2$ and $l = 3$ was poor for the 11.5 MeV data (fig. 1 bottom).

The apparent inconsistency and failure of DWBA analysis in this case run contrary to the success normally experienced with (d, d') data at these bombarding energies and in this mass region [6]. Since the state is strongly excited in inelastic deuteron scattering, it seems reasonable to assume that it is not complex in nature and should fall within the range of applicability of conventional DWBA analysis invoking a one-step angular momentum transfer process. Of course, one possible explanation for the failure in this case is that the level at 3.12 MeV is a multiplet [7]. However, no multiplet structure was observed in the present (d, d') work or in recent high resolution (11 keV) ^{60}Ni(p, p') measurements [8].

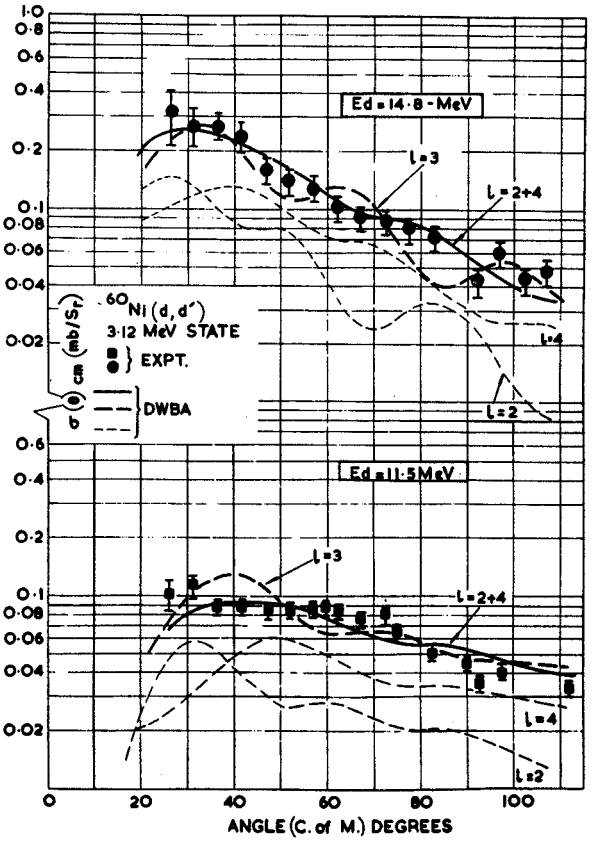

Fig. 1. Deuteron angular distributions for the 3.12 MeV state in ^{60}Ni and their comparison with $l = 3$ cross sections and combinations of $l = 2$ and 4 cross sections calculated with the DWBA code JULIE.

* Present address: Brookhaven National Laboratory, USA.
** Present address: Saha Institute, Calcutta, India.
‡ Present address: A. E. R. E., Harwell.
‡‡ Present address: Nuclear Physics Laboratory, Daresbury.

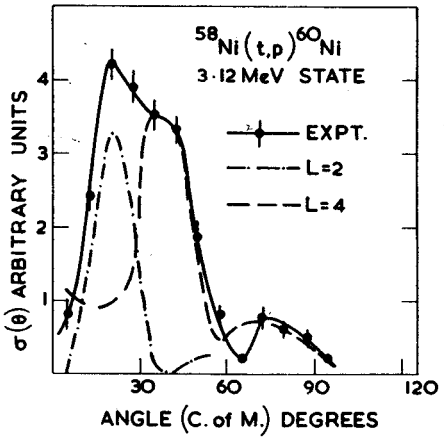

Fig. 2. Decomposition of the 3.12 MeV state proton angular distribution into those for $l = 2$ and 4 transitions in the ^{58}Ni(t,p)^{60}Ni reaction measured at $E_t = 12$ MeV.

Recently some ^{58}Ni(t, p)^{60}Ni measurements have been made at Aldermaston [9] (E_t = 12 MeV, resolution 15 keV) and once again there was no direct evidence for multiplet structure in the 3.12 MeV state. It has been demonstrated earlier [9, 10] that proton angular distributions are very characteristic of the angular momentum transfer in the (t, p) reactions in this mass region. However in the case of the 3.12 MeV state it was found that the data could be described only by a suitable linear combination of $l = 2$ and $l = 4$ angular distributions taken from (t, p) studies at this energy on Ni isotopes to well authenticated 2^+ and 4^+ states (fig. 2). The same procedure was tried on the 11.5 MeV (d, d') angular distribution when it was found that no permissible combination except $l = 2$ and $l = 4$ described the data satisfactorily (fig. 1 bottom). In the case of the 14.8 MeV (d, d') angular distribution [4] the combination of $l = 2$ and $l = 4$ DWBA calculations fits the experimental data a little better than $l = 3$ (fig. 1 top). It is noteworthy that, as expected, both sets of (d, d') data have been successfully fitted with the same ratio of $l = 2$ and $l = 4$ peak cross sections.

Thus, in the context of the conclusions from (t, p) studies i. e. the 3.12 MeV state is a 2^+, 4^+ doublet, DWBA analyses consistently explain both sets of (d, d') data.

The authors are indebted to Dr. R. M. Drisko for lending them a copy of the DWBA code JULIE.

References

1. R. H. Fulmer and W. W. Daehnick, Phys. Rev. 139 (1965) B579.
2. R. K. Mohindra and D. M. Van Patter, Phys. Rev 139 (1965) B274;
   S. M. Shaffroth and G. T. Wood, Phys. Rev. 149 (1966) 827.
3. C. M. Lederer, J. M. Hollander and I. Perlman, Table of Isotopes-sixth edition (John Wiley and Sons, Inc., 1967).
4. R. K. Jolly, Phys. Rev. 139 (1965) B318.
5. R. K. Jolly, M. D. Goldberg and A. K. SenGupta, Nucl. Phys., to be published.
6. R. K. Jolly, M. D. Goldberg, A. K. SenGupta, AERE Report-R5798.
7. R. G. Tee and A. Aspinall, Nucl. Phys. A98 (1967) 417.
8. W. Darcey, R. Chapman and S. Hinds, to be submitted to Nucl. Phys.
9. J. H. Bjerregaard et al., Nucl. Phys. A103 (1967) 33.

* * * * *

Reprinted from THE PHYSICAL REVIEW, Vol. 182, No. 4, 1073–1082, 20 June 1969
Printed in U. S. A.

Proton Spin Flip in the Reaction $^{12}C(p, p')^{12}C^*$ [4.44 MeV]*

J. J. KOLATA† AND A. GALONSKY
Cyclotron Laboratory, Michigan State University, East Lansing, Michigan 48823
(Received 14 January 1969)

The angular correlation between protons inelastically scattered from the first excited state of ^{12}C and the subsequent 4.44-MeV deexcitation γ radiation perpendicular to the scattering plane was measured for 26.2- and 40.0-MeV incident proton energy. This correlation has previously been shown to be related to the fraction of protons undergoing spin flip along this direction. As has been observed at lower bombarding energies, the spin-flip probability peaks at large proton scattering angles; observed here are probabilities as high as 0.35 near 150°. The spin-flip probability for all inelastic scattering to the 4.44-MeV state is 3%. The data were compared to the predictions of the distorted-wave Born approximation, using collective-model and microscopic-model form factors. The expected sensitivity to the spin-dependent part of the nucleon-nucleus interaction was confirmed. However, it was found that the observed spin flip was almost entirely accounted for by distortions in the entrance and exit elastic channels, due to the spin-orbit term in the optical-model potential. No definite conclusions regarding the spin-dependent part of the inelastic interaction could be reached from the ^{12}C data, possibly owing to the failure of the assumptions of the optical model for such light nuclei. It appears that meaningful information regarding the spin dependence of the reaction mechanism producing the excited state can be obtained from spin-flip data only for those nuclei having well-determined optical-model parameters.

I. INTRODUCTION

SEVERAL experimental techniques are available for studying the spin dependence of the nucleon-nucleus interaction. In particular, one might investigate the inelastic scattering of polarized protons,[1] or the effects of target polarization on a particular reaction.[2] Either of these methods involves the preparation of an initial system with known spin orientation; the relative scarcity of such data reflects the experimental difficulties encountered. Alternatively, it is possible to determine the angular dependence of polarization of the residual nucleus, when the initial system is completely unpolarized. Usually, one observes the angular correlation involving the scattered particle and the deexcitation γ radiation. It can be shown,[2,3] in the context of the distorted-wave Born approximation (DWBA) with unique total transferred angular momentum, that the information obtained by this method is the same as that obtained by scattering from polarized targets. Therefore, such measurements can provide valuable data concerning the spin dependence of nuclear reaction

* Work supported in part by the National Science Foundation.
† Present address: Naval Research Laboratory, Washington, D.C. 20390.
[1] M. P. Fricke, E. E. Gross, and A. Zucker, Phys. Rev. **163**, 1153 (1967); C. Glashausser, R. DeSwiniarski, and J. Thirion, *ibid.* **164**, 1437 (1967).
[2] L. J. B. Goldfarb and D. A. Bromley, Nucl. Phys. **39**, 408 (1962).
[3] G. R. Satchler, Nucl. Phys. **55**, 1 (1964).

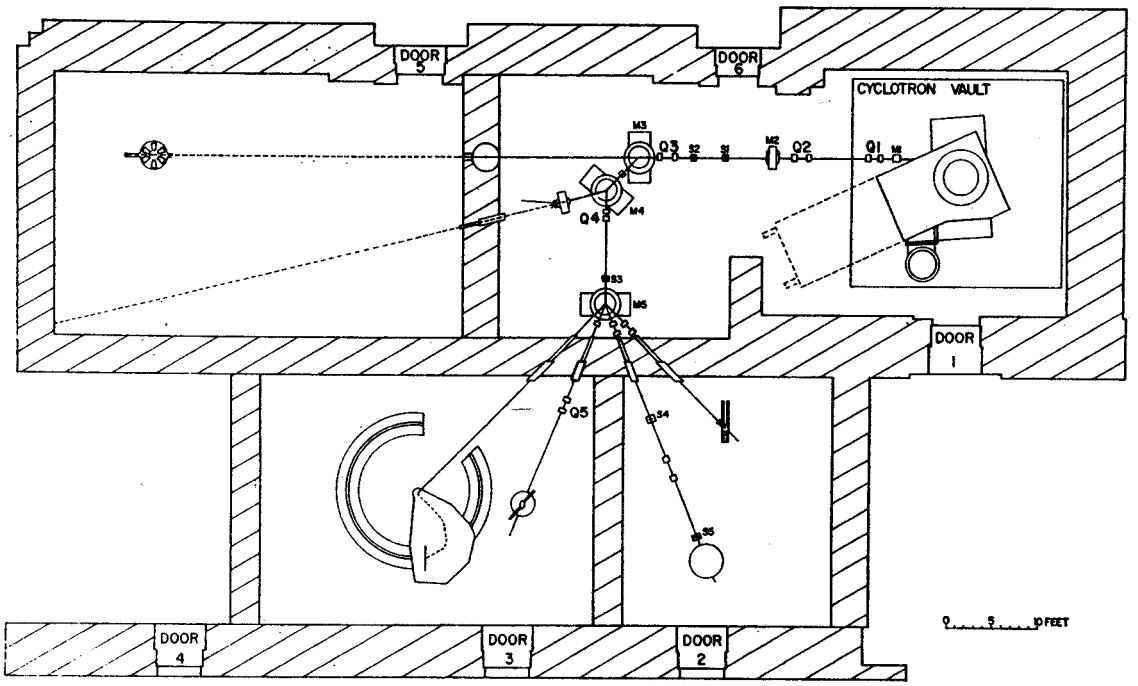

FIG. 1. Scale drawing of the cyclotron and ancillary beam-handling equipment. Q1–Q5 are quadrupole doublets. Energy analysis is accomplished by the bending magnets M3 and M4. S1–S3 are the beam-defining apertures mentioned in the text.

mechanisms for the wide range of nuclei for which polarized targets are unavailable; in addition, they can provide supplementary information in those cases for which inelastic scattering of polarized protons has been measured. The chief disadvantage of the method lies in the need to perform a coincidence experiment.

The angular correlation function for the case in which γ radiation is detected in the plane determined by the incident beam and the scattered particle (in-plane correlation) has been analyzed in the DWBA by several authors.[4,5] Banerjee and Levinson[5] predicted the form

$$W(\theta_\gamma) = A + B \sin^2 2(\theta_\gamma - \epsilon_1) + C \sin^2(\theta_\gamma - \epsilon_2), \quad (1)$$

and associated the last term with the presence of spin flip in the interaction. Such a term has been observed,[6] but it has proved to be very difficult to extract the relevant spin-flip probability, which is expected to be quite sensitive to the spin dependence of the nucleon-nucleus interaction.

Recently, Schmidt *et al.*[7] have pointed out that spin flip could be more easily studied through an angular correlation in which the γ radiation is detected along the normal to the scattering plane (γ-perpendicular correlation). They were able to show that this correlation is directly proportional to the spin-flip probability, in the case of a $0^+ - 2^+$ transition. The argument may be extended with minor modifications to the excitation of a $1^\pm$ or 2^- state from a 0^+ ground state. We have used this method to investigate proton spin flip in the excitation of the first 2^+ state in ^{12}C by 26.2- and 40.0-MeV protons. The data have been analyzed in the DWBA, with several different reaction models, in an attempt to determine the type of information about spin-dependent nucleon-nucleus forces which can be extracted from spin-flip measurements.

In Sec. II, we present a description of the experimental method and the determination of the spin-flip probability. Section III is devoted to the discussion of the DWBA analysis, including the reaction models and optical-model parameters used.

II. EXPERIMENTAL METHOD

A. Beam Line

Figure 1 is a scale drawing of the beam transport system. A proton beam from the Michigan State University Isochronous Cyclotron was focussed by a set of quadrupole doublets on the object slit S1 of an energy analysis system formed by magnets M3 and M4. The properties of this system has been investigated previously,[8] so that we were able to calculate the

[4] G. R. Satchler, Proc. Phys. Soc. (London) A68, 1037 (1955); J. S. Blair and L. Wilets, Phys. Rev. 121, 1493 (1961).
[5] M. K. Banerjee and C. A. Levinson, Ann. Phys. (N.Y.) 2, 499 (1957).
[6] H. Yoshiki, Phys. Rev. 117, 773 (1960); T. H. Braid, J. L. Yntema, and B. Zeidman, Argonne National Laboratory Report No. 6358, p. 11 (unpublished).
[7] F. H. Schmidt, R. E. Brown, J. B. Gerhart, and W. A. Kolasinski, Nucl. Phys. 52, 353 (1964).
[8] G. H. Mackenzie, E. Kashy, M. M. Gordon, and H. G. Blosser, IEEE Trans. Nucl. Sci. 14, 450 (1967); J. L. Snelgrove and E. Kashy, Nucl. Instr. Methods 52, 153 (1966).

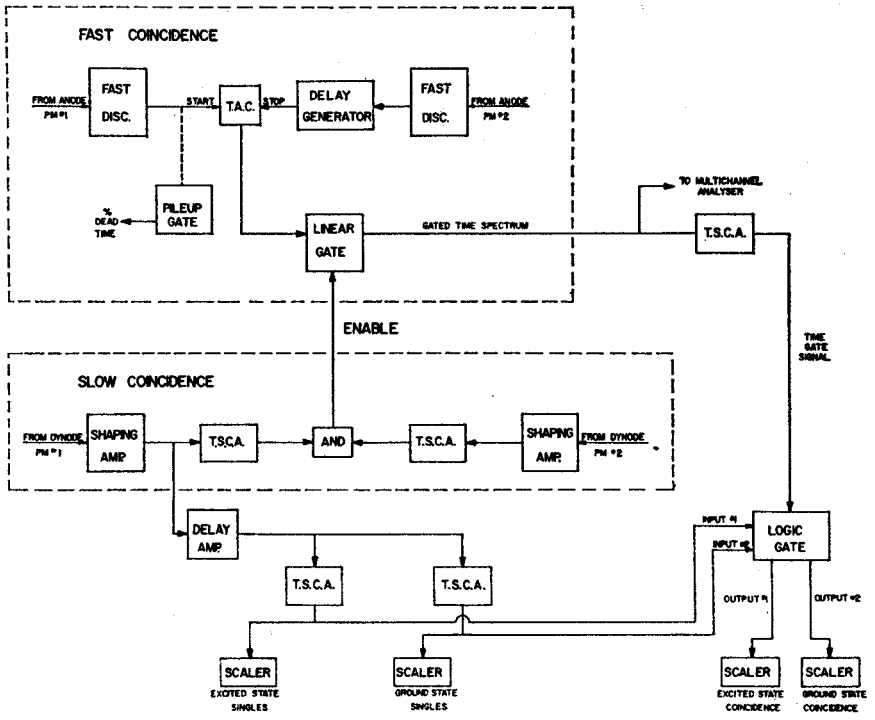

FIG. 2. Block diagram of the electronics. TAC is a time-to-amplitude converter. TSCA is a timing single-channel analyzer, which gives an output when the bipolar-input signal crosses zero.

transmitted beam energy to ± 0.1 MeV. The energy spread in the beam, determined from the slit openings, varied from 25–50 keV full width at half-maximum (FWHM).

The analyzed beam was deflected into the appropriate experimental area by magnet M5, and focused on the target by the final quadrupole doublet Q5. Typical beam spot size was 4 mm wide by 2 mm high, with an angular spread of less than $\pm 0.5°$. No collimating slits were used near the target in an attempt to keep background radiation in the experimental area to a minimum. Instead, the beam was positioned by observing a 0.125-mm-thick plastic scintillator at the target position, using a closed-circuit television system. Fiducial marks were inscribed on the scintillator. In this way, the beam could be centered to within 1 mm. The scintillator was inserted several times during the course of a run to check against centering drifts, which did not occur. After passing through the target, the beam was collected in a 7.5-cm-diam Faraday cup placed 2 m beyond the target position.

The target was a 26.5-mg/cm^2 graphite foil[9]; its uniformity was determined to be better than $\pm 1\%$ by monitoring elastic proton scattering from various areas of the sample. The energy loss ΔE in the target was 495 keV at 26 MeV, and 350 keV at 40 MeV. The mean proton energy E_p was determined by subtracting $\frac{1}{2}\Delta E$ from the energy determined by the beam transport system. The target was contained in a small evacuated chamber with 0.125-mm-thick Mylar windows.

[9] Speer Carbon Co., Inc., Carbon Products Div., St. Marys, Pa.; Shield Grade 9326.

B. Detectors and Electronics

Scattered protons were detected in a 3.8-cm-diam by 1.9-cm-thick NaI(Tl) scintillator mounted on an RCA 8575 photomultiplier. The energy resolution of this system was typically 600-keV FWHM at 24 MeV. Target-to-detector distance was 18–24 cm, and the full angle subtended at the circular collimator was 6°–8°. The detector was mounted on a remotely adjustable arm which could be positioned to $\pm 0.1°$.

Deexcitation γ radiation was detected in a 5-cm-diam by 7.5-cm-long NaI(Tl) scintillator, also mounted on an RCA 8575 photomultiplier. The best energy resolution obtained was 7.5% FWHM for the 662-keV γ ray from ^{137}Cs. This assembly was positioned on the normal to the scattering plane to within 4 mm, and the distance from the beam line to the center of the scintillator was 41 cm, corresponding to an 0.5° angular positioning uncertainty; the scintillator subtended a full angle of 7° at its center. The γ detector was shielded from background radiation by a 130-kg cylindrical Pb shield.

A block diagram of the electronics is shown in Fig. 2. Anode pulses from the photomultipliers were used to start and stop a time-to-amplitude converter (TAC). The time spectrum was gated by the output of a conventional zero-crossing slow coincidence unit with a resolving time (2τ) of 1 μsec. Timing single-channel

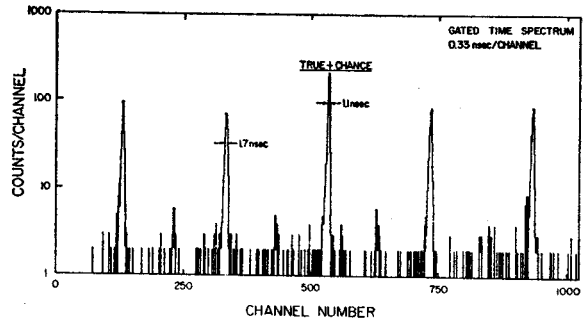

FIG. 3. Gated time spectrum taken at 26 MeV. The indicated resolution is the FWHM of the peak. The "chance" peaks have a somewhat larger width due to the contribution from the burst width of the beam. When the chance peak is subtracted from the "true+chance" events, the resulting "true" peak has a width of 0.9 nsec (FWHM). The small peaks between the main beam bursts are due to the background coming from the Faraday cup, which was located 2 m beyond the target position.

analyzers (TSCA) provided both time and pulse-height information in the slow coincidence channel. In practice, they were used to reduce the number of accidental coincidences due to low-level background pulses in both detectors.

A typical gated time spectrum taken at 26 MeV is shown in Fig. 3. At this energy, the pulse-repetition rate of the beam is 15.1 MHz, so that the separation between beam bursts is 66 nsec. The relative delays have been adjusted so that the peak containing true coincidences occurs near the center of the spectrum. Typical resolution obtained for this peak was 1 nsec (FWHM), and the best value obtained was 0.8 nsec (FWHM). The somewhat larger width of the accidental peaks is due to a contribution from the pulse width of the beam. The small peaks between the main beam bursts correspond to accidental coincidences with background γ radiation coming from the Faraday cup. A window set around the "true+chance" peak in this time spectrum was narrow enough to keep these events, as well as a large fraction of the continuous background between peaks, from contributing to the accidental rate.

The count rate in both detectors was kept below 10^4 counts/sec at the fast discriminator output. Observation of the shaping amplifier outputs, and a measurement of the average time between pulses using a pileup gate, indicated that coincidence losses due to dead time were small at these count rates. The largest dead-time correction made was 14%.

C. Data Reduction

The output of the coincidence circuitry was used to gate both the elastic and inelastic (4.44-MeV) events. Since the elastically scattered protons cannot be in true coincidence with a 4.44-MeV γ ray, these events give a measure of the accidental rate. The number of accidental coincidences N_A was determined from the expression

$$N_A = N_{gsc}(N_{4.4s}/N_{gss}), \quad (2)$$

where N_{gsc} is the number of ground-state coincidences, and N_{gss} ($N_{4.4s}$) is the total number of ground-state (inelastic 4.4-MeV) singles events.

The number of true coincidences at each angle was normalized to the total number of inelastic 4.44-MeV events, and the experimental angular-correlation function was calculated using the equation

$$W(\theta_p) = N(\theta_p)/\epsilon_\gamma\Omega_\gamma, \quad (3)$$

where $\epsilon_\gamma\Omega_\gamma$ is the product of the efficiency and solid angle of the γ-ray detector, and $N(\theta_p)$ is the normalized number of true coincidences. The product $\epsilon_\gamma\Omega_\gamma$ was measured[10] for each setting of the γ-ray discriminator in the slow coincidence unit, using the method described in Ref. 7. The accuracy of the measurement was $\pm 9\%$ at 26.2 MeV and $\pm 14\%$ at 40.0 MeV.

The spin-flip probability S_1 was determined, apart from a small correction term, from the equation[7]

$$S_1(\theta_p) = (8\pi/5)W(\theta_p). \quad (4)$$

The correction term mentioned is due to the finite acceptance angle of the two detectors, and its magnitude depends on the details of the population of the various

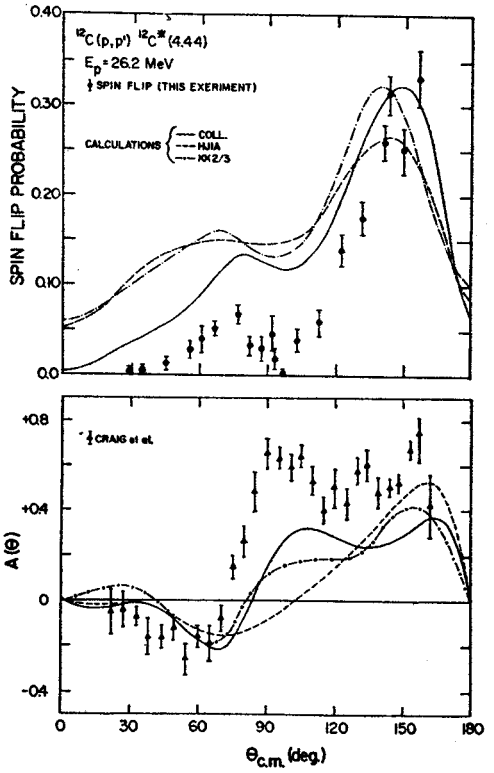

FIG. 4. Spin-flip and inelastic asymmetry at $E_p = 26.2$ MeV. The spin-flip data are from the present experiment; the asymmetry data are taken from Ref. 28. The various curves are the results of DWBA calculations in the collective model (COLL), and in the microscopic model using impulse approximation (HJIA) and Kallio-Kolltveit (KK2/3) form factors.

[10] R. Sager, National Science Foundation Undergraduate Research Participation Program Report, Michigan State University, 1967 (unpublished).

magnetic sublevels of the 2^+ state.[7] However, a maximum and minimum value for the correction term can be determined. For a circular proton (γ ray) detector aperture subtending an angle of $2\epsilon_p$ ($2\epsilon_\gamma$) rad, it can be shown[11] that the maximum and minimum corrections are given to second order by

$$\Delta S_1(\max) = -\tfrac{1}{2}[\epsilon_\gamma^2+\tfrac{1}{2}\epsilon_p^2-\tfrac{1}{32}(\epsilon_p^4/\epsilon_\gamma^2)] \times[3-(44\pi/5)W(\theta_p)]-\tfrac{3}{5}\pi\epsilon_p^2W(\theta_p)-\tfrac{1}{2}(3/2)^{1/2}\epsilon_p^2 \times[1-(8\pi/5)W(\theta_p)], \quad (5)$$

$$\Delta S_1(\min) = -\tfrac{1}{2}[\epsilon_\gamma^2+\tfrac{1}{2}\epsilon_p^2-\tfrac{1}{32}(\epsilon_p^4/\epsilon_\gamma^2)] \times[1-(28\pi/5)W(\theta_p)]+\tfrac{3}{5}\pi\epsilon_p^2W(\theta_p). \quad (6)$$

We have applied a correction equal to the average of these limits, and included in the uncertainty in S_1 a contribution equal to one-half the difference of the limits. Both the correction and its uncertainty were very small, since $\epsilon_p^2=\epsilon_\gamma^2=3.4\times10^{-3}$ for this experiment. As an example, the correction is $(-4.8\pm3.3)\times10^{-3}$ for $S_1=0.100$.

The measured spin-flip probabilities appear in Figs. 4 and 5. The error bars shown correspond to the relative errors only. There is an uncertainty in the absolute spin-flip probability of 9% for the data taken at 26.2 MeV, and 14% for the 40.0-MeV data, owing to the uncertainty in the efficiency of the γ-ray detector.

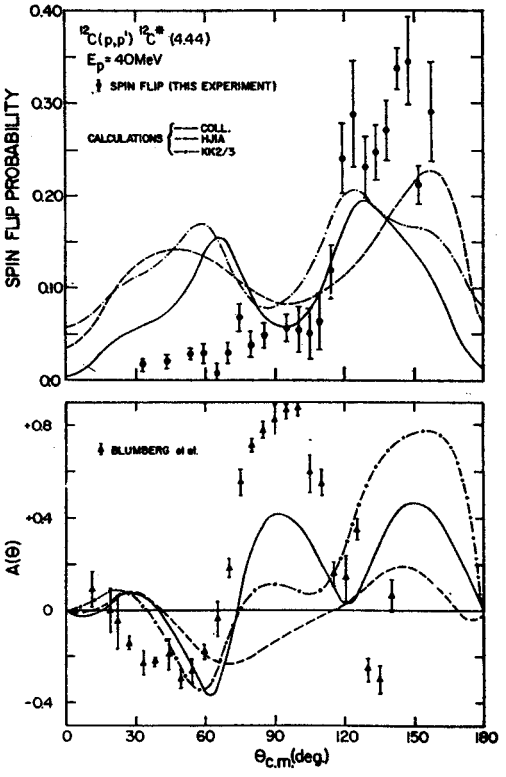

FIG. 5. Spin-flip and inelastic asymmetry at 40 MeV. The spin-flip data are from the present experiment; the asymmetry data are taken from Ref. 27. The various curves are the results of DWBA calculations (see caption, Fig. 4).

III. ANALYSIS

A. Transition Amplitude

In the zero-range DWBA theory of inelastic scattering, the transition amplitude takes the form[3]

$$T_{fi}=\chi_{m_f'm_f}^{(-)*}(r)\,\langle\psi_f \mid V \mid \psi_i\rangle\chi_{m_i'm_i}^{(+)}(r)\,dr, \quad (7)$$

where m denotes the z component of spin. This expression neglects particle-exchange effects.

The functions χ_i and χ_f are the distorted waves, which are eigenstates of elastic scattering from the target in its initial and final state, respectively. They are usually generated from an optical-model potential using parameters which fit the elastic scattering data. Note that the spin-orbit term present in the optical-model potential can couple different spin projections, so that the distorted waves are, in general, nondiagonal matrices in spin space. The off-diagonal terms ($m\neq m'$) lead to a nonzero spin-flip amplitude.

The remaining factor in the expression (7) for the transition amplitude is the matrix element of the interaction causing the transition, taken between the initial and final states of the target. It contains all of the information about the structure of these states and the mechanism which couples them, and can be looked upon as producing transitions between the elastic scattering eigenstates χ_i and χ_f. Since this matrix element will, in general, be spin-dependent, it can also couple different spin projections and therefore produce a nonzero spin-flip amplitude.

The transition amplitude T_{fi} is usually expanded in terms of reduced amplitudes[3] corresponding to the transfer of a definite total angular momentum $\mathbf{j}$, orbital angular momentum $\mathbf{l}$, and spin angular momentum $\mathbf{s}$ to the nucleus during the inelastic event. These transferred angular momenta are determined from the relationships

$$\mathbf{j}=\mathbf{J}_f-\mathbf{J}_i, \quad \mathbf{s}=\mathbf{S}_i-\mathbf{S}_f, \quad \mathbf{l}=\mathbf{j}-\mathbf{s}, \quad \pi_i\pi_f=(-1)^l, \quad (8)$$

where the transition is $(J^\pi)_i\rightarrow(J^\pi)_f$ and $\mathbf{S}_i$ ($\mathbf{S}_f$) is the spin of the incident (scattered) particle. Note that the value of each of these angular momenta during the inelastic event is to be used. This is not necessarily the same as the asymptotic value. For example, a reduced amplitude labeled by $s=0$ may still contribute to spin flip ($s=1$ asymptotically) through the distortions induced by the spin-orbit term in the optical potential.

B. Reaction Models

The radial part of the nuclear matrix element, or form factor,[3] was calculated using three different reaction models. The first two were microscopic models, in which the nuclear wave functions were taken to be shell-model states, and the effective interaction potential

[11] J. J. Kolata, thesis, Michigan State University, 1969 (unpublished).

V was assumed to be the sum of two-body forces. The third was a collective model, in which the nuclear wave functions were taken to be the eigenstates of **J**, the total angular momentum of the nucleus, and the effective interaction potential was generated from a deformed optical-model potential.

1. Microscopic Models

Assuming that multiple scattering processes are unlikely, the projectile interacts with the target nucleus through an interaction potential of the form[12]

$$V=\sum_i v_{ip}-U, \tag{9}$$

where U is the optical potential used to generate the distorted waves, and v_{ip} is the two-body interaction between the projectile and the ith nucleon in the target. Furthermore, v_{ip} is usually approximated by the expression[12–14]

$$v_{ip}=V_0(|\mathbf{r}_i-\mathbf{r}_p|)+V_\sigma(|\mathbf{r}_i-\mathbf{r}_p|)\boldsymbol{\sigma}_i\cdot\boldsymbol{\sigma}_p, \tag{10}$$

where $\boldsymbol{\sigma}_i$ ($\boldsymbol{\sigma}_p$) is the spin operator for the target (projectile) nucleon. This expression neglects the tensor and spin-orbit forces known to be present in the interaction between free nucleons.[15,16] The main justification for this truncation is simplicity; noncentral two-body forces are much more difficult to work with,[17] and the present state of the theory does not seem to justify using the extra parameters. However, tensor forces have been used to study certain reactions.[18]

We have used two types of radial dependence in the expression (10). The first was of the form

$$V_s(r)=V_s\exp(-\alpha_s r)/\alpha_s r \qquad (s=0,1). \tag{11}$$

The range and strength parameters were obtained[19] in the impulse approximation by fitting the Fourier transform of a single Yukawa to the nucleon-nucleon scattering amplitude calculated from the central part of the Hamada-Johnston potential.[16] The interaction so determined is complex and spin-dependent, and both the range and strength parameters vary with incident proton energy. The second form for the radial dependence of Eq. (10) was derived from the Kallio-Kolltveit shell-model effective interaction.[20] The resulting interaction was real, spin-dependent, and independent of energy. In addition, a factor depending on the two-thirds power of the nucleur matter density, which seems to improve the agreement between theory and experiment,[21] was included. In both cases, the wave functions of Gillet and Vinh Mau[22] were used in the calculation of the form factor.

2. Collective Model

In the collective model, the inelastic interaction is derived from a deformed, nonspherical optical potential, which is expanded in a Taylor series about the mean radius. The interaction is taken to be that part of the expansion which occurs to first order in the deformation parameter.[23] Thus, the shape of the form factor is given by a radial derivative of the optical-model potential.

It has been customary to deform only the real and imaginary central part of the optical potential[23]; more recent studies, however, indicate that the spin-orbit[1,24] terms must also be deformed to account for the observed polarization in inelastic proton scattering. The spin-orbit term is particularly difficult to handle, since the deformed part contains a gradient operator leading to nonradial terms. Calculations have been performed using the full prescription[24,25] and also with a somewhat simplified version of the spin-orbit term[1] which does not contain the gradient operator.

We have calculated collective-model form factors for a deformed complex central potential. Such an interaction is spin-independent and can contribute no $s=1$ amplitude. In this model, then, the entire spin-flip cross section is due to spin-orbit distortions in the elastic channels.

C. Optical-Model Potential

Optical potentials used in the DWBA calculations were determined from an analysis of published elastic cross-section[26–28] and polarization[28–30] data taken at 26.2, 40.0, and 49.5 MeV. We used a local optical potential of the form

$$U(r)=-Vf(x_R)-i(W-4W_D d/dx_I)f(x_I)$$
$$+(\hbar/m_\pi c)^2(V_{so}+iW_{so})\boldsymbol{\sigma}\cdot\mathbf{l}(1/r)(d/dr)f(x_{so}), \tag{12}$$

where $f(x_k)=[\exp(x_k)+1]^{-1}$, $x_k=(r-r_kA^{1/3})/a_k$, to

[12] G. R. Satchler, Nucl. Phys. **A95**, 1 (1967).
[13] A. K. Kerman, H. McManus, and R. M. Thaler, Ann. Phys. (N.Y.) **8**, 551 (1959).
[14] M. B. Johnson, L. W. Owen, and G. R. Satchler, Phys. Rev. **142**, 748 (1966).
[15] K. E. Lassila, M. H. Hull, Jr., H. M. Ruppel, F. A. McDonald, and G. Breit, Phys. Rev. **126**, 881 (1962).
[16] T. Hamada and I. D. Johnston, Nucl Phys. **34**, 383 (1962).
[17] G. R. Satchler, Nucl. Phys. **77**, 481 (1966).
[18] C. Wong, J. D. Anderson, J. McClure, B. Pohl, V. A. Madsen, and F. Schmittroth, Phys. Rev. **160**, 769 (1967).
[19] H. McManus, F. Petrovich, and D. Slanina, Bull. Am. Phys. Soc. **12**, 12 (1967); F. Petrovich, D. Slanina, and H. McManus, Michigan State University Report No. MSPT-103, 1967 (unpublished).
[20] A. Kollio and K. Kolltveit, Nucl. Phys. **53**, 87 (1964).
[21] A. M. Green, Phys. Letters **24B**, 384 (1967); A. Lande and J. P. Svenne, *ibid.* **25B**, 91 (1967).
[22] V. Gillet and N. Vinh Mau, Nucl. Phys. **54**, 321 (1964).
[23] R. H. Bassel, G. R. Satchler, R. M. Drisko, and E. Rost, Phys. Rev. **128**, 2693 (1962).
[24] H. Sherif and J. S. Blair, Phys. Letters **26B**, 489 (1968).
[25] R. O. Ginaven, E. E. Gross, J. J. Malanify, and A. Zucker, Phys. Rev. Letters **21**, 552 (1968).
[26] J. K. Dickens, D. A. Haner, and C. N. Waddell, Phys. Rev. **132**, 2159 (1963).
[27] J. A. Fannon, E. J. Burge, D. A. Smith, and N. K. Ganguly, Nucl. Phys. **A97**, 263 (1967).
[28] L. N. Blumberg, E. E. Gross, A. VanDerWoude, A. Zucker, and R. H. Bassel, Phys. Rev. **147**, 812 (1966).
[29] R. M. Craig, J. C. Dore, G. W. Greenlees, J. Lowe, and D. L. Watson, Nucl. Phys. **79**, 177 (1966).
[30] R. M. Craig, J. C. Dore, G. W. Greenlees, J. Lowe, and D. L. Watson, Nucl. Phys. **83**, 493 (1966).

TABLE I. Optical-model parameters which produced the fits to the ^{12}C elastic data shown in Figs. 6 and 7.[a]

E_P (MeV)	V (MeV)	r_R (F)	a_R (F)	W_D (MeV)	r_I (F)	a_I (F)	V_{so} (MeV)	r_{so} (F)	a_{so} (F)	χ_σ^2/N_σ	χ_P^2/N_P[b]
26.2	48.48	1.07	0.634	3.33	1.34	0.682	7.34	1.01	0.485	22	7
40.0	45.06	1.08	0.689	5.19	1.25	0.533	7.45	1.08	0.485	22	18
49.5[c]	43.36	1.08	0.712	6.61	1.21	0.527	8.16	1.02	0.531	56	6

[a] As mentioned in the text, the final calculations were performed with a surface imaginary form ($W=0.0$) and a real spin-orbit term ($W_{so}=0.0$).

[b] The experimental uncertainties quoted in Refs. 26–30 were used in the computation of χ_σ^2 and χ_P^2. $N_\sigma(N_P)$ is the number of cross-section (polarization) data points.

[c] The data at 49.5 MeV were analyzed to aid in the determination of the energy dependence of the parameters. The fits obtained are not shown

which is added the Coulomb potential of a uniformly charged sphere of radius $1.20A^{1/3}$ F and charge Ze interacting with a point charge. Here, r_k and a_k are the usual radius and diffuseness parameters of the optical model,[1] and k refers to one of (R, I, so). All calculations were performed with the search code GIBELUMP,[31] which minimizes $\chi_T^2=\chi_\sigma^2+\chi_P^2$ using the standard definition of χ^2.[1] When two sets of parameters gave equivalent χ_T^2, preference was given to the set resulting in smaller χ_P^2.

Preliminary searches were made with volume imaginary ($W_D=0$) and surface imaginary ($W=0$) potentials, and also with a mixture of the two forms. In the latter case, it was found that W and W_D were strongly correlated. That is, the search code tended to drive one or the other of them to zero, depending on initial conditions. This correlation has been previously noted[32] for ^9Be and ^{12}C. For this reason, pure surface imaginary potentials, which seemed to give somewhat better fits than volume types, were used throughout the final analysis. Furthermore, it was found that the optimum value for the imaginary spin-orbit depth W_{so} tended to be very close to zero, in agreement with previous observations[1,32]; it was therefore set equal to zero in the remaining searches. The other 9 parameters were allowed to vary independently; the final values obtained for them appear in Table I. The corresponding fits are shown in Figs. 6 and 7.

The optical-model potentials for the entrance and exit channels in the DWBA calculations were determined from a smooth curve representing the observed energy dependence of the parameters presented in Table I. The resulting values appear in Tables II and III. No attempt was made to include the effects of a possible spin-spin interaction in the exit channel. This type of interaction has been shown to be negligible[33] for nuclei as light as ^{27}Al.

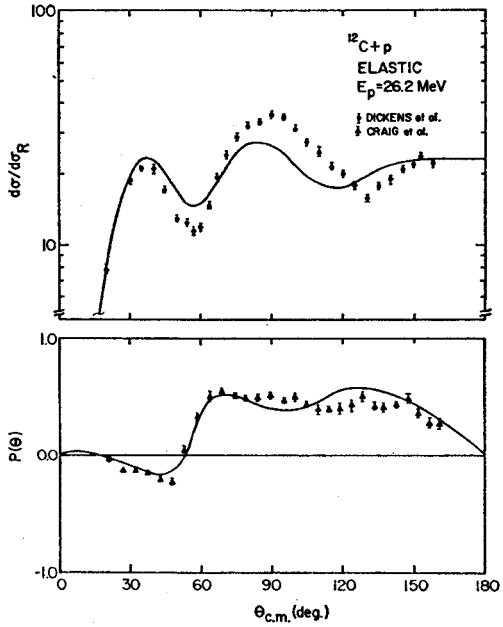

FIG. 6. Optical-model fits to ^{12}C elastic data at $E_p=26.2$ MeV, using the parameters of Table I. The cross-section data are taken from Ref. 25; the polarization data are taken from Ref. 28.

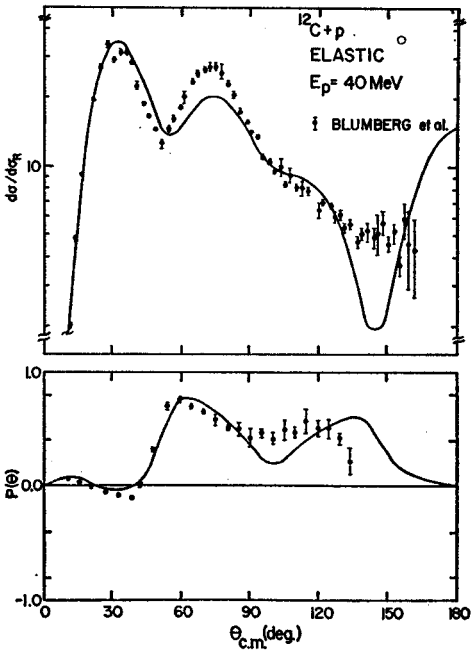

FIG. 7. Optical-model fits to ^{12}C elastic data at $E_p=40$ MeV, using the parameters of Table I. The data are taken from Ref. 27.

[31] FORTRAN-IV optical-model search code written by F. G. Perey and modified for the CDC-3600 by R. M. Haybron at the Oak Ridge National Laboratory.

[32] G. R. Satchler, Nucl. Phys. **A100**, 497 (1967).

[33] L. Rosen, J. E. Brolley, Jr., and L. Stewart, Phys. Rev. **121**, 1423 (1961).

TABLE II. Entrance-channel optical-model parameters used in the DWBA calculations.

E_P (MeV)	V (MeV)	r_R (F)	a_R (F)	W_D (MeV)	r_I (F)	a_I (F)	V_{so} (MeV)[a]	r_{so} (F)	a_{so} (F)
							8.10	1.13	0.555
26.2	48.5	1.07	0.636	3.38	1.34	0.648	7.13	1.04	0.472
							6.30	0.96	0.415
							8.50	1.10	0.550
40.0	45.0	1.08	0.685	5.15	1.26	0.570	7.65	1.04	0.500
							7.00	0.96	0.465

[a] For the spin-orbit parameters, the first (third) number given is the largest (smallest) value the parameter can have such that χ_T^2 is increased by less than 25% from its minimum value. The second number given is the "optimum" value of the parameter.

D. Calculations

The inelastic data have been analyzed in the DWBA,[34] using form factors calculated according to the three models previously described.

1. Differential Cross-Section Predictions

Figure 8 shows the differential cross sections predicted by the collective model ("COLL"), the impulse approximation ("HJIA"), and the Kallio-Kolltveit interaction ("KK2/3"), along with the inelastic scattering data of Refs. 26 and 28. The predictions of the collective model are normalized to the experimental total cross section; the value of the deformation parameter determined from the normalization was 0.66, in agreement with previous results.[32]

The best agreement with the cross-section data was obtained from the collective model, at both 26.2 and 40 MeV. The impulse-approximation calculations are in rather poor agreement with experiment at 26.2 MeV, although the situation improves somewhat at the higher energy. On the other hand, it should be noted that the predictions of the Kallio-Kolltveit interaction are not very different from those of the collective model at either energy. None of the calculations was able to reproduce the small backward peak observed in the 40.0-MeV differential cross section.

2. Asymmetry and Spin-Flip Predictions

The inelastic asymmetries and spin-flip probabilities calculated with the three models are shown in Figs. 4 and 5, along with the experimental data. Both microscopic-model calculations include the contributions of an $s=1$ amplitude arising from the spin-dependent part of the interaction. The collective model in which the spin-orbit part of the optical potential is not deformed does not lead to such an amplitude.

The agreement obtained with the experimental inelastic asymmetry data was at best only qualitative, even in the collective model. The phase predictions of this model are reasonably good at both energies, but the calculated magnitudes are far too small. The impulse-approximation predictions are again quite different from those of the collective model, and are in generally poorer agreement with experiment; the quality of the fits obtained in this model deteriorated at the higher energy, where the cross-section fits, Fig. 8, improved. Finally, it should be noted that the predictions of the Kallio-Kolltveit model again resemble those of the collective model.

TABLE III. Exit-channel optical-model parameters used in the DWBA calculations.

E_P (MeV)	V (MeV)	r_R (F)	a_R (F)	W_D (MeV)	r_I (F)	a_I (F)	V_{so} (MeV)[a]	r_{so} (F)	a_{so} (F)
							8.00	1.13	0.555
26.2	50.0	1.07	0.626	2.77	1.36	0.675	6.98	1.04	0.464
							6.10	0.96	0.400
							8.30	1.15	0.550
40.0	46.0	1.08	0.670	4.65	1.28	0.594	7.46	1.04	0.490
							6.75	0.96	0.450

[a] For the spin-orbit parameters, the first (third) number given is the largest (smallest) value the parameter can have such that χ_T^2 is increased by less than 25% from its minimum value. The second number given is the "optimum" value of the parameter.

[34] The code was written by R. M. Haybron and T. Tamura. The routine to calculate the spin-flip probability was added by one of us (J.K.). All calculations were performed on the SDS $\Sigma-7$ computer at the cyclotron laboratory.

The spin-flip predictions of the three models are in semiquantitative agreement with the experiment data. The largest discrepancies occur at the forward angles, where the spin flip probability is consistently overestimated. The predicted total spin-flip probabilities are much too large, as can be seen from the data presented in Table IV.

It is interesting that the collective model, which contains no $s=1$ amplitude, predicts a spin-flip probability in reasonable agreement with the experimental data. We conclude that the observed spin-flip is almost entirely due to the distortions introduced into the entrance and exit elastic-channel wave functions by the spin-orbit term in the optical potential. This implies

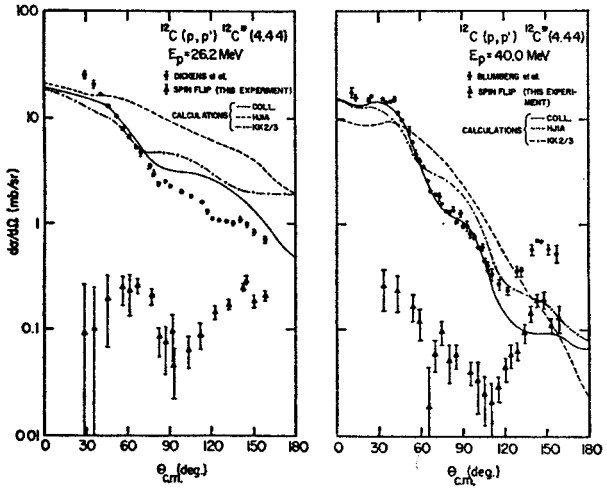

FIG. 8. Inelastic cross-section data for first excited state of ^{12}C, for $E_p=26.2$ and 40 MeV. The 26.2-MeV data are taken from Ref. 25. The 40-MeV data are taken from Ref. 27. The spin-flip cross sections at both energies were determined by multiplying the spin-flip probabilities (see Figs. 4 and 5) by the appropriate differential cross section. The various curves are the results of DWBA calculations (see caption, Fig. 4).

that if any meaningful information regarding the $s=1$ part of the inelastic interaction is to be obtained from spin-flip data, the experiment must be performed for nuclei having very well determined optical-model parameters so that the effects of spin-orbit distortion can be separated from those of the $s=1$ amplitude of the inelastic interaction.

We have performed a series of calculations in which the parameters of the spin-orbit term in the optical potential were varied in an attempt to determine the sensitivity of the spin-flip predictions to these parameters. First, we determined the range over which the parameters could be varied such that χ_T^2 for the fits to the elastic data increased by less than 25%. The limits of the range appear in Tables II and III for each of the parameters. Distorted-wave calculations were then made using the upper or lower limits for one of the parameters, while fixing the remaining parameters at

TABLE IV. Total spin-flip probability.

E_p (MeV)	Experiment	Theory (COLL)	Theory (HJIA)	Theory (KK2/3)
26.2	0.0275±0.0055	0.0875	0.1480	0.1420
40.0	0.0325±0.0075	0.0720	0.1190	0.1190

their optimum values. In each case, the form factors given by the impulse approximation were used. The results of these calculations at 26.2 MeV appear in Figs. 9 and 10. It appears that spin-flip predictions are slightly more sensitive to the spin-orbit parameters than are the inelastic asymmetries. In fact, it should be possible to use the spin-flip data to determine the spin-orbit term in the optical potential for those cases in which a polarized beam is unavailable. This has already been done[35] for the scattering of ^3He on ^{12}C. A major difficulty is that it is not practical to program an automatic search routine for DWBA calculations.

In the same spirit, a number of calculations was performed in an attempt to determine the effect of the $s=1$ amplitude on the predictions of the microscopic

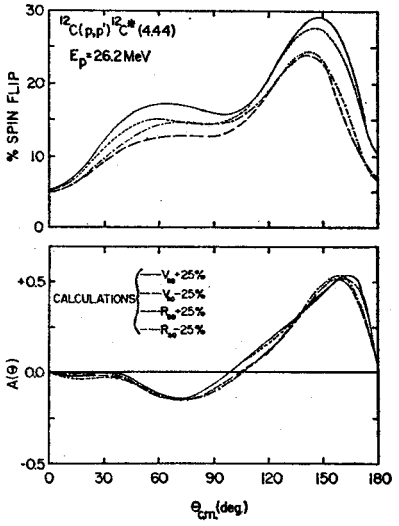

FIG. 9. Distorted-wave Born-approximation calculations for spin-flip and inelastic asymmetry in the reaction $^{12}C(p, p')^{12}C^*$ [4.44] at $E_p=26.2$ MeV. The various curves correspond to different spin-orbit parameters in the optical-model potentials, as described in the text. The notation $V_{so}+25\%$, for example, means that the spin-orbit depth used was the largest value which gave less than 25% increase in χ_T^2 over its minimum value in the optical-model analysis. Similarly, $R_{so}-25\%$ means that the spin–orbit radius used was the smallest value which gave less than 25% increase in χ_T^2. The corresponding values for V_{so} and R_{so} in the entrance and exit channels appear in Tables II and III. All other parameters were fixed at their optimum values. The form factor used in all calculations was that given by the impulse approximation.

[35] D. M. Patterson and J. G. Cramer, Phys. Letters **27B**, 373 (1968).

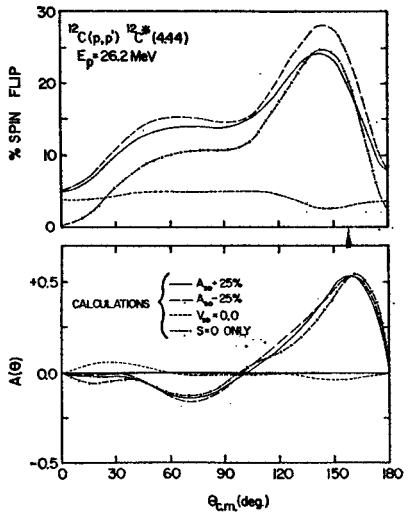

FIG. 10. Distorted-wave Born-approximation calculations for spin-flip and inelastic asymmetry in the reaction $^{12}C(p, p')^{12}C^*$ [4.44] at E_p=26.2 MeV. The notation (A_{so}±25%) is explained in the caption to Fig. 9. The calculation with V_{so}=0.0 gives an indication of the spin flip and asymmetry due to the $s=1$ part of the inelastic interaction. The calculation with $S=0$ only shows the contribution to the spin flip and asymmetry due to spin-orbit distortions in the elastic channel wave functions. The form factor given by the impulse approximation was used for all these calculations.

model, again using impulse approximation form factors. Two types of calculations were performed. In the first case, the optimum optical-model parameters of Tables II and III were used, but the $s=1$ amplitude was set equal to zero. In the second type of calculation, the $s=1$ amplitude was that predicted by the impulse approximation, and the spin-orbit term in the optical potential was set equal to zero. The results of these calculations at 26.2 MeV also appear in Fig. 10. It is clear that the $s=1$ amplitude has a negligible effect on the asymmetries, and only a small effect on the spin-flip predictions. The predicted spin-flip probability is increased by an amount which is almost independent of angle, so that the greatest differences occur at the forward angles, where the spin flip is smallest.

IV. CONCLUSIONS

The spin-flip probability for protons inelastically scattered from the first excited state of ^{12}C has been measured for incident proton energies of 26.2 and 40.0 MeV. The data exhibit large backward peaks similar to those observed at lower energies[7] and for other nuclei.[24] Comparison with DWBA calculations indicates that semiquantitative fits to the experimental data can be obtained with collective-model and microscopic-model form factors. The predictions display a marked sensitivity to the spin-orbit term in the optical potential, and are only slightly affected by the presence of an $s=1$ amplitude in the microscopic-model form factors.

No definite conclusions regarding the spin-dependent part of the inelastic interaction can be obtained from the present data. In fact, the addition of an $s=1$ amplitude to the microscopic form factors seemed to make the agreement with experiment worse in that it significantly increased the predicted spin flip at the forward angles, where it was already too large. However, in view of the inability of any of the models to reproduce the inelastic assymmetries, and considering the fact that optical-model parameters which adequately fit all of the elastic data could not be found, it would seen that the difficulty lies in the failure of the assumptions of the optical model for nuclei as light as ^{12}C. If this is the case, then accurate spin-flip measurements for heavier nuclei having well determined optical-model parameters may give useful information regarding the spin dependence of the inelastic reaction mechanism.

ACKNOWLEDGMENTS

The authors would like to thank R. Sager for his help in the collection of the data and the measurement of the γ detector efficiency. In addition, we would like to acknowledge the help of Dr. B. Preedom in the optical-model analysis. The microscopic-model form factor programs and the impulse-approximation calculations were due to F. Petrovich. We are indebted to Dr. R. Haybron for supplying the DWBA code, and to Dr. P. Locard and Dr. S. Austin for their helpful comments on the DWBA calculations.

Reprinted from ANNALS OF PHYSICS
Vol. 50, No. 3, December 1968
Printed in Belgium

Orbit Properties of the Isochronous Cyclotron Ring with Radial Sectors*

M. M. GORDON

Cyclotron Laboratory, Michigan State University, East Lansing, Michigan 48823

The isochronous cyclotron considered here consists of a ring of radial magnet sectors separated by straight sections. The general features of such cyclotrons are discussed, and a complete analysis is presented of their orbit properties using the hard-edge approximation. This analysis proceeds through the transfer matrix technique, which is simplified by the symmetry of the magnet structure; the only complication arises from the inconstancy of the magnetic field index resulting from the isochronism condition. Computed orbit properties are presented and discussed for a wide variety of possible geometries; these properties include the extreme values of the beam widths, as well as the focusing frequencies, as a function of the energy. Problems associated with certain resonances are also considered. The results indicate that isochronous cyclotrons of this type should be quite capable of producing proton beams at energies up to about 500 MeV.

I. INTRODUCTION

Construction of an isochronous cyclotron in the form of a "ring", somewhat like a synchrotron, is not a novel concept. Indeed, an Isochronous Cyclotron Ring with spiralled sectors which will accelerate protons from 70 to 500 MeV, is now being constructed at ETH in Zurich (*1*). The present paper considers the simplest form of such accelerators, the Isochronous Cyclotron Ring with radial sectors. This simplicity manifests itself both in the constructional features of these cyclotrons, and in the analysis of the orbit properties.

The Isochronous Cyclotron Ring with radial sectors consists of N identical magnets each having a constant angular width $\Delta\theta$ corresponding to a "magnet fraction" $f = N(\Delta\theta)/2\pi$. The ring has an inner radius and an outer radius corresponding to the chosen energy range. Fig. 1 shows schematically a four-sector magnet geometry with each magnet having $\Delta\theta = 45°(f = 0.5)$ and with inner and outer radii chosen to correspond to a 20–200 MeV energy range. Similarly, Fig. 2 shows a six-sector geometry with $\Delta\theta = 18°(f = 0.3)$ corresponding to a 20–500 MeV energy range. In both cases the inner radius, and hence the injection energy,

* This work has been supported by the National Science Foundation, partly at Indiana University.

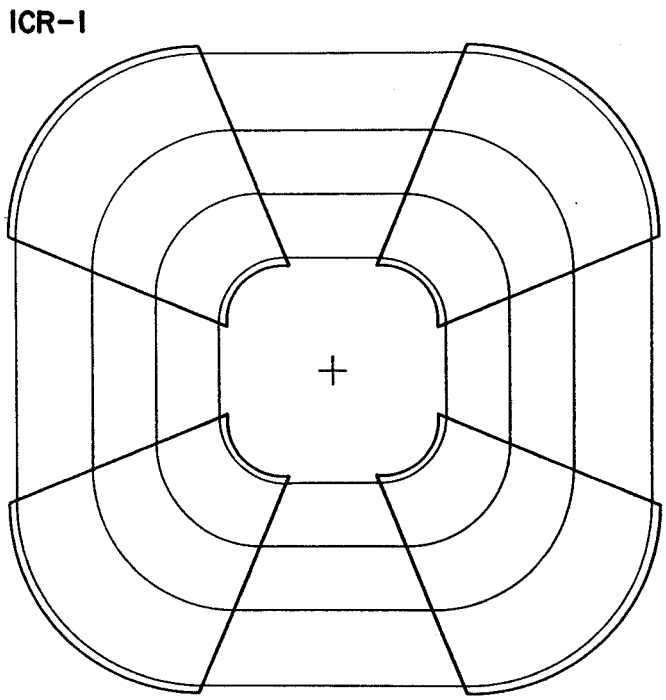

FIG. 1. Four-sector isochronous cyclotron ring with magnets having constant angular width $\Delta\theta = 45°$ (magnet fraction, $f = 0.5$). The orbits which are shown correspond to the following proton energies: 20, 50, 100, and 200 MeV.

has been chosen rather arbitrarily; in actual practice, this choice must be based on a variety of engineering considerations. For the machines depicted in Figs. 1 and 2, a low energy ring of similar construction could be used to produce the 20 MeV beam required for injection.

Since the radiofrequency structures (dees or cavities) would be situated in the "valleys" between the magnets (straight sections), the magnet gaps could be quite small. The use of narrow gap magnets substantially improves the vertical focusing properties of these magnets. Assuming flat pole-faces, then all the important surfaces of each magnet would be flat surfaces, which greatly simplifies the construction of these magnets even when they are very large. Each magnet, together with its coils and pole-face windings, could be constructed separately and then properly assembled into the ring. Since ample space is available in the straight sections, it should be possible for the radiofrequency accelerating system to produce a large energy gain per turn. Alternate straight sections could be used for the rf system operating at the main frequency, with the remaining straight sections occupied by

a third harmonic rf system designed to produce a "flat-top" on the effective voltage wave form; such a design could yield separated turns together with a considerable increase in the duty factor (*2*). Since this third harmonic system would be relatively small, the same straight sections which it occupies could also be used for beam injection and beam extraction.

The Isochronous Cyclotron Ring requires an injected beam obtained from an external ion source or from a lower energy ring. The use of a ring geometry for the lowest energy stage eliminates the central region problems associated with the conventional cyclotron, which stem from the weak vertical focusing and from the constraints imposed by an internal ion source. The external source required for the ring permits the tailoring of the properties of the injected beam so as to match most effectively the transmission characteristics of the machine. In addition, the beam injection system for the ring can quite readily be adapted for use with a source

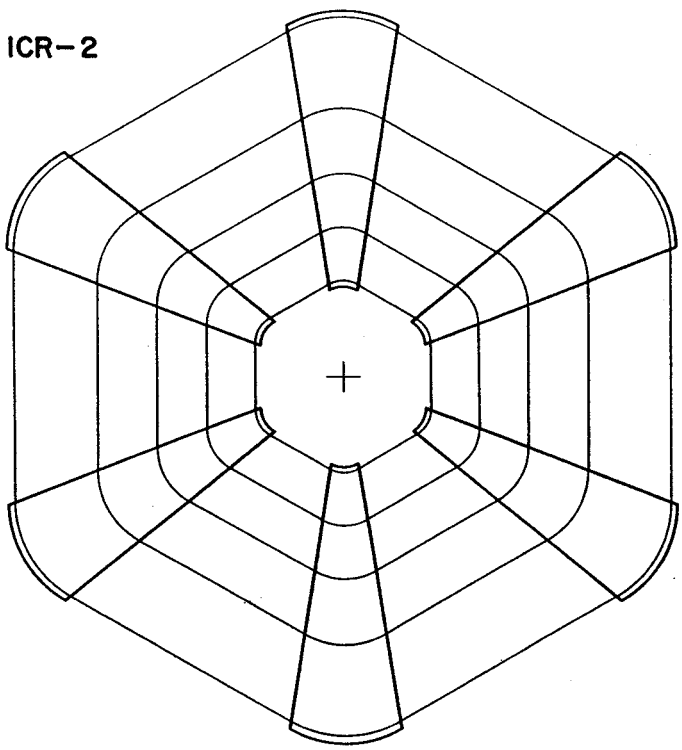

FIG. 2. Six-sector isochronous cyclotron ring with magnets having constant angular width $\Delta\theta = 18°$ (magnet fraction, $f = 0.3$). The orbits which are shown correspond to the following proton energies: 20, 50, 100, 200, and 500 MeV.

of polarized ions. Finally, the presence of straight sections in the ring greatly simplifies the problem of beam injection.

As shown in Figs. 1 and 2, each equilibrium orbit consists of circular arc segments within the magnets joined by straight line segments in the valleys. Thus, it is assumed that the angular width of the magnet edge region, within which the magnetic field falls off to zero, is negligibly small compared with the angular width of either the magnet or the valley (hard-edge approximation); this is a reasonable approximation for the small magnet gaps considered here. For a fixed orbital frequency the velocity v is proportional to the radius of curvature ρ of the circular arc; as a result, the fixed inner and outer radii of a given geometry specify only the ratio v_f/v_i where v_i and v_f are the initial and final velocities of the particle. For example, the four-sector geometry depicted in Fig. 1, which was chosen for a 20–200 MeV energy range, could just as well be used for a 2.6–20 MeV energy range. The orbit geometry is clearly the same at all energies except for a scale factor. Moreover, this geometry is independent of the orbital frequency and would therefore remain the same if the final energy or the accelerated ion were changed.

The magnetic field B is constant along the circular arc segments of each equilibrium orbit. Thus, each of these circular arcs represents an iso-gauss contour line, and the pole-face windings used to produce the desired field variation should be shaped accordingly. Since the orbit geometry is invariant under a change of orbital frequency, the same set of pole-face windings should be applicable under all operating conditions. To satisfy the isochronism condition, the value of B along a given circular arc must be proportional to the corresponding value of γ, the relativistic mass factor; a sufficient number of pole-face windings must be provided so as to produce this required field variation with reasonable accuracy. If γ_i and γ_f are the initial and final values of γ over the energy range of the ring, then γ_f/γ_i specifies the ratio of maximum to minimum values of B which must be produced within the ring. For example, for the 20–200 MeV ring depicted in Fig. 1, this ratio is about 1.2 which seems quite feasible; however, for the 20–500 MeV ring depicted in Fig. 2, the field ratio is about 1.5 which may be difficult to achieve in practice. The 20–500 MeV machine could be built in two stages with the first stage going to, say, 200 MeV; although the required field variation would be easier to produce in each ring, such a design is faced with the difficult problem of extracting the 200 MeV beam from the first stage and injecting this beam into the second stage.

All the properties of the horizontal and vertical linear oscillations, such as the focusing frequencies and the beam widths, as a function of the energy depend only on the number of sectors N and the magnet fraction f characterizing the geometry. Because of the isochronism condition, the vertical focusing frequency ν_z decreases with energy; however, since $\nu_z \cong [(1/f) - 1]^{1/2}$ at $E = 0$, for values of f between

0.2 and 0.5, the initial value of ν_z is sufficiently large so that the vertical focusing remains quite good over a substantial energy range. Actually, as will be seen in Section VI, the variation of the maximum beam width as a function of energy provides a proper criterion for the adequacy of the vertical focusing. Because of the problems encountered with various resonances, for a given value of N, certain values of f must be excluded from consideration, while for other f values the feasible energy range must be restricted. The four-sector geometry shown in Fig. 1 with $f = 0.5$ posesses exceptionally good orbit properties and avoids serious resonance problems over the entire proton energy range up to about 300 MeV; the same can be said for the six-sector geometry, depicted in Fig. 2, with $f = 0.3$ for all proton energies up to about 500 MeV. Many other geometries also posess very favorable orbit properties, and all deserve serious consideration.

II. GEOMETRY AND ISOCHRONOUS FIELD

Because of the symmetry of the magnet configuration, consideration is required of only one-half of a sector for a complete analysis of the properties of the equilibrium orbits and their associated linear oscillations. Figure 3 exhibits the geometry of the half sector upon which the analysis is based. The magnetic field extends from $\theta = 0$, the center of the magnet, to $\theta = \alpha$, the edge of the magnet, at which point the field is assumed to drop abruptly to zero; from $\theta = \alpha$ to $\theta = \delta$, the center of the valley, the field is therefore zero. If $\Delta\theta$ is the constant angular width of the magnet, and if f is the magnet fraction defined in the preceding section, then:

$$\delta = \pi/N, \qquad \alpha = (\Delta\theta)/2 = f\delta. \tag{1}$$

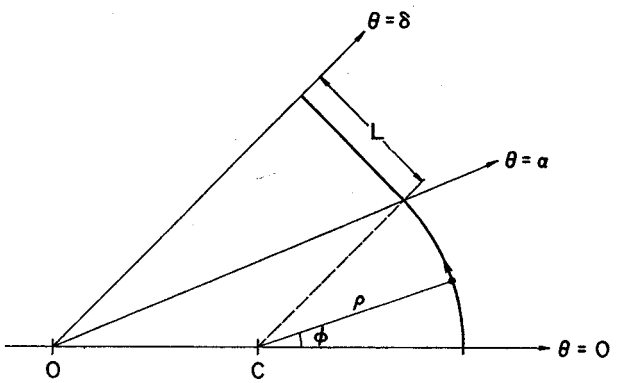

FIG. 3. Geometry for one-half of a sector, from the center of a magnet to the center of a valley, showing the equilibrium orbit and the various parameters describing this geometry.

The portion of the equilibrium orbit (EO) shown in Fig. 3 consists of a circular arc segment of constant radius of curvature ρ from $\theta = 0$ to $\theta = \alpha$, and a straight line segment of length L from $\theta = \alpha$ to $\theta = \delta$. The point C is the center of the circular arc segment of the EO, and the distance from the origin O (machine center) to the point C is given by:

$$OC = b\rho, \tag{2a}$$

$$b = (\sin(\delta - \alpha))/(\sin \alpha). \tag{2b}$$

The angle ϕ shown in Fig. 3 constitutes a polar angle relative to the point C, and specifies the position of the particle along the EO within the magnet; thus, $\phi(\theta = 0) = 0$ and $\phi(\theta = \alpha) = \delta$. The length of the circular arc portion of the EO shown in Fig. 3 is $\rho\delta$, so that the length L of the straight line segment can be specified by the parameter a as follows:

$$L = a(\rho\delta), \tag{3a}$$

$$a = b(\sin \delta)/\delta. \tag{3b}$$

Thus, if f_0 is the fraction of the arc length of the EO which is within the magnet, then:

$$f_0 = (1 + a)^{-1} = f[1 + (1/3)(1 - f)^2 \delta^2 + \cdots], \tag{4}$$

where the second expression represents an expansion in powers of δ^2.

An arc length variable s is introduced such that $s = \rho\phi$ within the magnet; thus, $s = 0$ at the center of the magnet, $s = s_0$ at the edge of the magnet, and $s = s_1$ at the center of the valley, where:

$$\begin{aligned} s_0 &= \rho\delta, \\ s_1 &= \rho\delta + L = \rho\delta(1 + a). \end{aligned} \tag{5}$$

It follows then that the total arc length of the EO around the machine is given by:

$$2Ns_1 = 2\pi\rho/f_0 = vT, \tag{6a}$$

where v is the velocity of the particle and T is its period of rotation. Setting $2\pi/T = f_0\omega$, then:

$$v = \rho\omega, \tag{6b}$$

where ω is the constant angular velocity of the particle within the magnet relative to the point C in Fig. 3.

If the magnetic field B is perfectly isochronous, then T, and hence ω, is a constant

independent of the energy of the particle. In this case, the value of B along the circular arc segment of the EO is given by:

$$B(\rho) = (m_0\omega/q)\gamma, \tag{7a}$$

where m_0 and q are the rest mass and charge of the ion, and γ is given by:

$$\gamma = (1 - \beta^2)^{-1/2}, \tag{7b}$$

with $\beta = v/c$. This then is the isochronous magnetic field, and it should be noted that the circular arcs which form the iso-gauss contours for this field are not concentric. If ω_{rf} is the circular RF frequency, then $\omega_{rf} = 2\pi h/T = h\omega f_0$, where h is the integral harmonic ratio.

III. LINEAR MOTION

The displacement of the particle from the EO is described by the coordinates $x(s)$ and $z(s)$ where s is the arc length along the EO. The vertical coordinate z represents the displacement perpendicular to the median plane. The horizontal coordinate x represents a displacement in the median plane in the direction of the outward normal to the EO at the given value of s; this definition of x coincides with the one customarily used in synchrotron orbit analyses. We depart from customary practice by employing the conjugate momenta p_x and p_z rather than (dx/ds) and (dz/ds), where:

$$p_x = p(dx/ds), \qquad p_z = p(dz/ds); \tag{8}$$

although this change is a minor one, it has the advantage of making phase space consequences (via Liouville's theorem) completely transparent. We also adopt "modified cyclotron units" wherein the momenta p_x, p_z, and p have units of length the same as x, z, and ρ; that is, for example,

$$p = (\beta\gamma)(c/\omega) = \rho\gamma, \tag{9}$$

as follows from Eqs. (6,7). This convention has the advantage of rendering the transfer matrices dimensionless.

Within the magnet the coordinate system corresponds to cylindrical polar coordinates centered at the point C of Fig. 3; the position of the particle is specified by the variables $(\rho + x, \phi, z)$ relative to this point. In order to calculate orbit properties, the median plane field B of Eq. (7) must be expressed in terms of the variables x and ϕ, bearing in mind that the origin C of this coordinate system changes with the energy of the particle. Consider the point P with coordinates

$(\rho + x, \phi)$ relative to the point C; the point P lies on a different circular iso-gauss contour the center of which is at the point C', such that the distance $C'P = \rho'$, and the distance $OC' = b\rho'$ (cf. Eq. (2)). Considering then the triangle CPC', it follows that:

$$(\rho')^2 = (\rho + x)^2 + b^2(\rho' - \rho)^2 - 2b(\rho' - \rho)(\rho + x)\cos\phi, \tag{10}$$

so that $\rho' = \rho$ for $x = 0$. This equation can readily be solved for ρ' in terms of ρ, x, ϕ; the value of $B(\rho')$ at the point P is then given by Eq. (7) with ρ replaced by ρ'. For most analytical purposes, the value of B is expanded in powers of x; for example, to first order,

$$\begin{aligned} B(\rho') &= B(\rho) + x(dB/d\rho)(\partial\rho'/\partial x), \\ (\partial\rho'/\partial x) &= (1 + b\cos\phi)^{-1}, \end{aligned} \tag{11}$$

as follows from Eq. (10).

For linear oscillations about the EO, the key parameter is the field index k defined by: $k = (\rho/B)(\partial B/\partial x)$. Upon using Eq. (11) this becomes:

$$k(\phi) = (\beta\gamma)^2(1 + b\cos\phi)^{-1}, \tag{12}$$

since B is proportional to γ, and ρ is proportional to β as given in Eqs. (6, 7). Thus, k is a function of ϕ, and is smaller than $(\beta\gamma)^2$ to which it reduces when $f = 1$, that is, when the magnet occupies the complete sector. The value of k obtained from Eq. (12) applies, of course, only within the magnet; that is, from $\phi = 0$ to $\phi = \delta$, in the half sector under consideration here.

The differential equations for the linear oscillations about the EO within the magnet are:

$$(d^2x/d\phi^2) + [1 + k(\phi)]x = 0, \tag{13a}$$

$$(d^2z/d\phi^2) - k(\phi)z = 0, \tag{13b}$$

where $k(\phi)$ is given by Eq. (12). In order to construct the transfer matrices, two linearly independent solutions of each of these equations are required over the range: $s(\phi = 0) = 0$ to $s(\phi = \delta) = s_0$, that is, from the center to the edge of the magnet. Approximate solutions of these differential equations will be discussed in Section V; however, the structure of these equations is sufficiently simple to make them quite amenable to numerical solution with a digital computer. Note that within the magnet $p_x = \gamma(dx/d\phi)$ and $p_z = \gamma(dz/d\phi)$ as follows from Eqs. (8, 9) in the units adopted here.

At the edge of the magnet ($s = s_0$) the field drops abruptly to zero, and in this "hard-edge" approximation the values of p_x and p_z change discontinuously

at this point (*3*). From the orbit geometry depicted in Fig. 3, it follows that the field index at the magnet edge is given by:

$$k_{\text{edge}} = -\tan(\delta - \alpha)\, \Delta(\phi - \delta), \tag{14a}$$

where $\Delta(\phi - \delta)$ is a Dirac delta function. It then follows from Eq. (13) that the impulsive change in p_x and p_z at the magnet edge is given by:

$$\Delta p_x(s_0) = +\gamma t x(s_0), \tag{14b}$$

$$\Delta p_z(s_0) = -\gamma t z(s_0), \tag{14c}$$

where the symbol t stands for:

$$t = \tan(\delta - \alpha). \tag{15}$$

This change in p_z can be recognized as the "edge focusing" arising from the field component B_θ at the magnet edge. A particle with positive x actually arrives at the magnet edge "early" so that its momentum vector rotates through a smaller angle than for the EO; thus, the change Δp_x simply compensates for the extra rotation and does not constitute, therefore, any actual defocusing at the magnet edge.

From the edge of the magnet at $s = s_0$ to the center of the valley at $s = s_1$, the magnetic field is identically zero so that the values of p_x and p_z do not change in this region. Thus, the values of the orbit coordinates and momenta at the center of the valley are given by:

$$\begin{aligned} p_x(s_1) &= p_x(s_0) + \gamma t x(s_0), \\ x(s_1) &= (1 + ta\delta)\, x(s_0) + (a\delta/\gamma)\, p_x(s_0), \\ p_z(s_1) &= p_z(s_0) - \gamma t z(s_0), \\ z(s_1) &= (1 - ta\delta)\, z(s_0) + (a\delta/\gamma)\, p_z(s_0), \end{aligned} \tag{16}$$

where the values at $s = s_0$ are obtained from the solutions of Eq. (13), and where $L/p = (a\delta/\gamma)$ following Eqs. (3, 9). Thus, the phase space vectors (x, p_x) and (z, p_z) can be traced from the center of the magnet to the center of the valley, thereby completing the description of these vectors over the required half sector. As will be seen in the next section, this information is sufficient to determine the linear oscillation properties throughout the complete sector.

IV. TRANSFER MATRIX PROPERTIES

In this section (y, p_y) will be used to stand for either (x, p_x) or (z, p_z) whenever a given relation applies equally well to both. If the phase space vector (y, p_y) is represented by the column matrix $Q(s)$, then following Courant and Snyder (*4*),

the transfer matrix $M(s)$ for one sector ($\Delta s = 2s_1$) starting at the point s is defined by:

$$Q(2s_1 + s) = M(s)\, Q(s). \tag{17a}$$

This transfer matrix is written as follows:

$$M(s) = I \cos \mu + J(s) \sin \mu; \tag{17b}$$

where I is the unit matrix, and

$$\mu = \nu_y(2\pi/N) = 2\nu_y\delta; \tag{17c}$$

$$J(s) = \begin{pmatrix} \alpha(s) & \beta(s) \\ -\gamma(s) & -\alpha(s) \end{pmatrix}. \tag{17d}$$

The quantity ν_y is the focusing frequency; the quantities $\alpha(s)$, $\beta(s)$, $\gamma(s)$ are periodic functions of s with periodicity equal to one sector, and satisfy the following relation:

$$\beta(s)\,\gamma(s) = 1 + \alpha^2(s). \tag{18}$$

In order to avoid confusion, the α, β, γ used in the preceding sections will not be used at all in this section, while the $\alpha(s)$, $\beta(s)$, $\gamma(s)$ introduced here will appear only in this section. Note that $\alpha(s)$, $\beta(s)$, $\gamma(s)$ are all dimensionless in the units adopted here; using the subscript "c" to designate the same quantities as used by Courant and Snyder, then the following relations hold: $\alpha_c = \alpha$; $\beta_c = p\beta$; $p\gamma_c = \gamma$.

Suppose that the transfer matrix $M(s)$ is repeatedly applied to the vector $Q(s)$, then the sequence of phase space points $(y,\ p_y)$ so generated will lie on an ellipse whose equation is given by:

$$\gamma(s)\, y^2 + \beta(s)\, p_y^2 + 2\alpha(s)\, y p_y = A^2, \tag{19}$$

where A is a constant independent of s. This "eigen-ellipse" is characteristic of the given point s in the sector, and is determined by the values of the periodic functions α, β, γ at this point. The area of this ellipse is πA^2, so that if the ellipse is examined at different values of s, its eccentricity and orientation may change, but not its area. Upon differentiating Eq. (19), the maximum values of y and p_y are found to be:

$$\begin{aligned} [y(s)]_{\max} &= A[\beta(s)]^{1/2}, \\ [p_y(s)]_{\max} &= A[\gamma(s)]^{1/2}. \end{aligned} \tag{20}$$

Consider now a beam of particles all at the same energy E, and suppose that their

(y, p_y) phase space points at the given value of s completely fill the eigen-ellipse given by Eq. (19); that is, the ith particle has $A_i \leqslant A$. It follows then that the "widths" Δy and Δp_y for the entire beam of particles are given by:

$$\Delta y = 2A[\beta(s, E)]^{1/2}, \tag{21a}$$

$$\Delta p_y = 2A[\gamma(s, E)]^{1/2}, \tag{21b}$$

and since A is constant, these relations determine the widths as a function of s. Now the area πA^2 is an invariant, and under conditions of adiabatic acceleration, the relations (21) specify the variation of the beam widths as a function of the energy E as well as the position s. These relations can be applied to any accelerated beam, and the value of the amplitude A can be determined from the smallest eigen-ellipse which completely encloses the phase space area occupied by the beam at injection (or anywhere else); obviously, for maximum efficiency the beam should completely fill the eigen-ellipse. Evidently, a knowledge of the widths $[\beta(s, E)]^{1/2}$ and $[\gamma(s, E)]^{1/2}$ as a function of s and E provides much more detailed information on the focusing produced by the magnet structure than does the focusing frequency ν_y ; the value of ν_y is important mainly in determining the location of various resonances. It should be noted that Liouville's theorem requires only that the phase space area occupied by the beam remain constant; on the other hand, the assumptions of linearity (including the absence of resonances) and adiabaticity together specify in detail the nature and evolution of this phase space area throughout the machine. It should also be noted that the functions β and γ, as defined here, already contain all the "adiabatic damping" factors.

Suppose that at the given energy E, two independent solutions (y_1, p_{y1}) and (y_2, p_{y2}) are obtained for the linear equations of motion over one complete sector from $s = 0$ to $s = 2s_1$, with their initial conditions given by (1, 0) and (0, 1), respectively. Consider then the matrix $Y(s)$ formed from these solutions as follows:

$$Y(s) = \begin{pmatrix} y_1 & y_2 \\ p_{y1} & p_{y2} \end{pmatrix}; \tag{22a}$$

then, since $Y(0) = I$, the unit matrix, it follows that $Y(s)$ is the transfer matrix from $s = 0$ to a given s; that is,

$$Q(s) = Y(s)\, Q(0). \tag{22b}$$

Since the Hamiltonian is invariant under a displacement in s by one sector, it also follows that:

$$Q(s + 2s_1) = Y(s)\, Y(2s_1)\, Q(0), \tag{22c}$$

which, when compared with Eq. (17), yields the following equations:

$$M(0) = Y(2s_1); \tag{23a}$$
$$M(s) = Y(s)\, M(0)\, Y^{-1}(s); \tag{23b}$$
$$J(s) = Y(s)\, J(0)\, Y^{-1}(s). \tag{23c}$$

Thus, Eq. (23a) can be used to calculate the value of ν_y (within limits) as well as the values of $\alpha(0)$, $\beta(0)$, and $\gamma(0)$; then, Eq. (23c) can be used to calculate α, β, and γ at all other s values for the complete sector.

The time reversal operator T can be represented by the following matrix:

$$T = \begin{pmatrix} 1 & 0 \\ 0 & -1 \end{pmatrix} = T^{-1}, \tag{24a}$$

which has the effect of replacing p_y by $-p_y$ while leaving y unchanged. For the symmetric magnet geometry being considered here, the Hamiltonian is invariant under reflection in s about any symmetry point such as $s = 0$ (the center of a magnet "hill"), or $s = s_1$ (the center of a "valley"). This symmetry yields the following relations:

$$Q(s) = Y(s)\, Q(0) = TY(-s)\, TQ(0), \tag{24b}$$
$$Q(s + s_1) = Y(s + s_1)\, Y^{-1}(s_1)\, Q(s_1) = TY(s_1 - s)\, Y^{-1}(s_1)\, TQ(s_1), \tag{24c}$$

so that:

$$Y(-s) = TY(s)T, \tag{25a}$$
$$Y(s_1 + s) = TY(s_1 - s)\, Y^{-1}(s_1)\, TY(s_1). \tag{25b}$$

Hence, the solutions generated in the preceding section over half the sector from $s = 0$ to $s = s_1$ can thereby be extended to the remaining half of the sector.

From Eq. (23a) and Eq. (25b), it follows that:

$$M(0) = TY^{-1}(s_1)\, TY(s_1), \tag{25c}$$

which, upon evaluation and identification via Eq. (17), yields the following results:

$$\sin^2(\nu_y \delta) = -y_2(s_1)\, p_{y1}(s_1), \tag{26a}$$
$$\alpha_h = 0, \qquad \gamma_h = 1/\beta_h, \tag{26b}$$
$$(\beta_h)^2 = -[y_2(s_1)\, p_{y2}(s_1)]/[y_1(s_1)\, p_{y1}(s_1)], \tag{26c}$$

where the subscript "h" designates the value at the center of the hill ($s = 0$). From Eq. (23c) and the fact that $\alpha_h = 0$, it can also be shown that:

$$\beta(s) = \beta_h y_1^2(s) + \gamma_h y_2^2(s), \tag{27a}$$
$$-\alpha(s) = \beta_h y_1(s)\, p_{y1}(s) + \gamma_h y_2(s)\, p_{y2}(s), \tag{27b}$$
$$\gamma(s) = \beta_h p_{y1}^2(s) + \gamma_h p_{y2}^2(s). \tag{27c}$$

Further analysis provides the following symmetry relation for $J(s)$:

$$J(-s) = -TJ(s)T; \tag{28}$$

so that $\beta(s)$ and $\gamma(s)$ are both symmetric about any symmetry point, while $\alpha(s)$ is antisymmetric about such points; consequently, $\alpha = 0$ at any symmetry point. Thus, the values of α, β, γ need only be calculated for half of a sector because of this symmetry. The relations (26, 27, 28) will therefore permit the calculation of ν_y as well as the values of α, β, γ at any point in the sector from the given values of $Y(s)$ from $s = 0$ to $s = s_1$. In particular, for $s = s_1$ at the center of the valley, the following values are obtained:

$$\alpha_v = 0, \qquad \gamma_v = 1/\beta_v, \tag{29a}$$

$$(\beta_v)^2 = -[y_1(s_1)\ y_2(s_1)]/[p_{y1}(s_1)\ p_{y2}(s_1)], \tag{29b}$$

where the subscript "v" indicates the center of a valley. The foregoing relations are quite general in that they will apply to any symmetric magnet structure.

Since the quantity β specifies the beam width as a function of position and energy via (21a), it is of considerable importance to determine at which values of s this function has its maximum and minimum values. The derivatives of β are given by:

$$p(d\beta/ds) = -2\alpha(s), \tag{30a}$$

$$p(d\alpha/ds) = K(s)\,\beta(s) - \gamma(s), \tag{30b}$$

where $K_x = (p/\rho)^2(1 + k)$, and $K_z = -(p/\rho)^2 k$; these equations can be derived by differentiating the relations (27) and using the equations of motion. Thus, β has a maximum or minimum value wherever $\alpha = 0$. Moreover, since $\alpha = 0$ at each symmetry point ($s = 0$, $s = s_1$), then β must have an extremum at such points. In addition, β may have an extremum at the magnet edge ($s = s_0$) since the value of α is discontinuous at this point and may pass through zero. Using the subscript "e" to denote the value at the edge of the magnet, the discontinuity in α is given by:

$$\Delta\alpha_e = \pm(p/\rho)\, t\beta_e, \tag{31}$$

as can be seen from Eqs. (14, 27b), where the (+) sign applies to the z-motion, and the (−) sign to the x-motion. Since $K = 0$ in the valley, then Eq. (30b) shows that α must be positive following the magnet edge, and then decreased to zero at the center of the valley; as a result, β has a minimum value β_v at the center of the valley for both the x-motion and z-motion. Since $K_z < 0$ within the magnet, the value of α starts from zero at the center of the hill and decreases out to the magnet edge; thus, β_z must have a minimum value β_{zh} at the center of the hill. Therefore, β_z must have its maximum value β_{ze} at the magnet edge (this is consistent with the

fact that α_z from (31) increases across the magnet edge); the value of β_e is found to be:

$$\beta_e = \beta_v + (a\rho\delta/p)^2 (\beta_v)^{-1}, \tag{32}$$

from Eqs. (27a, 16) and $\alpha_v = 0$. Now Eq. (31) shows that α_x decreases at the magnet edge, and since it is positive beyond this point, then α_x must also be positive prior to the magnet edge, and β_x cannot have an extremum at this point; as a result, α_x must be positive for $0 < s < s_0$ (provided $\nu_x < N/2$), and β_x must have a maximum value β_{xh} at the center of the hill. Introducing the width function W,

$$W(s, E) = [\beta(s, E)]^{1/2}, \tag{33}$$

the foregoing conclusions can be summarized as follows: for the x-motion, W_x has its maximum value W_{xh} at the center of a hill and decreases continuously to its minimum value W_{xv} at the center of a valley; for the z-motion, W_z has a minimum value W_{zh} at the center of a hill, rises to its maximum value W_{ze} at the magnet edge, and then decreases to a second minimum value W_{zv} at the center of a valley; that is,

$$W_{\max} = W_{xh}, W_{ze}; \tag{34a}$$

$$W_{\min} = W_{xv}, W_{zh}, W_{zv}. \tag{34b}$$

The values of W_{xh}, W_{zh}, W_{xv}, and W_{zv} can be calculated from the corresponding values of β_h and β_v obtained from Eqs. (26c, 29b); the value of W_{ze} can then be calculated using Eq. (32).

The beam "divergence" width Δp_y is determined by the quantity γ as a function of position and energy as can be seen from Eq. (21b). The derivative of γ is given by:

$$p(d\gamma/ds) = 2K(s)\,\alpha(s), \tag{35}$$

as obtained by differentiating (27c), and where K is given following (30). From the foregoing discussion, it can be concluded that $(d\gamma/ds) > 0$, for $0 < s < s_0$, for both the x-motion and the z-motion; it therefore follows that γ has a minimum value $\gamma_h = 1/\beta_h$ at the center of the hill in both cases. Within the valley, γ has a constant value $\gamma_v = 1/\beta_v$ for both cases. For the x-motion, $|\alpha_x|$ decreases at the magnet edge so that γ_x has its maximum value γ_{xe} just prior to this point. For the z-motion, the value of γ_z may either increase or decrease at the magnet edge depending on whether $|\alpha_z|$ increases or decreases at this point.

V. APPROXIMATE SOLUTIONS

In order to obtain approximate solutions of the differential equations (13), it should be noted that $k(\phi)$ varies quite slowly over the ϕ range of interest $0 \leqslant \phi \leqslant \delta$, particularly if N is large. As a consequence, a simple approximation

can be obtained by replacing $\cos\phi$ in the expression (12) by its average value: $\langle\cos\phi\rangle = (\sin\delta)/\delta$. In this case, $k(\phi)$ becomes equal to a constant:

$$k(\phi) \to k_0 = f_0(\beta\gamma)^2, \tag{36}$$

where f_0 is given by Eq. (4). This approximation simplifies the differential equations (13) such that their solutions become either circular or hyperbolic functions. The WKBJ approximation would, of course, yield improved results; however, the amount of this improvement does not warrant the extra complexity.

The solutions of the differential equations provide the matrix elements of $Y(s)$, as defined in (22) over the range $0 < s < s_0$. The elements of $Y(s_1)$ can then be obtained from Eq. (16). The values of ν_y can then be calculated from Eq. (26a); the beam widths given in (34) can be calculated by the procedure described thereafter. The approximate results so obtained have an error which can be shown to vary as $(1 - f)^2/N^4$; furthermore, although these results are exact for $E = 0$, the error increases with energy. The values of ν_x, ν_z, and the W's of (34) obtained from this approximation have been compared with more accurate values obtained by numerical integrations with the following results (cf. Tables III and IV): (a) for $N = 4$ and $f = 0.5$, the error in all quantities is less than 0.1 % for $E < 0.10$, less than 0.5 % for $E < 0.27$, and less than 1 % for $E < 0.34$; (b) for $N = 6$ and $f = 0.3$, the error is less than 0.1 % for $E < 0.43$, less than 0.5 % for $E < 0.73$, and less than 1 % for $E < 0.80$.

In order to obtain explicit, simple formulas, the above approximation can be pursued to its ultimate limit: $\delta \to 0 (N \to \infty)$. (This limiting case is similar to the so-called "smooth approximation".) In this limit, the following results are obtained:

$$\nu_{x0} = \gamma; \tag{37a}$$

$$(\nu_{z0})^2 = f^{-1} - \gamma^2; \tag{37b}$$

$$W_{y0} = (f\gamma\nu_y)^{-1/2}; \tag{37c}$$

where the width function W_{y0} is a constant independent of s in this approximation. These results work best when $(1 - f)$ is small and when $\nu_y \ll N/2$. These simple equations provide a true indication of the dependence of ν_y and W_y on the value of f and the energy E. It may be noted that the values of ν_{x0} and ν_{z0} are always smaller than the actual values.

In the nonrelativistic limit ($E \to 0$) the field within the magnets is constant so that $k = 0$. Simple analytical results can again be obtained in this case and although these results are strictly valid only for $E = 0$, they will be reasonably accurate for low energy cyclotrons. In particular, this approximation yields the following equations for ν_x and ν_z:

$$\sin(\nu_x\delta) = (\sin\delta)/(\cos(\delta - \alpha)); \tag{38a}$$

$$\cos^2(\nu_z\delta) = (1 - t\delta)(1 - at\delta); \tag{38b}$$

where $t = \tan(\delta - \alpha)$. An examination of (38a) reveals that for $f < f_m$, the value of ν_x falls in the $N/2$ stop-band; the value of f_m is given by:

$$f_m = (4 - N)/2. \tag{39}$$

Since the value of ν_x increases with energy, the restriction $f > f_m$ must hold for all energies. For $N = 2$, the value $f_m = 1$ shows that ν_x always lies in the stop-band, so that $N = 2$ must be ruled out (this is generally true for any isochronous cyclotron with an azimuthally varying field); for $N = 3$, only $f > 0.5$ is permissible; for $N \geqslant 4$, this consideration places no restriction on the possible f values. Analysis of Eq. (38b) shows that for $f < f'_m$, the value of ν_z will lie in the $N/2$ stop-band; the following formula can be used to determine f'_m:

$$\tan(2f'_m\delta) = 2(\tan^3 \delta)/(1 + 3 \tan^2 \delta). \tag{40}$$

This consideration produces the following restrictions: for $N = 3$, $f > 0.384$ ($< f_m = 0.5$); for $N = 4$, $f > 0.295$; for $N = 6$, $f > 0.182$; and for large N values, $f > \delta^2(1 + \delta^2)/(1 + 3\delta^2)$. Since ν_z decreases with energy, the restriction $f > f'_m$ does not hold at all energies for f'_m given above; however, values of

TABLE I

NON-RELATIVISTIC LIMITS ($E = 0$)

	$N = 3$		$N = 4$		$N = 6$		$N = \infty$
f	ν_x	ν_z	ν_x	ν_z	ν_x	ν_z	ν_z
0.90	1.009	0.339	1.004	0.336	1.002	0.335	0.333
0.85	1.021	0.429	1.009	0.425	1.003	0.422	0.420
0.80	1.038	0.514	1.016	0.507	1.006	0.503	0.500
0.75	1.062	0.596	1.025	0.587	1.010	0.581	0.577
0.70	1.093	0.679	1.037	0.667	1.014	0.660	0.655
0.65	1.135	0.765	1.051	0.749	1.019	0.740	0.734
0.60	1.191	0.855	1.067	0.835	1.025	0.824	0.817
0.55	1.273	0.952	1.087	0.927	1.032	0.914	0.905
0.50	1.500	1.060	1.110	1.029	1.039	1.012	1.000
0.45	*****		1.136	1.146	1.048	1.122	1.106
0.40			1.167	1.287	1.057	1.250	1.225
0.35			1.203	1.475	1.068	1.404	1.363
0.30			1.245	1.840	1.079	1.600	1.528
0.25				*****	1.092	1.877	1.732
0.20					1.106	2.377	2.000

f less than f'_m are probably too small to be of practical significance. Table I presents values of ν_x and ν_z obtained from (38) as a function of f for $N = 3$, $N = 4$, $N = 6$, and $N = \infty$. The listings for each N are terminated at the smallest f value consistent with the minima given above; the values of ν_x for $N = \infty$ are omitted since $\nu_x \equiv 1$ in this case. For a given f value, the results show that the value of N very significantly affects $(\nu_x - 1)$, but only mildly affects ν_z (except for quite small f values).

VI. DISCUSSION OF RESULTS

All the properties of the linear oscillations as a function of the energy E (expressed in m_0c^2 units) are completely determined by two geometric parameters, the number of sectors N, and the magnet fraction f; that is, these properties are independent of the rest mass and charge of the particle as well as the absolute magnetic field strength (or orbital frequency). A computer program has been developed which, for a given N and f, calculates as a function of E the most significant of these orbit properties: the horizontal and vertical focusing frequencies, ν_x and ν_z; the extreme values of the horizontal and vertical width functions listed in (34). The

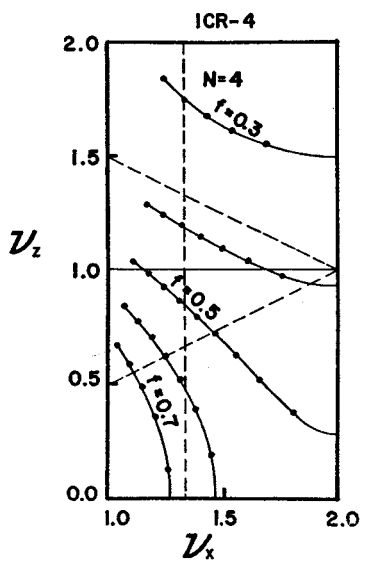

FIG. 4. Focusing frequencies for four-sector geometries. Five plots are shown of ν_z versus ν_x values for $f = 0.3, 0.4, \ldots, 0.7$ (reading from top to bottom). Blackened points are spaced at an energy interval $\Delta E = 0.05$ starting from $E = 0$ at the left. Dashed lines indicate the following resonances: $3\nu_x = 4$, $\nu_x - 2\nu_z = 0$, and $\nu_x + 2\nu_z = 4$.

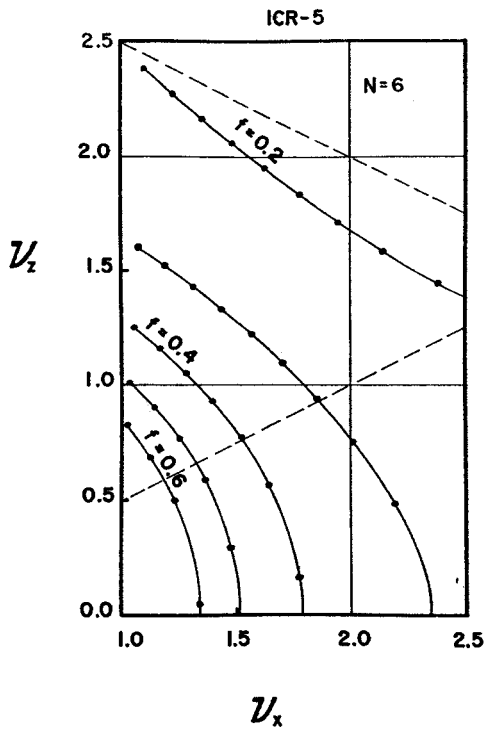

FIG. 5. Focusing frequencies for six-sector geometries. Five plots of ν_z versus ν_x values are given for $f = 0.2, 0.3, \ldots, 0.6$ (reading from the top). The blackened points are spaced at an energy interval $\Delta E = 0.1$ starting from $E = 0$ at the left. Dashed lines indicate the resonances: $\nu_x - 2\nu_z = 0$, and $\nu_x + 2\nu_z = 6$. The $f = 0.2$ curve, which is cut off at $\nu_x = 2.5$, continues until $\nu_x = 3$.

program begins at $E = 0$ and proceeds in constant ΔE steps until either $\nu_z = 0$ or $\nu_x = N/2$. The calculations are based on the formulas developed in Sections II, III, IV and assume only that the field is perfectly isochronous and that the hard-edge approximation is valid.

If g is the aperture of the magnet gap, then the validity of the hard-edge approximation requires that: $g \ll \rho\delta$, and $g \ll L = a\rho\delta$ (cf. (3)). This approximation will therefore be least reliable near injection at the lowest energies; in this case, the values of ν_z, and to a lesser extent ($\nu_x - 1$), will be lower than the corresponding hard-edge values (cf. Table I); nevertheless, the validity of the hard-edge approximation increases rapidly with energy since the value of ρ increases roughly as $E^{1/2}$. For rings with higher energy injection, the hard-edge approximation should be valid throughout.

Figures 4, 5, 6 show plots of ν_z versus ν_x for $N = 4$, 6, and 8, respectively. Each figure shows curves for five different f values: $f = 0.3(0.1)0.7$ for $N = 4$, and $f = 0.2(0.1)0.6$ for $N = 6$ and $N = 8$. The blackened points on each curve are spaced at a fixed ΔE interval starting at $E = 0$, so that the variation of ν_x and ν_z with energy is thereby indicated. These curves terminate either at $\nu_z = 0$ or at $\nu_x = N/2$, except that in Figs. 5 and 6 the drawings have been arbitrarily cut off at $\nu_x = 2.5$. Since ν_z decreases with energy while ν_x increases with energy, the slope of these curves is always negative; however, since $(d\nu_z/d\nu_x) \to 0$ as $\nu_x \to N/2$, the curvature reverses sign near the end of those curves which terminate at $\nu_x = N/2$. These figures also indicate the location of some of the "resonance lines" which are discussed below. Although they are rather striking, orbit properties for $N = 3$ will not be discussed here because these properties seem of little practical importance, except possibly for low energy cyclotrons (cf. Table I). In addition, values of $f < 0.2$ have been excluded from consideration here since such values of f would not only impose the

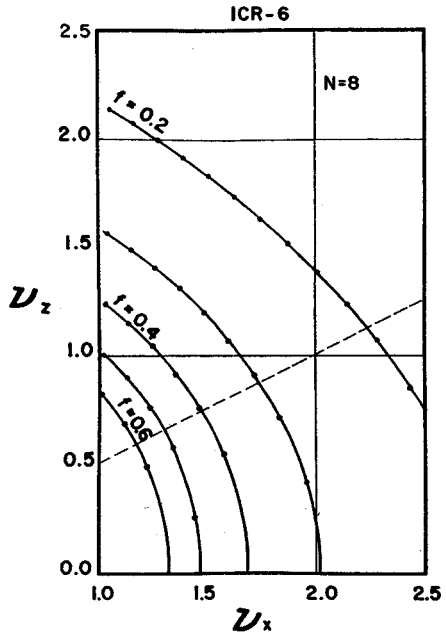

FIG. 6. Focusing frequencies for eight-sector geometries. Five plots are shown of ν_z versus ν_x values for $f = 0.2, 0.3, \ldots, 0.6$ (reading from the top). The blackened points are spaced at the constant energy interval $\Delta E = 0.1$ starting from $E = 0$ at the left. The dashed line indicates the $\nu_x - 2\nu_z = 0$ resonance. The curve for $f = 0.2$, which is cut off at $\nu_x = 2.5$, continues until $\nu_z = 0$.

TABLE II

MAXIMUM ENERGIES (in m_0c^2 units)

f	$N = 4$	$N = 6$	$N = 8$	$N = \infty$
0.2		0.91*	1.27	1.24
0.3	0.24*	0.86	0.84	0.83
0.4	0.33*	0.60	0.59	0.58
0.5	0.42*	0.43	0.42	0.41
0.6	0.31	0.30	0.29	0.29

greatest technical difficulties, but also appear unnecessary within the energy limits imposed on this type of cyclotron.

Table II presents values of the maximum energy $E_{\max}$ which can be obtained with a given f value for $N = 4$, 6, 8, and $N = \infty$. In most of the cases shown, $E_{\max}$ is reached when $\nu_z = 0$, while in the remaining cases (indicated in the table by an asterisk) $E_{\max}$ is reached when $\nu_x = N/2$. For a given value of N, the largest $E_{\max}$ is obtained for that value of f for which $\nu_z = 0$ and $\nu_x = N/2$ are reached simultaneously. The value of $E_{\max}$ represents an upper limit which cannot actually be achieved in practice since the vertical or horizontal beam width diverges when $\nu_z = 0$ or $\nu_x = N/2$, respectively. The values of $E_{\max}$ given for $N = \infty$ are obtained from (37b) by setting $\nu_{z0} = 0$.

The horizontal and vertical width functions, W_x and W_z, are defined via Eqs. (33, 21) and are given here in dimensionless cyclotron units. Since these functions specify the variation in the beam's dimensions throughout the ring, they therefore provide crucial information to the machine designer. For the vertical motion, the following relation holds:

$$\Delta z = (\Delta z_i)(W_z/W_{zi}), \tag{41}$$

where Δz is the actual beam width and W_z is the corresponding width function at a given position and energy, while Δ_{zi} and W_{zi} are the same quantities at injection (with an analogous relation between Δx and W_x). If, for example, the vertical beam aperture has a prescribed constant value throughout the ring, then the smallest value of W_{zi}/W_z within the ring will determine the largest Δz_i which can be successfully injected into the ring. If $\nu_z \ll N/2$, the value of W_{z0} obtained from Eq. (37c) provides a good estimate of the maximum width W_{ze} as a function of the energy, particularly if the correct value of ν_z is used. Thus, since the value of ν_z tends to decrease with energy faster than the value of γ increases, the value of W_{ze} generally increases with energy, and diverges as the $\nu_z = 0$ limit is approached. To compensate for this increase in W_{ze}, the vertical beam aperture could likewise

TABLE III

FOUR SECTOR ORBIT PROPERTIES

f	E	ν_x	W_{xh}	W_{xv}	ν_z	W_{zh}	W_{ze}	W_{zv}
0.3	0.00	1.245	2.486	1.218	1.840	2.591	2.610	0.625
	0.05	1.333	2.486	1.102	1.748	2.059	2.112	0.766
	0.10	1.430	2.535	0.983	1.675	1.813	1.893	0.851
	0.15	1.543	2.673	0.850	1.610	1.659	1.762	0.913
	0.20	1.689	3.065	0.679	1.548	1.550	1.673	0.965
	0.24	1.901	5.203	0.374	1.499	1.482	1.621	1.000
0.5	0.00	1.110	1.694	1.091	1.029	1.306	1.438	1.337
	0.05	1.174	1.649	1.014	0.979	1.296	1.440	1.350
	0.10	1.240	1.615	0.940	0.923	1.294	1.449	1.371
	0.15	1.310	1.594	0.868	0.862	1.299	1.467	1.400
	0.20	1.384	1.589	0.797	0.794	1.316	1.498	1.441
0.5	0.25	1.463	1.606	0.724	0.717	1.347	1.546	1.499
	0.30	1.552	1.660	0.646	0.627	1.403	1.622	1.585
	0.35	1.656	1.790	0.553	0.519	1.503	1.751	1.724
	0.40	1.798	2.212	0.414	0.376	1.724	2.022	2.006
	0.42	1.896	3.009	0.295	0.298	1.916	2.254	2.243
0.7	0.00	1.037	1.315	1.029	0.667	1.397	1.506	1.491
	0.05	1.091	1.264	0.968	0.587	1.449	1.570	1.558
	0.10	1.146	1.221	0.912	0.489	1.546	1.684	1.675
	0.15	1.202	1.183	0.859	0.360	1.758	1.924	1.918
	0.20	1.258	1.151	0.808	0.124	2.924	3.215	3.214

increase with energy; however, the increase in the isochronous field with energy tends to favor a corresponding decrease in the magnet gap towards the outside of the ring. A reasonable compromise consists in having the magnet gap and vertical beam aperture remain constant throughout the ring; moreover, such a choice clearly simplifies the construction of the machine. The increase in W_{ze} imposes limits on the feasible energy range for a given geometry; however, an increase in W_{ze} by 50 %, which could be tolerable, generally corresponds to a rather substantial energy range.

The properties of the width functions are well demonstrated by the data presented in Table III. This table displays part of the computer output for $N = 4$ with $f = 0.3$, 0.5, and 0.7. (The significance of the various W's is explained in connection with (34).) For the cases $f = 0.3$ and 0.5 the value of ν_x approaches $N/2$ at the end of the energy range, and as can be seen, the value of W_{xh} diverges, while W_{xv} approaches zero as the limiting value of ν_x is reached. The tendency for W_{xh} to

decrease in accordance with (37c) is evident only in the $f = 0.7$ case (and also at the beginning of the $f = 0.5$ case) since $\nu_x \ll N/2$ here. For $f = 0.7$ and 0.5, the value of W_{ze} tends to increase in accordance with (37c); as $\nu_z \to 0$ in these cases, the values of W_{zh}, W_{ze}, and W_{zv} tend to diverge together. In the $f = 0.3$ case, however, the value of W_{ze} initially decreases very rapidly because the value of ν_z is initially close to $N/2$; that is, whenever either ν_x or ν_z approaches $N/2$, the maximum width diverges while the minimum width decreases such that their product varies as $(f\gamma\nu)^{-1}$. An examination of this table shows that a four-sector geometry with $f = 0.5$ (depicted in Fig. 1) posesses exceptionally good orbit properties at all energies from $E = 0$ to $E = 0.3$ inasmuch as the maximum horizontal and vertical beam widths change by less than 15% over this energy range.

In order to demonstrate how the orbit properties depend on N, these properties are displayed in Table IV for $f = 0.3$ with $N = 6$, $N = 8$, and $N = \infty$. The data for $N = \infty$ are obtained from Eqs. (37a–c); in this case, $W_{x0} = W_{xh} = W_{xv}$, and $W_{z0} = W_{zh} = W_{ze} = W_{zv}$. With regard to the vertical motion, the values of W_{ze} remain nearly constant up to $E = 0.7$, and do not differ substantially in all

TABLE IV

ORBIT PROPERTIES FOR $f = 0.3$

N	E	ν_x	W_{xh}	W_{xv}	ν_z	W_{zh}	W_{ze}	W_{zv}
6	0.00	1.079	2.001	1.597	1.600	1.521	1.559	1.273
	0.20	1.316	1.724	1.282	1.434	1.413	1.473	1.264
	0.40	1.570	1.552	1.041	1.224	1.365	1.448	1.305
	0.60	1.852	1.466	0.838	0.943	1.404	1.517	1.432
	0.80	2.194	1.503	0.641	0.486	1.782	1.961	1.933
	0.86	2.321	1.568	0.574	0.182	2.842	3.145	3.139
8	0.00	1.041	1.913	1.702	1.565	1.492	1.515	1.371
	0.20	1.259	1.618	1.394	1.407	1.412	1.446	1.337
	0.40	1.482	1.412	1.170	1.200	1.391	1.437	1.359
	0.60	1.713	1.266	0.996	0.914	1.462	1.525	1.479
	0.80	1.955	1.161	0.855	0.416	2.003	2.112	2.100
	0.84	2.005	1.145	0.829	0.184	2.966	3.135	3.131
∞	0.00	1.00	1.826		1.528		1.477	
	0.20	1.20	1.522		1.376		1.421	
	0.40	1.40	1.304		1.172		1.425	
	0.60	1.60	1.141		0.879		1.539	
	0.80	1.80	1.014		0.306		2.462	
	0.82	1.82	1.003		0.145		3.558	

three cases. For the horizontal motion, the values of W_{xh} decrease monatonically in the three cases, except for the very end of the $N = 6$ case. These results contrast sharply with those for $N = 4$, $f = 0.3$ given in Table III; this contrast emphasizes the important effect of the proximity of $\nu = N/2$ on the values of the width functions. If only the variation of the W's is considered, the $f = 0.3$ geometry with $N \geqslant 6$ has excellent orbit properties up to $E = 0.7$; it may be noted, moreover, that the same conclusion holds for the $f = 0.2$ geometry up to $E = 0.8$ for $N = 6$, and up to $E = 1.1$ for $N = 8$.

VII. RESONANCES

The integral resonance $\nu_z = 1$ constitutes the most serious imperfection resonance for this type of cyclotron. Acceleration through this resonance poses very severe problems because of the postulated narrow magnet gaps. This resonance is driven by an error in the median plane field containing a radial component $\Delta B_r(\theta)$ with a first harmonic fourier component of amplitude ΔB_{r1}. Following acceleration through the $\nu_z = 1$ resonance, the beam will have developed a coherent vertical oscillation whose amplitude is given approximately by:

$$\Delta Z = \pi F[E_1 \mid d\nu_z/dE \mid]^{-1/2}, \tag{42}$$

where E_1 is the energy gain per turn, and $F = (q/p)\, r^2(\Delta B_{r1})$; a cursory examination of this formula reveals the severity of the problem. An appropriate set of coils could, in principle, be built into the ring so as to produce a corrective $\Delta B_r'$ with a harmonic of variable amplitude and azimuth which could, therefore, empirically cancel the troublesome error field otherwise present; such a mechanism could restore the beam to the median plane following the resonance. If, however, the machine is to operate with variable final energy (or with different ions), then the position of this resonance will not be fixed spatially and the design of the appropriate correcting coils would, therefore, be complicated. On the other hand, if crossing the $\nu_z = 1$ resonance is to be avoided, then the values of ν_z throughout the ring must be restricted to either $\nu_z < 1$ or $1 < \nu_z < 2$. As can be seen from Figs. 4–6, such a restriction limits the choice of admissible f values, or limits the feasible energy range for a particular f value. For values of $f \gtrsim 0.5$, the values of ν_z remain below $\nu_z = 1$ at all energies, and this restriction on f seems appropriate for low energy cyclotrons. For the $f = 0.3$ geometries whose orbit properties are given in Table IV, the values of ν_z remain above $\nu_z = 1$ at all energies up to $E = 0.54$, which would then become the energy limit for these geometries. As a further example, for $N = 8$ and $f = 0.2$, the requirement that $1 < \nu_z < 2$ restricts the available energy range from $E = 0.2$ to $E = 1.0$.

Unlike the conventional isochronous cyclotron, the design considered here

effectively avoids the difficulties associated with the $\nu_x = 1$ resonance at low energies since, as can be seen from Table I, the values of $(\nu_x - 1)$ are significantly above zero at $E = 0$ for values of f of practical interest. For $N = 4$ geometries the $\nu_x = 2$ resonance represents the stopband limit and must be carefully avoided (cf. Table III). For $N \geqslant 6$ geometries, the $\nu_x = 2$ resonance does not occur except for small f values; for $N = 6$, the $\nu_x = 2$ resonance occurs at $E = 0.63$ for $f = 0.2$, and at $E = 0.70$ for $f = 0.3$; for $N = 8$, this resonance occurs at $E = 0.80$ for $f = 0.2$, and at $E = 0.83$ for $f = 0.3$. The coherent horizontal oscillation induced by acceleration through the $\nu_x = 2$ resonance can be used to facilitate beam extraction for $N \geqslant 6$, provided that this resonance can actually be reached within the limitations imposed by other considerations.

The half-integral imperfection resonances $\nu_y = n/2$ (e.g., $\nu_x = 3/2$, $\nu_z = 1/2$ or 3/2) should pose far less serious problems than those presented by the integral resonances. Acceleration through a half-integral resonance can produce only an increase in the effective phase space area occupied by the beam, and if suitable precautions are taken, this increase will be minimal. If an error $\Delta k(\theta)$ exists in the field index having a nth fourier harmonic of amplitude Δk_n, then the value of ν_y in the vicinity of the resonance will be changed to ν_y^* given by the approximate formula:

$$(\nu_y^* - n/2)^2 = (\nu_y - n/2)^2 - [(\Delta k_n)/2n]^2. \tag{43}$$

Thus, for a range of energies in the neighborhood of $\nu_y = n/2$, the value of ν_y^* will have an imaginary component (stop-band); the duration and strength of this imaginary component are each proportional to Δk_n. If the incoherent oscillations within the beam prior to the resonance are characterized by a maximum amplitude A (cf. Eq. (21)), then after acceleration through the resonance, this amplitude will be increased by ΔA given approximately by:

$$\Delta A = A[\pi(\Delta k_n)/2n]^2 \, [E_1 \mid d\nu_y/dE \mid]^{-1}. \tag{44}$$

With proper care it should be possible to achieve $(\Delta A)/A < 0.1$, in which case the half-integral resonance traversal would not represent a serious barrier. The one situation to be avoided is where ν_z starts out at low energy close to 1/2 or 3/2 and then hovers about this value over an appreciable energy range because of a failure in the hard-edge approximation.

For $N = 4$ geometries, the essential third-order (in the Hamiltonian) resonance $\nu_x = 4/3$ frequently occurs within a desirable energy range as can be seen in Fig. 4 and Table III. For the narrow gap magnets of constant angular width being considered here, the fourier component $B_4(r) \cos 4\theta$ of the median plane field increases rather slowly with radius (this increase being almost entirely produced by the isochronism requirement); consequently, the nonlinear driving force for the $\nu_x = 4/3$

resonance is exceptionally weak, so that acceleration through this resonance should produce only an insignificant distortion of the beam's phase space area. This situation contrasts markedly with that obtaining in spiral-ridge magnets, where the spiralling produces very strong nonlinear forces. This situation also differs substantially from that obtaining in the ORNL four-sector electron cyclotron (*5*); although that cyclotron had radial sectors, since the field contained only a few fourier components, the value of $B_4(r)$ was forced to increase rapidly with radius in order to produce adequate vertical focusing throughout the machine; by contrast, the magnet structure considered here has a large number of strong fourier components contributing significantly to the vertical focusing. For $N = 6$ configurations, the $\nu_x = 6/3$ resonance coincides with the $\nu_x = 2$ resonance, and contributes to the effects of the latter (discussed above) only if large amplitudes are generated in traversing this resonance. The fourth-order essential resonance $\nu_x = N/4$ (e.g. 6/4 or 8/4) poses even less of a problem than the $\nu_x = N/3$ resonance. The corresponding essential resonance $\nu_z = N/4$ (in particular, 4/4 or 6/4) in the vertical motion should produce no difficulties provided, as must be required, the vertical extent of the beam is sufficiently small compared to the magnet gap so that the vertical motion is essentially linear throughout.

Among the essential nonlinear coupling resonances, those requiring the greatest attention are the third-order resonances: $\nu_x + 2\nu_z = N$, $\nu_x - 2\nu_z = 0$; and to a lesser extent the fourth-order resonances: $2\nu_x + 2\nu_z = N$, $2\nu_x - 2\nu_z = 0$; while the higher order resonances are again presumably neligible. Furthermore, the linear imperfection resonances $| \nu_x \pm \nu_z | = n$ should also be investigated. In plots of ν_z versus ν_x the "difference" resonances and the "sum" resonances appear as lines having positive and negative slopes, respectively; to avoid clutter, only the third-order essential resonances are shown in Figs. 4–6 insofar as these resonance lines fall within the given boundaries of the drawings. The nonlinear resonances should be relatively weak since the only strong field gradient occurs across the magnet edge, and this gradient varies slowly with radius; as a result, if the beam is reasonably well-centered on the equilibrium orbit, then acceleration through a nonlinear coupling resonance should proceed without significant damage, provided the resonance is traversed fairly rapidly. This proviso is clearly fulfilled by the difference resonances since the slopes of these resonance lines are opposite in sign to that for the ν_z versus ν_x curve of the accelerating particles. With regard to the sum resonances, however, for certain values of f the ν_z versus ν_x curves closely parallel resonance lines. Obviously, such a situation invites potentially disasterous results and should be strictly avoided; as a consequence, for a given value of N, certain values of f should be definitely excluded from consideration.

For $N = 4$, the $\nu_x + 2\nu_z = 4$ resonance is the most serious coupling resonance, and this line falls between the curves for $f = 0.36 - 0.37$ such that $| \nu_x + 2\nu_z - 4 | < 0.07$ at all energies up to $E = 0.25$, and such values of f

must therefore be excluded; however, the $f = 0.4$ curve has $| \nu_x + 2\nu_z - 4 | > 0.25$ at all energies, and should be quite acceptable. For $N \geqslant 6$, the $\nu_x + 2\nu_z = N$ resonance line does not come close to the ν_z versus ν_x curves for $f \geqslant 0.2$ (cf. Figs. 5-6). For $N = 4$, the $2\nu_x + 2\nu_z = 4$ resonance line (which coincides with $\nu_x + \nu_z = 2$) is closely bracketed by the curves for $f = 0.55 - 0.56$ at all energies up to $E = 0.2$, and values of f in this vicinity should also be excluded; however, the $f = 0.5$ curve has $2\nu_x + 2\nu_z > 4.28$ over its entire energy range, and should therefore be acceptable. For $N = 6$, the $2\nu_x + 2\nu_z = 6$ (or $\nu_x + \nu_z = 3$) resonance line should exclude values of f close to $f = 0.26 - 0.27$, since the curves for these f values closely parallel the resonance line at all energies up to $E = 0.6$; however, the curve for $f = 0.3$ is satisfactory since $2\nu_x + 2\nu_z < 5.6$ in this case over the entire useful energy range. For $N \geqslant 8$, the $2\nu_x + 2\nu_z = N$ resonance line does not appear close to the ν_z versus ν_x curves for values of f considered important here. The linear imperfection resonances are presumably less serious since they can, in principle, be counteracted by appropriate measures; nevertheless, these resonances should be avoided if possible. It is therefore worth noting that for $N \geqslant 6$, the $\nu_x + \nu_z = 2$ resonance line closely parallels the curves for $f = 0.51 - 0.52$ at the interesting energies; moreover, the $\nu_x + \nu_z = 3$ resonance line is bracketed by the curves for $f = 0.30 - 0.32$ for $N = 4$, and is crossed twice by curves with $f \cong 0.24$ for $N = 8$.

The foregoing discussion represents only a general survey of the various resonances encountered in this type of cyclotron; these resonances should be investigated more thoroughly when a specific geometry is being given serious study. Considering the limitations imposed by all the resonances, the four-sector geometry with $f = 0.5$ has very good orbit properties at all energies up to about $E = 0.3$ (cf. Fig. 1 and Table III); moreover, studies carried out at Indiana University show that for this geometry the values of ν_z actually lie below $\nu_z = 1$ at low energies due to the failure of the hard-edge approximation. The six-sector geometry with $f \cong 0.3$ posesses desirable orbit properties and avoids resonance difficulties at all energies up to about $E = 0.5$ (cf. Fig. 2 and Table IV). Many other configurations also appear promising, particularly for rings operating within a restricted energy range.

The present analysis has considered only one possible arrangement of magnet sectors consisting of "wedge-shaped" magnets. The general arrangement for wedge-shaped magnets can be defined by three parameters: (a), the angular width of the wedge; (b), the displacement (positive or negative) of the apex of the wedge from the machine center; and (c), the angle between this displacement and the line bisecting the wedge. The present paper has explored only those cases for which the parameters (b) and (c) are both equal to zero. Other symmetric configurations can be obtained by varying the parameter (b) while retaining the parameter (c) equal to zero. If both of these parameters are different from zero, then the geometry becomes asymmetric and posesses some of the attributes of spiralled magnet sectors.

In addition, a sector could contain more than one wedge-shaped magnet. All these possibilities remain to be investigated.

This paper is indirectly an outgrowth of a previous paper which presented, among other topics, a qualitative discussion of a 200 MeV Isochronous Cyclotron Ring with radial sectors (*2*). Some of the ideas expressed in that paper have been suitably modified and extensively developed for use in the proposed 200 MeV cyclotron being designed at Indiana University. It was as a result of my interaction with Martin Rickey and Bryce Bardin at Indiana University that the work described in the present paper was conceived and carried out. I am therefore indebted to these people for fruitful discussions and for their encouragement of this work.

RECEIVED: July 1, 1968

REFERENCES

1. J. P. BLASER AND H. A. WILLAX, *IEEE Trans. Nucl. Sci.* NS-13, 194 (1966).
2. M. M. GORDON, *Nucl. Instr. and Meth.* **58**, 245 (1968).
3. J. J. LIVINGOOD, "Principles of Cyclic Particle Accelerators," Chapter 4. D. Van Nostrand, Princeton, 1961.
4. E. D. COURANT AND H. S. SNYDER, *Ann. Phys.* **3**, 1 (1958).
5. BLOSSER, WORSHAM, GOODMAN, LIVINGSTON, MANN, MOSELEY, TRAMMEL, AND WELTON, *Rev. Sci. Instr.* **29**, 819 (1958).

PRINTED IN BRUGES, BELGIUM, BY THE ST. CATHERINE PRESS, LTD.

Reprinted from THE PHYSICAL REVIEW, Vol. 182, No. 4, 1104–1105, 20 June 1969
Printed in U. S. A.

Gamma Rays from Protons on ^{10}B, and the Excitation Energy of the First Excited State of ^{10}C†

R. A. PADDOCK, S. M. AUSTIN, W. BENENSON, I. D. PROCTOR, AND F. ST. AMANT
Physics Department, Cyclotron Laboratory, Michigan State University, East Lansing, Michigan 48823
(Received 20 January 1969)

The energy of the first excited state of ^{10}C has been measured using the $^{10}B(p, n\gamma)^{10}C$ reaction. The excitation energy was found to be 3.3527 MeV, with an error assignment of 1.5 keV. Also reported are excitation energies for the first four excited states of ^{10}B.

I. INTRODUCTION

THE $^{12}C(p, t)^{10}C$ reaction leading to the ground and first excited states of ^{10}C often produces useful calibration triton peaks for studies of nuclei using the (p, t) reaction. A measurement of the threshold for the $^{10}B(p, n)^{10}C$ reaction by Freeman, Jenkin, and Murray[1] has established the mass excess of the ^{10}C ground state

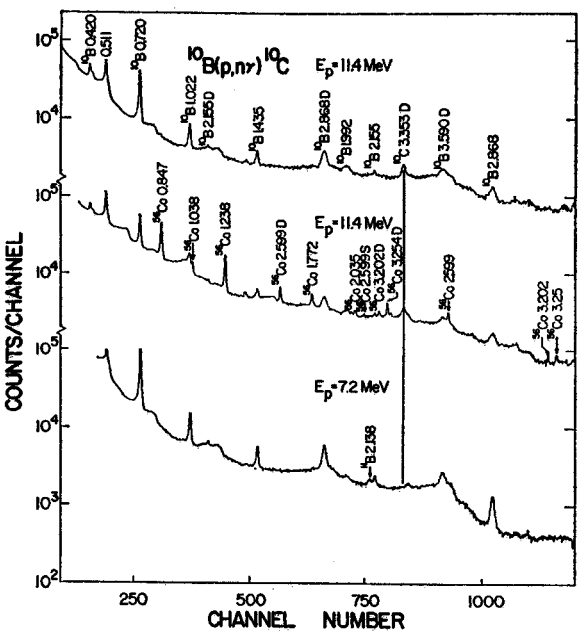

FIG. 1. Spectra of γ rays from the proton bombardment of ^{10}B. The upper spectrum was taken at a beam energy of 11.4 MeV, as was the middle spectrum, which also includes γ rays from a ^{56}Co source. The lower spectrum was taken below threshold for the production of ^{10}C in its first excited state. The vertical line indicates the position of the double-escape peak of the γ_1 ray from the ^{10}C first excited state.

with an error of ± 2 keV. The object of the present experiment was to measure the excitation energy of the first excited state with comparable accuracy.

A recent paper by Brunnader, Hardy, and Cerny[2] gives the results of their $^{10}B(^3He, t)^{10}C$ measurement (3.339 MeV[3] $\pm$15 keV) and a summary of previous measurements. They arrive at an average value for four different experiments of 3.344$\pm$0.008 MeV. The previous measurement with the smallest error[4] (3.35$\pm$0.01 MeV) was performed by observing the $^{10}B(p, n\gamma)^{10}C$ γ ray in NaI. In the present experiment the (p, n) reaction on ^{10}B was also used to produce the ^{10}C, but a Ge(Li) detector allowed a more precise measurement of the γ-ray energy.

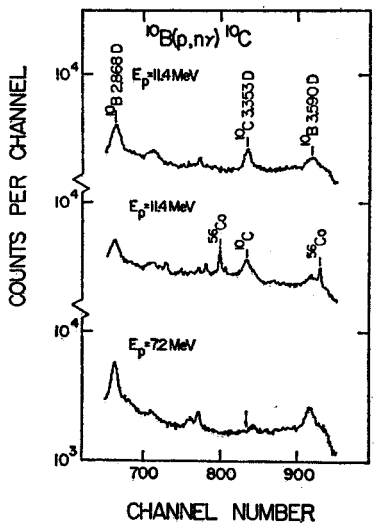

FIG. 2. Enlargement of region of interest of Fig. 1. The lower spectrum was taken at proton energy below threshold for the production of ^{10}C in its first excited state. The arrow indicates the position of the centroid of the ^{10}C peak.

II. EXPERIMENTAL PROCEDURE

An enriched ^{10}B (92.5%) target was bombarded by 11.4-MeV protons from the Michigan State University Sector Focused Cyclotron. The target thickness was about 2 MeV. The γ rays were detected with a 20-cm^2 Ge(Li) detector placed at an angle of 90° with respect to the beam to produce Doppler broadening symmetric about the γ-ray energy. Figure 1 shows spectra taken both with and without a ^{56}Co calibration source present

† Work supported in part by the National Science Foundation.
[1] J. M. Freeman, J. G. Jenkin, and G. Murray, Phys. Letters 22, 177 (1966).
[2] H. Brunnader, J. C. Hardy, and J. Cerny, Phys. Rev. 174, 1247 (1968).
[3] The mass excess quoted by the authors in Ref. 2 has been converted to excitation energy using the best value for the ground-state mass of ^{10}C (15.703 MeV).
[4] R. E. Segel, P. P. Singh, S. S. Hanna, and M. A. Grace, Phys. Rev. 145, 736 (1966).

TABLE I. Summary of experimental data on the first excited state of ^{10}C.

Experiment	Ref.	Excitation energy (MeV)
(p, n) threshold	a	3.336±0.020[b]
$^{10}B(^3He, t)^{10}C$	c	3.325±0.030[b]
γ decay	d	3.35±0.01
$^{10}B(^3He, t)^{10}C$	e	3.339±0.015[f]
γ decay	This work	3.3527±0.0015

[a] L. G. Earwaker, J. G. Jenkin, and E. W. Titterton, Nucl. Phys. 42, 521 (1963).
[b] These values are taken from Ref. 2, where they were corrected for the best value of the ^{10}C ground-state mass.
[c] N. Mangelson, F. Ajzenberg-Selove, M. Reed, and C. C. Lu, Nucl. Phys. 88, 137 (1966).
[d] Reference 4.
[e] Reference 2.
[f] See Ref. 3.

at the detector during the run. The double-escape peak from the first excited state of ^{10}C is bracketed by two ^{56}Co γ rays, the energies of which are known to within 0.25 keV. Over-all resolution for the ^{56}Co γ rays was 11-keV full width at half-maximum (FWHM), while the resulution for the γ rays from the target was 14 keV FWHM. Additional runs were taken with a proton energy of 7.2 MeV, which is below the 8.5-MeV threshold for production of ^{10}C in its first excited state. The lower spectrum of Fig. 1 is a run below threshold, and one can see that the peak of interest is absent but that there is a small unidentified peak 20 keV above it. Figure 2 shows the region surrounding the peak of interest.

Calibration curves were established using the γ rays from ^{56}Co.[5] An energy of 3.3521 MeV was assigned to the γ ray from the first excited state of ^{10}C, with an error of 1.5 keV. This error assignment is based on contributions from three sources. The first is uncertainty in the calibration curve. The second is due to possible gain shifts between runs, which was minimized by making use of digital stabilization of the electronics and analyzer. The third contribution is based on background subtraction, which was made difficult by the presence of the small peak about 20 keV higher in energy than the peak of interest. This peak produces a small asymmetry in the shape of the ^{10}C two-escape peak. The maximum deviation in the centroid measurement due to the contribution of this peak and other background uncertainities was 0.5 keV. Each of the other two above-mentioned sources of error was estimated to contribute less than 0.5-keV uncertainty. Statistical errors were small compared to these sources of error. The three errors were added linearly, since they are basically estimates of maximum systematic error.

Correcting the γ-ray energy for the recoil energy of the ^{10}C nucleus, the excitation energy of the state in ^{10}C is 3.3527 MeV with an error of 1.5 keV. This value is in agreement with the average of previous measurements (Table I), and has an uncertainty comparable to that in the ground-state mass.

TABLE II. γ-ray transitions in ^{10}B.

Transition energy (keV)	Transition
720.1±2.0	(1-0)
1022.0±2.0	(2-1)
1435.1	(4-3), (3-1)
2155.6±2.0	(3-0)
2868.5±2.0	(4-1)

TABLE III. Energy levels in ^{10}B.

Level	Energy (keV) This work	Ref. 6
0	Ground state	Ground state
1	720.4±1.9	717.3±0.8
2	1742.3±2.3	1740±2
3	2155.4±1.9	2154±3
4	3589.7±2.2	3585±4

Several other γ rays were identified with states in ^{10}B produced by the reaction $^{10}B(p, p')^{10}B^*$. The energies of the associated transitions (γ-ray energies corrected for the recoil energy of the ^{10}B nucleus) are given in Table II. The 413-keV γ ray corresponding to the transition from the 2155- to the 1742-keV level was also observed, but was outside the range of the calibration and was not used in calculating the energy levels. The 1435-keV peak is an unresolved doublet correspondng to the 3590- to 2155-keV transition and the 2155- to 720-keV transition as observed by Segel *et al.*[4] The γ-ray energies obtained from cascades are consistent to well within the errors from the direct transitions. A weighted average of the cascade and direct values was used to assign the excitation energies given in Table III. The previous values of the low-lying levels of ^{10}B from the compilation of Lauritsen and Ajzenberg-Selove[6] are also given in Table III. The agreement is good except for a small discrepancy in the first-excited-state energy.

[5] P. H. Barker, R. D. Connor, Nucl. Instr. Methods 57, 147 (1967).

[6] T. Lauritsen and F. Ajzenberg-Selove, Nucl. Phys. 78, 1 (1966), especially p. 110.